

Katholieke
Universiteit
Leuven



FACULTEIT
WETENSCHAPPEN

DEPARTEMENT
NATUURKUNDE

Anisotropy-induced magnetic properties of layered structures and arrays

Promotoren:
Prof. Dr. Y. Bruynseraede
Dr. K. Temst

Proefschrift ingediend tot het
behalen van de graad van
Doctor in de Wetenschappen
door

Eddy Kunnen

2000

Dankwoord

Graag wil ik mijn oprechte dank uitspreken aan de volgende mensen welke onontbeerlijk waren voor het tot stand komen van dit werk.

Mijn promotor Prof. Dr. Y. Bruynseraede en zijn team voor het uitbouwen en onderhouden van het laboratorium, het financieren van de nodige scholen en werkverblijven, en het naar buiten brengen van zijn klare en kritische geest. 'Meten is weten' is meer dan een uitspraak, het is werkwijze, een manier van onderzoek doen. Dit kan enkel in een degelijk uitgebouwd laboratorium met de nodige gespecialiseerde mensen waarin het gereedschap van de onderzoeker de verschillende aangeboden technieken en internationale contacten zijn. Bedankt hiervoor.

Mijn copromoter Dr. Kristiaan Temst voor de nodige steun en raad in het veldwerk, het verwerken van al mijn 'eerste versies' (thesis, IWT, artikels, ...) en het geven van feedback hierop, Als doctoraatsstudent heb ik dankzij jou van een voortreffelijke begeleiding mogen genieten, ik hoop dat je dit nog voor vele anderen mag zijn, bedankt hiervoor.

The other members of the jury, Prof. Dr. G. Borghs, Prof. Dr. V.V.M Moshchalkov, Prof. Dr. M. Rots, Prof. Dr. C. Van Haesendonck and Prof. Dr. H. Zabel for reading my thesis and the given advise and remarks. The view of specialized and experienced persons is essential for making improvements. Thank you for your efforts.

Dr. Margriet Van Bael, Ivan Gordon en Martin Lange voor de SQUID metingen. Dr. Ruud Vullers, Dr. Alexander Volodin en Maarten Cannaeerts voor de AFM en MFM metingen. Eric Seynaeve voor de SEM experimenten. Johan Swerts voor de MOKE metingen en de neutronenondersteuning. Dankzij jullie inzet en tijd was het mogelijk meer inzicht te verwerven via de multi-instrumentele infrastructuur van het laboratorium. Bedankt voor jullie tijd.

Christophe Coeck, Jef Haesaerts, Marianne Jennes, Philippe Mispelter, Herman Tuyls, Marc Verbrugge en de mensen van de werkplaats. Zonder jullie is onderzoek onmogelijk daarom bedankt voor de vlotte hulp die ik overal kreeg.

Dr. André Vantomme, Suzy Hogg en Annelies Falepin voor de RBS metingen en de samenwerking. Bedankt voor jullie tijd.

Dr. Laszlo Bottyan, Dr. Lajos Denes Nagy, Dr. Johan Meersschaut Dr. Johan Dekoster, Dr. Stefan Degroote and Marton Major for the fruitful cooperation on the spin flop phenomenon and the IMBL support. Thanks for the efforts.

Dr. Andreas Hoser and Dr. Helmut Fritzsche for the excellent support before, during and after, the beam time at the Hahn-Meitner-Institute Berlin. Thanks for the nice results.

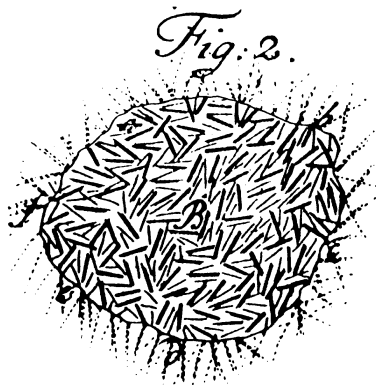
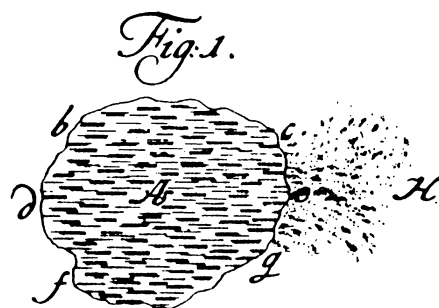
Het Vlaams Insituut ter bevordering van het Wetenschappelijk Technologisch onderzoek in de industrie (IWT) voor de financiële ondersteuning.

Mijn bureaugenoten (?) Dr. Kris, Vital, Rik en Geert, voor de uitgebreide wetenschappelijke discussies en de echte *ontiegelijke* lol die we hebben beleefd en nog steeds beleven binnen en buiten het bureau. Dat dit nog lang moge duren.

De ruime vriendenkring Ruud, An, Lieve, Ivan, ... voor de toffe momenten die we samen hebben doorgebracht en nog doorbrengen, feestjes, recepties, Nieuwjaar, de sportwedstrijden, kienen, ... het zijn de mensen rondom je die het onderzoek aangenaam maken. Bedankt.

Tenslotte wil ik mijn 'thuis' en mijn familie bedanken voor de steun en het dragen van de momenten dat ik er niet was. Woorden hiervoor zijn overbodig en schieten tegelijkertijd tekort, dit zegt ons samenzijn, het enige dat echt telt.

Eddy Kunnen
Juni 2000



An illustration taken from the *Principia Rerum Naturalium*, a treatise published in 1734 by Emanuel Swedenborg (1688-1772), Swedish scientist, philosopher, and theologian. The drawings indicate his view of the difference between magnetized (Fig. 1) and unmagnetized (Fig. 2) iron. They are in remarkable agreement with the modern domain theory of ferromagnetism, which came almost two centuries later [Cul72].

Contents

Chapter 1 Introduction	10
Chapter 2 Theoretical aspects and overview of magnetic anisotropy studies	13
2.1 General aspects of ferromagnets	13
2.1.1 Anisotropy, magnetic domains and the magnetization process	13
• Introduction	13
• Anisotropy	15
• Shape anisotropy	15
• Crystal anisotropy	18
• The magnetization process	21
2.1.2 Electrical transport properties	22
• Introduction	22
• The anisotropic magnetoresistance effect	23
• The pseudo Hall effect	27
2.2 Antiferromagnetically coupled Fe/Cr multilayers	29
2.2.1 Introduction	29
2.2.2 The structure of Fe/Cr superlattices	30
2.2.3 Interlayer exchange coupling	31
• IEC due to quantum interferences	34
• IEC due to antiferromagnetism in the spacer layer	37
• Discussion	39
2.2.4 Giant Magnetoresistance	40
2.2.5 The spin flop transition	44
2.3 Antiferromagnetism of Cr films	45
2.3.1 Introduction	45
2.3.2 The magnetic structure of bulk Cr	46

• The spin density waves	46
• The origin of the Cr antiferromagnetism	49
• The magnetic reflections	52
• Effect of stress	55
• Magnetic field dependence	56
2.3.3 State-of-the-art	57
2.4 Magnetic anisotropy in magnetic arrays	61
2.4.1 Introduction & state-of-the-art	61
Chapter 3 Experimental techniques	64
3.1 Preparation	64
3.2 Characterization	68
3.2.1 Diffraction	68
• RHEED measurements	70
• X-ray diffraction	72
• Structural characterization	73
• Synchrotron Mössbauer Reflectometry	74
• Neutron diffraction	76
• Neutron Reflectometry	79
• High angle neutron diffraction	84
3.2.2 The Magneto-Optical Kerr effect	89
3.2.3 Rutherford Backscattering	94
3.2.4 Scanning Probe Microscopy	95
3.2.5 Resistivity measurements	97
Chapter 4 Experimental results	99
4.1 The magnetic structure of Fe/Cr multilayers	79
4.1.1 Introduction	99
4.1.2 Preparation and characterization	99
4.1.3 Unpolarized Neutron Reflectometry	105
4.1.4 Polarized Neutron Reflectometry	111
• In zero field	111

• Polarized neutron reflectivity in magnetic field	117
4.1.5 The nature of the spin flop transition	121
• The interlayer domain wall model	121
• The intralayer domain wall model	123
4.1.6 Magnetization measurements	124
4.1.7 Resistivity measurements	129
4.1.8 Synchrotron Mössbauer Reflectivity (SMR)	138
4.1.9 Simulations	140
4.1.10 Discussion and conclusions	144
4.2 The magnetic structure of thick Cr films	145
4.2.1 Introduction	145
4.2.2 Preparation and characterization	148
4.2.3 Neutron diffraction measurements on MgO substrate	154
4.2.4 The magnetic structure of a MgO(001)/Cr(5000Å) film	157
• Temperature dependence	157
• Magnetic field dependence	163
• Discussion	165
4.2.5 The magnetic structure of a MgO(001)/Cr(5000Å)/Fe(75Å)/Ag(75Å) film	168
• Temperature dependence	168
• Magnetic field dependence	172
• Discussion	177
4.2.6 The magnetic structure of a MgO(001)/Cr(50Å)/[Au(30Å)/Cr(30Å)] ₁₀ Cr(5000Å) film	177
• Temperature dependence	177
• Magnetic field dependence	181
• Discussion	182
4.2.7 The magnetic structure of an annealed MgO(001)/	

Cr(5000Å) film	183
• Temperature dependence	183
• Magnetic field dependence	187
• Discussion	189
4.2.8 Discussion	191
4.3 The magnetic structure of a Ni array	192
4.3.1 Introduction	192
4.3.2 Preparation and structural characterization	192
4.3.3 Magnetic characterization	196
4.3.4 Resistivity properties	202
• The anisotropic Magnetoresistance	203
• The pseudo Hall effect	209
4.3.5 Discussion	213
Chapter 5 Conclusions	215
References	219
Symbols	233
Abbreviations	235
Nederlandse samenvatting	237
Publications	254
Curriculum Vitae	256

Chapter 1

Introduction

The subject of this thesis is situated in the field of magnetic thin films and small structures. Modern fabrication techniques nowadays permit to control the thickness of structures down to the atomic level while the lateral size is reduced below the micrometer range. Quantum mechanic and size effects become more and more important for the understanding of the physical features of these systems. An extra motivation for the research of this scaling down are the industrial needs. The evolution in IC's demands a steady increase of the amount of circuits/memory cells per unit area. In addition the reading/writing speeds push the devices towards their limits. A recent example where sciences encountered the industry is the discovery of the Giant Magnetoresistance effect (GMR) [Bai88]. The resistivity of these materials is strongly affected by the probed magnetic field making them ideal sensors [Prinz95, Russek99]. Today, GMR-based reading heads are already used in the hard disk of a PC [Fer99, chapter D11, Boeck99]. Another application are the Magnetic Random Access Memories (MRAM) [Sim95, Fer99 chapter D6, Boeve99, Parkin99, Tehrani99]. Such MRAM's offer significant advantages like their non-volatile character, simplicity of the structure, high density and low dissipation [Wang99, Won99]. Apart from the applications, these phenomena attract a lot of attention from the fundamental side [Himp98]. Therefore, this work intends to

gain more insight in the physical phenomena on which these systems are based and to contribute to their fundamental understanding.

We will focus on the area of *magnetic anisotropy* and this topic will be approached using three model systems. Firstly, the archetype of the GMR material, Fe/Cr multilayers, will be studied for its magnetic properties. These magnetic multilayers are already profoundly studied from various points of view [Hei94a, Hei94b]. Still, as we will show, major new phenomena related to the magnetic anisotropy can be observed in these systems. The anisotropy will play an important role in the direction of the magnetization in the epitaxial Fe layers and its re-orientation when an external field is applied.

Secondly, inspired by recent observations, single epitaxial Cr films are investigated. Thick epitaxial chromium films challenge physicists because of their complex anisotropic magnetic phase diagrams[Faw88, Zab99]. Our study aims at a better understanding of the anisotropical features in these magnetic phase diagrams. Finally, in the framework of magnetization processes and domain structures, a Ni array (maze or antidotlattice) is studied. Artificially made holes in a Ni film induce a magnetic shape anisotropy, as will be shown.

In summary, each of the above mentioned systems exhibits particular types of *anisotropy-induced magnetic properties*. The results, embedded in the necessary background, will be presented in the following way :

In Chapter 2, the theoretical aspects and an overview of the magnetic anisotropy studies are given. In the first section, the necessary concepts

of magnetism will be introduced. Subsequently, an introduction and presentation of the state-of-the-art for the three topics that are dealt with, i.e. Fe/Cr multilayers, thick Cr films and Ni arrays, is given.

Chapter 3 presents the experimental framework in which the research is carried out. Depending on the desired information different techniques are used. A basic introduction towards the principles of these tools is given.

The experimental results are discussed in Chapter 4. A first section will deal with the magnetic features of an antiferromagnetically coupled Fe/Cr multilayer. After the preparation and structural characterization, the magnetic properties like domain structure and magnetization process are investigated. A new type of spin flop transition was discovered and its properties have been systematically investigated.

In the second section of Chapter 4, the magnetism in thick epitaxial Cr layers is taken under consideration. Their magnetic phase diagram shows anisotropic peculiarities that are not well understood. In order to shed more light on this problem, the substrate on which the films are grown is varied and the induced effects on the magnetic phase diagram are evaluated.

In the third section of Chapter 4 the emphasis shifts from crystal anisotropy towards shape anisotropy. The influence of holes on the magnetic properties of a Ni film is investigated [Cow97, Torr99, Jia97a, Jia97b]. For the interpretation a parallel study of the properties of a flat Ni film is carried out. It will be presented that the

presence of the holes creates a magnetic anisotropy in the Ni film.

An overview of the main conclusions is given in Chapter 5.

Chapter 2

Theoretical aspects and overview of magnetic anisotropy studies

In what follows a brief introduction to the used concepts and physical phenomena related to magnetism is given.

Some general aspects of ferromagnets such as magnetic domains, anisotropy, the magnetisation process and the resistive properties will be treated in 2.1. Paragraph 2.2 is devoted to the study of Fe/Cr multilayers and the spin flop transition. In 2.3 the properties of Cr as bulk and as thin film will be reviewed. At the end, paragraph 2.4 will introduce magnetic arrays.

2.1 General aspects of ferromagnets

In this chapter general phenomena related to ferromagnets are treated. A more detailed description can be found in [Schä98, Fer99, Hei94a, Hei94b, Cul72, Cam82, Jac75, Ste54, Fey77].

2.1.1 Anisotropy, magnetic domains, and the magnetization process

- **Introduction**

Due to the itinerant exchange interaction, the 3d ferromagnetic materials Fe and Ni exhibit a spontaneous magnetization below their Curie temperature. A regular piece of Fe or Ni is not uniformly magnetized but consists of variously oriented magnetic domains. Within a magnetic domain the magnetization \mathbf{M} has a uniform direction. Domain walls wherein the magnetization changes orientation separate these magnetic domains, see fig. 2.1. The reason is the minimization of the dipole energy (also known as stray field energy or magnetostatic energy). Infinite subdivision into smaller domains is energetically not favorable as the formation of a domain wall increases the exchange energy [Schä98, Fey77]. A schematic presentation of this principle is given in fig. 2.1. where a domain wall is created so that the volume of the stray field is reduced.

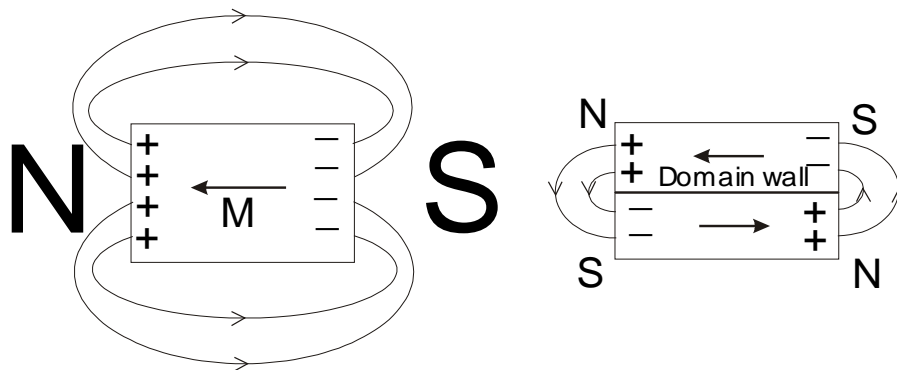


Fig. 2.1 The stray field energy is lowered by creating magnetic domains. The formation of a domain wall goes at the expense of the exchange energy and an equilibrium state is obtained.

The magnetization vectors in these domains are lying along well defined so called 'easy axes'. These axes also influence the shape of the

magnetization loop and therefore induce an anisotropic behaviour. The origin of this magnetic anisotropy can be related to several phenomena of which the two most relevant to this work will be treated in the following paragraphs.

- **Anisotropy**

The term 'anisotropy' refers to the orientation dependence of the studied properties. In this work, the magnetic anisotropy will play a central role and we may distinguish : shape anisotropy, crystal anisotropy, surface anisotropy, magneto-elastic anisotropy, growth-induced anisotropy, exchange anisotropy,

The two most relevant anisotropies connected to this work are the crystal anisotropy or magnetocrystalline anisotropy and the shape anisotropy. The crystal anisotropy will become important for explaining the magnetization behaviour in the Fe/Cr superlattices while the magnetization process in Ni arrays is dominated by the shape anisotropy.

As mentioned above, these anisotropies induce preferred directions for the magnetization. Pulling the magnetization away from these axes by applying a magnetic field costs energy. The total anisotropy energy G_{total} is given by [Fer99] :

$$G_{total}(\vec{m}) = G_{crystal}(\vec{m}) + G_{shape}(\vec{m}) + \dots \quad (2.1)$$

In eq. (2.1) the Gibbs free energy density G is used for describing these anisotropies in a single domain sample. The unity vector indicating the magnetization direction is denoted by \mathbf{m} .

- **Shape anisotropy**

It is commonly observed that the magnetization of a body is coupled to its shape. For example, in a compass needle the magnetization is aligned along the needle axis or in a thin film the magnetization is preferentially lying in the film plane. Shape anisotropy can be understood in terms of stray fields. As it costs energy to build up a magnetic field, the structure tries to lower its energy by reducing its stray field. It is exactly the same physical phenomenon that is at the origin for the formation of magnetic domains. The energy E_d associated with a magnetic field \mathbf{H}_d is :

$$E_d = \frac{1}{2} \mu_0 \int_{\text{all space}} H_d^2 dV . \quad (2.2)$$

This energy is always positive and becomes zero if the stray field H_d is everywhere zero. Expression 2.2 is mathematically equivalent to [Schä98]:

$$E_d = -\frac{1}{2} \int_{\text{sample}} \vec{H}_d \cdot \vec{M} dV \text{ with } \vec{M} = M_s \cdot \vec{m} , \quad (2.3)$$

and $M_s =$ saturation magnetization.

The integral in eq. (2.3) can be interpreted as the energy that the magnetization has in its demagnetizing field. The stray field inside the material is called demagnetization field as this fields tends to demagnetize the material. Therefore the subscript 'd' is used.

In order to interpret this energy in relation to the shape of the sample, the demagnetization field as function of the distribution of the magnetization should be calculated. The potential theory gives the following solution for this

problem. The demagnetization field \mathbf{H}_d at position \mathbf{r} can be written as :

$$\vec{H}_d(\vec{r}) = -\text{grad } \Phi_d(\vec{r}) , \quad (2.4)$$

with the demagnetization potential Φ_d given by :

$$\Phi_d(\vec{r}) = \frac{M_s}{4\pi\mu_0} \left[\int_{\substack{\text{sample} \\ \text{volume}}} \frac{\lambda_v(\vec{r}')}{|\vec{r} - \vec{r}'|} dV' + \int_{\substack{\text{sample} \\ \text{surface}}} \frac{\sigma_s(\vec{r}')}{|\vec{r} - \vec{r}'|} dS' \right] \quad (2.5)$$

with the magnetic volume charge density λ_v :

$$\lambda_v = \text{div } \vec{m} \quad (2.6)$$

and the magnetic surface charge density σ_s :

$$\sigma_s = \vec{m} \cdot \vec{n} , \quad \vec{n} \text{ the outward directed surface normal}$$

In the simple case of an ellipsoid with volume V and axes a , b , c , an analytical solution for the stray field energy is found :

$$E_d = \frac{1}{2\mu_0} V \vec{M}^t \cdot \vec{N} \cdot \vec{M} \quad (2.7)$$

with \mathbf{N} the demagnetization tensor :

$$\begin{pmatrix} N_a & 0 & 0 \\ 0 & N_b & 0 \\ 0 & 0 & N_c \end{pmatrix}$$

for which analytical expressions for N_a , N_b and N_c can be found in [Schä98]. As an example, the

tensors for an isotropic sphere and the limit of an infinite thin film expanded in the xy plane are given by :

$$N_{sphere} = \begin{pmatrix} 1/3 & 0 & 0 \\ 0 & 1/3 & 0 \\ 0 & 0 & 1/3 \end{pmatrix}, \quad N_{film} = \begin{pmatrix} 0 & 0 & 0 \\ 0 & 0 & 0 \\ 0 & 0 & 1 \end{pmatrix} .$$

More explicitly, for the case of an infinite thin film the demagnetization energy can be written as :

$$E_d(\vec{M}) = \frac{V}{2\mu_0} M_s^2 \cos^2(\theta) . \quad (2.8)$$

In eq. 2.8, θ is the angle between the magnetization and the normal to the plane. From the principle of minimization of the energy E_d , the magnetization is preferentially lying in the plane, $\theta = 90$ deg. In this configuration the stray field is zero.

In some cases other anisotropies than the shape anisotropy can have a more important contribution to the total anisotropy energy. An example of this phenomenon is the surface anisotropy. Atoms sitting at the surface are feeling a different environment than bulk atoms. For example a thin layer of Co atoms surrounded by Pt or Pd can exhibit a vertical anisotropy ($\mathbf{M} \perp$ to plane of surface) as observed in multilayer structures of these materials[Broe91, Zep89].

- **Crystal anisotropy**

Crystal anisotropy finds chiefly its origin in the spin - orbit coupling. It causes the magnetization

to align more easily along specific crystal axes and can therefore be seen as a kind of coupling of the magnetization to the crystal lattice. Figure 2.2 shows part of the magnetization loop of a spherical single Fe crystal along the different crystal axes. For a sphere the shape is uniform and therefore the shape anisotropy energy is constant. Saturating along the Fe[111] or Fe[110] direction (hard axes) requires a higher field than for the Fe[100] axis (easy axis). For Ni (fcc) the easy axis is Ni [111]. This extra energy for aligning the magnetization along a hard axis can be generally expressed as function of components (α_1 , α_2 , α_3) of \mathbf{m} projected on the crystal axes [Akul29]:

$$E_{crystal} = b_0 + \sum_i b_i \alpha_i + \sum_{i,j} b_{ij} \alpha_i \alpha_j + \sum_{i,j,k} b_{ijk} \alpha_i \alpha_j \alpha_k + \dots \quad (2.9)$$

The corresponding coefficients of the expansion $b_{ijk\dots}$ describe the material. Based on symmetry arguments this expression can be simplified for a cubic crystal in the following way [Fer99]:

$$E_{crystal}(\vec{m}) = K_0(T) + K_1(T) (\alpha_1^2 \alpha_2^2 + \alpha_2^2 \alpha_3^2 + \alpha_3^2 \alpha_1^2) + K_2(T) (\alpha_1^2 \alpha_2^2 \alpha_3^2) + \dots$$

Firstly, K_0 is an offset energy independent of the angle and is therefore usually ignored [Cul72]. Secondly, in the further used configuration the magnetization is initially lying in-plane as caused by the strong shape anisotropy. Also for each configuration the field will be parallel to the plane. For every studied situation α_3 can be assumed to be zero giving :

$$E_{crystal}(\vec{m}) = \frac{K_1(T)}{4} \sin^2(2\theta) \quad (2.10)$$

In this expression θ is the angle between the magnetization and a crystal axis. This anisotropy term will become important in describing the magnetization process in the Fe/Cr multilayers in the particular case of the spin flop transition. Finally, figure 2.3 shows the values for K_1 in the case of bulk Fe.

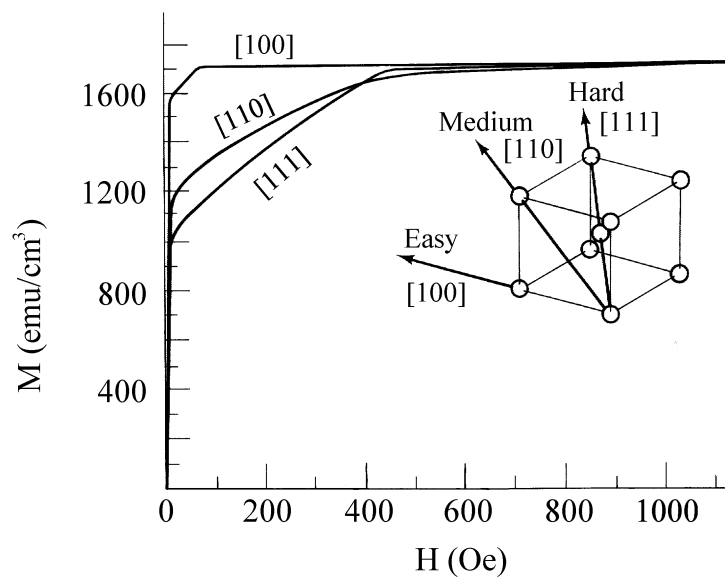


Fig. 2.2 Part of the magnetization loop for a spherical single crystalline Fe sample taken along the different crystal directions is shown. The curves show that the magnetic behaviour is coupled to the crystal lattice and the interaction is therefore named crystal anisotropy.

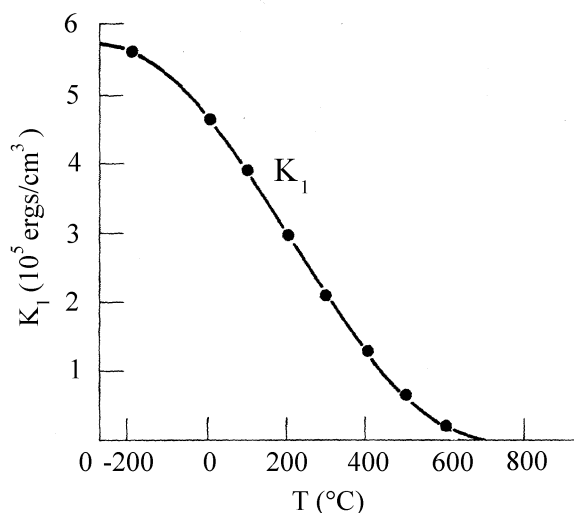


Fig. 2.3 The anisotropy constant K_1 for bulk Fe as function of temperature.

- **The magnetization process**

The evolution of the magnetic domains during the magnetization process is schematically shown in fig. 2.4 for a disk made of single crystal Fe. In zero field the magnetization in the different domains lies along the easy Fe[100] axes. If a field is applied, at first instance the domain walls move so that the domains with their magnetization along the field grow at the expense of the others [Cul72]. Also sometimes observed is the nucleation of a domain wall as the magnetic field can induce magnetic charges at the surface [Schä98]. Typically in low fields the magnetization process is dominated by domain walls. If the domain walls are pinned to the defects the magnetization changes abruptly (Barkhausen effect) inducing energy losses and therefore an hysteresis effect. For higher fields domain rotation comes in to play. Having a single domain the field will finally pull

the magnetization vector away from the easy axes towards the field direction. The latter is a reversible process.

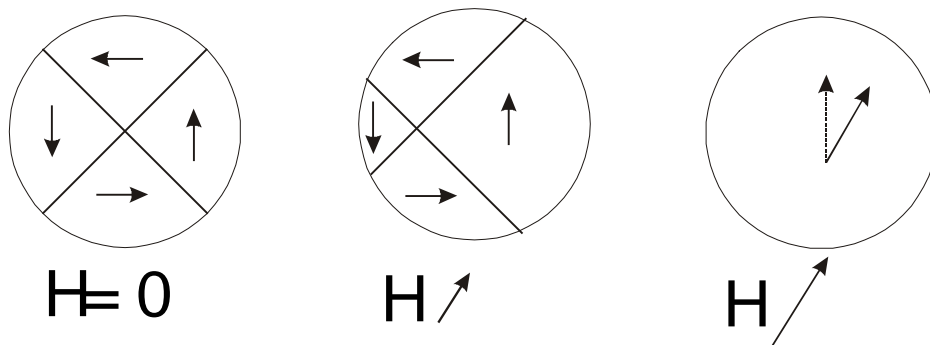


Fig. 2.4 The magnetization in the different domains is shown as function of field. For small fields domain wall movement is the dominant process while for higher fields domain rotation is important.

2.1.2 Electrical transport properties

• Introduction

Based on the symmetry of the problem a dependence of the transport (resistive) properties on the mutual orientation of magnetisation and current can be expected.

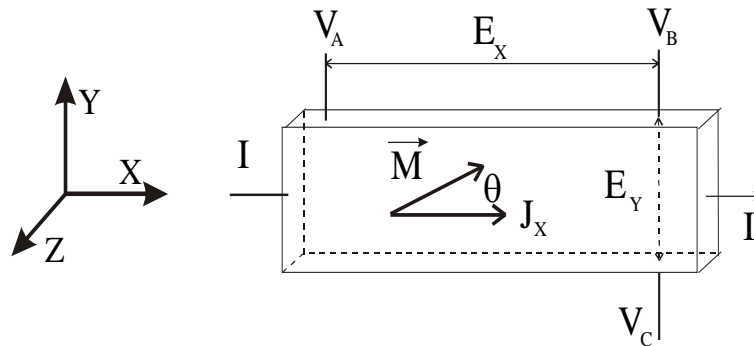


Fig. 2.5 *Used geometry for the discussion of the resistive properties.*

The measurement geometry in which these phenomena are discussed is shown in fig. 2.5. The electric field is denoted by \mathbf{E} , the current density by \mathbf{J} , the voltages at the different contacts by V_x , and for the angle between the magnetisation and current θ is used.

The description of such resistive anisotropic features for a magnetically saturated isotropic crystal can be done by the following relation for the electric field $\mathbf{E}=\boldsymbol{\rho}\mathbf{J}$ and the corresponding resistivity tensor $[\rho_{ij}]$ [Cam82] :

$$\vec{E} = \rho_{\perp}(B)\vec{J} + [\rho_{\parallel}(B) - \rho_{\perp}(B)]\left[\vec{m} \cdot \vec{J}\right]\vec{m} + \rho_H(B)\vec{m} \times \vec{J} \quad (2.11)$$

for

$$[\rho_{ij}] = \begin{bmatrix} \rho_{\perp}(B) & -\rho_H(B) & 0 \\ \rho_H(B) & \rho_{\perp}(B) & 0 \\ 0 & 0 & \rho_{\parallel}(B) \end{bmatrix} \quad \text{with } \vec{J} = \text{current vector}$$

where

$$\rho_{ij} = \rho_{ij} + \rho_{ij}^0(B) \quad . \quad (2.12)$$

The coefficients ρ_{ij} that are independent of B are called the 'spontaneous' or 'extraordinary' coefficients. The field dependent terms $\rho_{ij}^0(B)$ are the ordinary coefficients. For the introduction of the anisotropic magnetoresistance and the pseudo Hall effect which are intrinsic properties we will limit ourselves in the following discussion to the field independent terms.

- **The anisotropic magnetoresistance effect**

The observation that the resistivity of a ferromagnetic material depends on the angle θ between the magnetisation and the current is called the anisotropic magnetoresistance effect (AMR) or spontaneous resistivity anisotropy. Further development of the above description taking the definition of resistivity (eq. 2.13) into account [Cam82] :

$$\rho = \vec{E} \cdot \vec{J} / |\vec{J}|^2 \quad (2.13)$$

gives

$$\rho = \rho_{\perp} + (\rho_{//} - \rho_{\perp}) \cos^2 \theta \quad . \quad (2.14)$$

This relationship between the resistivity and the magnetic moment is qualitatively evaluated in figure 2.6. The resistivity is maximal ($\rho_{//}$) if the magnetisation is parallel or antiparallel to the current. A minimum in the resistivity (ρ_{\perp}) is achieved for the magnetisation being perpendicular to the current.

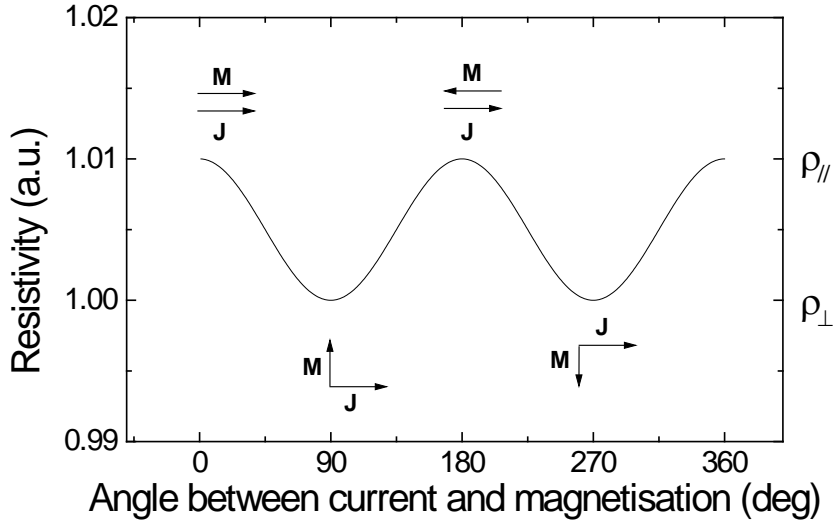


Fig. 2.6 The resistivity as function of the angle between the current and the magnetisation is shown according to eq. 2.14. A maximum is obtained for a parallel/antiparallel alignment while the resistivity is minimal for a perpendicular geometry.

In addition, if the magnetisation is isotropically distributed over all the directions in the three-dimensional space the resistivity is given by the following formula :

$$\rho_{B=0}^{3D} = \frac{\rho_{//} + 2\rho_{\perp}}{3} \quad . \quad (2.15)$$

On the other hand, an isotropical two-dimensional distribution, like in a thin film, leads to the following expression for the resistivity in zero field :

$$\rho_{B=0}^{2D} = \frac{\rho_{//} + \rho_{\perp}}{2} \quad . \quad (2.16)$$

The AMR effect originates from the spin orbit coupling and the precise mechanism can vary from system to system (3d metals, alloys consisting 4f impurities,...)[Con92]. For the transition metals Smit [Smit51] calculated the resistivity anisotropy and good agreement with the experiments is observed. The model is based on the theory of Mott for transition metals [Mott36].

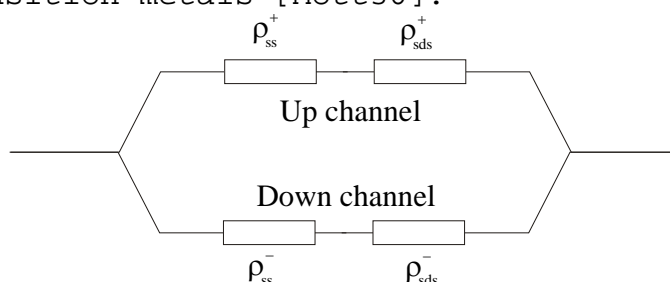


Fig. 2.7 *The two channel model of Mott for describing the conductivity in 3d metals.*

Mott assumed that the conductivity and thus the resistance of these metals is mostly due to the delocalised 4s electrons. Secondly, the spin flip processes during scattering from an s to an s state (ρ_{ss}) or from a s into a s via a d state (ρ_{sds}) are neglected. This gives the two current model for the resistivity presented in figure 2.7 where the current is carried by the 4s spin up (+) and 4s spin down (-) electrons.

Below the Curie temperature the 3d states having their spin parallel to the magnetization (spin up) are mostly occupied and cannot be scattered into. Most of the current is therefore carried by the 4s spin up electrons and the resistivity is determined by the ρ_{sds}^+ scattering.

The anisotropy comes into play via the spin orbit coupling. It causes a mixing of parallel and antiparallel 3d states so there are always empty parallel 3d states present. These empty 3d states

are not equally distributed in space but in such a way that an electron moving parallel to the magnetisation faces more possibilities for scattering than an electron in a transversal motion resulting in $\rho_{//} > \rho_{\perp}$.

The AMR-effect in the pure 3d metals amounts about 2% for Ni while it remains below 1% for Fe and Co. On the other hand in NiFe and NiCo alloys up to 20 % change is observed [Smit51]. The effect is weakly temperature dependent. In the context of this work the AMR-effect will be used for determining the direction of the magnetization.

- **The pseudo Hall effect**

A direct consequence of the difference in ρ_{\perp} and $\rho_{//}$ is the manifestation of a voltage perpendicular to the current direction. This effect is also often called planar Hall effect. The reference to the name Hall is only because of the 'perpendicular geometry'. One should keep in mind that the physics of the ordinary Hall effect and the pseudo Hall effect (PSHE) are different. The existence of the PSHE follows rigorously from eq. 2.11. Taking the geometry in fig. 2.5, the following equations are derived :

$$\begin{aligned}
 E_x &= J_x \rho_{\perp} + J_x (\rho_{//} - \rho_{\perp}) \cos^2 \theta, \\
 E_y &= J_x (\rho_{//} - \rho_{\perp}) \sin(\theta) \cos(\theta) = \frac{J_x}{2} \sin(2\theta) .
 \end{aligned}
 \tag{2.17}$$

The symbols E_x , E_y and J_x , J_y denote the x and y components of resp. the electric field \mathbf{E} and the current density \mathbf{J} . This formula is visualized in fig. 2.8. The PSHE is zero for a parallel/antiparallel or perpendicular arrangement for the magnetisation and the current. It reaches a extremal value in the intermediate cases at 45,

135, 225 and 315 degree. Furthermore, the PSHE is positive in the first and the third quadrant and negative in the second and the fourth quadrant. It follows that for two antiparallel spins the PSHE should be added. If there is a PSHE due to a magnetic component along the 45-225 degree axis it can only be cancelled having another magnetic component along the 135-315 degree axis.

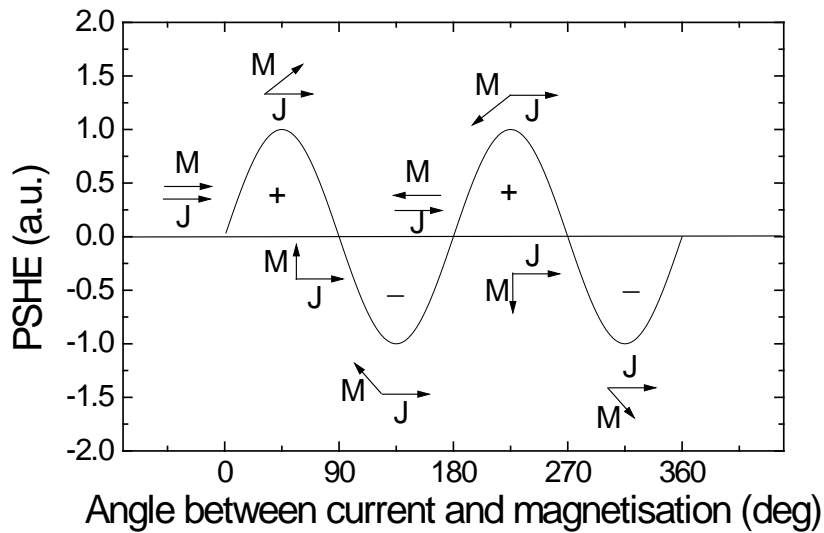


Fig. 2.8 A schematic diagram of the PSHE as function of the angle between the magnetisation and the current is shown.

This effect will be used in addition to the AMR to obtain information on the direction the magnetisation in the sample. In this respect, the PSHE is related to components of the magnetisation that are not perpendicular or parallel to the current. Such information is complementary to the AMR-effect since the latter is only related to the netto magnetisation component and does not reveal the composition.

Further, because of its dependence on $\sin 2\theta$, the PSHE is especially of interest for the case of an artificial antiferromagnet like antiferromagnetically coupled Fe/Cr superlattices. Opposite pointing spins induce the same PSHE and it can therefore be used to detect antiferromagnetically spins that are not directed along or perpendicular to the current direction.

2.2 Antiferromagnetically coupled Fe/Cr multilayers

2.2.1 Introduction

The development of modern deposition techniques and accessories made it possible to control thin structures down to an atomic level and to reveal new physics related to the quantum nature of the electron. In 1986 Grünberg [Grün86] discovered an antiferromagnetic alignment of the Fe magnetisations in a Fe/Cr/Fe trilayer. This phenomenon, known as Interlayer Exchange Coupling (IEC), is the origin of the Giant Magnetoresistance effect (GMR) which was measured by Fert et al. in 1988 [Bai88]. They found in such a Fe/Cr structure a resistivity drop of a factor two if a field was applied parallel to the layers. Parkin showed that the coupling between two magnetic layers oscillates as function of the thickness of the spacer layer [Par91]. Since then, a lot of interest has been paid to the study of these features and to integrate them in applications.

In this thesis we will focus on the Fe/Cr system grown on MgO(001) substrates. The IEC- and GMR-effect are already extensively studied up to now and therefore our aim is to gain more insight in the magnetisation process in these structures. After shortly introducing the structure of the Fe/Cr superlattices, (paragraph 2.2.2), the IEC

(paragraph 2.2.3) and the related GMR (paragraph 2.2.4) are explained. In the last paragraph (2.2.5) the spin flop transition will be discussed.

2.2.2 The Structure of Fe/Cr superlattices

Iron and Cr are both bcc and have a 0.6% small lattice mismatch which allows a crystallographically oriented growth. Furthermore, Fe grows epitaxial on MgO. The MgO(001) planes are parallel to the Fe(001) planes. Secondly, the in-plane MgO[110] direction is parallel with the Fe[100] axis. Such an epitaxial relationship is denoted as MgO(001)[110]//Fe(001)[100], see fig. 2.9. The bcc cubes of Fe and Cr fit on each other and are so oriented that the [001] cube axis is perpendicular to the sample surface (parallel to the MgO[001] axis). In plane, the Fe/Cr system is rotated over 45 degrees with respect to the MgO structure. In this geometry the lattice mismatch between the Fe/Cr system and MgO is 3%.

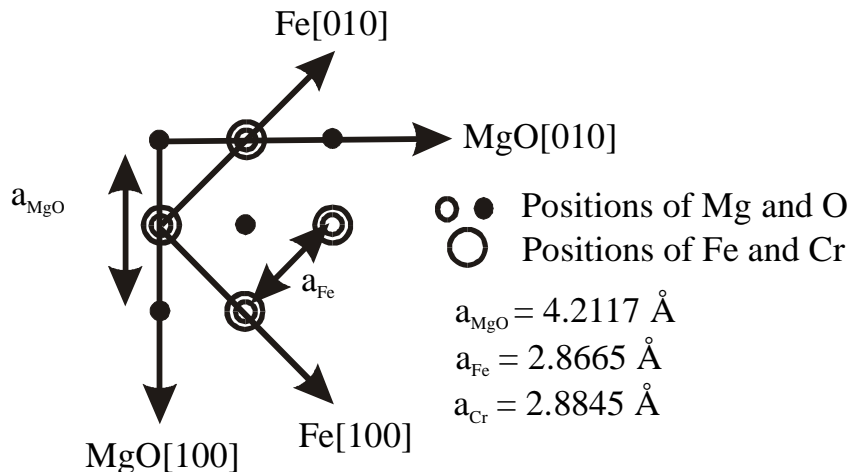


Fig. 2.9 The epitaxial relationship between the MgO substrate and the Fe/Cr superlattice. The bcc Fe/Cr lattice is in plane rotated over 45° with respect to the MgO lattice.

By alternating deposition of Fe and Cr, a multilayer structure can be grown as shown in fig. 2.10. For an appropriate choice of the Cr thickness an antiferromagnetic alignment of the magnetisations in consecutive Fe layers is achieved.

Since in zero field the magnetisation is directed in the plane along the easy axes, four antiferromagnetic domain configurations are possible, see fig. 2.10. For each easy axis ([100] and [010]) the magnetisation in the toplayer can either point along or in the opposite direction of the axis giving the four types of domains sketched in fig. 2.10. The arrows indicate the direction of the magnetisation. It is important to emphasize that the presentation of these domains in fig. 2.10 is only of schematic purpose. As shown by Rürhig [Ruhr91], the domain configuration in a real antiferromagnetically coupled Fe/Cr multilayer is irregular and does not exhibit a clear closing of the magnetic flux as sketched in fig. 2.10.

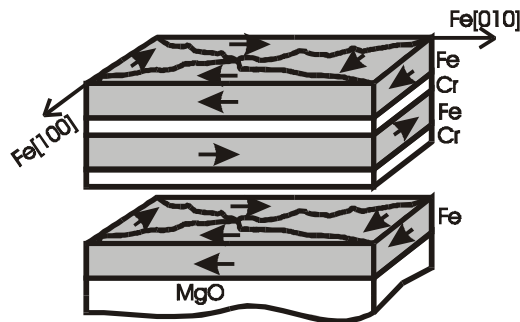


Fig. 2.10 Schematic presentation of an epitaxial antiferromagnetically coupled Fe/Cr multilayer.

2.2.3 Interlayer exchange coupling

The IEC is an interaction that influences the direction of the magnetizations in two ferromagnetic layers separated by a spacer layer. Since its discovery [Erw86, Maj86] it has been studied in various systems and it still attracts a great deal of interest. An illustration of this phenomenon for the Fe/Cr system is given in fig. 2.11 and fig. 2.12. Figure 2.11 shows the setup of the experiment while the observation is done in fig. 2.12. As a substrate a flat Fe whisker is taken with two magnetic domains having their magnetization in opposite direction, see fig. 2.11. On top of this Fe whisker, a Cr layer is grown in a wedge shape (0-20nm). Secondly, this Cr layer is covered with a thin Fe layer (2 nm), see fig. 2.11

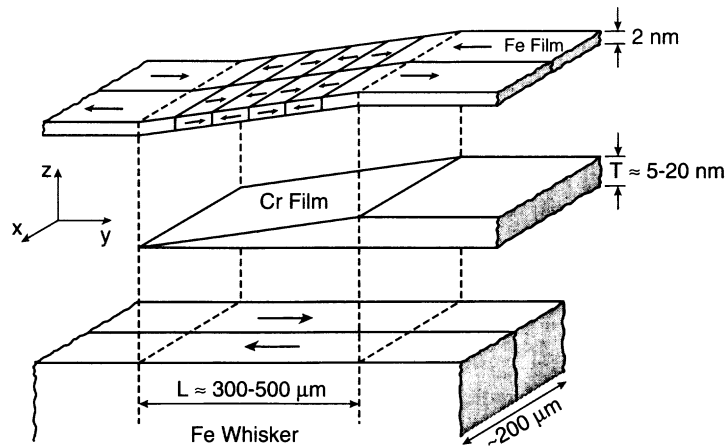


Fig. 2.11 Overview of the SEMPA experiment of Unguris et al. [Hei94b, p. 117]. The arrows indicate the magnetisation direction in the Fe layers.

To determine the direction of the magnetisation in this structure, Secondary Electron Microscopy with Polarization Analysis (SEMPA) measurements are carried out, presented in fig. 2.12. The colour

(black or white) denotes the direction of the magnetisation. Figure 2.12a shows the blank Fe whisker. Clearly two domains that have their magnetisation opposite oriented are present. After deposition of the Cr wedge, the magnetisation in the Fe toplayers shows an oscillatory behaviour as function of the Cr thickness, see fig. 2.12a,b. It switches between a ferromagnetic and an antiferromagnetic orientation with respect to magnetisation direction of the the underlying Fe whisker. Next to a long period oscillation a short period oscillation shows up at a higher growth temperature.

Different phenomena, depending on the properties of the spacer layer, are related to the origin of this interaction. In the context of this work the relevant mechanism for Fe/Cr will be discussed.

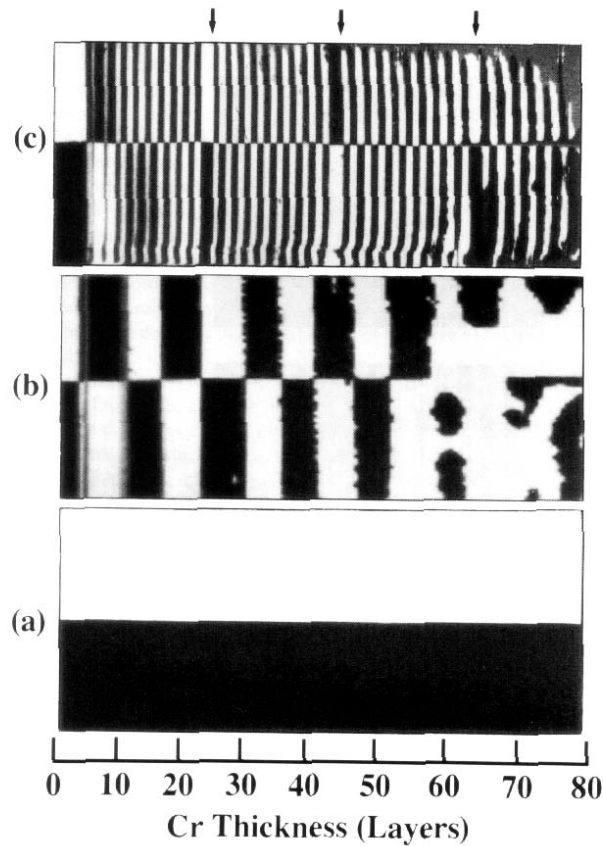


Fig. 2.12. *Experimental SEMPA images from Unguris et al. [Hei94b]: (a) the blank Fe whisker consisting of two magnetic domains, (b) after growth of the capping Fe layer at 30°C, (c) after growth of the capping Fe layer at 350°C. The arrows at the top indicate the phase slip centers.*

- **IEC due to quantum interferences**

A first mechanism that gives rise to IEC is the spin dependent confinement of the electrons. It is especially of use for non-magnetic spacer layers (noble metals) and is explained by means of fig. 2.13. Before entering the explanation it is

worthwhile to mention that various approaches are used to describe this type of IEC, like the Ruderman-Kittel-Kasuya-Yosida (RKKY) model,... . The mechanism which is now widely accepted for the IEC is based upon quantum interferences in the spacer layer due to spin-dependent confinement and will be discussed below [Fer99, chapter B8].

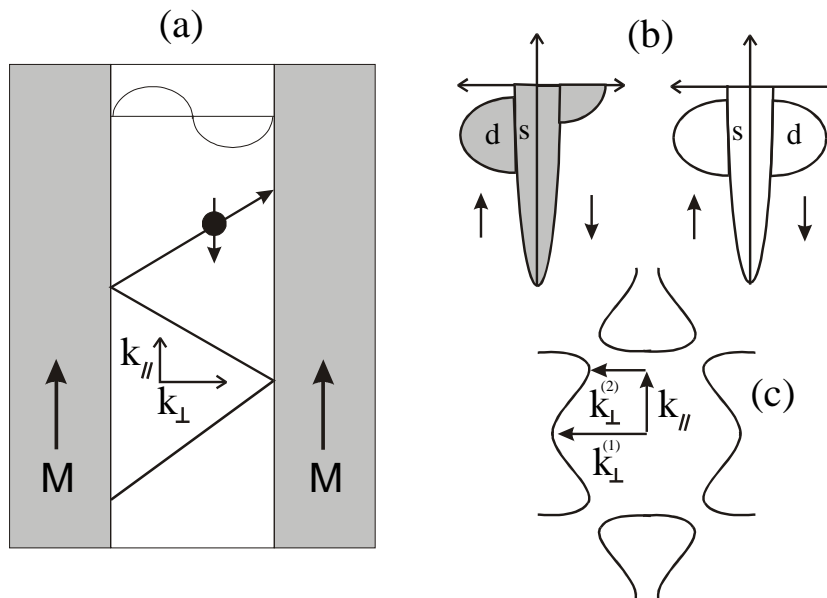


Fig. 2.13 The basic concepts for explaining the IEC due to quantum interferences are sketched : (a) confinement of electrons, (b) the band structure of magnetic material (gray) and the spacer (white), (c) stationary momentum vectors in the Fermi surface.

The principle of IEC by interference can be explained within the framework of a one-dimensional quantum well [Grün99b]. Figure 2.13 shows two ferromagnetically coupled magnetic layers separated by a non-magnetic spacer layer. The spin-up conduction electrons of the spacer layer (s-

electrons) can penetrate the magnetic layers. For the spin down electrons empty d-states in the magnetic layer are present at the interface, see fig. 2.13 b. Therefore the transmission of these electrons into the magnetic layer is reduced and thus the spin-down electrons are confined within the spacer.

In similarity with the one-dimensional quantum well model, we regarded the energy levels for the spin-down electrons as quantized. Increasing the spacer thickness causes the energy levels to drop. Each time a level crosses the Fermi level it is populated giving a higher density of states and thus the kinetic energy of the system is increased. Hence, the ferromagnetic arrangement is destabilized and an antiferromagnetic ordering is established. The latter is possible because for an antiferromagnetic arrangement the width of the one-dimensional quantum well is affected and thus also its energy levels. Further increase of the spacer thickness lowers the energy as the levels sink more below the Fermi level and at certain point the ferromagnetic arrangement will become stable. This physical picture illustrates the oscillatory character of the IEC.

Furthermore, it can be shown that the most dominant contribution to the total energy comes from electrons sitting at positions at the Fermi surface. More precisely, parts of the Fermi surface parallel to the interfaces of the trilayer contain relatively much electrons having a same momentum k_{\perp} directed perpendicular to this interface. Since k_{\perp} is constant within a certain area these positions are named stationaire.

For obtaining the oscillation period one should calculate the difference in spacer thickness between two successive crossings of the Fermi level by discrete energy levels. In the one-dimensional

quantum well model a higher energy level contains an extra node. Therefore the periodicity can be calculated by including an extra wavelength within the boundaries giving. In order to do that the spacer should be increased with half of the wavelength which gives the following equation :

$$D_{oscillation} = \frac{\lambda_{K\perp}}{2} = \frac{\pi}{k_{\perp}} \quad (2.18)$$

For the phenomenological description of this type of IEC, the IEC coupling energy is developed in powers of the scalar product between the two magnetisations \mathbf{M}_1 , \mathbf{M}_2 . Only the two first angular dependent terms are taken into account :

$$E_{IEC} = -J_1 \frac{\vec{M}_1 \cdot \vec{M}_2}{|\vec{M}_1| |\vec{M}_2|} - J_2 \left(\frac{\vec{M}_1 \cdot \vec{M}_2}{|\vec{M}_1| |\vec{M}_2|} \right)^2 = -J_1 \cos(\theta) - J_2 (\cos(\theta))^2 \quad (2.19)$$

The first term, the bilinear contribution, contains the constant J_1 which expresses the strength for an antiferromagnetic alignment. The second term is the biquadratic contribution that favours a 90° alignment. The second term is necessary as this 90° ordering is observed [Ruhr91] and it explains the curvature of the magnetisation loop. Having only a bilinear contribution would result in a linear dependence of the magnetization as a function of the magnetic field.

- **IEC due to antiferromagnetism in the spacer layer**

If the spacer has a magnetic structure there is a direct interatomic nearest-neighbour exchange coupling between the outer layers of the spacer and the adjacent atoms of the magnetic layer. For

antiferromagnetic spacer layers such as Cr or Mn, a two monolayer periodicity in the coupling strength can then be expected. The principle is explained by means of fig. 2.14.

The nearest-neighbour interaction between the outer layers of the spacer (white) and the ferromagnetic layer (gray) is taken to be antiferromagnetic as is the case for the Fe/Cr system. Because this nearest-neighbour interaction and the antiferromagnetism in the spacer layer, the relative orientation between adjacent Fe layers is depending on the spacer thickness. It oscillates between an ferromagnetic and an antiferromagnetic arrangement with a monolayer periodicity.

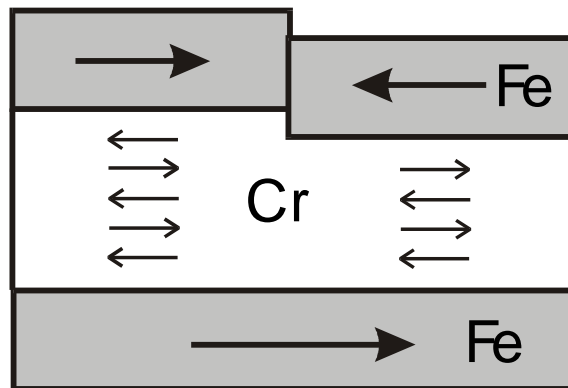


Fig. 2.14 *The IEC due to an antiferromagnetic spacer layer is shown. The ferromagnetic layers (gray) are (antiferromagnetically) coupled to the neighbouring spacer atoms. Depending on the spacer thickness, an ferromagnetic or antiferromagnetic alignment of the adjacent Fe layers occurs.*

The energy related to this type of IEC coupling is described by a formula proposed by Slonczewski [Slon95] :

$$E_{IEC} = C_+(\theta)^2 + C_-(\pi - \theta)^2 \quad (2.20)$$

Since the coupling switches between ferromagnetic and antiferromagnetic by adding a layer, the energy can be written in terms of both contributions. The first term in formula 2.20 represents the tendency to a ferromagnetic alignment while the term containing C_- stands for the antiferromagnetic alignment. If the interface is not perfectly flat both contributions differ from zero which can result in a frustrated state with a 90° ordering. The coupling in Fe/Mn/Fe trilayers can be described by this mechanism [Grün99a] as it could also be of valid for antiferromagnetic insulating spacer layers like NiO [Heij99]. In describing the magnetization loop this mechanism differs from the IEC by interference near saturation. Equation 2.20 predicts an asymptotically behaviour while according to formula 2.19 saturation is reached at finite fields [Grün99a].

• Discussion

The IEC due to quantum interferences comes into play for the Fe/Cr system for explaining the long range periodicity in the IEC having a period of 12 Cr monolayers. It is still of nowadays interest to find the proper corresponding stationary state in k -space [Dong97, Koel99]. The exact description of the observed short period oscillation of 2.11 monolayers is not yet clear as the two above discussed mechanisms can overlap for the Cr system [Grün99b]. In the past, the short period modulation and its phase slips have been described in the non-magnetic IEC by interference taking the corresponding stationary vectors in the Fermi surface. These stationary vectors indicate simultaneously the spin density wave giving them

the name nesting vectors (see later paragraph 2.3). Thus, since chromium is an itinerant antiferromagnet the second mechanism can also influence the coupling if the Cr spacer is magnetic. Several interesting works are carried out to shed light on this problem [Meer95, Kun99, Full96]. Up to now, effects on the coupling related to the magnetic structure of Cr are observed for larger spacer thicknesses [Full95, Schr97, Ank97]. Finally, to do more justice to the IEC phenomena it is necessary to mention that IEC is also observed in other systems like magnetic layer separated by a metallic amorphous spacer layer [Bürg98], bilayers [Aliev97], semiconducting spacers [Brin94], rare-earth systems [Erw86, Maj86], alloys [Vri97, Fuch97], In certain cases other mechanisms, like dipole-dipole interactions between rough magnetic layers and spin polarized tunnelling, ... can be responsible for the observed IEC [Grün99b].

2.2.4 Giant Magnetoresistance

The GMR effect in the Fe/Cr system is related to the magnetic state of the Fe layers. If the layers are antiferromagnetically arranged at zero field the resistance is 'high' ($\rho_{\text{antiparallel}}$). The parallel alignment which has lower resistivity (ρ_{parallel}) is reached by applying a sufficiently strong field. The GMR effect is usually expressed according to eq. 2.21 and can amount up to 220% [Scha94] at 1.5K for the Fe/Cr system or 65% for the Co/Cu system at RT [Par91b]. In general it can be much larger than the AMR effect that is usually only a few percent. It therefore carries the prefix 'Giant'.

$$GMR (\%) = 100 * \frac{\rho_{\text{antiparallel}} - \rho_{\text{parallel}}}{\rho_{\text{parallel}}} \quad (2.21)$$

The phenomenon that gives rise to the change of the resistance is the spin depending scattering, i.e. the resistance for a conductance electron is depending on the relative orientation of its spin and the direction of the magnetisation in the surrounding material [Swag97]. The electrons having their spin parallel to the magnetisation are defined as the majority electrons while the minority electrons have the opposite spin. In the particular case of Fe the minority electrons will experience a lower resistance, as will be explained later.

For explaining the GMR effect it will be assumed that the spin orientation is conserved during scattering events. This leads to the principle of a two current model as already mentioned for the AMR effect. Adapted for respectively a parallel or antiparallel arrangement of the Fe layer the following resistor schemes in fig. 2.15 are obtained. For the antiparallel arrangement the situation is symmetric for the spin up and spin down electrons. Consequently, the total resistance is the same for majority and minority electrons. An asymmetric situation shows up if the magnetisations in the Fe layers line up. The majority electrons experience a higher resistance than the minority ones. The minority channel acts as a shunt and causes a drop of the resistivity.

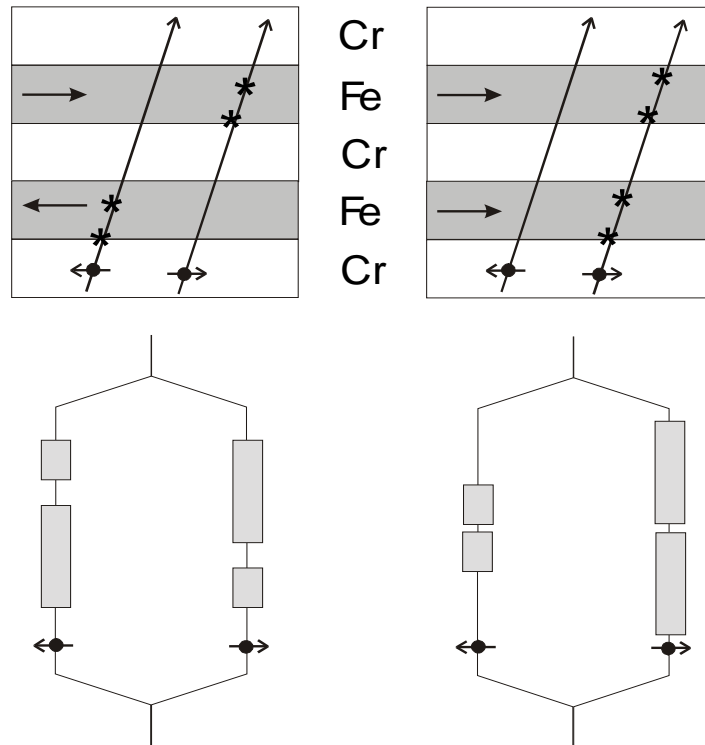


Fig. 2.15 Qualitative explanation for the GMR effect : Arrows in the Fe layers depict the magnetisation directions, the scattering events are indicated by asterisks. The resistivity is the same for the up as well as the down electrons in the antiferromagnetic arrangement. If the magnetisations are parallel aligned, then a 'shunt' is created along one of the spin channels.

The origin of the contrast in resistivity between the majority and minority electrons is usually discussed in terms of intrinsic and extrinsic factors.

The intrinsic contribution is related to the material properties. More precisely, the density of states at the Fermi surface of Fe is larger for the majority electrons. Hence, the amount of empty

states in which can be scattered into is larger for the majority electrons. For this reason the resistivity is also higher for the majority electrons because of the spin conservation. The situation is opposite for Co.

Extrinsic spin dependent scattering is caused by defects. Defects like a Cr atom in a Fe matrix exhibit spin dependent scattering and enhance the contrast. Moreover, it was recently shown that with a proper choice of the materials the GMR can be tuned until eventually a positive GMR instead of a negative GMR [Hsu97].

Furthermore, the principle shown in fig. 2.15 requires that the conduction electrons sense more than one Fe layer. This condition is fulfilled in a trivial way if the current is directed perpendicular to the layers (CPP geometry). The limiting length scale in the CPP geometry is therefore determined by the spin flip length of the electrons. If the current is applied in the plane (CIP geometry) there is no netto current perpendicular to the plane. However, most of the Fermi electrons have a non-zero velocity component in this direction. These electrons can sense several magnetic layers if not diffusively scattered in the spacer. In the CIP geometry it is therefore necessary to have a sufficient long mean free path [Swag97].

At the end, the above mentioned conditions can also be fulfilled in other systems. For example granular alloys consisting of ferromagnetic areas in a metallic matrix exhibit also a GMR effect [Van95, Malkinski99, Viegas98]. The antiferromagnetic arrangement can also be obtained by use of magnetic materials that have a different coercivity [Hol94]. A last related example are the Tunnel Magnetoresistance (TMR) materials in which the electrons tunnel through a non-conducting layer from one magnetic layer to the other. The

contrast in the scattering can be enhanced by using half metallic ferromagnets, i.e. materials that are an insulator for one spin direction and metallic for the other [Det99].

2.2.5 Spin flop transition

Spin flopping is observed in traditional antiferromagnets having a uniaxial anisotropy. In zero field the magnetic moments line up along the easy axis. When a field is applied along this axis, the spins flop at a certain critical field, called the spinflop field H_{sf} , and arrange themselves perpendicular to this field, see fig. 2.16.

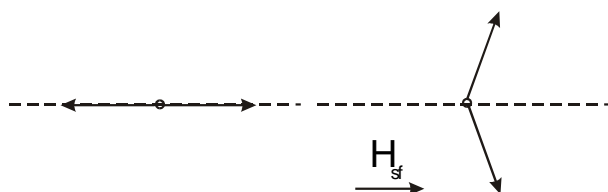


Fig. 2.16 The spin flop transition in a uniaxial system is shown. The dotted line indicates the easy axis. At the spin flop field H_{sf} the spins orient perpendicular to the field.

The underlying reason for this phenomenon is the lowering of the Zeeman energy by rotating the created netto magnetic moment along the field. This decrease in energy should compensate the increase in anisotropy energy because after the spin flop, the moments are turned away from the easy axis.

The discovery of IEC in magnetic multilayers made it possible to create artificial antiferromagnets.

It took little time until an antiferromagnetically coupled magnetic multilayer with a uniaxial anisotropy was studied for the spin flop transition [Wang94]. This experiment proved also the existence of a surface or edge effect. Spins sitting at the surface feel a different anisotropy and exchange coupling because they have only one neighbouring spin. This causes a surface spin flop (SSF) state and the spinflop occurs at a lower field than expected. Next to the study of [Wang94] and [Zeid96] not much experimental work on the spin flop transition in artificial antiferromagnets has been published. In contrary, this phenomenon attracts more attention from the theoretical side [Tral94, Chu97, Pap98, Dan99, Mich99]. However most of the works are carried out for a system containing an uniaxial anisotropy. In our work the spinflop transition is observed in a system having a four fold anisotropy. This opens new perspectives on the nature of how the transition can occur. Therefore this topic will be further discussed in paragraph 4.1.

2.3 Antiferromagnetism of Cr films

2.3.1 Introduction

The Fe/Cr system has been intensively studied during the latest decade because of the exchange coupling and peculiar resistivity properties. Since bulk single crystalline Cr is an antiferromagnet, its magnetic structure could affect the exchange coupling. As mentioned above this is still a question which is not solved clearly today and it is from this perspective that an extra interest in the magnetism of Cr films has arisen. As will be shown further, the magnetic structure of Cr films differs considerably from the

bulk single crystalline behaviour. Anisotropic properties are observed up to a thicknesses of 5000Å. Knowing the bulk behaviour is indispensable for discussing these properties. Therefore this will be treated in paragraph 2.3.2. The following paragraph 2.3.3 will focus on Cr films and provides an overview of the present state-of-the-art.

2.3.2 The magnetic structure of bulk Chromium

- **The spin density waves**

The first observation of an antiferromagnetic structure in Cr was done by Shull [Shull53]. In the following years the precise magnetic structure, the phase diagram and an explanation for these

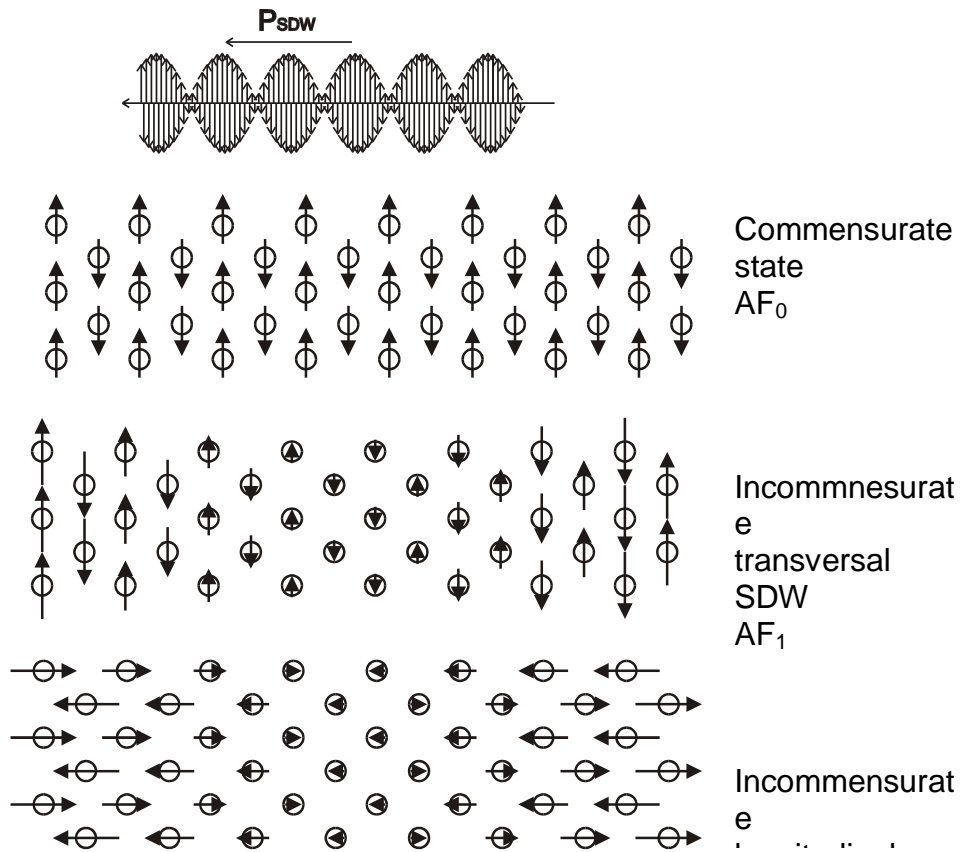


Fig. 2.17 The different magnetic states of Cr are shown. In the upper figure the principle of an incommensurate SDW is shown. In the lower figures the three states, AF_0 , AF_1 and AF_2 are presented.

observations were established. A recent and comprehensive overview of this work done on pure Cr is given by Fawcett [Faw88].

Bulk single crystalline Cr exhibits an antiferromagnetic structure below its Néel temperature T_N of 311K. This antiferromagnetic structure emanates from the electrons at the Fermi surface and it is therefore named an itinerant

antiferromagnetism (non-localized electrons). The resulting antiferromagnetic structures are called spin density waves (SDW) and are shown in fig. 2.17.

The spins in fig. 2.17 are oriented along the [100] type axes and are sinusoidally modulated along one of these axes, see fig. 2.17. This modulation is incommensurate with the crystalline lattice and the amplitude of the modulation is about $0.6 \mu_B$. The modulation periodicity P_{SDW} is denoted with the wave vector Q and is slightly temperature dependent going from 80\AA (about 27 unitcells) at RT to 60\AA (about 20 unitcells) at 4.2K.

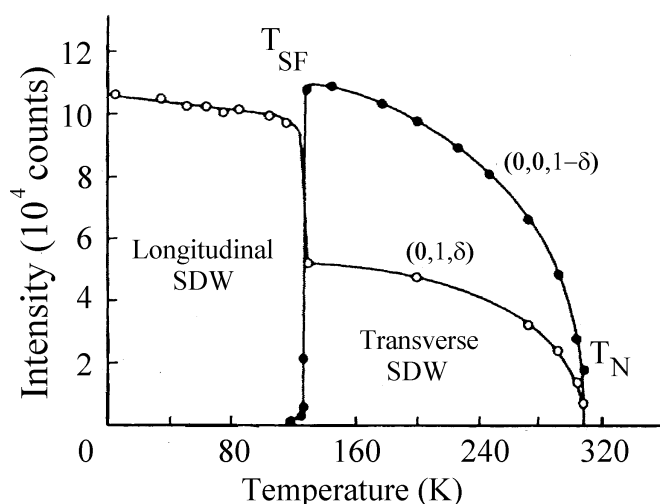


Fig. 2.18 The magnetic phase diagram for bulk single crystalline Cr is shown as determined from neutron diffraction. The antiferromagnetic structure disappears above the $T_N = 311\text{K}$. Below T_N a T-SDW is formed until T_{SF} below which the L-SDW state is stable.

Furthermore, the spins can either be oriented perpendicular to Q giving a transversal spin

density wave (T-SDW) AF_1 or parallel to Q resulting in a longitudinal spin density wave (L-SDW) AF_2 , see fig. 2.17. The actual state depends on the temperature and is shown in the phase diagram of fig. 2.18. From the Néel temperature the T-SDW is stable down to the spin-flip temperature $T_{SF} = 123K$. Below the spin flip temperature the L-SDW exists.

Next to the T-SDW and the L-SDW a commensurate state (C-SDW) AF_0 is observed in non-single crystal samples and in Cr-alloys [Faw88, Faw94]. This structure is shown in fig. 2.17. The spins in the simple antiferromagnetic C-SDW state are alternately pointing up and down without the sinusoidal modulation.

- **The origin of the Cr antiferromagnetism**

Atomic chromium has a $(Ar)4s^13d^5$ electronic structure. These discrete energy levels start to overlap as the interatomic distance decreases, leading to the formation of a band structure and a Fermi level as depicted in fig. 2.19.

The itinerant antiferromagnetism in Cr is related to the exchange interaction which is the extrapolation to solids of Hund's rule for atoms. If the density of states at the Fermi level is high (Fe, Co, Ni) then a parallel alignment of spins is favoured. The underlying reason is the competition between the Coulomb repulsion energy and the kinetic energy in their contribution to the total energy. Setting spins parallel increases the kinetic energy as the Pauli principle forbids the same spins on one energy level. Thus higher energy levels should be occupied for doing this. On the other hand the electrons are not sitting anymore in the same level and the contribution of the repulsive Coulomb interaction is reduced. For a high density of states at the Fermi level the

contribution of the kinetic energy will be small and therefore ferromagnetism occurs in Fe, Co and Ni.

For Cr (Mn) the density of states at the Fermi surface is lower and a ferromagnetic alignment is not preferred. From this point of view it does not directly imply a paramagnetic ground state. In contrary, Overhauser [Over62] showed that for a free electron gas a lower energy state than the paramagnetic state can be found by the formation of a SDW. He also showed that a SDW with wave vector $Q = 2k_F$ is most likely to minimize the energy.

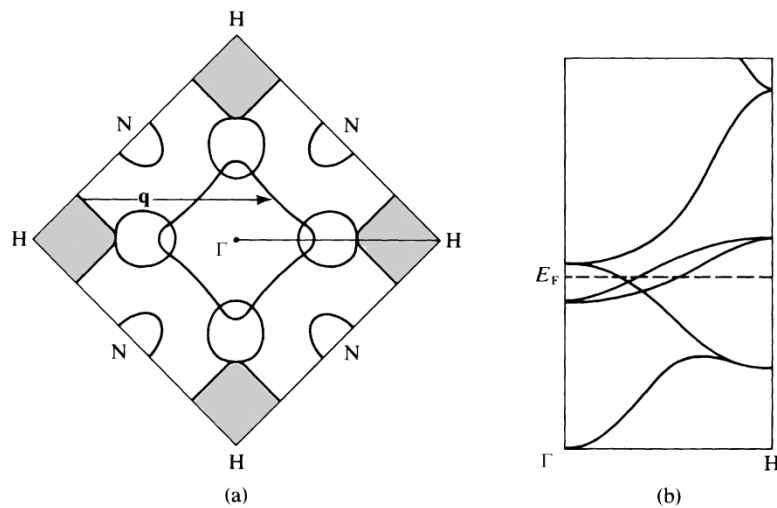


Fig. 2.19 (a) An (001) section of the Fermi surface of Cr; (b) and the band structure along the cross-section Γ -H [Har80].

The calculations were carried out in the single particle approximation (Hartree - Fock). The principle is most easily understandable in the case of a one dimensional free electron gas. The idea is based on a more efficient use of the exchange

interaction (Coulomb interaction) by letting the spins rotate continuously to form a helical structure. Qualitatively speaking, this spin dependent periodic potential leads to a distortion of and a gap in the band structure of a free electron model, and thus the total kinetic energy can be reduced. The resulting wave functions are a mixture of two wave functions that have the opposite spin and their \mathbf{k} vectors differ by \mathbf{Q} , the wave vector of the spin wave [Arrot66]. Finally, the effective decrease in exchange energy can be doubled by superposition of a left handed and a right handed helical wave, resulting in the linear spin density waves shown in fig. 2.17.

Figure 2.19 shows that the Fermi surface of Cr is likely to be suitable for this reasoning. There is an electron surface and a hole surface present having a similar shape. Their positions differ by a wave vector \mathbf{Q} with a size comparable to the Fermi surface so that these surfaces can be nested in each other by translation over \mathbf{Q} . Lomer [Lomer62] discussed this artefact of the Cr Fermi surface and how the total energy could be reduced by the introduction of a spin dependent potential with periodicity \mathbf{Q} . In the following years this model was refined and a clearer picture is obtained [Loucks65, Koeh66, Fedd66]. The reason that the higher members from the same chemical group, Mo and W, do not exhibit antiferromagnetism is that due to the large overlap of the 4d and 5d shell their bands are much broader. The density of states is therefore lower and the total energy is much more sensitive to a repopulation of the \mathbf{k} states.

The simple commensurate antiferromagnetic state does not appear in single crystalline Cr and its origin is therefore related to the introduced disturbances like defects and or impurities. Since in this work only pure Cr is considered, the

discussion of the AF_0 state will be restricted to this case. The AF_0 phase can also appear in alloys. The commensurate state has been observed in the first studies of Cr by neutron diffraction and has led at that time to confusion about the Néel temperature of Cr [Faw88, Shull53]. Later on, Bacon et al. [Bacon61, Bacon69] related the origin of the commensurate state in pure Cr to the disruption of the periodic lattice by defects and the strains which they induce. Loss of the periodicity seems to be essential as this state has not been observed in experiments on single Cr crystals [Sab66]. This is qualitatively in agreement with the calculations of Rice [Rice70]. He studied the effect of an imperfect nesting of the electron and hole surfaces and found a first order behaviour of the Q vector for the commensurate-incommensurate transition. Loss of the periodicity due to defects and their strains could influence the band bending and thus alter this surface.

- **The magnetic reflections**

Another important issue to treat here are the neutron diffraction experiments. Since the magnetic state of Cr will be studied by this technique it is necessary to introduce the reflections of the different magnetic states in the reciprocal space, see fig. 2.20.

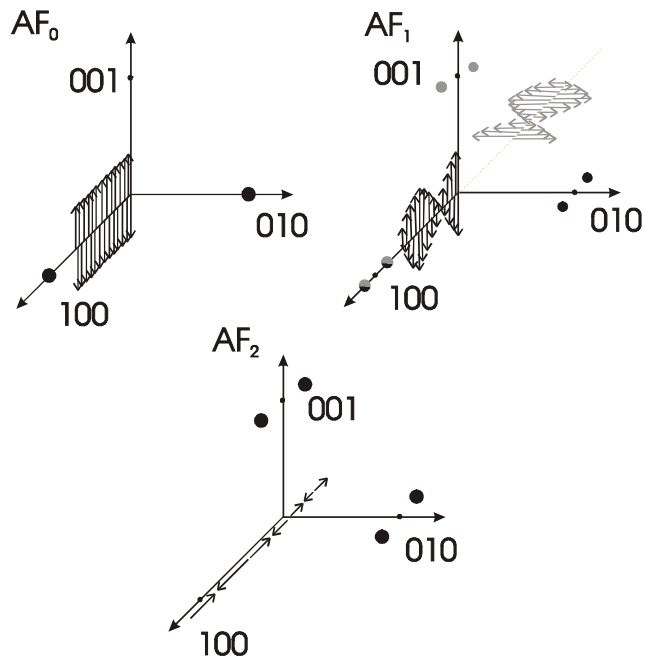


Fig. 2.20 The three possible observed antiferromagnetic structures and their reflections as observed from neutron diffraction.

The commensurate state AF_0 has a periodicity of a single Cr unit cell and therefore these reflections can be found around the (001) type reciprocal lattice points. However, for unpolarized neutron scattering one has to take into account the angle α between the scattering vector \mathbf{q} and the direction of the spins. The magnetic scattering amplitude is proportional to the sinus of this angle [Halp39, Will66, Bacon75]. Thus, the scattering vector \mathbf{q} should be perpendicular to the spins for observing any intensity. In summary, the AF_0 state with the spins directed along the [001] axis, see fig. 2.20, can only be observed at the (100) and the (010) reciprocal points.

State	Spins	//	Spins	//	Spins	//
-------	-------	----	-------	----	-------	----

	[100]	[010]	[001]
AF ₀	(010), (001)	(100), (001)	(100), (010)
AF ₁ along [100] (in-plane)	Spins // Q	(1±δ,0,0)& (±δ,0,1)	(1±δ,0,0)& (±δ,1,0)
AF ₁ along [010] (in-plane)	(0,1±δ,0)& (0,±δ,1)	Spins // Q	(0,1±δ,0)& (1,±δ,0)
AF ₁ along [001] (out-of- plane)	(0,0,1±δ)& (0,1,±δ)	(0,0,1±δ)& (1,0,±δ)	Spins // Q
AF ₂ along [100] (in-plane)	(±δ,1,0)& (±δ,0,1)	Spins ⊥ Q	Spins ⊥ Q
AF ₂ along [010] (in-plane)	Spins ⊥ Q	(1,±δ,0)& (0,±δ,1)	Spins ⊥ Q
AF ₂ along [001] (out-of- plane)	Spins ⊥ Q	Spins ⊥ Q	(1,0,±δ)& (0,1,±δ)

Table 2.1 *The different magnetic states of Cr and the corresponding reflections in the reciprocal space are shown.*

For the SDW, the spins have an extra sinusoidal modulation giving a superstructure. This positive-negative alternation or antiphase-domain structure results in a destructive interference at exactly the (100) type reciprocal lattice points [Bacon75, Bacon61]. Around the (100) points the interference conditions are not completely fulfilled and partial reinforcements is obtained giving satellite reflections. Keeping the rule in mind that the

spins should be perpendicular to the scattering vector \mathbf{q} , gives the satellites reflections shown in fig. 2.20. The position of the satellites with respect to the reciprocal lattice is denoted by δ . The value for δ in units of $2\pi/a$, where a indicates the lattice constant of Cr, ranges between 0.048 at low temperature up to 0.036 near the Néel temperature. For a T-SDW having its Q vector along the [100] axis two satellites show up at $(1\pm\delta,0,0)$. Depending on the spin polarization two additional reflections show up at $(\pm\delta,1,0)$ or $(\pm\delta,0,1)$. In general both polarizations are present so that the satellites at (100) have twice the intensity of the ones at $(\pm\delta,1,0)$ and $(\pm\delta,0,1)$. The L-SDW with Q along [100] has only reflections at $(\pm\delta,1,0)$ and $(\pm\delta,0,1)$ and none at (100). Summarizing these results we present the reflections in table 2.1.

- **Effect of stress**

Isotropic pressure like hydrostatic pressure lowers the Néel temperature with an amount of $dT_N/dP = 5.2 \cdot 10^{-8} \text{ Km}^2/\text{N}$ [Mit65] and the spin flip temperature with $dT_{SF}/dP = 5.8 \cdot 10^{-8} \text{ Km}^2/\text{N}$ [Ume68]. Anisotropic pressure like compression can affect the domain distribution. In the general case different domains along the three different crystal axes are present in single crystalline pure Cr. In this respect, Bastow et al. [Bast66] showed that cooling through the Néel temperature while applying compressive stress produces samples with the Q wave vectors perpendicular to the stress direction. Barak et al. [Barak82] calculated the effect of stress on the Q and spin directions. Barak found that the most stable directions for the Q vectors are the one perpendicular to which the compressive stress is applied. Furthermore, they derived that

the polarization of the spins will be parallel to the axis along which the compressive strain is induced.

These pressure dependencies are used by Williams [Will79,Will81] to model the phase diagram of strained chromium. Their model is based on the strain distribution around defects. These strains cause a broadening and shift of the Néel - and spin flip temperature. Their results are in reasonable agreement with the experimental observations. In their model the AF_0 state is assumed in regions where the defect separation is less than δ , the period of the SDW.

- **Magnetic field dependence**

Another anisotropic external disturbance is the magnetic field. Firstly, cooling through the Néel temperature while applying a sufficiently high magnetic field (24kOe) along a cubic axis produces a single Q state. For such a field cooled sample the SDW propagates along the field cooled axis. The single Q state is rather stable and heating above T_N or high magnetic fields (16T) is necessary to destroy it.

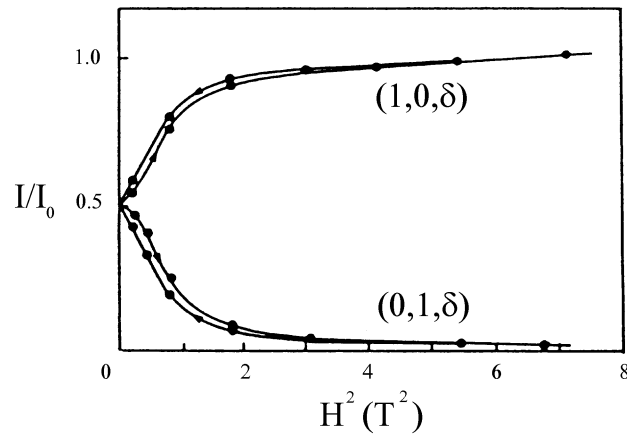


Fig. 2.21. Polarization of the T-SDW by a magnetic field [Wern68].

Secondly the polarization of the T-SDW can be affected by applying a field along the antiferromagnetic spins. Figure 2.21 shows the experiment of Werner et al. [Wern68]. They produced a single domain sample by the procedure described above. The T-SDW in this sample propagates along the [001] axis. The spins are equally distributed along the [100] and [010] axis. In the next step, a field is applied along the [100] axis. In similarity to the spinflop discussion in the previous paragraph, the spins orient perpendicular to the field. Consequently, the $(0,1,\pm\delta)$ disappear and the $(1,0,\pm\delta)$ satellites grow with the same amount. Saturation is obtained at about 15 kOe.

2.3.3 State-of-the-art

As mentioned before, the interest in the magnetic state of Cr films is arisen from its contribution to the IEC. At first instance Fe/Cr multilayers

where studied. Meerschaut et al. [Meer95] studied Fe/Cr multilayers with varying Cr thickness using Perturbed Angular Correlation Spectroscopy (PACS). They found that the Cr is paramagnetic for spacer thicknesses below 60 Å. At the same time a similar investigation is carried out by Fullerton et al. [Full95] using magnetization and resistivity measurements. Fullerton found the crossover to the paramagnetic state at a Cr thickness of 42Å. Furthermore, in this experiment a vanishing of the biquadratic coupling is observed if the sample is cooled below its Néel temperature [Full95, Full96b]. Additionally, Schreyer et al. have found the presence of a commensurate state for a Cr thickness of 42Å using neutron diffraction [Schr97]. Inspired by this work other studies on Ag/Cr [Dem98] superlattices and single thick Cr films are engaged [Meer98]. On the latter we will focus in this work.

An elaborated study of the magnetism in thin Cr films is carried out by the group of Zabel et al. [Sonn98, Böd98, Böd99, Zab99] using synchrotron and neutron diffraction. They investigated Cr films with [Böd99] and without [Sonn98] a capping layer. Their films are grown on a $\text{Al}_2\text{O}_3(1-102)/\text{Nb}(001)(500\text{Å})$ substrate and have a (001) orientation. For improving the structure, the films are annealed at 750°C. The observed thin film behaviour differs from the bulk single crystalline phase diagram. In general the three possible states, AF_0 , AF_1 , and AF_2 are observed. The orientation of the antiferromagnetic spins and the SDW propagation vectors is highly anisotropic, in contrary to the normal bulk behaviour.

The single Cr films (1000Å-4000Å) [Sonn98] exhibit at high temperatures ($T > 250\text{K}$) an AF_0 state having the spins out-of-plane. At lower temperatures an I-SDW is formed during a gradual transition. The L-

SDW propagates always out-of-plane and is more abundant at low temperatures. The T-SDW can be as well in-plane as out-of-plane oriented.

Covering the Cr film with a Cu cap layer does not alter significantly the phase diagram compared to the Cr-Cr-oxide or Cr-vacuum interface, i.e. an out-of-plane spin direction and propagation of the SDW.

On the other hand covering the thick (3000Å) Cr films with an Fe cap layer causes the SDW to lay preferentially in the plane while the spins remain out-of-plane. Thus an in-plane T-SDW is formed. The AF₀ phase in the Fe capped systems is present below 200K and the spins are directed out-of-plane. Only for low temperatures (T<50) a reoriented in-plane polarized AF₀ state is found [Böd99].

If the Cr layer is sandwiched between Fe layers and the thickness is reduced from 3000Å to 250Å again an out-of-plane T-SDW is found. For these thin Cr layers the spins are reoriented towards in the plane, parallel to the magnetization in the Fe-layers. Replacing the Fe cap layer by another ferromagnetic material like Ni, Co does not alter significantly the phase diagram for thick Cr films (2000Å) directly deposited on the Nb/sapphire substrate. A surface layer like Pb, which is highly polarizable, gives an intermediate result.

Several suggestions are made to explain these observations.

For the single Cr(1000Å-4000Å) [Sonn98] they showed in a strain and stress analysis that this magnetic behaviour is unlikely caused by the epitaxially induced strains. The in-plane lattice parameter of Cr on Nb/sapphire is expanded and the out-of-plane follows a non-Poisson like behaviour, i.e. an extra out-of-plane strain has to be taken into account.

According to Barak [82] the measured strains should induce the opposite effect on the SDW than observed. However, this in-plane lattice expansion is in accordance with predominant out-of-plane spin direction.

In [Böd99] it is suggested that for these single thick Cr films the contrast in in-plane ($\xi_{//}$) and out-of-plane (ξ_{\perp}) structural coherence length can be responsible for the out-of-plane orientation of I-SDW. The out-of-plane structural quality is better as the in-plane ($\xi_{//} < \xi_{\perp}$).

Additionally surface neutron scattering experiments [Böd98b] showed that the AF_0 state is located near the Nb interface where the structure is poor because of the Nb-Cr mismatch lattice mismatch induced relaxation. The I-SDW develop towards the top as the structural quality improves. Furthermore, it is shown to be plausible [Böd99] that the C-SDW exists regions that are smaller than the period of the I-SDW.

In summary, the antiferromagnetic spins in thick Cr films on Nb/sapphire are mostly oriented out-of-plane. Only at low temperatures ($T < 50K$) an in-plane behaviour can be found in ferromagnetic capped layers and also for Cr films sandwiched between Fe layers. In the latter case the in-plane polarization becomes more important with decreasing Cr thickness.

Concerning the SDW for large Cr thicknesses there is always an AF_0 contribution present having its spins out-of-plane for temperatures above 250K. In the ferromagnetic capped systems this AF_0 state persist at temperatures below 250K. The I-SDW is in-plane directed for thick Cr films with a

ferromagnetic cap layer and for the greater part out-of-plane for films with no or a Cu cap layer.

2.4 Magnetic anisotropy in magnetic arrays

2.4.1 Introduction & State of the art

In the third chapter of this thesis, the shape anisotropy will be studied. More precisely, submicron structures will be envisioned. The present preparation techniques permit a lateral scaling down to the sub-micron range. Magnetic structures of these dimensions are intensively studied because they exhibit interesting fundamental phenomena and are closely related to possible applications like data storage. Especially of interest are isolated structures such as dots and magnetic lines. Epitaxial Fe dots having a lateral size of 0.1-1 μ m and a height of 50nm exhibit a multi domain state [Hanson99]. Furthermore the competition between the shape anisotropy - and crystalline anisotropy is investigated experimentally and theoretically in micron sized epitaxial Fe elements [Dao99, Yu99]. Not only the shape and size of the magnetic dot become important but also the distance between them [Evoy20]. As the dipolar coupling gets stronger the shape of the magnetisation loop gets more rectangular. On the other hand if permalloy ($\text{Ni}_{80}\text{Fe}_{20}$) dots are closely packed in a square lattice a corresponding fourfold anisotropy was found [Mathieu97]. Additionally, the size of the systems decreases steadily towards below the 100 nm range [Hagin99, Cui99, Savas99]. In this respect, other techniques like the combination of Scanning Tunnel Microscopy (STM) and Chemical Vapour Deposition (CVD) cover the gap between these submicron structures and the world of the clusters and atoms (<10 nm). Wirth [Wirth99] reported

recently on Fe pillars that are 9-20nm in width and 50-250nm in height grown by this hybrid technique. Eventually the smallest structures down to the atomic level are accessible for study by preparation techniques such as clusters deposition and self assembly during growth [Schein99, Pad99, Chamb91, Möller96].

If the dots are electrically connected the magnetic reversal process can be studied by transport measurements [Martin98]. This leads us to the wide variety of investigations on lines, bars and wires [Qiang97, Wegrowe99]. Wegrowe et al studied the magnetoresistance in single Ni and Co nanowires and made a major progress towards their understanding on the basis of AMR. Next to the domain structure [Ebels97] and the reversal process, the domain wall itself can be of interest [Xu99, Shigeto99, Tani99] in these structures.

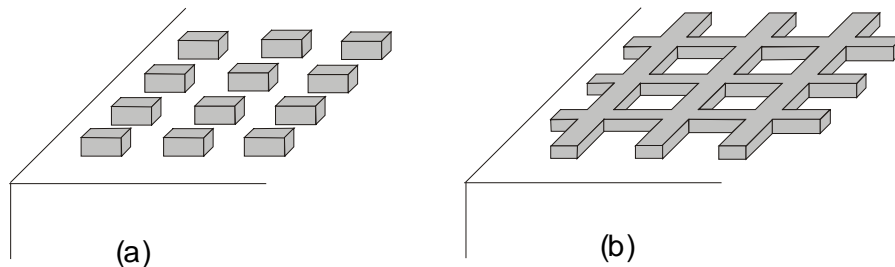


Fig. 2.22 *The dot (a) and the antidot lattice or maze (b).*

In contrast, the magnetic properties of the complement or negative of these isolated structures such as the antidot lattice or array, see fig. 2.22 are much less known [Cow97]. Cowburn et al. [Cow97] studied such an antidot lattice in a 400Å

Permalloy film. They found that the antidots affect the domain distribution at remanence and envisioned a possible way for data storage. Inspired by this work Torr calculated the magnetic structure of these engineered materials [Torr99]. It was shown that for a large separation of the antidots a diagonal arrangement of the magnetization shows up in respect to the antidot lattice.

Next to the intrinsic magnetic properties, interest arises from hybrid structures in combination with superconductors. It is recently shown that a magnetic array covered with a superconductor can increase its critical current [Temst].

Motivated by the above mentioned observations, the investigation of a sub micron magnetic Ni array is carried out and discussed in chapter 4.3. Nickel is chosen because it has the largest AMR (2%) of the three 3d ferromagnets Fe,Co, Ni and thus the magnetic properties will be more pronounced in the resistivity measurements.

Chapter 3

Experimental techniques

3.1 Preparation

All structures studied in this thesis are produced by Molecular Beam Epitaxy (MBE). The MBE apparatus is since 1996 part of the larger Ion and Molecular Beam Laboratory (IMBL) facility that is sketched in fig. 3.1.

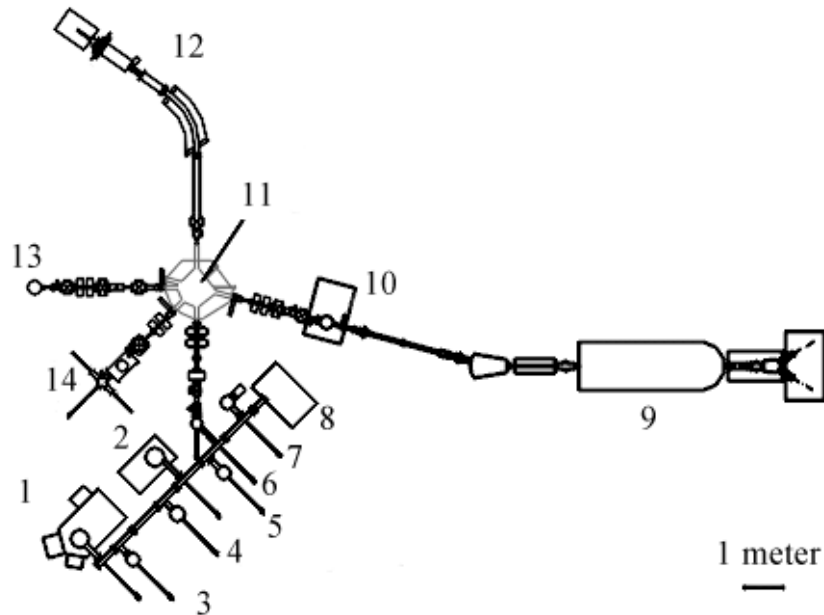


Fig. 3.1 The floor plan of the the IMBL : (1) Ribier MBE, (2) Meca2000 MBE, (3) CEMS, (4) AES, LEED and sputtering, (5) annealing chamber, (6) soft landing, (7) STM, (8) clean room bench, (9) Pelletron, (10) RBS, (11) splitting magnet, (12) LIS, (13) evaporation chamber, (14) implantation.

This facility combines different techniques. Next to the first Ribier MBE system (1) in which mainly metals and silicides are evaporated, recently a second MBE (2) system from Meca2000 is installed for the deposition of rare-earth materials. The two systems are connected via a ultra high vacuum (UHV) tube with different characterisation and preparation chambers in UHV conditions : Conversion Electron Mössbauer Spectroscopy (CEMS) (3), Auger Electron Spectroscopy (AES) (4), sputtering (4), Low Energy Electron Diffraction (LEED) (4), soft landing (5), annealing chamber (6), Scanning Tunneling Microscopy (STM) (7), clean room bench (8). Secondly, this UHV system is connected via the

soft landing chamber with the ion laboratory consisting of : the Pelletron accelerator (9), Rutherford Backscattering (RBS) chamber (10), switching magnet (11), Leuven Ion Separator (12), evaporation unit (13), implantation chamber (14). Because of its relevance to this work, firstly the Riber MBE system will be treated in more detail. The principle of MBE is to evaporate the material in a UHV environment. The evaporated beam of atoms condenses on a substrate and forms a layer. A drawing of the setup is shown in fig. 3.2. It shows the MBE apparatus and a side view of the UHV tube. Introducing the sample into the UHV occurs via an extension of the UHV tube which serves as an air lock. The substrates are mounted on two inch molybdenum blocks that are placed on a magnetic train. This train is moved in the UHV tube by moving two external magnets. In this way the different experiments as sketched in fig. 3.1 are accessible under UHV conditions. Transfer sticks allow to take the blocks off the train and to put them into the desired chamber and vice versa. For the MBE system the blocks are attached to a manipulator with a heater. The sample can be rotated during growth for improving the homogeneity and the growth temperature can be varied in the range of room temperature (RT) - 1000°C. The evaporation is done by two electron beam guns (e-guns) and six Knudsen cells, see fig. 3.2 items (5) and (6).

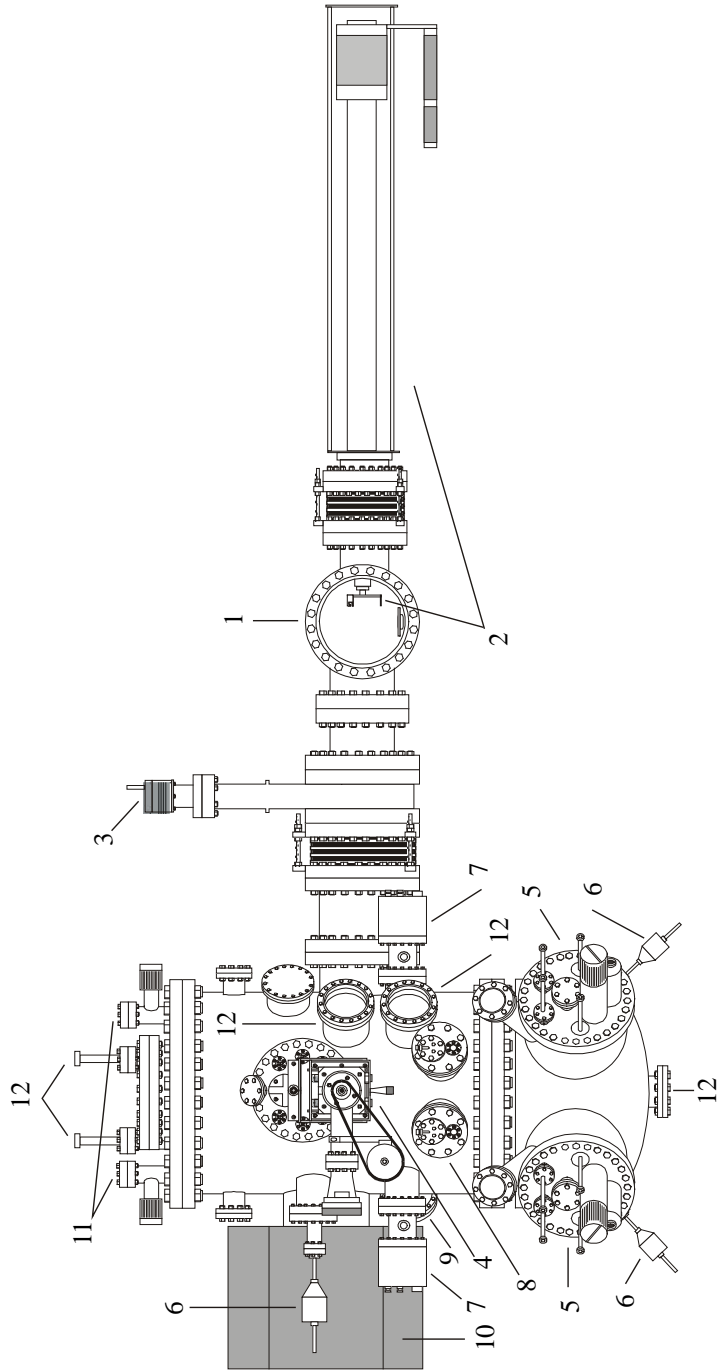


Fig. 3.2 The MBE setup : (1) the UHV transport tube, (2) the transfer stick, (3) valve, (4) sample manipulator, (5) e-guns, (6) Knudsen cells, (7) QMS, (8) XTC's, (9) RHEED, (10) ion pump, (11) Liquid Nitrogen connections, (12) windows.

Both e-guns contain four materials, resp. (Co, Si, Cr, Fe) and (Fe, Ni, Si, Zr) while the cells are used for evaporation of Au, Ag, ⁵⁶Fe, ⁵⁷Fe, ¹⁰⁹Ag, and Mn.

The base pressure of the MBE is about $2 \cdot 10^{-11}$ mbar and an increase up to 10^{-10} mbar is observed during evaporation. Pumping is performed using an ion pump and a nitrogen shroud while during bake-out additionally a Ti sublimation pump is switched on. The evaporation rate, typically 0.1Å-1Å/s, is controlled by temperature stabilization of the Knudsen cells. For the e-guns the regulation of the rate is based on a feed back system : a quadrupole mass spectrometer (QMS) measures the evaporation and the power is adapted to achieve a constant rate. Since the signal of the quadrupole mass spectrometer is proportional to the rate an independent calibration has to be performed to know the exact rate.

For this purpose three quartz oscillators are available. One of them can be placed at the sample position for the precise determination of the rate. The other two are used in combination with the e-guns to measure and eventually control the rate during evaporation. If necessary, an external calibration can be carried out by measuring the thickness of a calibration film using X-ray Diffraction (XRD). The complete growth process can be controlled by computer.

Finally, a Reflection High Energy Electron Diffraction (RHEED) installation enables the in-situ investigation of the growth. This technique will be discussed in more detail in paragraph 3.2.

3.2 Characterization

3.2.1 Diffraction

Diffraction occurs when a wave interacts with a periodic potential. The wave is scattered and constructive interference occurs only in specific directions. These directions are determined by wavelength and the difference in path.

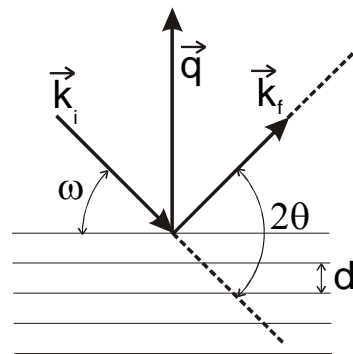


Fig. 3.3 *The measurement geometry for diffraction and the Bragg law are shown.*

The principle is shown for a plane wave in fig. 3.3 and the conditions for constructive interference are given by the Bragg law : $2d\sin(\theta)=n\lambda$, d being the distance between the diffracting planes, θ half of 2θ see fig. 3.3, $n > 0$ and integer, λ the wavelength. The incoming wave is denoted with the wave vector \mathbf{k}_i and the outgoing with \mathbf{k}_f . The difference between the incoming and outgoing wavevector is the scattering vector $\mathbf{q} = \mathbf{k}_f - \mathbf{k}_i$. In this work electrons, photons and neutrons will be used for performing diffraction experiments. Firstly, the Reflection High Energy Electron Diffraction (RHEED) setup will be explained in paragraph 3.2.1. Secondly, diffraction by photons will be discussed. Next to the XRD setup a brief contribution to the synchrotron radiation is given. Thirdly, the neutron diffraction will be elucidated in paragraph 3.2.3.

- **RHEED measurements**

The Reflection High Energy Electron Diffraction setup is mounted in the MBE for in-situ investigations of the structure. The electrons are emitted from a filament and accelerated over a 10 kV potential giving them 10keV of kinetic energy and thus a wavelength of 0.12Å.

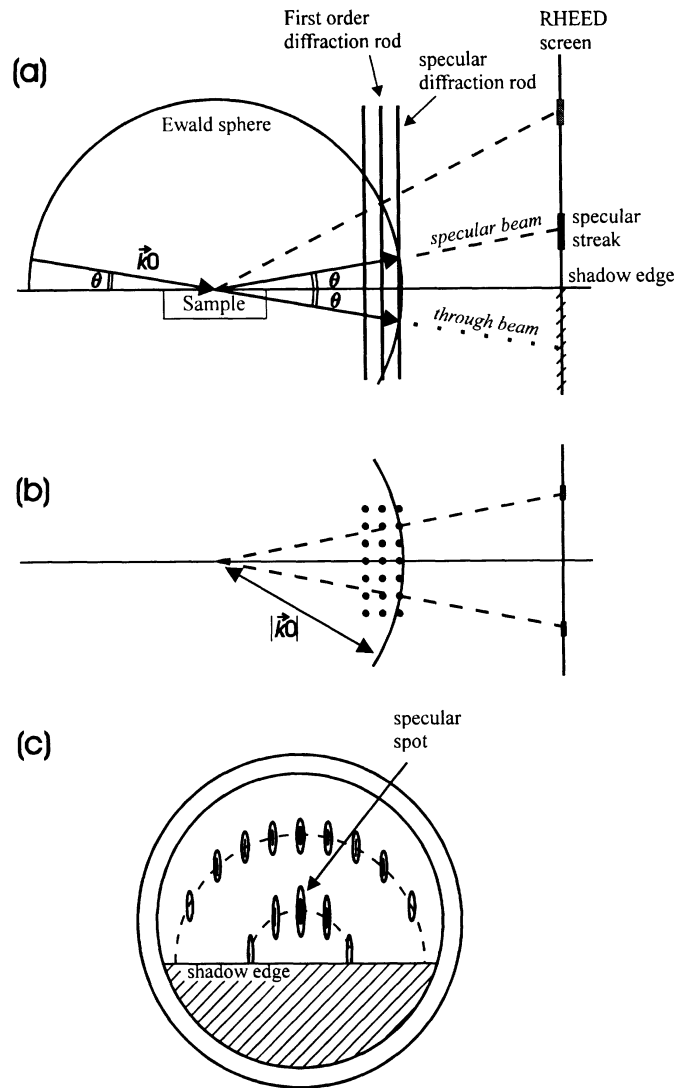


Fig. 3.4 The RHEED setup. (a) sideview of the incoming/ reflected beam and the crosssection of the Ewald sphere with the reciprocal rods, (b) topview of figure (a), (c) The RHEED pattern visualized on the fluorescent screen.

The beam strikes the sample surface under a small angle ($< 5^\circ$). Together with the limited penetration depth of the electrons, these grazing incidence conditions restrict the interaction of the electrons to the top layers of the sample. The diffracted electrons are visualized by a flat fluorescent screen. A schematic overview of this setup is shown in fig. 3.4.

RHEED is a basic tool for thin film investigations. It provides information about the structure of the growing film, i.e. if the structure is epitaxial, textured or polycrystalline. A perfectly crystalline flat two-dimensional surface gives the pattern shown in fig. 3.4c. Short lines, called streaks are lying on the circumference of a circle. Due to the two-dimensional nature of the surface, the reciprocal lattice is represented by a set of reciprocal lines. In addition, the limited resolution the energy of the electrons causes the Ewald sphere to have a finite thickness. Hence, the intersection of the Ewald sphere with the reciprocal rods results in these short lines.

For a rough surface the streaks broaden and grow in length at first instance. A further increase of the roughness results in separated diffraction spots which are not longer placed on a semi-circular arc. This pattern originates from diffracted electrons in transmission through the structures.

On the other hand, the formation of a textured lattice leads to an intensity distribution along concentric circles. For a polycrystalline or amorphous lattice a smeared-out intensity is observed and no clear diffraction spots can be discerned.

- **X-ray diffraction**

The diffraction measurements using X-rays is carried out on two types of X-ray sources nl. the Rigaku Dmax II rotating anode and secondly using synchrotron radiation. The Rotating Anode is used for the structural characterization , while synchrotron radiation was applied for synchrotron Mössbauer reflectometry.

- **Structural characterization**

The rotating anode generates X-rays by accelerating electrons towards a rotating Cu target. The rotation is performed to reduce the local heating of the anode and to achieve a higher intensity. The anode can be operated at a maximum power of 12kW. To prolong the lifetime of the filament, a power of 4kW is commonly used.

The incident electrons create vacancies in the K shell by knocking out the K electrons. X-rays with a specific wavelength are emitted when a higher placed electron from the L shell fills up this vacancy. The following three wavelengths are produced : $\text{CuK}_{\alpha 1}$ (1.540598 Å), $\text{CuK}_{\alpha 2}$ (1.544418 Å) and CuK_{β} (1.392249 Å). The CuK_{β} radiation is suppressed by use of a Ni filter and a post-sample flat Ge crystal monochromator. The measurements are performed on a goniometer in Bragg Brentano configuration. Figure 3.3 shows a schematic picture of the measurement geometry. The angle between the diffracting planes and the incoming beam is denoted with ω and the position of the detector with respect to the incoming beam is called 2θ . The angle ω determines the position of the sample while 2θ selects the periodicity which is probed. In general two types of measurements are performed nl. the ω - 2θ scan and the ω -scan. During the ω - 2θ scan $2*\omega$ equals the value of 2θ and \mathbf{q}

remains perpendicular to the diffracting planes. These scans are used to determine the distance between the lattice planes. During the ω -scan only ω is varied and 2θ is set on a fixed value. In this way only the sample moves and thus also the reciprocal lattice. Therefore this type of scans determines the spread in orientation of the diffracting planes.

- **Synchrotron Mössbauer Reflectometry**

Charged particles that are accelerated emit electromagnetic radiation. This phenomenon is applied in synchrotrons to produce intense beams that are used for various purposes. The high intensity produced by a synchrotron is a necessity for performing Synchrotron Mössbauer Reflectivity (SMR). It is therefore a relative new technique. SMR [Déak96, Chumakov99] (^{57}Fe) relies on the excitation of the ^{57}Fe nuclei in the sample, a $^{57}\text{Fe}/\text{Cr}$ multilayer in our case. After excitation with the Mössbauer wavelength of 0.860\AA , the nuclei decay by emitting radiation. This emitted radiation is called the nuclear resonant scattering and has a time structure. Furthermore, it depends on the Bragg geometry of the measurement, see fig. 3.3. From this nuclear resonant the hyperfine structure of the nuclei can be probed. Moreover, it can be used to determine the magnetization in the Fe layers. Toellner et al. [Toel95] showed that in the nuclear resonant ω - 2θ pattern of an antiferromagnetically coupled Fe/Cr layer, a peak shows up at the antiferromagnetic Bragg position. SMR is sensitive to the magnetic structure in magnetic multilayers [Toel95, Bott98] and it is for this purpose that the technique is applied. Because its complexity and the limited number of experiments in this thesis, it is not the intention

to discuss SMR from a profound theoretical point of view. In contrary, the technique will be introduced from the experimental side. The here presented measurements are carried out at the BW4 beamline at the DORIS storage ring in HASYLAB at DESY. The ring contains typically a 140 mA current of 4.5 GeV positrons grouped in 5 bunches. By use of a wiggler a white electromagnetic beam (2keV-30keV) is produced, see fig. 3.5. A first double Si(111) premonochromator reduces the energy range to 2 eV. Secondly a nested monochromator, made out of a single Si crystal filters down to a width of 10 meV around the Mössbauer energy of ^{57}Fe , 14.413 keV or 0.860Å. This beam is used for performing the SMR experiments.

As above mentioned for the SMR experiments, the photons emitted from the nuclei are of interest. Since the measurement geometry is that of a regular low angle X-ray reflectivity measurement, it is necessary to distinguish between the nuclear resonant intensity and the regular X-ray diffraction from the electronic structure. To solve this problem, the synchrotron beam is pulsed.

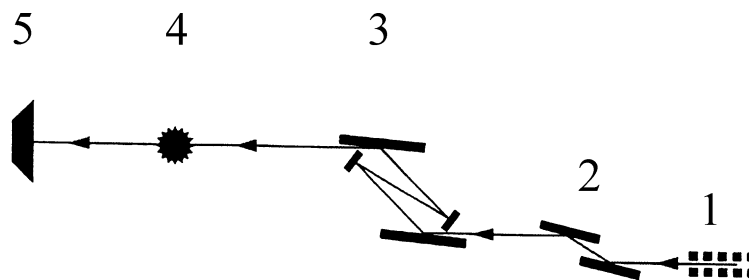


Fig. 3.5 The SMR setup. A white beam is generated using a wiggler (1), (2) double premonochromator, (3) nested monochromator, (4) scattering experiment, (5) photodiode.

The positrons in the accelerator are confined in bunches (10^{-12} s). Therefore the electromagnetic radiation is pulsed and can be monitored as function of time after each bunch has passed the wiggler. The scattering at the electrons occurs instantly ($< 10^{-12}$ s) while the lifetime of the nuclei is of the order of 10^{-7} s. This difference in timescale for the two processes permits us to distinguish between them. Photons directly arriving are purely electronically scattered. If the photons have interacted with the nucleus they are delayed. It is important to emphasize that this nuclear scattering contains information on the state of the nuclei but is also affected by the electronic scattering. Firstly, the delayed radiation can be integrated and monitored as function of angle like for a regular X-ray reflectivity measurement. Secondly, for each angle the intensity varies as function of time, i.e. a quantum beating occurs. In the further presented measurements, only the ω - 2θ dependency will be discussed.

- **Neutron diffraction**

The third type of particle that is used for performing diffraction experiments are neutrons. Neutron scattering provides chemical and magnetic information from the studied structure. The chemical information originates from scattering at the nuclei of the atoms. This is a point like (nucleon-nucleon) interaction (strong force) since the wavelength of the thermal neutrons is larger (1-10Å) than the nucleus (10^{-13} Å). Therefore no angle dependence, as present for the X-rays scattering, shows up in the scattering length, see fig. 3.6. The scattering length f expresses how

strong particles are scattered. For X-rays, scattering is caused by the electron cloud which is of the same size as the photon wavelength resulting in an angular dependence of the scattering strength.

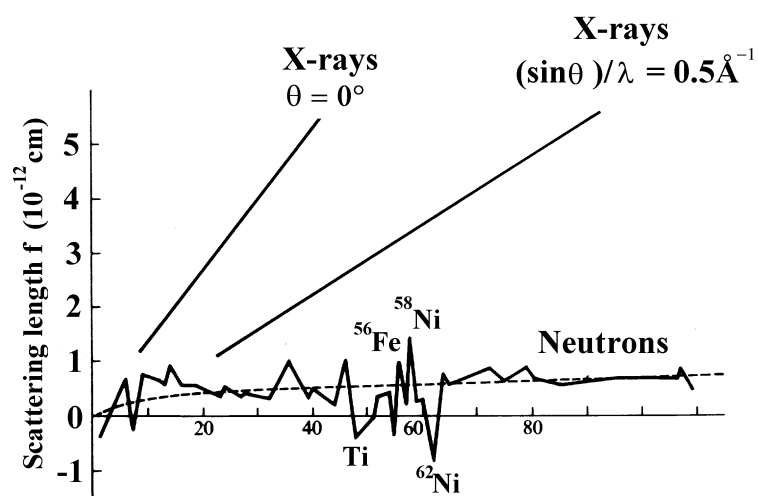


Fig. 3.6 The scattering length for neutrons compared to that of photons.

In this work the advantage of the magnetic scattering is used. The neutron carries a magnetic moment ($\mu_n = 9.66 \cdot 10^{-27} \text{ Am}^2$) and thus

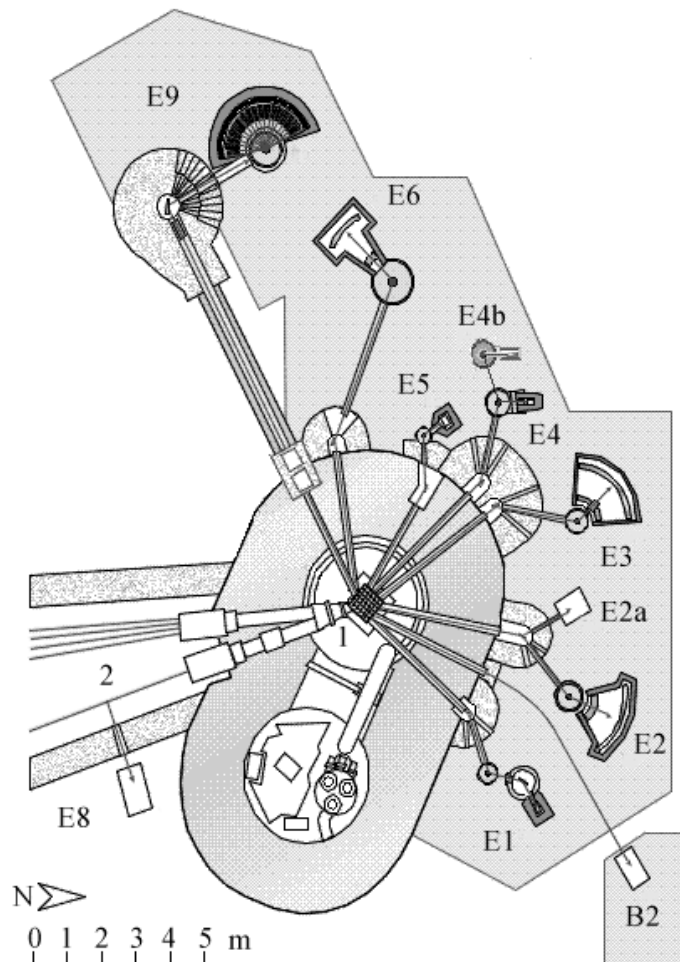


Fig. 3.7 The ground plan of the reactor and the experimental hall at the HMI, Berlin. (1) core of the reactor (2) neutron guides towards the neutron guide hall. The different instruments are named E x.

an additional scattering occurs in magnetic materials. The strength of this magnetic scattering (magnetic scattering length) is of the same order of magnitude as for the nuclear

scattering. Because in most cases the studied magnetic properties are caused by the electron cloud, the magnetic scattering strength is angle dependent, i.e. the scattering strength drops for higher q values. The discussion of both types of scattering will be treated further for the two specific cases that are presented in this work i.e. polarized neutron reflectometry and high angle neutron diffraction.

Both type of experiments are carried out in the Hahn-Meitner-Institut at the Berliner Neutron Scattering Centre (BENSC). The neutrons are generated in the light water cooled BER-2 reactor having 10 MW of thermal power. Neutrons are produced by fission of ^{235}U and are thermalised by the surrounding water. They leave the reactor via transparent windows and are further guided via neutron guide lines. The energy distribution of the neutrons is described by a Maxwell-equation and a maximum intensity is achieved around 1.8\AA or 25 meV at RT.

The reflectometer V6 is placed in the neutron guide hall and receives neutrons with longer wavelengths. The longer wavelength is generated by a second moderation through a cold source having pressurized hydrogen at 27K. An overview of the reactor is given in fig. 3.7.

• Neutron Reflectometry

The magnetic structure of Fe layers in the epitaxial Fe/Cr multilayers is studied in a neutron reflectivity setup. A scheme of this setup is shown in fig. 3.8. A first monochromazation occurs via Bragg scattering on a pyrolytic graphite filter, see fig. 3.8, having a lattice spacing of 3.355\AA . This graphite crystal is placed in the neutron guide and all neutrons satisfying the Bragg law are

diffracted. Since not only the wavelength λ but also $\lambda/2$, $\lambda/3$, ... fulfil the Bragg conditions, a second filtering is necessary. Therefore a polycrystalline Be block is cooled down to 80K. The largest lattice spacing of Be is about 2\AA and again based on Bragg scattering all wavelengths shorter than 4\AA are deflected. The wavelength used at the reflectometer is 4.66\AA . After the Be-filter the beam size is defined by a two slit system. The beam is reflected at the sample and detected using gas tubes with pressurized ^3He . Finally, a monitor is used for counting in-situ the flux so that fluctuations in the intensity of the source are cancelled.

If more information on the magnetic structure is needed a polarization analysis can be carried out. To perform such Polarized Neutron Reflectivity (PNR) measurements a single spin direction (down) of the neutron is selected by use of a polarizing supermirror.

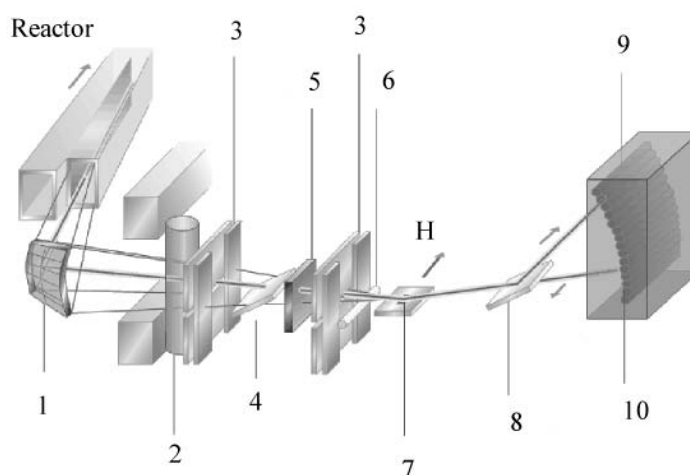


Fig. 3.8 The V6 apparatus for polarized neutron reflectivity is shown. (1) focussing monochromator, (2) Be-filter, (3) slit system, (4) polarizing supermirror, (5) flipper, (6) monitor, (7) sample, (8) analyzing supermirror, (9) detector, (10) ^3He tube.

After the mirror a flipper can switch the spin of the incident neutrons. During the interaction with the sample the neutron spin can be altered. A second supermirror separates the spin-down and spin-up contribution so that they are simultaneously detected. This geometry allows to detect the four possible reflectivities : up-up, down-down, up-down and down-up can be measured. From these intensities the direction of the magnetic moment in the sample with respect to the neutron spin is determined. A magnet can be mounted to apply an external field and if necessary temperature dependency is achieved using a closed cycle cooler.

A description of this scattering geometry can be found in [Fer99 ChapterB3, Zab98, Zab94, Fel93]. Figure 3.9 shows the different components.

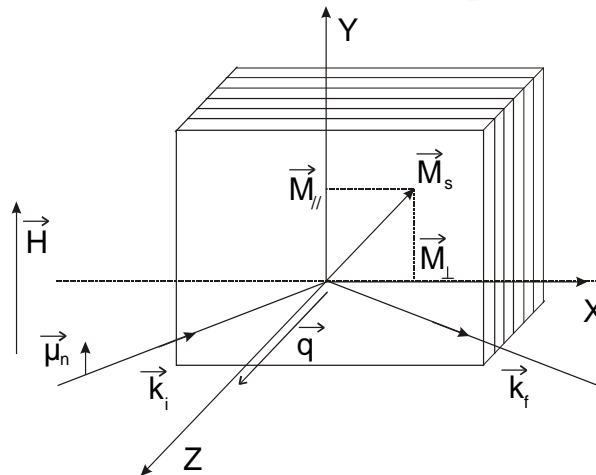


Fig. 3.9 The polarized neutron reflection geometry.

The scattering vector $\mathbf{q} = \mathbf{k}_f - \mathbf{k}_i$ is oriented along the z-axis, perpendicular to the diffracting planes and the neutron spin up state is oriented along the y-axis. The magnetisation \mathbf{M}_s is directed in the plane having a component $\mathbf{M}_{//}$ parallel to the neutron spin and a component \mathbf{M}_{\perp} perpendicular to the neutron spin.

In the quantum mechanical approach, the interaction can be described by the Schrödinger equation (3.1) :

$$\left[-\frac{\hbar}{2m}\Delta + \left(V - \frac{\hbar^2 \vec{k}^2}{2m} \right) \right] \Psi = 0. \quad (3.1)$$

The symbols in equation (3.1) are defined as Planck's constant \hbar , the Laplacian operator $\Delta = \partial^2/\partial x^2 + \partial^2/\partial y^2 + \partial^2/\partial z^2$, V the potential introduced by the sample, \mathbf{k} the neutron wave vector and m the mass of the neutron. For polarized neutron reflectivity measurements the spin, as chosen by the supermirror and flipper, is taken into account. Therefore the wave function Ψ is described by a spinor (3.2):

$$\Psi \rightarrow \begin{pmatrix} \Psi_+(\vec{r}) \\ \Psi_-(\vec{r}) \end{pmatrix}. \quad (3.2)$$

The wave function $\Psi_+(\mathbf{r})$ is related to the state having the spin of the neutron directed along the external field H while for $\Psi_-(\mathbf{r})$ the spins are opposed to the field. The magnetic as well as the nuclear sample-neutron interaction is described by the one-dimensional potential $V(z)$:

$$V(z) = \frac{2\pi\hbar^2}{m} b\rho - \gamma\mu_N \vec{\sigma} \cdot \vec{B}. \quad (3.3)$$

The first term in equation 3.3 describes the nuclear scattering. The nuclear scattering length of the material is given by b and the density of the material by ρ . The magnetic interaction of the spins with the magnetic induction $\mathbf{B} = \mathbf{H} + 4\pi\mathbf{M}$ is given by the second term in which $\boldsymbol{\sigma}$ stands for the three Pauli matrices :

$$\sigma_{\perp} = \begin{pmatrix} 0 & 1 \\ 1 & 0 \end{pmatrix}, \quad \sigma_{//} = \begin{pmatrix} 1 & 0 \\ 0 & -1 \end{pmatrix}, \quad \sigma_z = \begin{pmatrix} 0 & -i \\ i & 0 \end{pmatrix}. \quad (3.4)$$

Further, the magnetic moment of the neutron equals $\gamma=1.913$ times the nuclear magneton μ_N . Substitution of equations 3.2 - 3.4 into 3.1 taking the scattering geometry and thus the one-dimensionality of the potential $V(z)$ into account results in a system of coupled linear differential equations :

$$\begin{aligned} \Psi_+''(z) + \left[k_{0z}^2 - 4\pi b\rho + \frac{2m\gamma\mu_n}{\hbar^2} B_{//} \right] \Psi_+(z) + \frac{2m\gamma\mu_n}{\hbar^2} B_{\perp} \Psi_-(z) &= 0 \\ \Psi_-''(z) + \left[k_{0z}^2 - 4\pi b\rho - \frac{2m\gamma\mu_n}{\hbar^2} B_{//} \right] \Psi_-(z) + \frac{2m\gamma\mu_n}{\hbar^2} B_{\perp} \Psi_+(z) &= 0 \end{aligned} \quad (3.5)$$

If in equation 3.5 $B_{\perp} = 0$, then no mixing terms are present and only non-spin flip scattering occurs, i.e., during the scattering process the spin of the neutron remains the same. On the other hand $B_{//} = 0$ results in only spin-flip scattering, i.e. after scattering the spin of the neutron is reversed. Classically it can be understood from the view point of precession. If the magnetic induction \mathbf{B} is

oriented perpendicular to the spin of the neutron, a precession around \mathbf{B} towards the other spin state occurs. Therefore polarized neutron diffraction provides information on the orientation of the magnetisation within the sample. In practice, the model is implemented in a recursive formalism in similarity with the approach for optics like low angle X-ray diffraction and the information is obtained via simulation of the four possible cross-sections : up-up, up-down, down-down, down-up.

- **High angle neutron Diffraction**

The second setup is the E1 triple axis spectrometer of which the floor plan is shown in fig. 3.10. This high angle apparatus is used to study the magnetic state of the epitaxial Cr films.

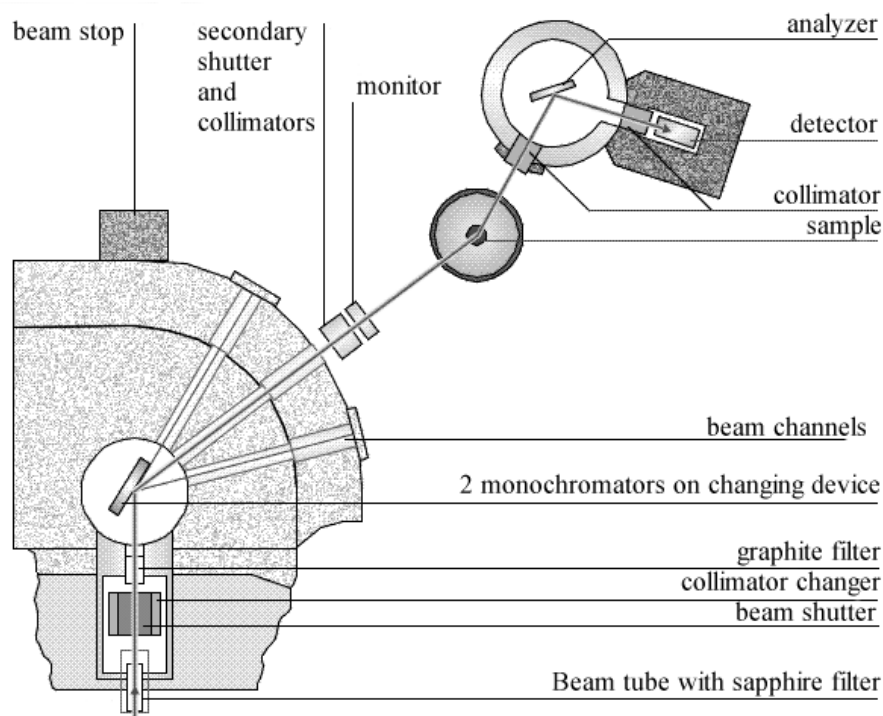


Fig. 3.10 *The E1 triple axis apparatus is schematically sketched.*

The neutrons leave the neutron guide and a first filtering occurs by two sapphire single crystals which scatter out all wavelengths smaller than 0.8\AA . The second filter is a pyrolytic graphite filter with the c-axis parallel to the beam. This filter suppresses the higher orders of 2.422\AA neutrons. The filters are positioned in such a way that the contribution to the background is as low as possible.

After the filtering a second pyrolytic graphite filter in reflection geometry diffracts (first axis) the 2.422\AA neutrons towards the sample (second axis). Collimators (20', 40', 80', open) determine the divergence of the beam and a monitor is placed for measuring the intensity. The

goniometer carrying the sample has a large bearing surface such that cryostats or heavy superconducting magnets can be fitted on it. A third axis, the analyzer, is present for inelastic scattering events. Since we are focussing on elastic scattering this axis is set to zero during our experiments. Finally, the whole setup can be moved on a 'Tanzboden' i.e. it floats on pressurized air over the ground.

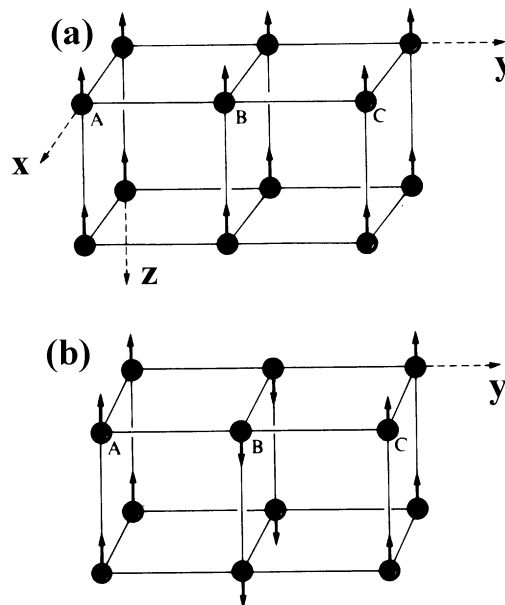


Fig. 3.11 A ferromagnetic system (a) and an antiferromagnetic system (b) are shown.

The setup allows to carry out polarized measurements. However for the study of the magnetism of epitaxial Cr layers no polarization analysis as shown for the reflection geometry is necessary. Therefore the incident beam consists of unpolarized neutrons. A description of unpolarized neutron diffraction can be found in [Bacon75]. The

observed intensity I_{hkl} for the (hkl) reflection is proportional to the square of the structure factor F_{hkl} and given by :

$$|F_{hkl}|^2 = \left| \sum_n b_n \exp(2\pi i(hx_n/a + ky_n/b + lz_n/c)) \right|^2 + \left| \sum_n \bar{q}_n^m p_n \exp(2\pi i(hx_n/a + ky_n/b + lz_n/c)) \right|^2 \quad (3.6)$$

The first term corresponds to the nuclear scattering while the magnetic interaction is given by the second term. In equation 3.6, the summation occurs over the atoms in the unit cell, b_n stands for the nuclear scattering length of atom and the unit cell itself is defined by the three distances a, b, c . On the other hand for the magnetic term, the magnetic scattering length p_n represents the strength of the interaction between the magnetic moments of the neutron and the atom. In this magnetic contribution an extra factor, i.e. the magnetic scattering vector \bar{q}^m shows up. As derived by Halpern and Johnson [Halp39] this vector is defined as :

$$\bar{q}^m = \bar{\xi}(\bar{\xi} \cdot \bar{K}) - \bar{K} , \quad (3.7)$$

where $\bar{\xi}$ is the unity vector in the direction perpendicular to the diffracting planes and \bar{K} the unity vector in the direction of the atomic spin. The magnetic structure factor \bar{F}_{magn} :

$$\bar{F}_{magn} = \sum_n \left(\bar{\xi}(\bar{\xi} \cdot \bar{K}_n) - \bar{K}_n \right) p_n \exp(2\pi i(hx_n/a + ky_n/b + lz_n/c)) \quad (3.8)$$

is therefore a vector quantity. This relationship between the spin orientation and the regular scattering vector $\mathbf{q} = \mathbf{k}_f - \mathbf{k}_i$ (\mathbf{q} is \perp to diffracting planes at constructive interference conditions) imposes an extra restriction on the observed intensity. Magnetic scattering from spins directed along \mathbf{q} does not occur since \mathbf{q}^m equals zero for such a geometry. Further, it can be seen from equation 3.6 that the magnetic and nuclear contributions do not interfere and are therefore additive.

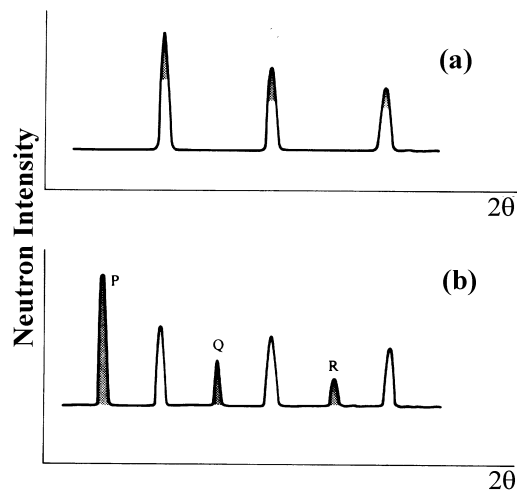


Fig. 3.12 The diffraction pattern of a ferromagnet (a) and an antiferromagnetic (b). The magnetic scattering (shaded area) is additive to the nuclear (white) intensity. For the antiferromagnet additional reflections P,Q,R arise at intermediate sites.

To illustrate this feature it is informative to compare the intensity profiles generated by a ferromagnet and an antiferromagnet. These structures are shown in fig. 3.11. In fig. 3.11 (a) a ferromagnetic structure is presented. The spins

are pointing for all atoms in the same direction so that the magnetic scattering vector \mathbf{q}^m in equation 3.6 is the same for all the atoms (A,B,C) and can be brought in front of the summation. Therefore at the positions of the structural reflections an additional (shaded area) intensity occurs, see fig. 3.12 (a). For an antiferromagnet, see fig. 3.11 (b) the situation is different. Remark that for a simple antiferromagnet the magnetic unit cell has twice the size of the chemical unit cell. As can easily be derived from equation 3.6, no magnetic scattering occurs at the structural reflections because \mathbf{q}^m is opposite for atoms A and B. Moreover, at half the angles in the reciprocal space a pure magnetic peak shows up, see fig. 3.12. The magnetic state of Cr is more complicated and a full evaluation of equation 3.6 over the complete magnetic unit cell is necessary to explain the diffraction pattern. An overview of the main results for Cr is given in paragraph 2.3.2.

3.2.2 The Magneto-Optical Kerr effect

The Magneto-Optical Kerr effect (MOKE) setup is used to investigate the magnetic behaviour of thin films. The MOKE effect refers to the change in the properties of linear polarized light that is reflected by a magnetic material, in our case thin films. Depending on the orientation between the magnetization three contributions are distinguished, see fig. 3.13. The longitudinal (a) and polar (b) Kerr effects are manifested as an induced ellipticity and rotation of the linear polarization due to an magnetization component that is oriented in the plane of the incident and reflected beam. The transverse Kerr effect is caused by the magnetic component perpendicular to the plane of incident and reflected beam and

results in intensity variations of the reflected beam [Zvez97].

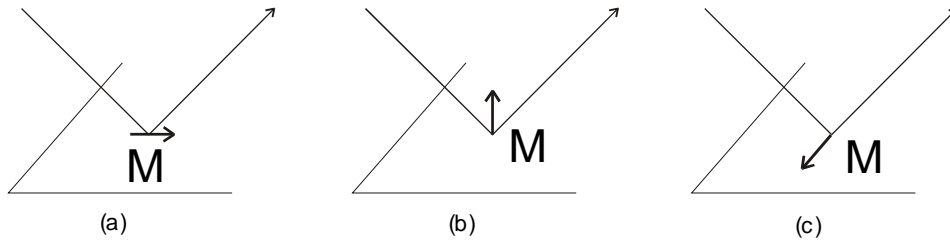


Fig. 3.13 The contributions to the Kerr effect as function of the magnetization direction is shown. (a) longitudinal Kerr effect, (b) Polar Kerr effect, (c) transversal Kerr effect.

The microscopic origin of the Magneto-Optical Kerr effect is related to the exchange splitting and the spin orbit coupling, a thorough description can be found in [Fer99 chapter C5,C6,C7 and C8, Schä98]. An intuitive picture towards its understanding is given in fig. 3.14. The figure treats the longitudinal case since this is the geometry of the experimental setup in our laboratory. The principle is also valid for the polar and transversal geometry.

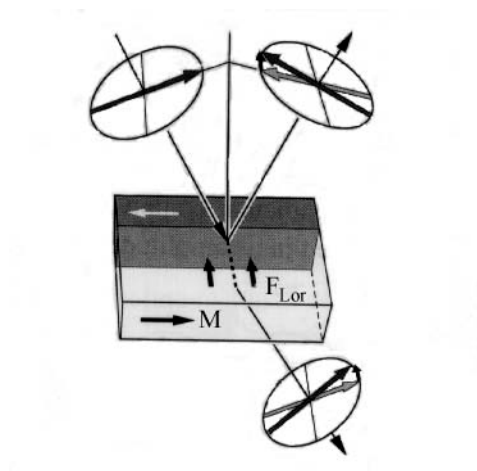


Fig. 3.14 *Explanation of the longitudinal Kerr-effect following the concept of the Lorentz force [Schä98, p. 26]*

In figure 3.14, the light is linear polarized in the plane of reflection. The electrons in the sample will undergo an oscillation due to electric field \mathbf{E} of the light. Due to the Lorentz force their trajectory is altered according to the Lorentz force $\mathbf{F}_{\text{Lor}} = -\mathbf{M} \times \mathbf{E}$. Because of the Huygens' principle the polarization of the reflected light is affected and a small rotation of the polarization shows up.

Our setup is based on the longitudinal Kerr effect while the polar geometry can be configured as well. The setup is sketched in fig. 3.15 and is home built. A 20mW HeNe gas tube laser (632nm) or a 7mW 780nm laser diode are used as light source. The beam can be shaped by a 50 μm round pinhole. Lenses focus or defocus the beam on the sample and eventually the intensity can be dimmed by a gray plate. The last component between the sample and laser is always the polarizer since it is undesirable to affect the polarization by other optical components. It polarizes the light linear in the plane of the incident and reflected beam. The sample can be manually rotated for measuring anisotropic features while the vertical position is computer controlled. The vertical positioning is a handy tool if the physical properties vary over the sample surface like for wedge shaped samples. The composition of these samples varies gradually in such a way that the induced physical properties like IEC or magnetization can be studied systematically on one sample. The water-cooled electromagnet provides a field range up to 1T.

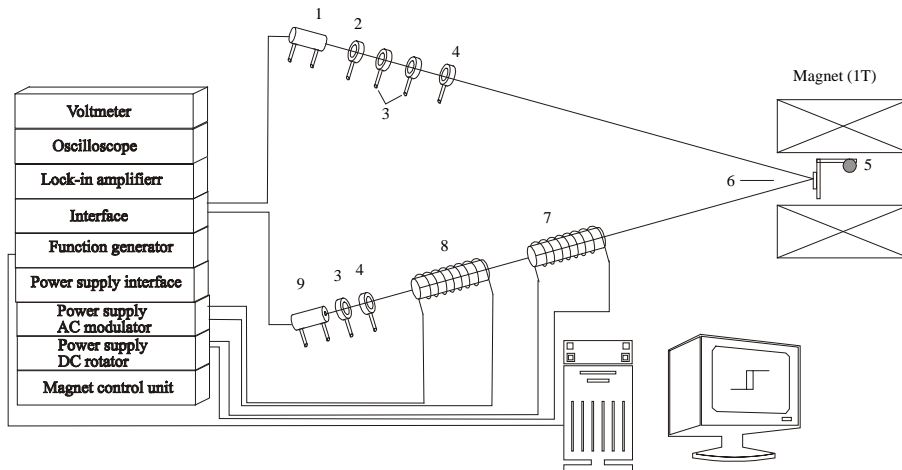


Fig. 3.15 The MOKE setup. (1) Laser, (2) pinhole, (3) lenses, (4) polarizer, (5) micrometer screw, (6) sample, (7) DC rotator, (8) AC modulator, (9) detection system.

During the measurement the polarization of the reflected beam is rotated over typically a few millidegree (mdeg) depending on the magnetization of the sample. In order to measure this deviation several components are used. Firstly, the reflected beam propagates through the DC rotator. This optical rotator is calibrated and rotates the polarization back to its original zero value so that the exact Kerr angle is measured. Such a rotator consists of a coil wound around a Faraday glass. The name Faraday is related to the transmission geometry while Kerr refers to reflection. This glass rotates the polarization according to the following formula (3.9) :

$$\alpha = V \cdot L \cdot B \quad (3.9)$$

The value for the induced rotation α , 1 deg at maximum, equals the Verdet constant V of the glass (20.7 rad/T*m) times length $L = 10$ cm of the glass

times the magnetic field $B = 0.01$ T. Secondly, an AC modulator is used. The AC modulator is identical to the rotator but the magnetic field is alternating and thus the induced rotation is oscillating. Thirdly, an analyzing polarizer is set in extinction and converts the polarization information into intensity. After passing the filter (for 780 or 632 nm) the intensity is detected by a photodiode. A mathematical expression clarifying the measurement principle is given below, formula 3.10 - 3.12. The analyzing polarizer is described by the Malus law. The total rotation angle φ results from several contributions, the Kerr rotation φ_K , a manual misalignment φ_0 , and the modulation $\varphi_M \sin \omega t$. The rotator function is excluded and will be explained later on.

$$I = I_0 \sin^2 \varphi \cong I_0 \varphi^2 \quad (3.10)$$

$$\varphi = \varphi_K + \varphi_0 + \varphi_M \sin(\omega t) \quad (3.11)$$

The sinus can be neglected since the angles are small and finally two time dependent terms with frequency resp. ω and 2ω are obtained :

$$I \cong \text{Constant} + 2\varphi_M I_0 (\varphi_0 + \varphi_K) \sin(\omega t) + \varphi_M^2 I_0 \sin^2(\omega t) \quad . \quad (3.12)$$

The amplitude of the ω dependent term is proportional to the Kerr rotation and by use of a lock-in a dc reading is achieved. The setup can work without the rotator. During measurements with the rotator the signal is kept constant. The current generating the magnetic field in the rotator is proportional to the Kerr-rotation, see formula 3.9, and after calibration the exact value is obtained.

In figure 3.15 the longitudinal geometry is shown. However it is also possible to measure in polar geometry, i.e. the sample surface is perpendicular to the magnetic field and the light passes through the two poles of the magnet.

3.2.3 Rutherford Backscattering

Rutherford Backscattering (RBS) measurements are carried out in collaboration with the group of A. Vantomme [AV98]. The RBS technique is based on the energy analysis of backscattered He ions. A schematic drawing of the setup is shown in fig. 3.16.

The incident beam has an energy of 2.9 MeV and is generated by a two-step process in the Pelletron. Firstly the He atoms are negatively charged and then accelerated over positive potential of about 1.45 MeV. In the middle of the Pelletron, the atoms are stripped resulting in positive ions that are a second time accelerated over the decreasing potential. After leaving the Pelletron, the 2.9 MeV beam is focussed using a quadrupole magnets. Finally, a bending magnet directs the ions towards the RBS chamber.

This energy is reduced after its interaction with the sample. The amount is depending on the mass of the nucleus. Therefore this energy loss determines the type of atom that is responsible for the backscattering. Secondly, during its path the particle loses energy because of the interaction with the electrons and thus a depth profile of the chemical structure can be achieved. In this respect, the detector has an energy resolution of 15 keV resulting in a depth resolution of about 50Å in common conditions. Thirdly, the concentration is estimated from the amount of backscattered particles. The sensitivity on the concentration is depending on the composition of the sample since

the cross-section for backscattering varies with the square of the atomic number. For heavy atoms surrounded by a light matrix sensitivities up to one monolayer and less can be reached.

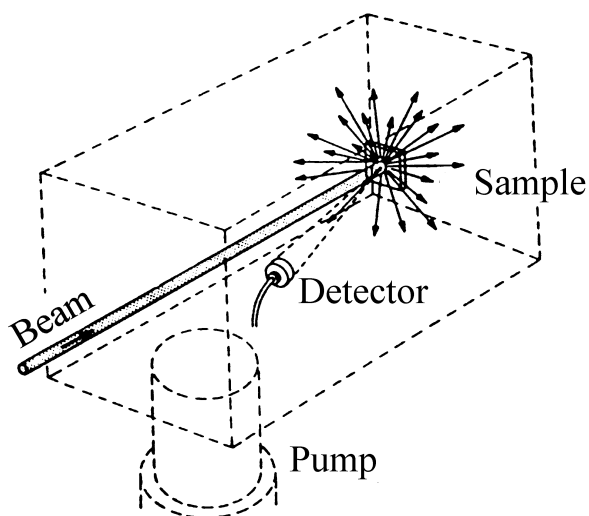


Fig. 3.16 A *schematic representation of the RBS setup is given.*

In practice, the information is derived from simulating the backscattered pattern using the RUMP computer program[DOOL85].

Finally, a last relevant phenomenon called channeling will be mentioned. If the path of the incident ions is parallel to the arrangements of atoms in the sample, channeling occurs. The backscattered yield diminishes and a minimum is obtained for exact alignment. The ratio between the backscattered yield at channeling geometry and at random incidence is a measure for the sample quality.

3.2.4 Scanning Probe Microscopy

Scanning Probe microscopy (SPM) is a general principle for studying surfaces. A sharp probe tip is brought in the vicinity of the surface and from their interaction information is extracted. A variety of interactions can be observed leading to the different techniques : STM, Scanning Hall Microscopy (SHPM), Surface Near Field Optical Microscopy (SNOM), Atomic Force Microscopy (AFM), Magnetic Force Microscopy(MFM), ... The latter two will be discussed in more detail because of their relevance to this work.

In AFM, a sharp tip is attached to a flexible cantilever. The tip moves over the surface driven by piezos, see fig. 3.17. If a height difference is encountered, the tip bends and the laser beam shining on top of the cantilever is deflected. This deflection is probed by a split-photodiode connected to a feedback mechanism. The feedback systems adjust the piezos so that the height remains constant. In this way the topography of a surface is mapped. The maximum scan range is about 50 μ m and the lateral resolution is in order of a few nanometer. In general the resolution is not as good as for STM but AFM offers the advantage of studying also non-conducting surfaces.

If during the measurement the tip stays in contact with the sample, the AFM is operating in contact mode. Next to the contact mode, a tapping mode can be used. In the tapping mode the cantilever oscillates near it's resonance frequency. The tip-surface interaction affects the amplitude of the oscillation that is kept constant using a feedback mechanism.

MFM is based on the same principle. The tip is now magnetic and therefore the bending of the cantilever is sensitive to the magnetic strayfields that are leaking out of the sample. These magnetic fields are of a longer range than the Van der Waals

atomic forces. Therefore the magnetic signal can be separated by scanning in 'non-contact' with the surface, typically 20-200nm above the surface. This scanning above the surface reduces the resolution until a few tens nanometer.

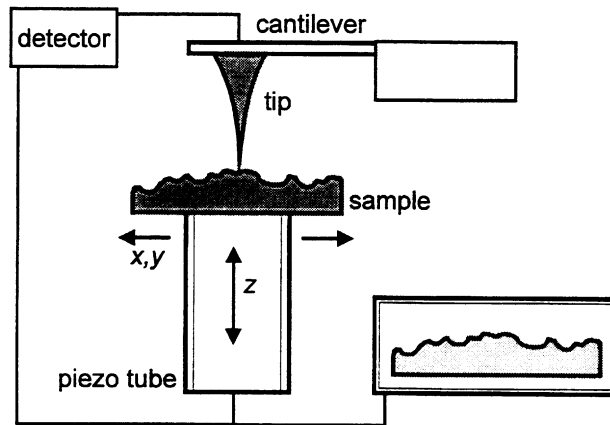


Fig. 3.17 *The principle of AFM is shown.*

3.2.5 Resistivity Measurements

The resistivity measurements are carried out in a standard oxford ^4He cryostat with a temperature range from 2-300K. The magnetic field can be swept up to 8T (10T if cooled below the lambda point 2.2K) in steps of 1mT. The sample can be tilted within a range of 100 deg with respect to the field. All measurements are carried out in standard four probe geometry. An appropriate pattern is directly achieved by evaporation on a resist pattern or by etching chemically a film. Figure 3.18 shows the pattern used for the etching. In the direct method a resist layer is spun on the substrate. The necessary pattern is written in the resistlayer by e-beam and removed during development. After deposition, the superfluous

material is washed away in a bath of boiling acetone. If the pattern is chemically etched into a film, the resist layer is spun on top of the film. Writing of the pattern occurs now using a UV light and a mask. After development of the resist, the film is etched using an acid.

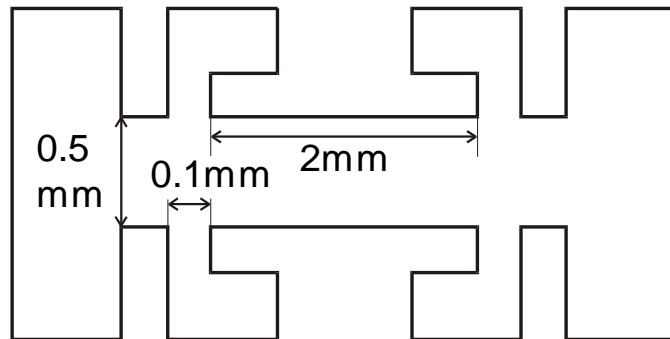


Fig. 3.18 The pattern used for the electrical measurements is shown.

Chapter 4

Experimental results

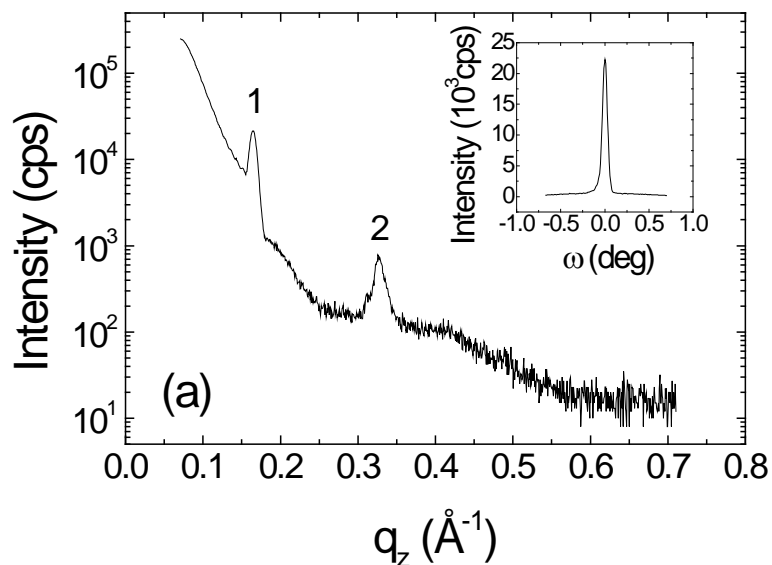
4.1 The magnetic structure of Fe/Cr multilayers

4.1.1 Introduction

In the last ten years a lot of attention has been paid to metallic multilayers because of the GMR effect and the antiferromagnetic coupling of adjacent magnetic layers. Since these effects are nowadays relatively good understood, we will focus in this chapter on the behaviour of the magnetization in antiferromagnetically coupled Fe/Cr multilayers on MgO(001) substrates. After preparation the samples are characterized using XRD, magnetization- and magnetoresistivity measurements. Using neutron reflectometry we could observe a spinflop transition which is further investigated by MOKE, SQUID and resistivity measurements. Finally, we measured the spin flop transition using synchrotron Mössbauer reflectometry.

4.1.2 Preparation and characterization

The samples are grown on $2 \times 2 \text{ cm}^2$ MgO(001) substrates by MBE. This relatively large size of the substrate is necessary to compensate the low neutron flux and to achieve a higher reflected intensity. After introduction, adsorbates on the surface that can disturb the epitaxial growth are removed by annealing the substrates for 15' at 600°C in 10^{-10} mbar. Next, Fe and Cr are deposited in an alternating way at a rate of typically 0.5 \AA/s while the pressure remains below 1×10^{-9} mbar. During the evaporation the substrate is rotated to ensure a good homogeneity. The samples are grown while the substrate is held at 50°C .



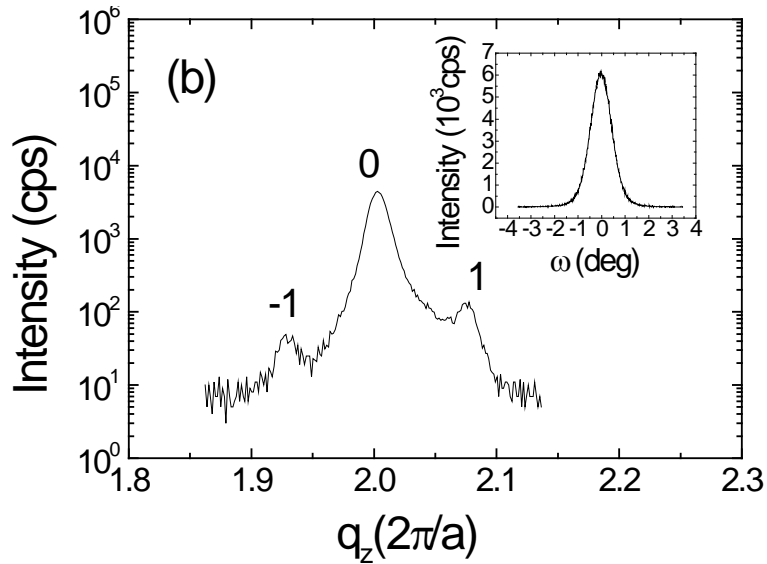


Fig. 4.1.1 Low (a) and high angle (b) XRD diffraction patterns for the $\text{MgO}(001)/[\text{Fe}(26\text{\AA})/\text{Cr}(13\text{\AA})]_{20}$ multilayer. The corresponding ω -scans, taken at resp. $q_z = 1.65 \text{ \AA}^{-1}$ and $q_z = 2$ are shown in the insets.

The structural characterization using XRD is shown in fig. 4.1.1. Figure 4.1.1a shows the low angle XRD pattern for the $\text{MgO}(001)/[\text{Fe}(26\text{\AA})/\text{Cr}(13\text{\AA})]_{20}$ multilayer. In the following we will focus on this sample because it shows a spinflop transition that is not observed in the other samples studied by neutron reflectometry.

Since the low angle XRD pattern (Fig.4.1.1a) is sensitive to the modulation of the scattering density such as the chemical Fe/Cr modulation, clear first and second order Bragg peaks at $q_z = 0.165$ and 0.326 \AA^{-1} appear due to the 39 \AA Fe/Cr modulation. Information about the overall layering quality is obtained from the ω -scan around the first order reflection shown in the inset of fig. 4.1.1a. The width of 0.07 deg equals the instrumental resolution and represents the spread

on the layering. It is therefore an upper limit for the layering. Furthermore, this small diffuse background can contain information on the lateral roughness.

The high angle regime, which is sensitive to the atomic structure, is shown in fig. 4.1.1b. The superlattice peaks are found around the (002) reflection of Fe (Cr) confirming a 002 oriented growth. Next to the 0th order superlattice peak the two satellites (-1,+1) are present, indicating a relatively low interface roughness. The inset shows the ω -scan taken around the 0th order superlattice peak. The mosaic spread on the grain as derived from this ω -scan is 0.9 deg. Finally, in plane information is obtained by measuring the (112) reflections while rotating the sample around the [001] axis. Four distinct reflections were observed proving the complete epitaxy. In conclusion the XRD measurements prove the crystallographic oriented growth and the multilayer structure.

Since the thickness of the Cr (13Å) is taken around the maximum of the antiferromagnetic coupling, a GMR effect and an antiferromagnetic coupled magnetization loop is expected. In order to investigate these magnetic properties MOKE magnetisation measurements at room temperature (RT) and magnetoresistance measurements are performed.

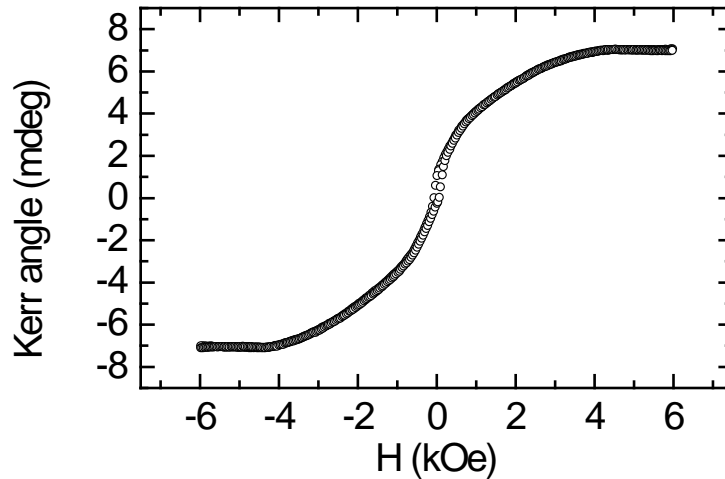


Fig. 4.1.2 MOKE magnetization curve of the $\text{MgO}(001)/[\text{Fe}(26\text{\AA})/\text{Cr}(13\text{\AA})]_{20}$ multilayer. The curvature is typical for antiferromagnetically coupled Fe layers having a biquadratic term.

Figure 4.1.2 shows the MOKE measurement. The small remanent magnetisation and the high saturation field of 4 kOe is typical for antiferromagnetically coupled layers. Secondly, the loop has a curvature. If the coupling has a strict bilinear nature, a linear behaviour of the magnetisation is expected. The curvature is explained by the second order term or biquadratic contribution. In summary, we can deduce from these measurements that at least at the surface the adjacent Fe layers are antiferromagnetically coupled and thus a GMR effect should be present.

The magnetoresistivity measurements are shown in fig. 4.1.3. At 4.2K there is a 10% GMR effect and at RT 4%. Saturation at RT is obtained at about 4 kOe when the magnetizations in the Fe layers line up as which is in agreement with the MOKE magnetisation measurements.

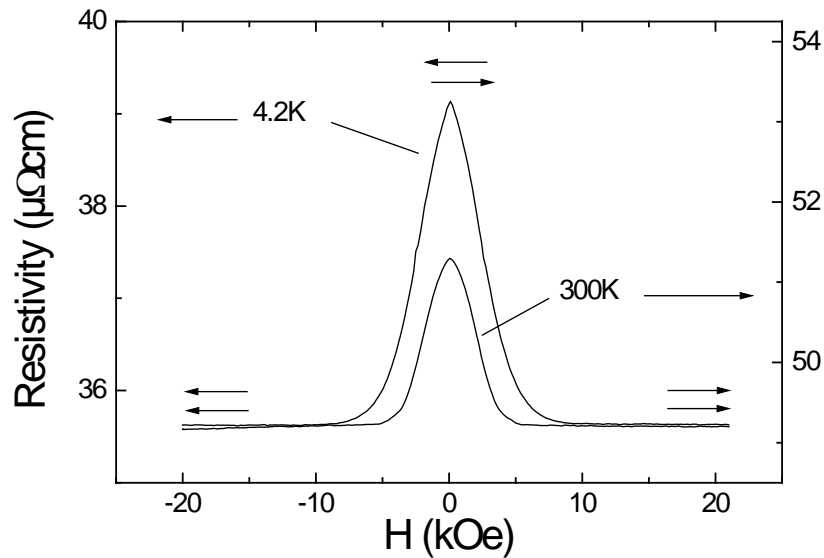


Fig. 4.1.3 *Magnetoresistivity measurements of a MgO(001)/[Fe(26Å)/Cr(13Å)]₂₀ multilayer. The pairs of arrows indicate the magnetization direction of two adjacent Fe layers.*

The relative low GMR effect can be explained by the high resistivity values of resp. 50 (at RT) and 40 $\mu\Omega\text{cm}$ (at 4.2K). The estimated mean free path for these values is about 12Å, which is comparable to the spacer thickness. In order to achieve a high GMR effect in CIP geometry the main free path should be larger than the spacer thickness [Swag97]. Nevertheless there is a clear GMR effect present which saturates at resp. 0.5T-1T.

In general we conclude from the XRD measurements that the samples are epitaxial and well layered. From the MOKE and the magnetoresistivity measurements we deduce that antiferromagnetically coupled domains are present.

4.1.3. Unpolarized Neutron Reflectometry

One of the most common methods to visualize magnetic periodic structures is neutron diffraction. More specific, for thin magnetic multilayers neutron reflectometry is the recommended technique. Figure 4.1.5 shows the specular low angle neutron reflectivity pattern of the $\text{MgO}(001)/[\text{Fe}(26\text{\AA})/\text{Cr}(13\text{\AA})]_{20}$ multilayer.

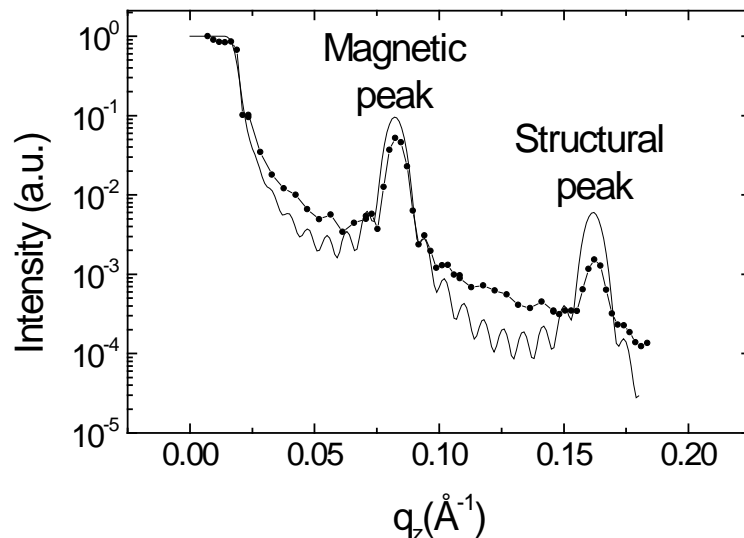


Fig. 4.1.4 Unpolarized neutron reflectivity curve for a $\text{MgO}(001)/[\text{Fe}(26\text{\AA})/\text{Cr}(13\text{\AA})]_{20}$ multilayer. The solid points are the measured data and the line is a simulation.

Up to $q_z = 0.02 \text{ \AA}^{-1}$ ($\omega = 0.4 \text{ deg}$) the neutrons undergo total reflection and cannot sense the buried structure. Therefore the reflectivity is 100% in this regime and thus the intensity is normalized to the value of one. For higher angles the neutrons penetrate the multilayer and constructive interference arises at $q_z = 0.082 \text{ \AA}^{-1}$ and 0.162 \AA^{-1} . X-ray diffraction measurements, see

fig. 4.1.4, learn us that the intensity at $q_z = 0.162 \text{ \AA}^{-1}$ is generated by the chemical periodic potential of the successive bilayers and is therefore the first order structural peak. The peak at $q_z = 0.082 \text{ \AA}^{-1}$ corresponds to a periodicity of 80 \AA which is the double of the chemical modulation. This is exactly the periodicity of the magnetic structure since the layers are antiferromagnetically coupled. Because of this antiferromagnetic coupling it takes twice the chemical period for having the complete magnetic unit cell. As will be shown in further measurements, see fig. 4.1.5, this peak is from pure magnetic origin and represents the antiferromagnetically coupled Fe layers. The solid line is a simulated reflectivity pattern of a antiferromagnetically coupled $\text{MgO}(001)/[\text{Fe}(26 \text{ \AA})/\text{Cr}(13 \text{ \AA})]_{20}$ multilayer using the program written at the Hahn-Meitner-Institute based on the Parratt algorithm [Parr54]. The Parratt algorithm is based on a recursive approach taken the refraction index of the different layers into account. Although the discrepancy between the measured and simulated curve is relatively high, it will help us in interpreting several features of the measured patterns.

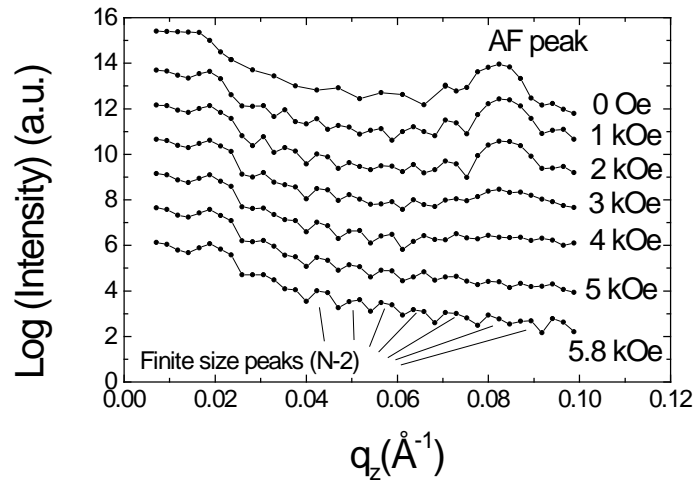


Fig. 4.1.5 *Specular diffraction pattern around the antiferromagnetic reflection as function of field is shown.*

The reflectivity as function of magnetic field in ω - 2θ geometry is shown in fig. 4.1.5. The magnetization in the Fe layers aligns with the applied field resulting in a decrease of the antiferromagnetic peak. At the saturation field the magnetic modulation is commensurate with the chemical modulation and the N-2 intermediate finite size reflections between the successive Bragg reflections are clearly visible.

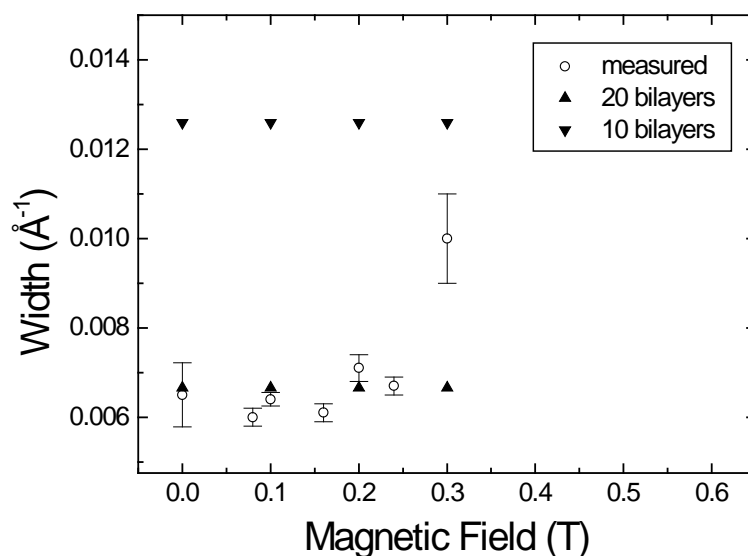


Fig. 4.1.6 The width of the magnetic reflection in ω - 2θ configuration is shown as function of magnetic field. The antiferromagnetic structure remains coherent upon magnetization.

Investigation of the width of the magnetic reflection in ω - 2θ geometry gives an estimation of the amount of successive antiferromagnetically coupled bilayers. Via the Scherrer law, the width of the peak measures the coherent scattering length of the structure. Figure 4.1.6 shows this width as a function of magnetic field. In addition to the measured widths, a simulation with the above mentioned program for the same type of multilayer existing of 20 and 10 bilayers is shown. If the coherence of the magnetic structure breaks down during magnetization then a broadening of the peak occurs similar to the diffraction pattern of a multilayer having less bilayers. This is not the case as can be observed in fig. 4.1.6. The antiferromagnetic structure remains approximately coherent upon saturation. Only in the vicinity of

the saturation field a decrease in the coherence length shows up.

During this magnetization process the off-specular intensity is measured by taking ω -scans around the antiferromagnetic peak, see fig. 4.1.7. Apart from roughness, these scans contain information about the lateral magnetic correlation. The width of the peak equals the instrumental resolution which allows to estimate a lower limit of 3 μm for the lateral size of the antiferromagnetic domains. If the antiferromagnetic domains would have a size smaller than 3 μm a broadening should occur according to the kinematic approach [Felcher94].

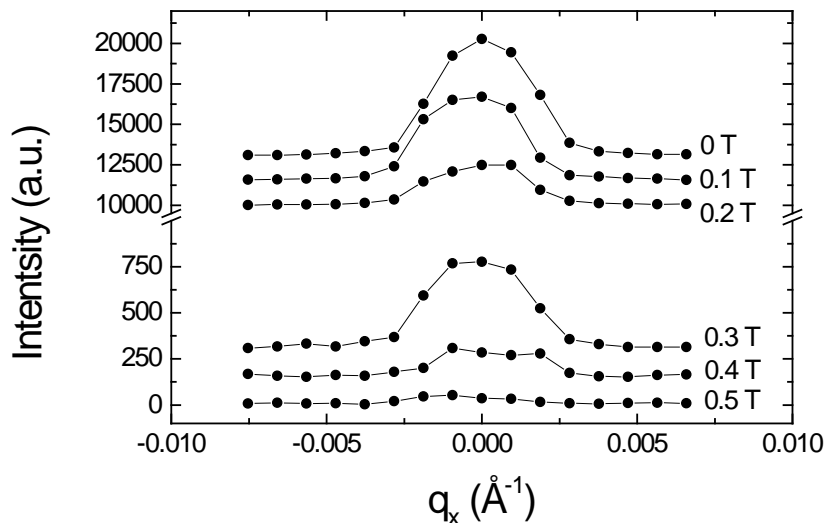


Fig. 4.1.7 The off-specular intensity as function of field is measured by taking ω -scans at the antiferromagnetic reflection.

A more direct view of the domain structure is given by MFM measurements in fig. 4.1.8. Before the measurement the sample was magnetised along an easy axis. Firstly, a chain of 4 μm large magnetic

structures can be perceived in these figures. This chain separates two homogeneous regions. Within the lateral resolution of the MFM the homogeneous regions can be interpreted as domains. The exact interpretation of the chain remains unclear. It can be a domain wall [Sacha99] as also a smaller domain structure.

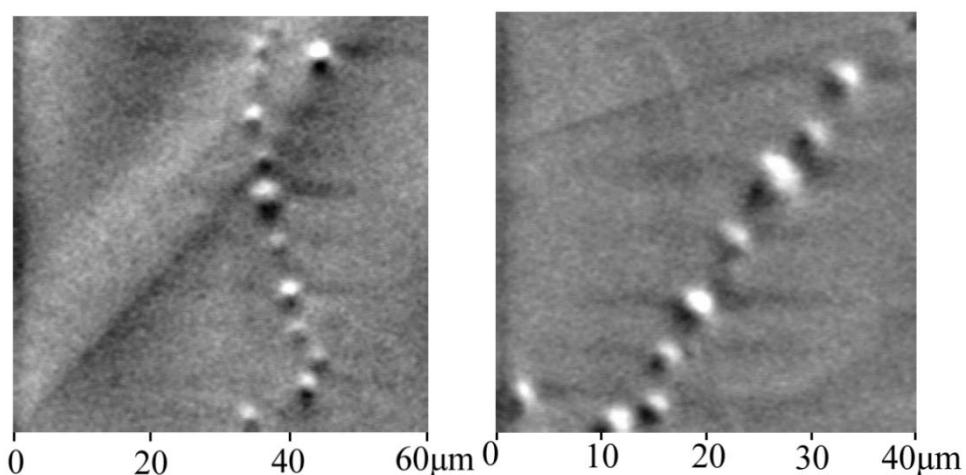


Fig. 4.1.8 *MFM measurements showing the domain structure of the toplayer. Two domains are separated by a magnetic chain structure.*

Nonetheless it is clear that these chains extend further than the maximum MFM scan range of 60 μ m. Irregular 'floral' large domain structures have earlier been observed in Fe/Cr/Fe trilayers by use of Kerr microscopy [Ruhr91]. The large size and irregularity is directly related to the antiferromagnetic alignment of the magnetizations. For an antiferromagnetic alignment the stray field is minimized so that the magnetostatic energy is less sensitive to the domain configuration.

In the following chapter the spin flop transition will be shown. Magnetic Force Microscopy in a magnetic field could help distinguishing between an

Intralayer domain wall model (IAM) or an Interlayer domain wall based mechanism (IEM). An insurmountable problem in doing this is the limited scan range which prevents observation of movement of these domain walls. A more suitable technique is Kerr Microscopy in a magnetic field. In collaboration with Olivier de Haas [Oliv99] an attempt was made to visualize this effect. Unfortunately, the Fe layers are too thin ($25\text{\AA} < 150\text{\AA}$) and the contrast was too low.

As conclusion we can assume that using unpolarized neutron reflectivity an antiferromagnetic alignment of the magnetization in the Fe layers is observed. This antiferromagnetic structure remains continuous through the whole sample during magnetisation. As inferred from off-specular scans these domains have a lateral size of more than $3\ \mu\text{m}$. Finally, the large domain size is confirmed by Magnetic Force Microscopy.

4.1.4 Polarized Neutron Reflectometry

- **In zero field**

Polarized neutron diffraction will give us information about the direction of the antiferromagnetically aligned magnetic moments in the $\text{MgO}(001)/[\text{Fe}(26\text{\AA})/\text{Cr}(13\text{\AA})]_{20}$ multilayer. In zero field it is generally assumed and observed that the magnetization lies along an easy axis which is Fe[100] or Fe[010] [Cul72]. Therefore, the magnetization in a Fe layer is either pointing along or in the opposite direction of an Fe[100] or Fe[010] axis. This gives the four possible antiferromagnetic arrangements that are shown in fig. 4.1.9.

In order to study the distribution of these domains, polarized neutron reflectivity

measurements have been carried out. During these experiments the sample is aligned so that the neutron beam is incident along the Fe[100] direction and the spin of the up neutron points along the Fe[010] direction, see fig. 4.1.9. In this geometry spin flip scattering at the antiferromagnetic Bragg position will arise from antiferromagnetic domains having their magnetic moments directed along the Fe[100] direction. Non-spin flip scattering will result from antiferromagnetic domains oriented along the Fe[010] direction. If the antiferromagnetic moments are aligned along the Fe[110] direction, spin flip and non-spin flip scattering will be observed.

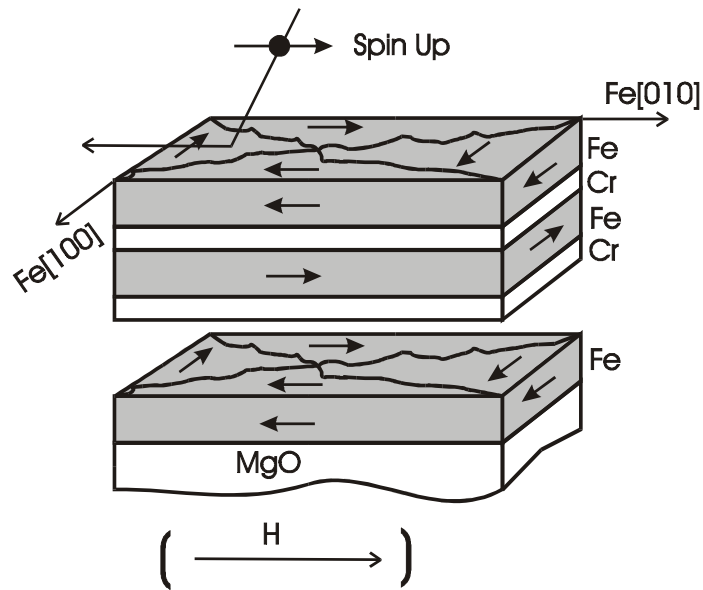
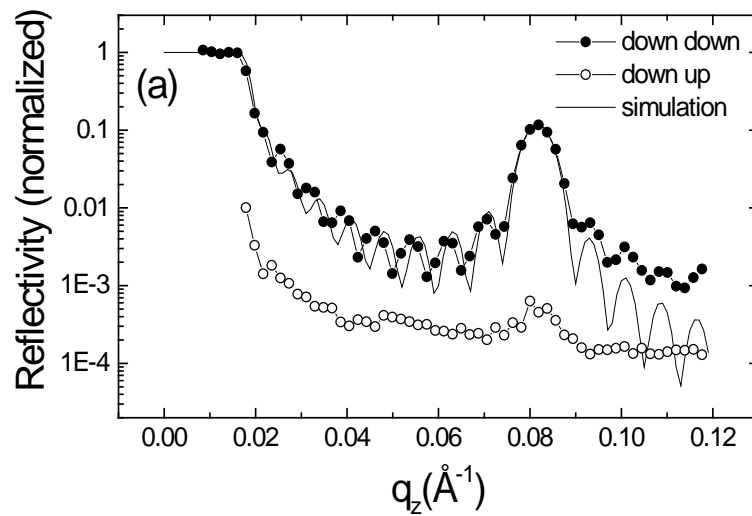


Fig. 4.1.9 Schematic presentation of the possible antiferromagnetic domains in respect to the measurement geometry for polarized neutron reflectometry.

Figure 4.1.10 shows the polarized ω - 2θ neutron reflectometry patterns for the spin up (b) resp. spin down (a) polarization. Along with the measured data a simulation of the non-spin flip scattering is shown. The intensity of the spin flip scattering is about 1 to 2 orders of magnitude lower than the intensity of the non-spin flip scattering. These results are a direct proof that in the greater part of the sample the antiferromagnetic domains are not equally distributed over the two easy axes. According to fig. 4.1.10 the majority (>95%) of the domains are oriented along Fe[010] and a minority along the Fe[100] axis.



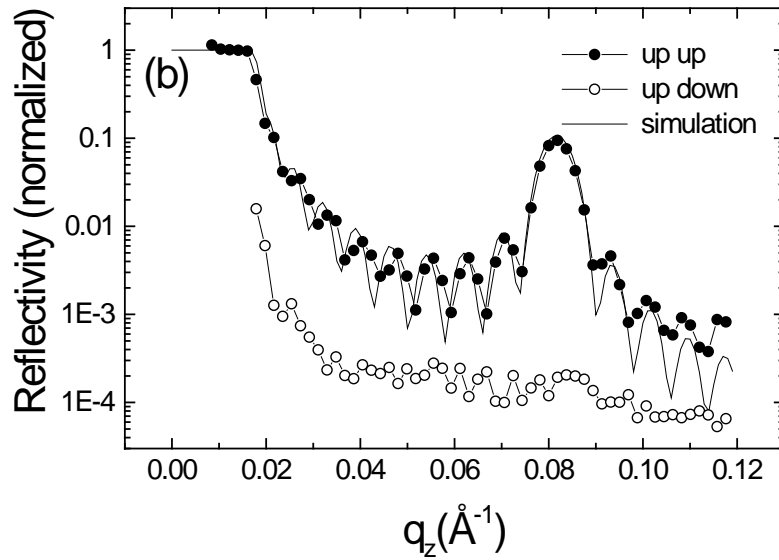


Fig. 4.1.10 The polarized ω - 2θ neutron reflectivity patterns are shown for the incident neutron having spin down (a) and spin up (b). The solid line is a simulation.

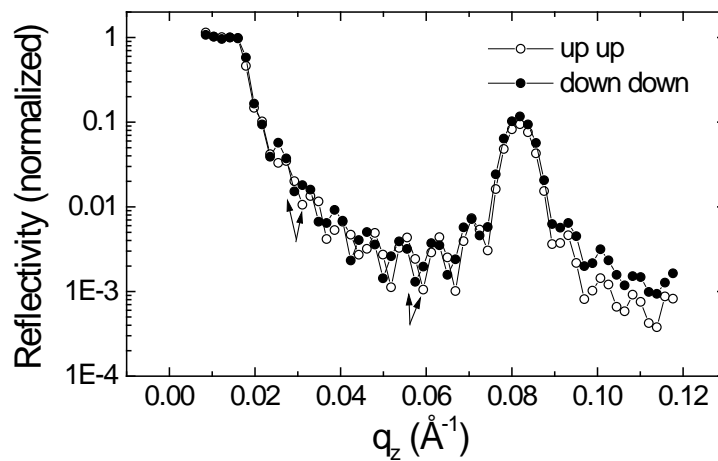


Fig. 4.1.11 The experimental reflectivity patterns for the up - up and down - down cross-sections. The positions of the intermediate finite size reflections differ for both spin orientations.

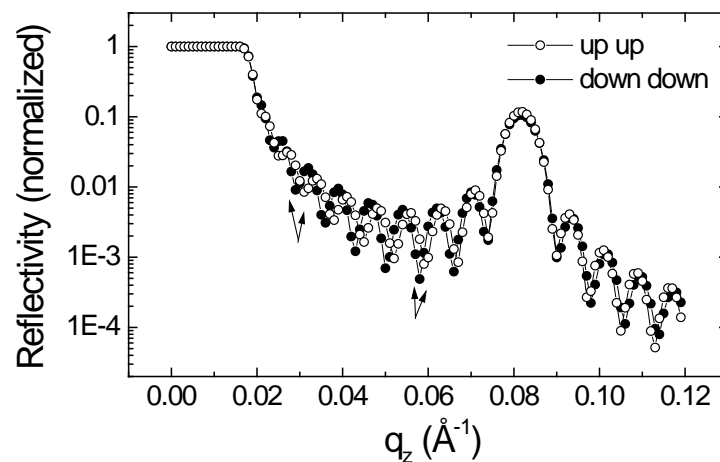


Fig. 4.1.12 The simulated up - up and down - down reflectivity pattern for a single domain sample. A closer look to the non-spin flip scattering shows that the positions of intermediate finite size peaks/minima differ for the up-up scattering and the down-down scattering, see fig. 4.11. The difference is more expressed for peaks near the total reflection edge. If the two possible domains, see fig. 4.1.9, with their spin along the Fe[010] axis are present in the same amount in the sample, then, considering the symmetry of the system, the situation for a spin up neutron and a spin down neutron is the same. Therefore the up-up and down-down reflection patterns should be identical. Moreover this difference can be simulated by assuming that one of these two domains is more abundant, see fig. 4.12. Figure 4.12 shows the up-up and down-down reflectivity patterns for a single domain sample.

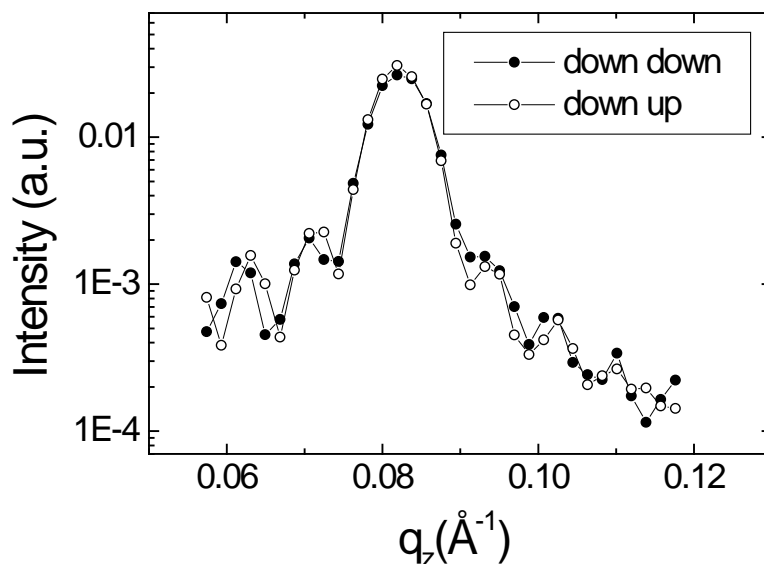


Fig. 4.1.13 The polarized ω - 2θ reflectivity pattern when the hard Fe[110] axis is parallel to spin of the incoming neutron spin.

Assuming that the complete sample is single domain would be incorrect because of the MFM measurements and the presence of a small remanent magnetization in the MOKE loop. One should take also in consideration that like all diffraction techniques neutron reflectometry is only sensitive to periodic structures. Disturbed areas or ferromagnetically coupled regions are not observed in these measurements. Nevertheless we can assume that most of the antiferromagnetic domains have the same direction of magnetization.

Figure 4.1.13 shows the ω - 2θ reflectivity pattern around the antiferromagnetic Bragg peak if the incoming beam is aligned along the Fe[110] direction. The magnetisation in the antiferromagnetic domains has now an equal component along both of the easy axes, i.e. Fe[100] and Fe[010]. Therefore the intensity of the spin

flip and non-spin flip scattering at the antiferromagnetic Bragg position is the same.

- **Polarized neutron reflectivity in magnetic field**

In the following experiment a magnetic field is applied along the Fe[010] axis and in the same direction as the spin up neutrons, see fig. 4.1.9. The ω - 2θ angles are set at the maximum of the antiferromagnetic peak and spin flip and non-spin flip scattering is monitored as function of field. Figure 4.1.14a shows a field scan up to saturation. At zero field there is only non-spin flip scattering indicating that the magnetization in the antiferromagnetic domains is parallel to the magnetic field direction. Already at a small field there is a complete switch from non-spin flip scattering towards spin flip scattering. For higher fields, the spin flip intensity decreases since also the antiferromagnetic peak vanishes at saturation. Figure 4.1.14b shows more details of this transition from non-spin flip scattering to spin flip scattering. The width of the transition is about 80 Oe. In terms of domains, this transition corresponds to a reorientation of the magnetic moments from parallel to the field towards perpendicular to the magnetic field, see fig. 4.1.15.

After reducing the field to zero from above the spinflop field (H_{sf}) the spin flip intensity remains. In order to observe the spin flop again the magnetization should be initially parallel to the applied field which can be obtained by turning the sample over 90 degrees.

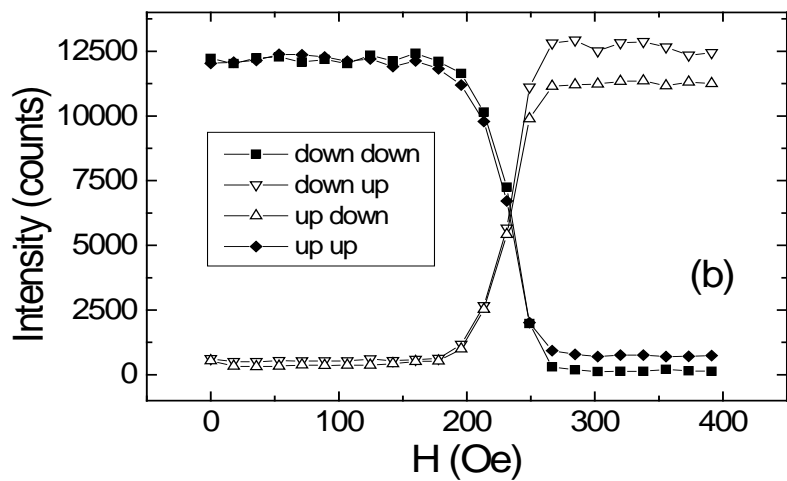
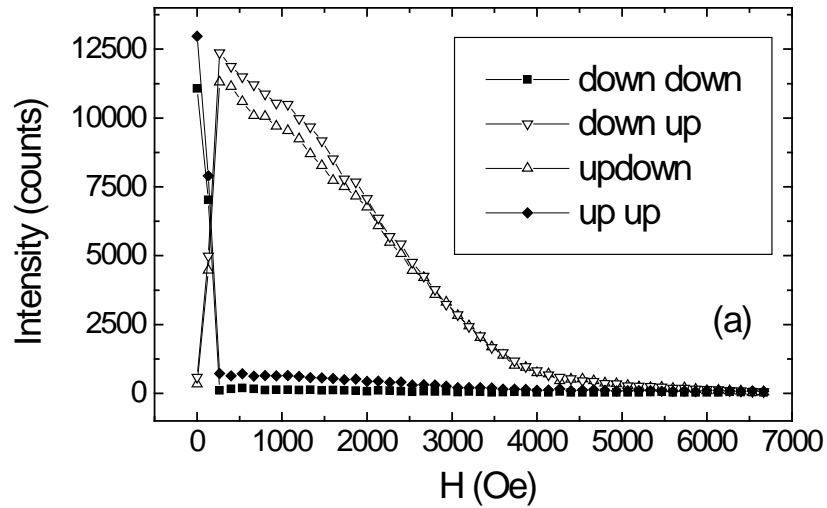


Fig. 4.1.14 a,b Polarized neutron reflectivity measurements of the spin flip and non-spin flip reflectivities taken at the maximum of the antiferromagnetic peak as function of field. Figure a shows next to the spinflop transition at low field the disappearance of the antiferromagnetic peak. Figure b shows the spin flop transition in detail.

Such a transition has been observed before in traditional antiferromagnets having uniaxial anisotropy and is called a spin flop [Cul72, p.239]. Next to the traditional antiferromagnets the spin flop transition has been observed in artificially antiferromagnets with an easy axis [Wang94, Zeid96]. Wang et al. showed the existence of a spin flop in antiferromagnetically coupled [211] oriented Fe/Cr multilayers [Wang94]. Zeidler et al. observed a surface spin flop state in Co/Cr multilayers. In our case two easy axes are present, which is the origin of the irreversibility of the transition.

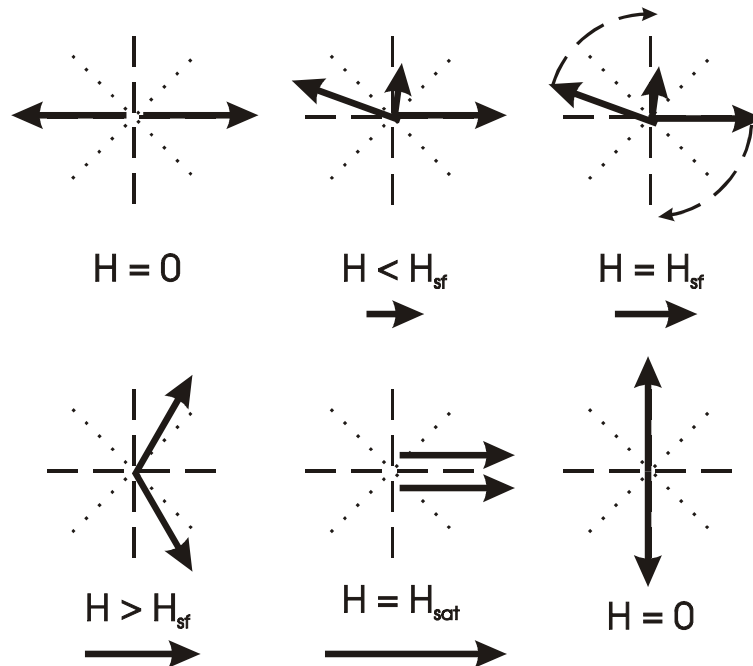


Fig. 4.1.15 Schematic presentation of the spin flop transition. The spins of the antiferromagnetically coupled Fe layers are represented by arrows, the easy axis by the striped lines and the hard axes by

the dotted lines. At the spin flop field H_{sf} , the spins reorient towards perpendicular to the field.

The spin flop transition is also visible if the field is applied along a hard Fe axis. The measurement geometry for the hard axis is the same as in fig. 4.1.9, but now the sample is rotated over 45 deg. The scan where the maximum of the antiferromagnetic peak is analysed as a function of the field is shown in fig. 4.1.16. At zero field there is the same amount of spin flip and non-spin flip scattering similar to the results shown in fig. 4.1.13. For higher fields the magnetic moments of the iron layer orient perpendicular to the field and non-spin flip and spin flip scattering split up. The transition with the field applied along the hard axis is much broader (500 Oe) than for a field along the easy axis (80 Oe) and saturates also at higher field. The latter is a direct result from the fact that now the axis perpendicular to the field is the hard axis.

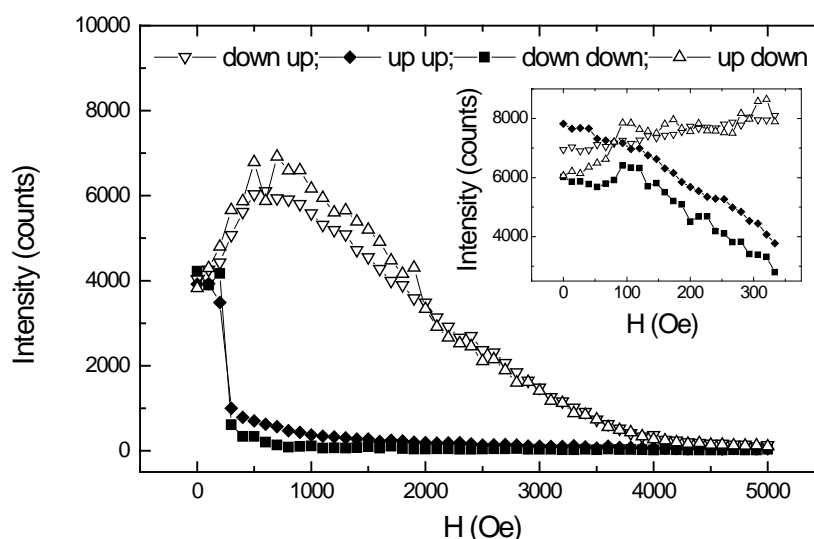


Fig. 4.1.16 Polarized neutron reflectivity measurement of the spin flip and non-spin flip reflectivities on the AF peak while the sample is magnetised along the hard axis. The spin of the incident neutron is parallel (up or down) to the field. The spin flop transition is more gradual as the spins have to align along the hard axis.

In summary we can conclude that using polarized neutron diffraction the distribution of domains in antiferromagnetically coupled Fe/Cr multilayers is studied. More specific, after magnetisation a preferred orientation of the magnetization in the antiferromagnetic domains is observed. Applying a magnetic field induces a spin flop transition so that the artificial antiferromagnet aligns perpendicular to the field.

4.1.5 The nature of the spin flop transition

The polarized neutron reflectivity results determine clearly the initial and final state of the spin flop transition. However, no experiments that reveal information on how the transition occurs have been carried out up to now. In this respect two models with a different physical nature are proposed. The goal of the further experiments is to find out which of them is mainly present during the spin flop transition in the antiferromagnetically coupled Fe/Cr layers with fourfold anisotropy.

- **The interlayer domain wall model**

The first model is called the interlayer domain wall model (IEM) and is based on the traditional approach of the system where a complete Fe layer is considered as a single spin. Taking the IEC

coupling, the anisotropy and the Zeeman energy into account, the system can be modelled using the following energy function :

$$E = \sum_{i=1}^{n-1} \left[-J_1 \cos(\theta_n - \theta_{n+1}) - J_2 \cos^2(\theta_n - \theta_{n+1}) \right. \\ \left. + N \sin^2 2(\theta_n - \theta_{n+1}) - HM \cos \theta \right] \quad (4.1.1)$$

The angle θ_n is taken between the field direction and magnetisation in layer n. The first term in equation (4.1.1) corresponds to the bilinear IEC between successive Fe layers and the amplitude is given by J_1 . The magnetization measurements in paragraph 4.1.2 have shown that there is an amount of biquadratic coupling present in the sample. The second term including J_2 represents this biquadratic contribution. Thirdly, since it is a feature related to the magnetic anisotropy in the system, a fourfold anisotropy term is taken into account. The relative strength of the anisotropy is denoted with N. Finally, the energy of the spin in the field is added as the fourth term that which represents the Zeeman energy.

In collaboration with M. Major [Bottyan] the transition field is calculated in terms of this traditional approach of anisotropy and couplings. His model reproduces earlier published data [Wang94]. The evaluation of this energy function is performed numerically and the spin flop field can be calculated if the parameters J_1 , J_2 , N and M are known.

In this model the magnetisation of an Fe layer has to overcome the anisotropy barrier during its switching from parallel to the field towards perpendicular to the field. This anisotropy barrier is caused by the intermediate [110] hard axis of the Fe layer. The picture having all Fe

layers crossing the [110] type axis at the same time is unlikely to happen. Because of energetic reasons it is more probable that first a single Fe layer will cross the barrier. Therefore a situation will occur where the angles between the magnetisation of the Fe layers will differ from 180 deg. Since this is a phenomenon between different Fe layers it is named in similarity an interlayer domain wall or IEM.

- **The intralayer domain wall model**

Next to the traditional approach a second mechanism based on the domain wall movements within an Fe layer is proposed i.e. the intralayer domain wall model (IAM). Domain walls within a ferromagnetic material always play a major role in the magnetisation process. Reversal mechanisms based on this type of domain wall movements can occur at lower fields than by rotation. Hence, it is obvious to think about a possible spinflop mechanism based on this principle as the later observed transition field is relatively small. The proposed model is explained by means of fig. 4.1.17.

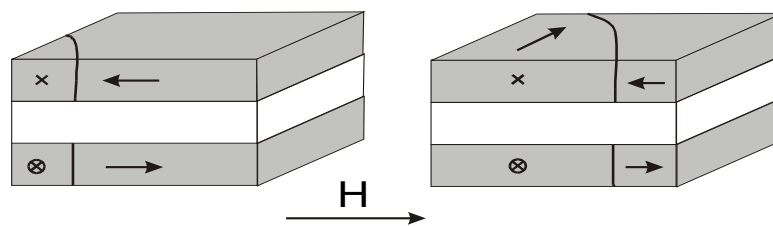


Fig. 4.1.17 *The spin flop transition via an intralayer domain wall movement.*

In the initial state the domains having their magnetic moments perpendicular to the field are small or absent. Applying a field results in

shifting the domain wall so that the 'perpendicular to field' domains grow. Next to shifting of the domain wall nucleation of new domains is also possible. From the point of the anisotropy energy there is almost no difference between the initial and the final state because of the fourfold symmetry. Therefore this can even happen at small fields and is mostly depending on the pinning of the domain walls. It is also clear that this mechanism is not valid in the case of a uniaxial anisotropy. The transition field in systems having uniaxial anisotropy is mainly determined by the exchange coupling and the anisotropy.

In connection to the surface spin flop state in the IEM one can also expect a surface effect here. Because of the smaller exchange coupling it is more likely that the transition starts at the surface. Intralayer domain walls in bulk Fe layers will be pulled by moving the domain wall in the surface layer due to the antiferromagnetic exchange coupling.

Keeping the above mentioned models in mind further experiments are carried out in order to shed more light on the nature of this spin flop transition in antiferromagnetically coupled multilayers with fourfold anisotropy.

4.1.6 Magnetization measurements

The spin flop transition was first observed by polarized neutron reflectivity. The next step was trying to see this transition in other measurements and to obtain more information on the nature of the transition. At first instance magnetisation measurements were carried out which will be discussed in this paragraph.

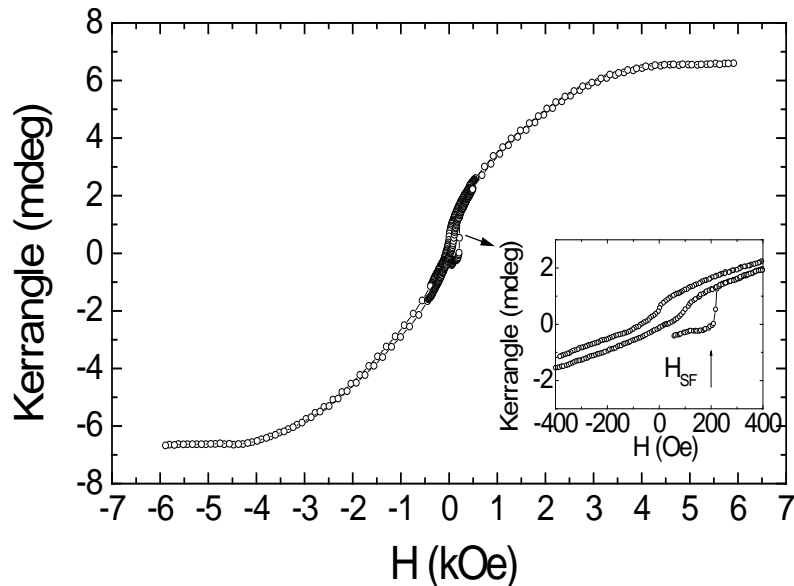


Fig. 4.1.18 MOKE magnetization loop starting from zero field. At 200 Oe, the position of the spin flop transition, a sharp increase in magnetization is observed.

In the paragraph 4.1.4 it was found that the magnetic moments of the antiferromagnetically coupled Fe layers are aligned along one of the two easy axes. In order to be sure that during the magnetization measurement the field is in the initial state applied along the magnetic moments, the sample was saturated along an easy axis and then rotated over 90 degrees in zero field. As observed from polarized neutron reflectivity the magnetization remains perpendicular to the field direction after the field is set to zero. Rotating the sample over 90 deg in zero field will align the magnetic moments parallel with the field direction. This procedure was carried out before each magnetization measurement. All shown magnetization measurements are carried out with the field along the easy axis.

Figure 4.1.18 shows the longitudinal MOKE measurement starting from zero field. In this geometry, changes in the MOKE signal are caused by magnetic moments along the field direction. At 200 Oe a sharp increase in the magnetization occurs. The magnetic field increases further until above the positive saturation field. Subsequently, the field is ramped down to the negative saturation field and from this point again increased until positive saturation. At the end a complete hysteresis loop is obtained starting from zero field. The second time that the spin flop field is crossed the transition does not appear anymore indicating an irreversible nature. In addition, the field at which the sudden increase in magnetization occurs coincides with the observed spin flop field observed in PNR. It is therefore reasonable to assume that this jump is due to the spin flop transition, although the presence of a ferromagnetic component cannot be excluded. Finally, the width of the transition is in the average (multiple measurements) about 35 Oe. This is less than in the PNR measurements and could be due to the smaller probed sample volume of about 1 mm² instead of 4 cm² as inhomogeneities could broaden this transition.

The MOKE measurements are only sensitive to the top layers (appr. 150Å) because of the limited penetration depth of light into metals. The behaviour of the whole sample as function of temperature is probed by SQUID measurements. Therefore the width of the transition as observed from these two techniques is an interesting property. The width of the transition is defined as the difference between the onset field and the field at which the transition is completed. If the width observed from the MOKE measurements is significantly smaller than from SQUID measurements,

then there exist an antiferromagnetic *interlayer* domain wall at a certain field.

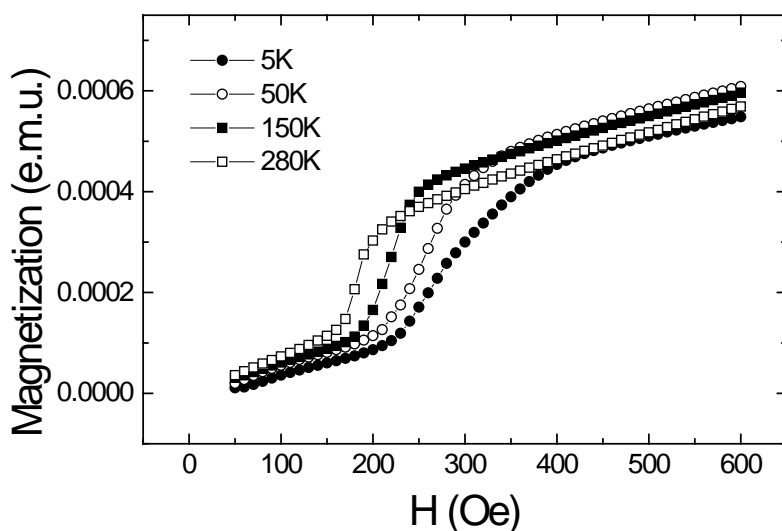


Fig. 4.1.19 Squid magnetisation measurements of the spin flop transition. Lowering the temperature causes the shift the transition to higher fields and to broaden the transition.

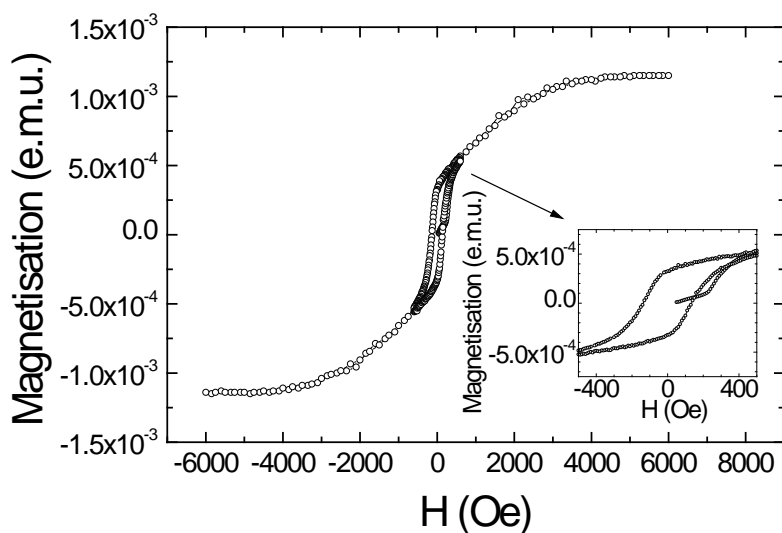


Fig. 4.1.20 *The spin flop transition measured by SQUID at 5K*

It would mean that while at the top (MOKE) the transition is completed, the bulk transition is still going on and thus an interlayer domain wall should be present.

The spin flop measured by SQUID at different temperatures is shown in fig. 4.1.19 and in addition a complete loop measured at the lowest temperature is shown in fig. 4.1.20. The field interval for the transition as observed from SQUID is somewhat broader (45 Oe) as for the MOKE, but one cannot claim with certainty a significant difference between them. Hence, both mechanisms IAM or IEM are possible.

Secondly, it is observed that for the complete loops such as in fig. 4.1.20 the transition is completed at the end of the irreversible part of the magnetization loop. In this part, domain wall movements are mainly responsible for the change of the magnetisation. In the reversible part, the change of magnetisation is mainly coming from rotation of the magnetic moments.

Finally, the temperature dependent measurements show that lowering the temperature causes H_{sf} to shift to higher fields and to broaden the transition. This broadening can be compared to the broadening of the irreversible part of the loop (the irreversible part of the loop is defined as field range where the magnetisation curves for the respectively the increasing and decreasing field do not overlap). Changes in magnetization during the hysterical part occur mainly by intralayer domain wall movements. If both broadenings are due to intralayer domain wall movement, then a similar temperature behaviour can be expected. Figure 4.1.21 shows the widths of both phenomena normalized by their maximum width and a reasonable

agreement is obtained. The data are too rough to claim that these two physical phenomena are closely related. Moreover it is not known in which accuracy they should coincide and neither can other casual agreements or effects be excluded. Nevertheless, the order of magnitude is correct and this feature could be of future use if carefully checked.

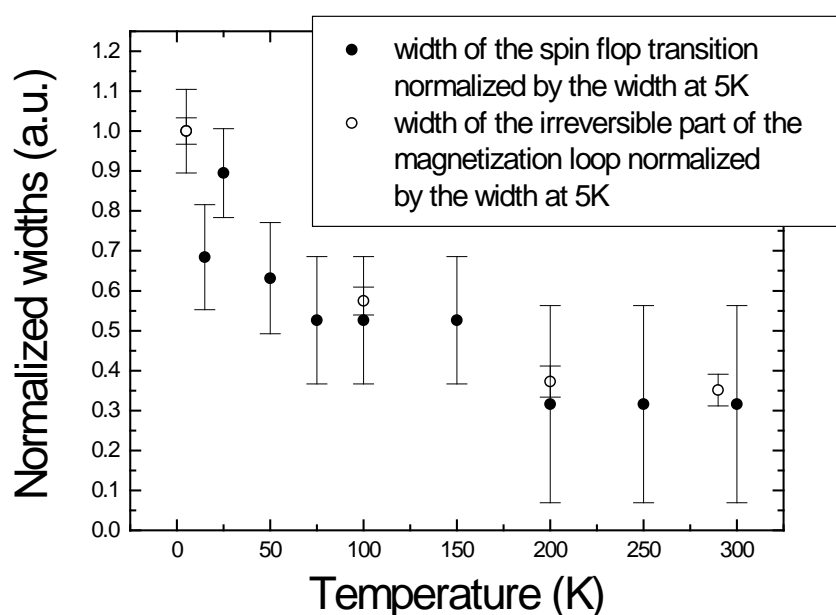


Fig. 4.1.21 Comparison of the broadening of the spinflop transition and the broadening of the hysteretical part of the magnetisation loop.

In summary, we can conclude that the spin flop transition is also present in the SQUID and MOKE magnetisation measurements. For low temperatures, the spin flop transition shifts to higher fields and broadens.

4.1.7 Resistivity measurements

In this paragraph the spin flop transition is studied by resistivity measurements and the pseudo

Hall effect. As in the samples showing a spin flop transition the magnetisation is initially laying along one axis and than jumps towards perpendicular to this axis. Such feature can be probed by monitoring the anisotropic magnetoresistance and a proper choice of the current path in respect to the crystal axes.

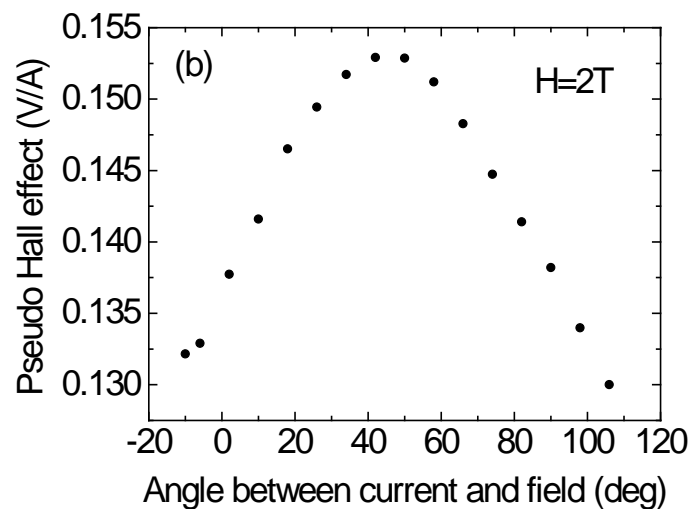
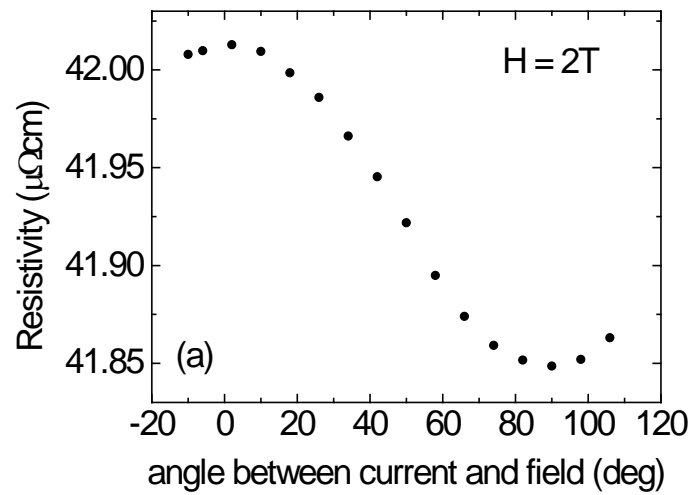


Fig. 4.1.22 *The anisotropic magnetoresistance (a) and the pseudo Hall effect (b) are shown by rotating the sample in a field of 2T. For this field value the magnetic moments line up with the field.*

Therefore we patterned the sample with the current path along one of the easy Fe axis. For the pattern size see fig. 3.18. Simultaneously, the pseudo Hall effect is monitored. Changes in the pseudo Hall effect are related to magnetic components that are not directed parallel or perpendicular to the current path. Furthermore, these measurements are sensitive to the entire sample while polarized neutron reflectivity is only sensitive to the antiferromagnetically coupled parts. In order to have a quantitative view on these effects and to confirm their relationship to the magnetisation, their amplitude is measured by saturating the sample (to overcome the GMR and the coupling) and by turning it in a field. Finally, as also for the magnetization measurements the sample is magnetically prepared as described in chapter 4.1.6.

Figure 4.1.22 a,b shows the resistivity and the pseudo Hall effect at 2T as function of angle between current and field at 280K. The resistivity follows a sinusoidal behaviour and is maximum at zero degree (current parallel to the field) and minimum at 90 degree (current perpendicular to the field). The pseudo Hall effect has its maximum value at 45 degree.

Figures 4.1.23 and 4.1.24 show the magnetoresistance measurements at 280K for both orientations of the current and sample, starting from zero field. The sample was magnetically prepared so that in the initial state the

magnetization is lying along the field direction. Depending on the measurement geometry an irreversible increase/decrease in resistivity is obtained at the spin flop field. The jump corresponds to the orientation of the magnetization from parallel to perpendicular to the current and vice versa.

Since the current probes all parts of the sample, in contrast to the PNR measurements which are only sensitive to the antiferromagnetically coupled domains, it is valuable to compare the change in resistance to the amplitude of the AMR effect. This is done for all measured temperatures in fig. 4.1.25.

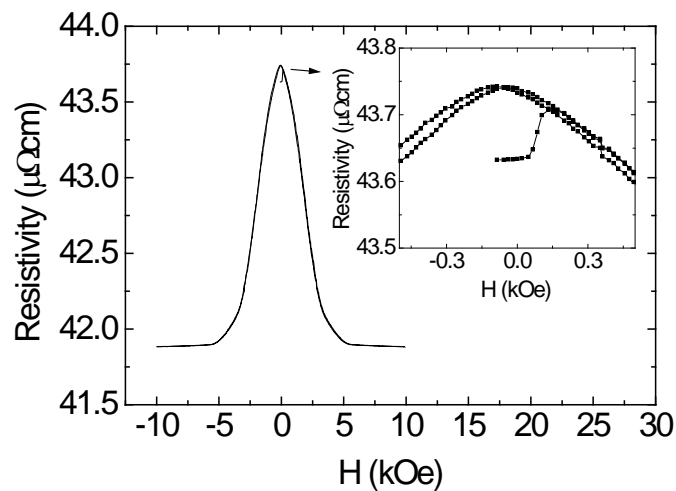


Fig. 4.1.23 Visualisation of the spin flop transition by resistivity measurements. Due to the anisotropic magnetoresistance effect an increase in the resistance is observed when the magnetisation jumps from a direction perpendicular to parallel to the current path.

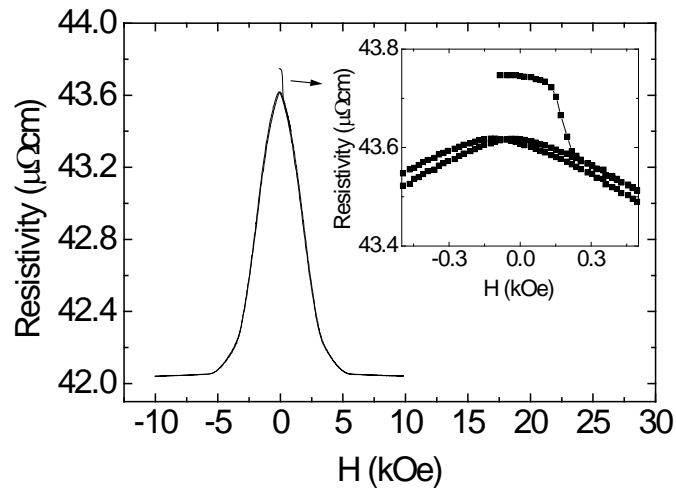


Fig. 4.1.24 Visualisation of the transition by resistivity measurements. Due to the AMR effect an increase in the resistance is observed at the moment that the spins jump from parallel to perpendicular to the current path.

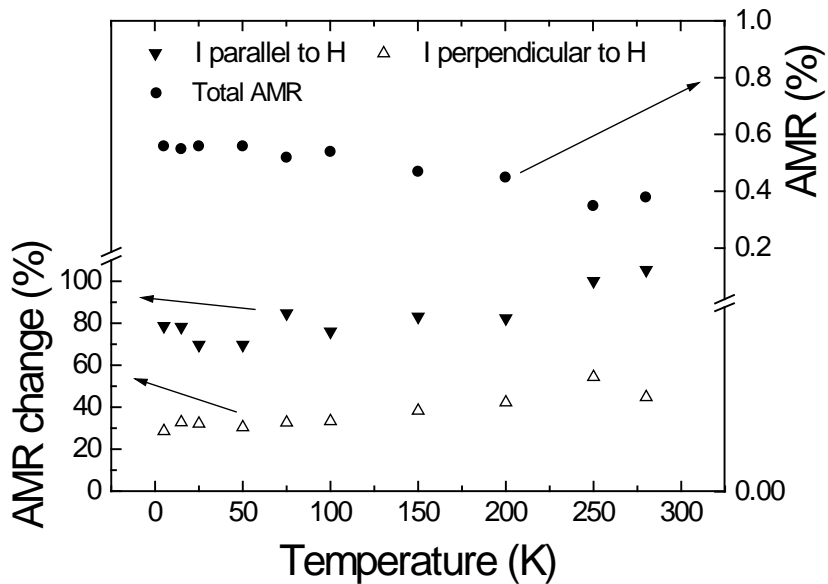


Fig. 4.1.25 *The change of the resistance during the transition is compared to the anisotropic magnetoresistance effect at that temperature (left axis). The AMR effect is expressed in percentage of the resistance (right axis).*

On the right axis the AMR effect as derived from measurements as shown in fig. 4.1.23 is expressed in percentage of resistance. This amplitude of the AMR effect is measured in saturation. Therefore these values indicate the maximal possible change in resistance (in %) caused by the AMR effect. The figure shows that the AMR effect is weakly temperature dependent.

The triangles correspond with the left axis. They represent the fraction of the AMR amplitude that is observed at the spin flop transition. During this transition the spins jump as earlier observed from parallel to the current path towards perpendicular to the current path and vice versa. In the perfect case all magnetic moments are initially parallel/perpendicular to the current path and all of them switch to a direction resp. perpendicular/parallel to the current path. The change in resistance would equal 100% of the AMR amplitude at that temperature. Experimentally, for the field along the current an overall ratio from 75% until 100% of the AMR effect is obtained. On the other hand, for the current perpendicular to the field nearly 50 % is reached. As in all previous measurements this asymmetry was not observed, a possible explanation can be found in patterning the sample. Since the domain sizes could be of the order of the pattern, edge effects can induce an anisotropy. This argument is in agreement with the fact that in zero field the domains are preferentially lying along the current path (long axis) as can be deduced from the resistivity data. Nevertheless it is clear from these measurements

that a considerable amount of the sample undergoes a spin flop.

Apart from studying the spinflop by magnetoresistance it was the intention to reveal any off-easy axis magnetisation components by means of monitoring the pseudo Hall effect during the spin flop.

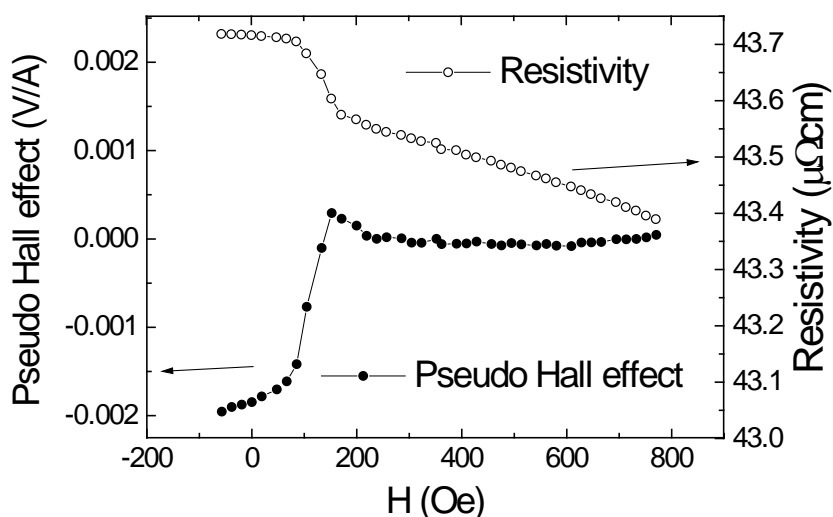


Fig. 4.1.26 Measurement of the AMR and PSHE during the spinflop transition. In the final state the spins are perpendicular to the current direction.

Since the pseudo Hall effect has the same sign and value for antiferromagnetic moments (due to its dependence on $\sin(2\theta)$), one can expect in an antiferromagnetically coupled lattice a signal during a IEM type transition for a single domain type sample. The latter is plausible according to the PNR measurements.

Figure 4.1.26 and 4.1.27 shows the resistivity and the pseudo Hall signal in detail for both measuring configurations. The Pseudo Hall measurements are corrected for the AMR and GMR contribution. For the field parallel to the current fig. 4.1.24, always an increase in the pseudo Hall voltage is observed

during the spin flop. For the field perpendicular to the current a similar decrease is observed.

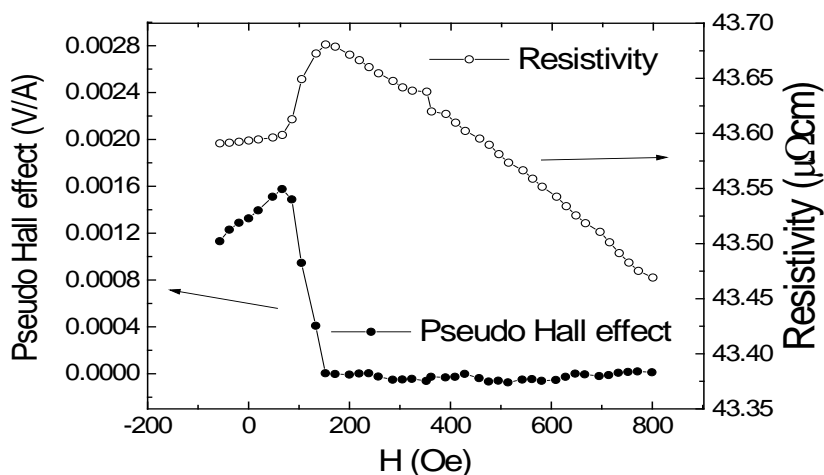


Fig. 4.1.27 Measurement of the AMR and PSHE during the spinflop transition. In the final state the spins are parallel to the current direction.

The tilt of the preceding part is either positive or negative depending on the demagnetisation process. The actual change of the pseudo Hall effect during spin flop is not sensitive to the demagnetisation process. The up and down jumps in the pseudo Hall effect can be explained as due to a small misalignment (5 deg.) of the current path and the crystal axis as the PSHE varies as $\cos(\theta)\sin(\theta)$. For a surface spin flop transition another behaviour is expected. If the transition occurs via a surface spin flop then a nucleation and a vanishing of a pseudo Hall effect can be expected during the transition. In these measurements a decrease or increase is observed. There is within the experimental resolution no evidence for such a behaviour.

Since the total amplitude of the pseudo hall effect has been measured, as shown in fig. 4.1.22, it can be normalized allowing a more quantitative interpretation. Taking the amplitude of the jump in pseudo Hall effect, fig. 4.1.26/27, as the limiting resolution for an off-easy axis component of the magnetisation gives fig. 4.1.28. The ratio is constant for all temperatures and amounts about 10% of the total possible pseudo Hall effect.

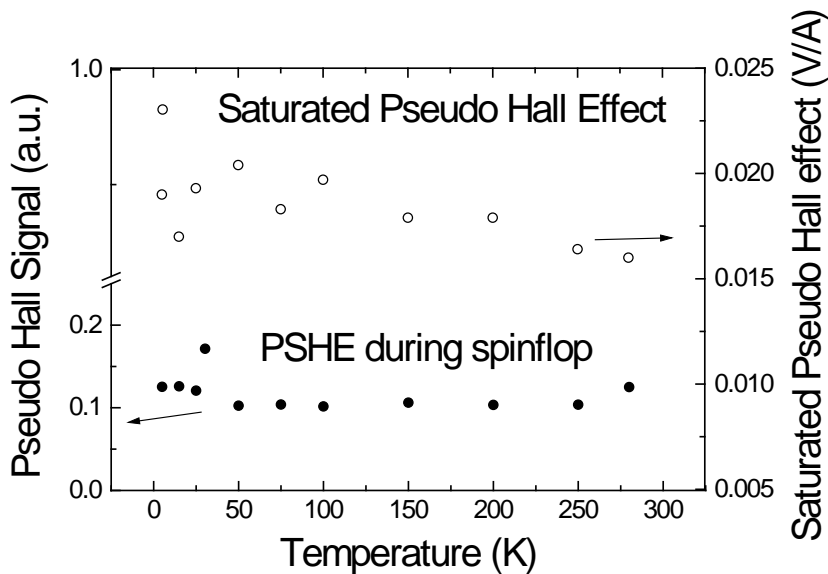


Fig. 4.1.28 Normalisation of observed PSHE to the maximal PSHE. No evidence of Fe layers pointing off easy axis is found within this resolution.

In summary, the spin flop transition is observed in magnetoresistance measurements as a consequence of the AMR. Quantitative analysis of these measurements show that up to 100% of the sample can undergo a spin flop transition. No evidence for an off easy axis component of the magnetization during the spin flop transition is found.

4.1.8 Synchrotron Mössbauer Reflectivity (SMR)

Up to now the spin flop transition is extensively characterized using different techniques to elucidate the nature of the transition. Using SMR it should also be able to visualise this transition. In collaboration with group of Bottyan and the Instituut voor Kern- en Stralingsfysica [Bottyan] it was suggested to do SMR because of its sensitivity to the orientation of the magnetic moments. For these experiments a series of new samples consisting of $\text{MgO}(001)/[^{57}\text{Fe}(25\text{\AA})/\text{Cr}(14\text{\AA})]_n$, $n=10,20$, multilayers were produced under the same circumstances but at a higher substrate temperature of $175\text{ }^\circ\text{C}$. The samples were characterized using XRD and MOKE. These samples were of somewhat better structural quality and the presence of a spin flop was checked by MOKE measurements. The spin flop transition occurs at 230 Oe , which is about the same as observed for the sample made of normal Fe. Remarkably it was not possible to find a spin flop transition in samples consisting of $n=10$ bilayers. Also the magnetization loop for these samples have a clear ferromagnetic contribution. This feature could be further investigated in the future and could speak in advantage of the IEM as the coupling through the layer is not constant. This thickness dependence of the coupling is also observed in other systems [Kohl97].

In order to avoid broadening due to inhomogeneities the MOKE measurements were done with a focussed and an expanded beam covering the complete sample. From both type of MOKE measurements a spin flop transition width of 40 Oe is found.

The next step are the SMR measurements. The results obtained at the DESY synchrotron are shown in fig. 4.1.29. The normal XRD reflectivity pattern in log

scale is shown in fig. 4.1.29 a. At $q = 0.18 \text{ \AA}^{-1}$ the first order Bragg peak due to the chemical modulation can be seen next to the intermediate N-2 satellites. The delayed photons are shown in fig. 4.1.29 b), c), d).

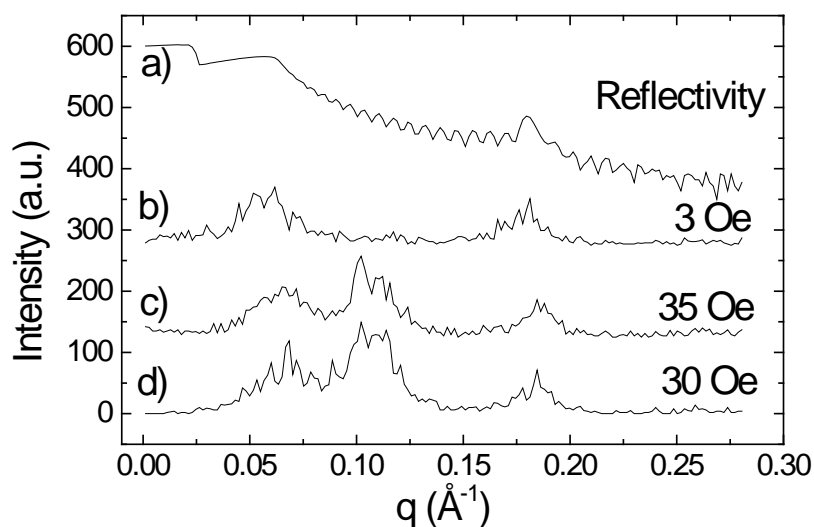


Fig. 4.1.29 The normal XRD reflectivity pattern is shown in fig. a. Figure b) shows the delayed photons before the spin flop. At a field of 35.5 mT the spin flop occurred, fig. c), and an antiferromagnetic Bragg reflex shows up at $q = 0.11 \text{ \AA}^{-1}$. After the field is reduced to 3mT the reflex is still present, fig. d).

Figure 4.1.29 b) is measured before the spin flop at the lowest achievable field of 30 Oe. The sample is magnetically prepared in such way a that the magnetic moment in the antiferromagnetically coupled Fe layers is pointing along the field. The field is directed perpendicular to the incoming X-ray beam. In this geometry there are only delayed photons detected near the total reflection edge $q = 0.06 \text{ \AA}^{-1}$ and at the first order Bragg reflection at

$q = 0.18 \text{ \AA}^{-1}$. No intensity is found at the antiferromagnetic position at $q = 0.11 \text{ \AA}^{-1}$. At field of 350 Oe, the spin flop occurred and the magnetisation in the Fe layers is now pointing perpendicular to the field and parallel to the incoming XRD beam. In the delayed photons reflectivity pattern, a peak shows up at the antiferromagnetic position. Figure 4.1.29d shows that the peak remains after the field is reduced to zero.

It is clear that the transition can be observed using this method, however the intensity is too low for achieving time resolved intensities. These time related spectra have earlier shown to be very sensitive to changes in the magnetic structure and could clarify between an IAM or IEM mechanism. Therefore the sample has been measured at a more powerful X-ray source at the ESRF. The analysis of these measurements is in progress but is not completed yet.

4.1.9 Simulations

Since the direct experimental investigation does not enlighten completely the nature of the spin flop transition, it is tried to achieve more insight using simulations.

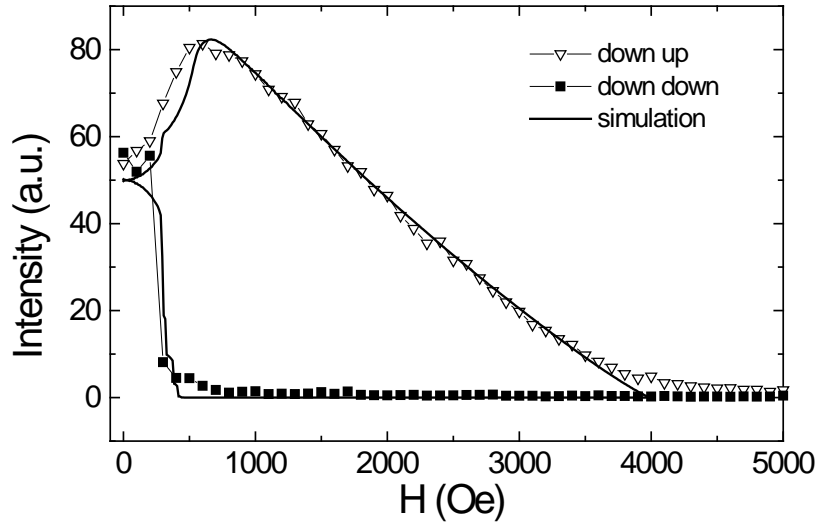


Fig. 4.1.30 *The simulation of the polarized neutron reflectivity at the antiferromagnetic peak positions with the field along the hard axis is shown.*

The simulations are carried out in collaboration with the group of Bottyan [Bottyan]. As earlier mentioned the theoretical calculations are done by Major Marton and the results will be discussed here. The Fe/Cr multilayer is modelled using the energy function of formula (4.1.1). The idea is now to extract from the experimental curves the strength of the bilinear and biquadratic coupling, and the anisotropy.

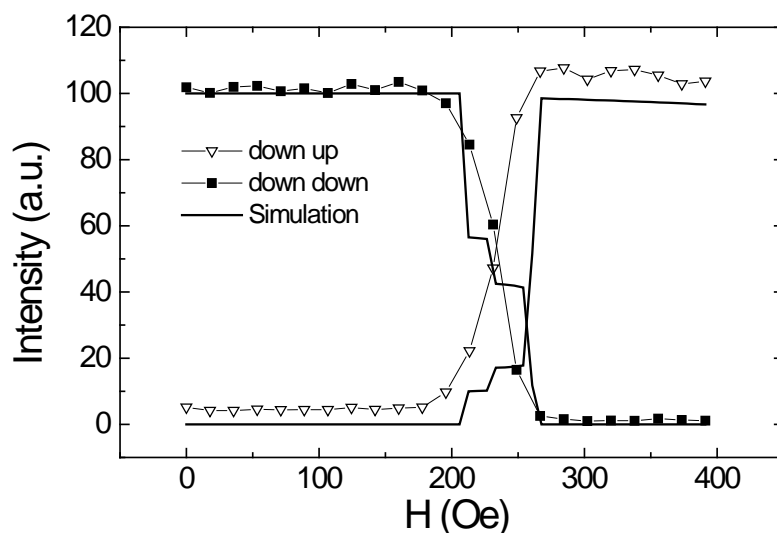


Fig. 4.1.31 *The simulation of the spin flop transition as observed from polarized neutron diffraction along the hard axis is shown.*

Based on this data a prediction for the spin flop field occurring via the IEM mechanism can then be calculated. The curve that contains all information concerning coupling strength and anisotropy is the polarized neutron reflectivity curve along the hard axis, fig. 4.1.30. Therefore these data are used to determine the parameters in formula (4.1.1). Figure 4.1.30 shows the best simulation together with the experimental curve. The values of the parameters are $J_1 = -1$, $J_2 = -0.15$, $N = 0.06$. Based on these values the behaviour starting with the field and spins along the easy axis can be calculated. The result for the polarized neutron reflectivity is shown in fig. 4.1.31 and the field at which the transition occurs is in good agreement with the experiment. This solution is checked on its stability [Bottyan]. Additionally, the computer simulation can learn us more on possible ways how the transition does occur. The outcoming results are schematically sketched in fig. 4.1.32.

At first instance all spins are parallel to the field and along the easy axis, see fig.4.1.32a. At the spin flop field an interlayer domain wall nucleates at the surface of the multilayer, fig. 4.1.32b. This interlayer domain wall propagates through the multilayer completing the spin flop transition, fig 4.1.32c, d. A continuous movie of this process can be seen at [Major].

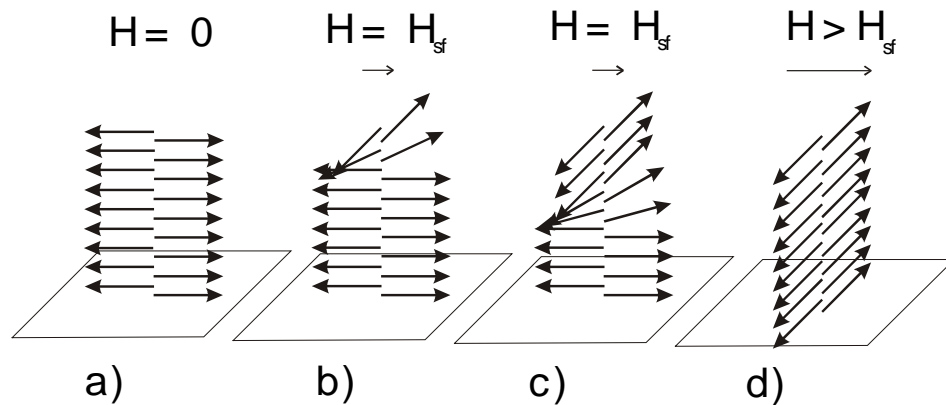


Fig. 4.1.32 The spin flop transition according to the interlayer domain wall model.

The physical picture shown in fig. 4.1.32 of an interlayer domain wall suggests the presence of a PSHE that directly and quantitatively can be compared to the experimental observations. Figure 4.1.33 shows the PSHE according to the IEM. During the spin flop transition the PSHE is non-zero because the spins in the interlayer domain wall are not aligned parallel or perpendicular to the current path. Furthermore, due to symmetry of the PSHE see paragraph 2.1.2.3, the PSHE for antiferromagnetic spins should be added. It results that the PSHE amounts about 20% of the maximal PSHE during the propagation of the domain wall. The maximal PSHE is observed if all spins are under an angle of 45 deg with the current path.

The experiments on the other hand show that the PSHE remains below 10% during the transition. Thus, if the spin flop transition occurs via the IEM as modelled then multiple domains (lateral) should be taken into account. In these domains the interlayer domain wall forms around resp. the Fe[1 1 0] and the Fe[$\bar{1} \bar{1} 0$] directions so that different induced PSHE's cancel out each other. The PSHE for a spin along Fe[110] opposite to the PSHE to that for the same spin along the Fe[$\bar{1} \bar{1} 0$] direction.

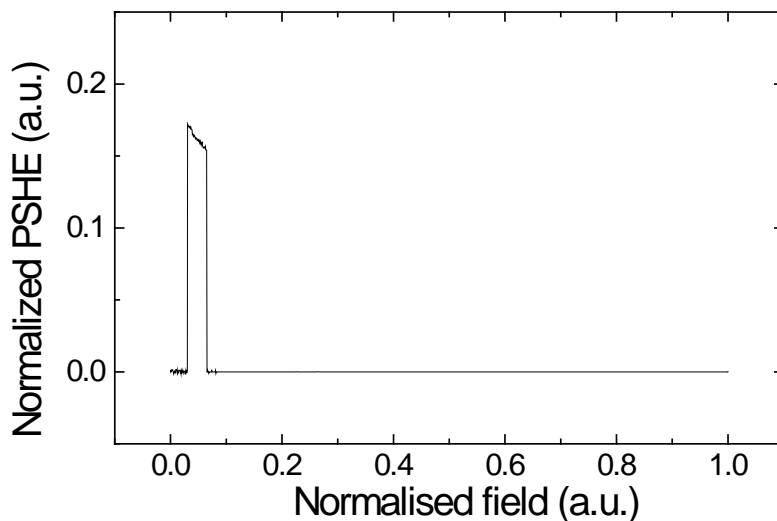


Fig. 4.1.33 *The PSHE during the spin flop transition in a single domain sample as derived from the numerical simulations. The values are normalized, i.e. the maximal PSHE equals 1.*

4.1.10 Discussion and conclusions

Antiferromagnetically coupled Fe/Cr multilayers have been grown and characterized using XRD, MOKE and resistivity measurements. By means of neutron reflectometry the existence of large antiferromagnetically coupled domains is confirmed. This antiferromagnetic structure is coherent

through the sample, even in fields up to saturation. Polarized neutron reflectometry showed that the magnetisations in all these domains are lying along one of the two easy axes. Furthermore it is found that only one type of antiferromagnetic sequences is present in the domains. Applying a field parallel to the antiferromagnetically arranged magnetic moments, causes a spin flop transition. The magnetic components orient perpendicular to the field. This type of spin flop transition in a system with fourfold crystal anisotropy is relatively new and further experiments are carried out in order to visualise its behaviour in magnetisation-, resistivity- and SMR experiments. Finally, two models that give more insight on its possible nature are proposed. In summary it can be stated that the domain structure and its behaviour during the magnetisation process in antiferromagnetically coupled Fe/Cr multilayers is studied.

4.2 The magnetic structure of thick Cr films

4.2.1 Introduction

The interest in the magnetism of Cr films has arisen from the Fe/Cr system and its features, see

chapter 2.3. First, an attempt to study the magnetism of these Cr spacer layers in Fe/Cr multilayers was made [Mosh97]. It turned out that it was experimentally too difficult for us to reveal the complete magnetic structure of these thin Cr spacers by neutron diffraction. However, single Cr films had recently shown an interesting behaviour that differs from single crystalline bulk Cr [Böd97,Sonn98,Böd99]. For a better understanding of these effects, the following nominal Cr films were grown :

- a) MgO(001)/Cr(5000Å) referred to as sample A
- b) MgO(001)/Cr(5000Å)/Fe(75Å)/Ag(75Å) referred to as sample B
- c) MgO(001)/Cr(50Å)/[Au(30Å)/Cr(30Å)]₁₀/Cr(5000Å) referred to as sample C
- d) Sample A annealed at 1000°C for 60' and pressure < $1 \cdot 10^{-7}$ mbar, referred to as sample D

At first instance the simplest case to study, i.e. a sample having a single 5000Å thick Cr layer, was grown and investigated. Based upon the observations of Bödeker et al. [Böd97], a second sample covered by an Fe/Ag layer was deposited. Analysing the results obtained from these samples gave evidence for a substrate-induced effect. From the structural characterization as well as the neutron diffraction an in-plane expansion of the lattice parameter was observed, caused by the fitting of the Cr unit cell to the larger MgO unit cell, see fig. 2.9. It was therefore interesting to grow a Cr film on another type of substrate which could induce the opposite strain. A good candidate is LiF ($a_{\text{LiF}} = 4.0263\text{Å}$) which allows the growth of epitaxial Cr films [Matt90] and it's lattice constant is 1% smaller than Cr. However, due to technical reasons another solution had to be found. Gold ($a_{\text{Au}} = 4.0789\text{Å}$) has a 0.1% smaller lattice

constant than Cr and is directly available in the MBE system. The rather complicated structure of sample D is necessary to overcome the following epitaxial incompatibilities. In a first attempt, it was tried to grow a Cr film on a thick Au film on MgO. Unfortunately, depositing Au directly on MgO did not retain the epitaxy. On the other hand, Au on a Cr seed layer preserves the epitaxy and RHEED showed a $5 \times$ Au surface reconstruction. Unfortunately, the further growth of Cr on this Au layer loses its crystallinity.

Neither did growing on an annealed Cr seed layer work. An annealed seed layer could be of interest since the strain could be relieved in this layer. After annealing, a 2×2 Cr surface reconstruction was formed but the further growth of Cr at 100°C is not epitaxial anymore. Therefore, the final structure starting with a Cr seed layer followed by a 600\AA thick $[\text{Au}(30\text{\AA})/\text{Cr}(30\text{\AA})]_{10}$ buffer to relax a possible induced strain of the MgO substrate was chosen to prove the hypothesis. Preceding experiments on Au/Cr multilayers showed good epitaxy of both lattices.

In addition sample A was annealed. Earlier investigations on bulk defect-rich Cr proved that the AF_0 phase is strongly reduced by an annealing treatment [Bacon69,Will81]. However, it was not clear if annealing also relaxes the strain in these layers. Therefore sample A was brought to 1000°C for one hour in UHV conditions.

The preparation and characterization of these films will be handled in paragraph 4.2.2. Paragraph 4.2.3 will introduce the reflections from a blank MgO substrate as observed from neutron diffraction. The determination of the magnetic phase diagram will be treated in resp. paragraph 4.2.3, 4.2.4, 4.2.5, 4.2.6 for the different samples. For the relevant cases, the strength of the anisotropy is

studied by applying a magnetic field. Finally, the obtained results are discussed in paragraph 4.2.7.

4.2.2 Preparation and characterization

The samples are, similar to the Fe/Cr multilayers, grown by MBE on $2 \times 2 \text{ cm}^2$ MgO(001) substrates. After cleaning the substrates for 15' at 600°C , pure Cr (99.99%) is deposited at a substrate temperature of 100°C and a rate of typically 0.5\AA for all samples. During evaporation the pressure remained for all samples between 10^{-9} and 10^{-10} mbar. In-situ RHEED during and after growth directly provided information on the epitaxy. Figure 4.2.1 shows a typical RHEED reflection pattern after the growth of the thick Cr layer.

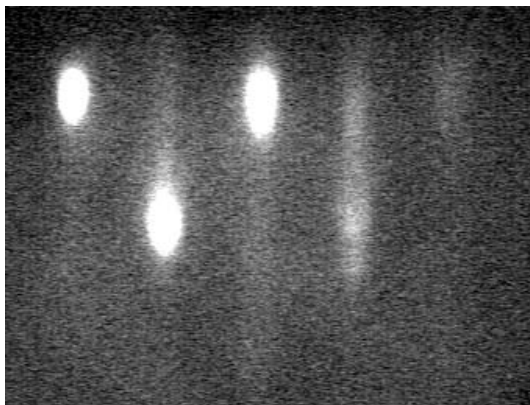


Fig. 4.2.1 A RHEED reflectivity pattern of a MgO(001)/Cr(5000Å) layer.

The epitaxial nature is proved by the presence of the separated diffraction spots. These reflections do not appear as streaks indicating a roughening after the growth of 5000\AA chromium.

The next step is ex-situ characterization by XRD. Figure 4.2.2 shows the high angle XRD diffraction pattern for sample A. The MgO (002) reflection shows up at $q_z = 3\text{\AA}^{-1}$ and a MgO(003) peak is visible at 4.5\AA^{-1} . Since MgO has a NaCl configuration its diffraction pattern is that of a fcc structure and thus the 003 reflection is forbidden.

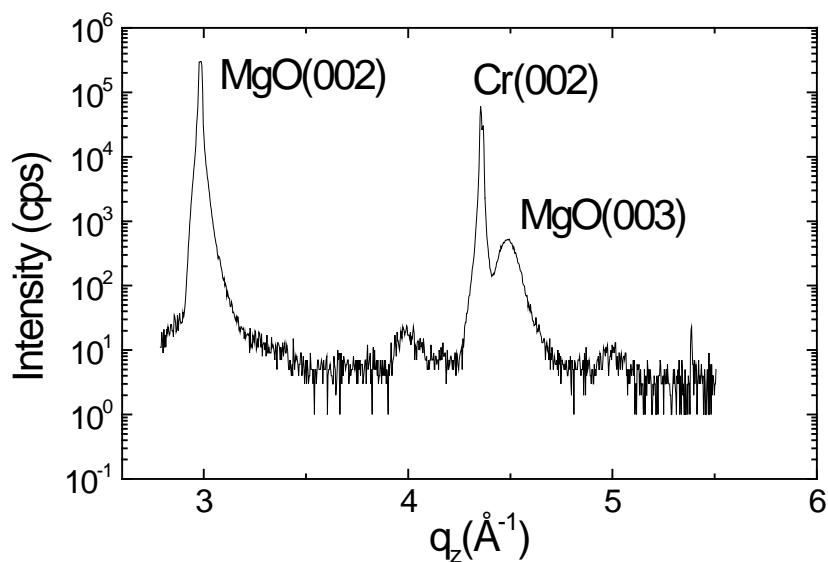


Fig. 4.2.2 *The high angle XRD diffraction pattern for sample A.*

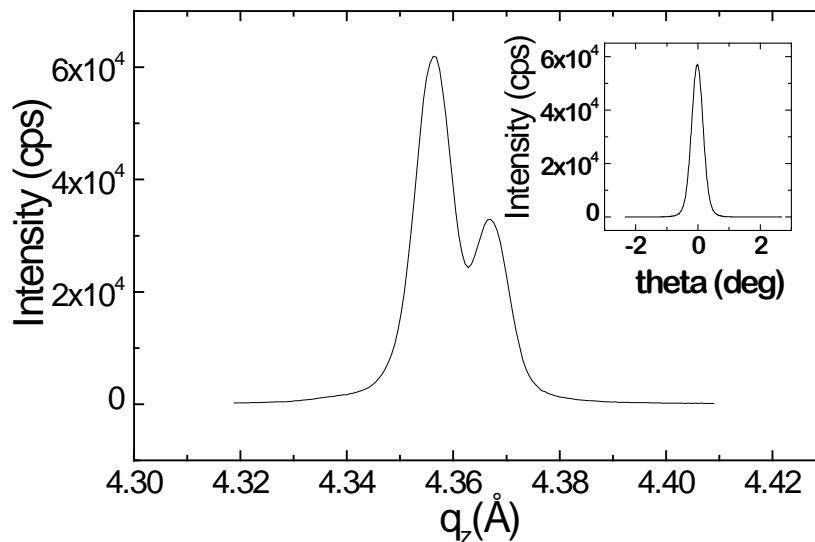


Fig. 4.2.3 The high angle XRD ω - 2θ diffraction pattern of sample A around the Cr(002) reflection. In the inset the ω -scan around this reflection is shown.

The fact that this peak appears in the MgO reflection could be explained by the incompletely vanishing structure factor because of the difference in atomic form factor between Mg and O. The only Cr reflection is Cr(002) at $q_z = 4.4 \text{\AA}^{-1}$ which indicates that the complete sample is 001 oriented. An enlargement of this peak is shown in fig. 4.2.3. Firstly, the double peak in fig. 4.2.3 is caused by diffraction of the $\text{CuK}_{\alpha 1}$ (1.540598\AA) and $\text{CuK}_{\alpha 2}$ (1.544418\AA) radiation on the Cr(002) planes. Secondly, shown in the inset, the rocking curve measured around the Cr(002) reflection has a half width of 0.37 degrees representing a relatively small mosaic spread of the grains. Thirdly, off-axis XRD measurements around the (112) type reflections confirmed the epitaxial relation between Cr and MgO.

The lattice parameter a_{\perp} perpendicular-to-plane as derived from these measurements is $a_{\perp}=2.882\pm 0.001\text{\AA}$. Table 4.2.1 gives an overview of this value for the different samples.

Sample	a_{\perp}
Bulk	$2.88459 \pm 0.00005 \text{\AA}$
A	$2.882 \pm 0.001 \text{\AA}$
B	$2.8831 \pm 0.0005 \text{\AA}$
C	$2.8843 \pm 0.0005 \text{\AA}$
D	$2.8853 \pm 0.0005 \text{\AA}$

Table 4.2.1 *The out-of-plane lattice parameter of the Cr unit cell for the different investigated samples is shown.*

The out-of-plane lattice parameter for sample A and B is less than the bulk value. For sample C, grown on the Au/Cr buffer, no significant deviation from the bulk value is found. Thirdly, for sample D the opposite change is observed. The out-of-plane lattice parameter is larger than the bulk value for this sample. The most probable reason is the underlying difference in the thermal expansion coefficient between Cr and MgO which will be discussed further. Finally, the annealing treatment improves the crystallinity since the width of the rocking curve is decreased down to 0.17 deg.

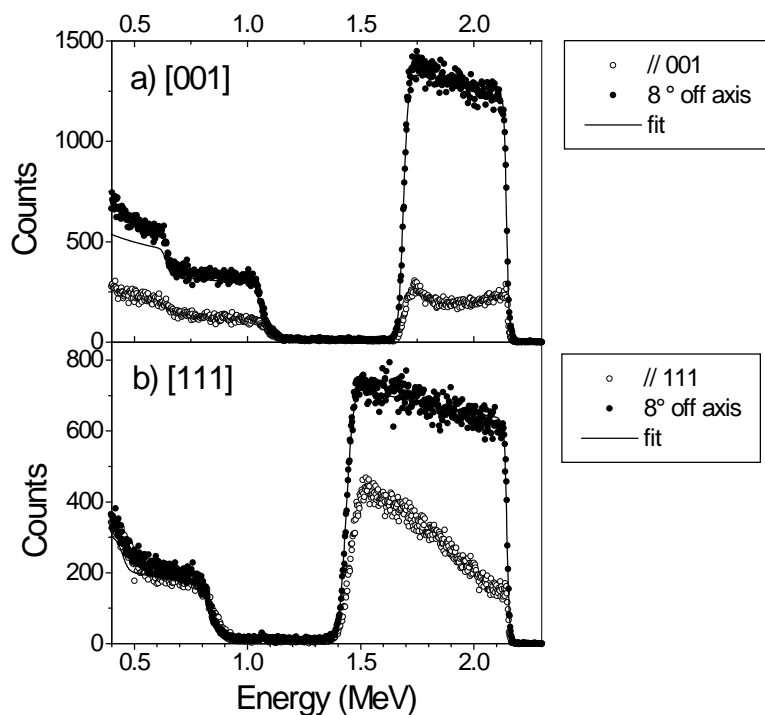


Fig. 4.2.4 Rutherford backscattering spectra taken on sample A around the Cr[001] (a) and the Cr[111] (b) crystal direction in channelling geometry (λ) and at random incidence (λ). The solid line is a fit using the RUMP code.

From the XRD measurements on sample A (B), a distortion of the Cr unit cell is expected. Since these measurements are near the resolution of the apparatus, other techniques need to be involved to confirm this deformation.

Therefore, in collaboration with the Instituut voor Kern- en stralingsfysica [AV98] an elaborate RBS study on sample A was carried out. Figure 4.2.4 shows the RBS results for the 2.9 MeV He^+ incoming beam around the Cr[001] (figure a) and the Cr[111] (figure b) direction. For both directions, a backscattered spectrum is taken with the beam

exactly along the corresponding crystal direction (channelling geometry), and one spectrum at a random (8 deg) off -axis position. The Cr signal is found above 1.75 MeV while below this value the MgO substrate is observed. Firstly, using a simulation based on the RUMP-code [Dool85] a thickness of 4600Å Cr is determined. Secondly, the backscattered yield in channelling geometry is drastically reduced compared to the random incidence spectrum. The ratio of the backscattered yield in channelling geometry and the random geometry is called the minimum yield χ_m and is a measure for the crystalline quality. For a perfect crystal, a minimum yield of 1.7% is expected and on the other hand 100% if the sample is polycrystalline. From our measurement, shown in fig. 4.2.4a, a ratio of 16% is determined, indicating a high defect concentration. Near the surface, the backscattered yield in the aligned geometry is slightly higher because of scattering from the first monolayer. In the bulk of the layer the yield is relatively constant. Only at the interface with the MgO, at 1.75 MeV, an enhanced backscattering is observed. This higher yield is caused by lattice imperfections such as misfit dislocations. These defects are created as the elastically strained Cr-layer relaxes.

In-plane information is obtained from additional channelling measurements along the off-normal Cr[011] (not shown) and Cr[111] axis (figure 4.2.4b). The epitaxial nature is confirmed from the positioning of the respective axes in the Cr-layer and the MgO substrate. The minimum yield measured along the Cr[111] axis is 45%, which is much higher than for a single crystal. Moreover, the width of the [111] channelling spectra is larger than theoretically expected. These observations are known to be due to an inferior crystallinity, such as a mosaicity. Hence, we can conclude that the Cr-

layer is heavily disordered. Moreover, the fact that a minor interface peak is still observed in these measurements (not shown), despite the rather high χ_m , confirms the large degree of relaxation in this film.

Furthermore, from the exact position of the Cr channelling minima, the elastic strain in the film can be determined. The angle between the [111] axis and the [001] is 54.74 deg for a perfect cubic lattice. If tensile strain (resp. compressive) is applied, then this angle will increase (resp. decrease). From measurements along the [111], $[3\ 2\ \bar{2}]$, $[7\ 5\ \bar{5}]$, $[4\ 3\ \bar{3}]$ axes a very small distortion of $\Delta\psi=0.09$ deg was derived. The angle $\Delta\psi$ is defined as the difference between the expected value of channelling minimum and the measured minimum. Taking the out-of-plane lattice parameter of $a_{\perp} = 2.882\text{\AA}$ as observed from XRD, an in-plane lattice parameter $a_{//} = 2.892\text{\AA}$ can be calculated.

Hence, it can be concluded that the Cr layer is (nearly) completely relaxed, confirming the XRD results. However, within the sensitivity of the channelling technique, a minor strain component cannot be excluded. Indeed, the measured tetragonal distortion suggests a minor tensile strain in accordance with the expected adaptation of the Cr unit cell on the MgO unit cell.

4.2.3 Neutron diffraction measurements on MgO substrate

Before entering into the neutron diffraction results for the different Cr layer, the ω -2 θ measurements on a blank MgO(001) substrate are shown. These measurements allow us to exclude some peaks as coming from the Cr film. Figure 4.2.5 shows us the ω -2 θ neutron scan around Cr(001), i.e.

the scattering vector \mathbf{q} is perpendicular to plane. The x-axis is expressed in units of the reciprocal Cr space since these units will be the standard for the further measurements on the Cr films. No strong MgO reflections due to the chosen neutron wavelength of $\lambda=2.422\text{\AA}$ are present in the vicinity of the Cr(001) position. However, the reflections of a thin film are weak because the low neutron intensity and the small amount of material. This means that a long counting time has to be taken into account and secondary effects such as reflections due to higher order wavelengths show up.

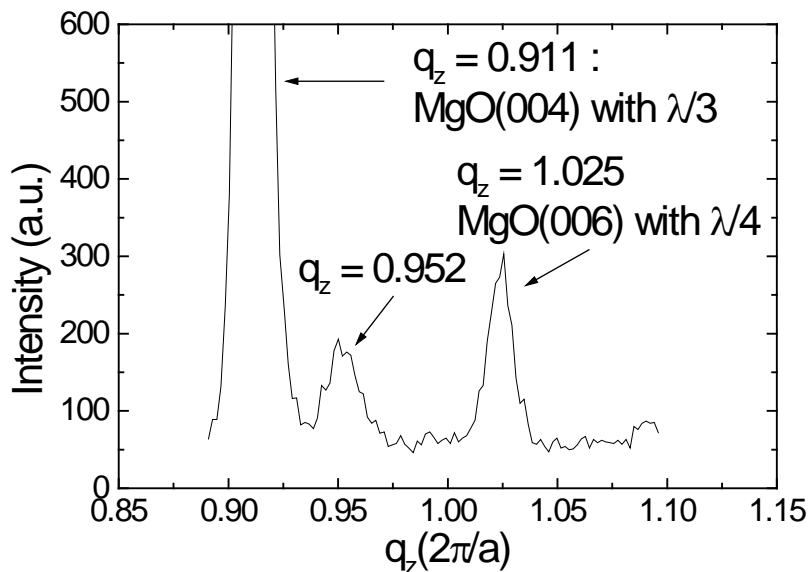


Fig. 4.2.5 The ω - 2θ neutron diffraction scan of an empty MgO substrate at the Cr(001) position ($q_z = 1$ corresponds to the Cr(001) reciprocal lattice point).

As mentioned in paragraph 3.2.1, the monochromatization is based on the Bragg reflection on a graphite crystal. For this graphite filter,

the wavelengths λ/n (n integer > 1) satisfy the Bragg law and pass the filter. The intensity of these λ/n neutrons is 10^{-3} times lower than for the 2.422\AA neutrons because of the sapphire cut-off crystal, see paragraph 3.2.1). Nevertheless, for relatively thick MgO single crystal these wavelengths cause clear reflections, see fig. 4.2.5 At $q_z = 0.911$ a strong peak originating from MgO(004) reflection and $\lambda/3$ neutrons is present. In addition $\lambda/3$ neutrons diffracting from the MgO(006) planes gives a peak at $q_z = 1.025$. Thirdly, there is an intensity present at $q_z = 0.952$. This peak is due to diffraction from 2.422\AA neutrons since it is not dependent on the intensity of the λ/n neutrons. The exact origin of this reflection is so far unknown, but this measurement shows that it is inherent to the MgO substrate. That this reflection originates from the MgO substrate is relevant as its position coincides with a further studied SDW satellite.

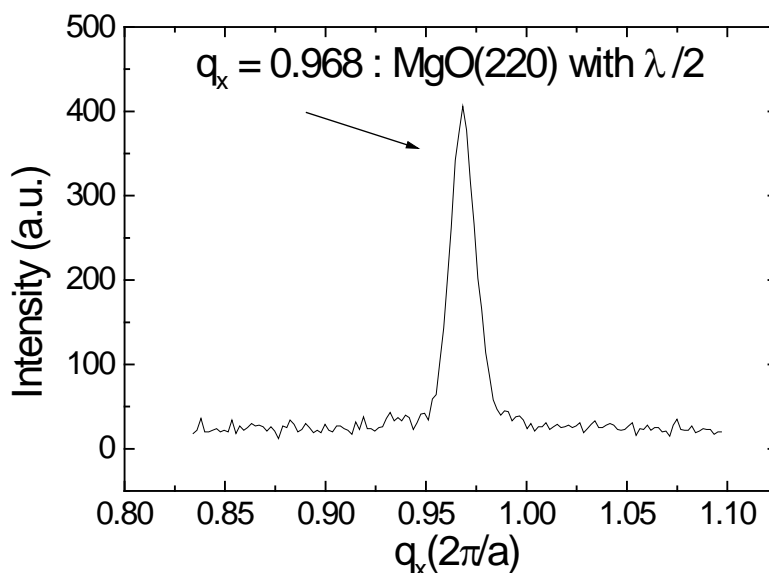


Fig. 4.2.6 The ω - 2θ neutron diffraction scan of a MgO substrate at the Cr(100) position ($q_x = 1$)

corresponds to the Cr(100) reciprocal lattice point).

The scan around Cr(100) is shown in fig. 4.2.6. The scattering vector is now directed in-plane along the MgO(110) direction. Since the penetration depth of neutrons is much larger than for X-rays in these materials, one can easily measure in transmission geometry, i.e. diffracted neutrons have to go through the 2 mm thick MgO substrate. From this point of view in-plane information is more easily obtained by neutron diffraction. Finally, the only higher order reflection in the vicinity of the Cr(100) direction is caused by diffracting $\lambda/2$ neutrons at MgO(220) planes.

During the first experiments it was not possible to solve to problem of the substrate scattering from the λ/n neutrons. Fortunately, an extra filter could be introduced during later experiments to suppress this scattering.

In conclusion, an empty MgO substrate is studied to clarify the origin of the observed reflections.

4.2.4 The magnetic structure of a MgO(001)/Cr(5000Å) film

- **Temperature dependence**

The first experiments were carried out on a single Cr layer. The sample is mounted in such a way that the scattering vector \mathbf{q} covers the xz reciprocal plane. The initial alignment of the sample is based upon the strong reflections of MgO. After this procedure the weak reflections of Cr are easily found because of the epitaxial relationship between Cr and MgO. For the determination of the magnetic phase diagram all possible satellites in the reciprocal xz plane, see fig. 2.20 , were scanned

and evaluated by using the notation of this figure. For the deduction of the magnetic state, the [100] and the [010] direction are assumed to be equivalent. Measurements were carried out in steps of about 50K. At first instance, the magnetic phase diagram as observed is discussed in term of the relevant temperatures, i.e. 20K, 200K, 250K and 400K. Supplementary temperature information is introduced in the later discussion. Figure 4.2.7 shows the ω - 2θ scan around the Cr(100) position. The peak at $q_x = 0.975$ is caused by the fraction of $\lambda/2$ neutrons diffracting from the MgO(220) planes. At 20K, a clear $(1+\delta, 0, 0)$ satellite at $q_x = 1.045$ proves the existence of an in-plane T-SDW along the [100] direction. The corresponding $(1-\delta, 0, 0)$ satellite is for the greater part overshadowed by the MgO(220) peak. At 200-250K these satellites disappear and a AF_0 state at the Cr(100) position shows up. This commensurate state is stable until the highest measured temperature of 400K.

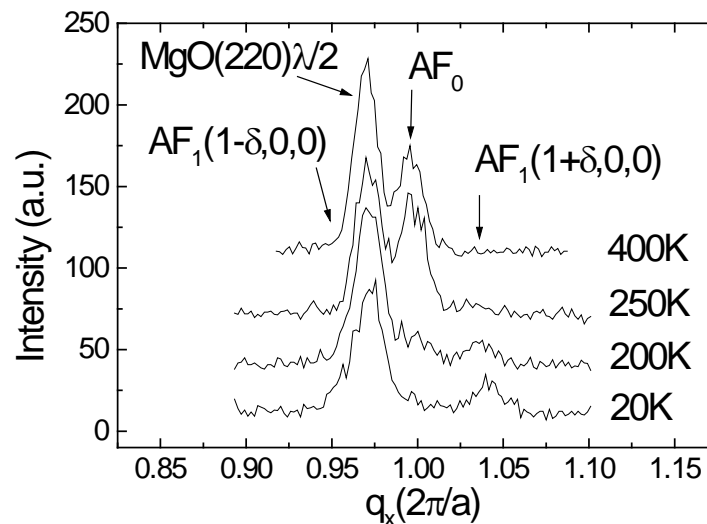


Fig. 4.2.7 Shows the q_x -scan along the $Cr(100)$ position. Below 200K Cr exhibits an in-plane T-SDW while above 200K the AF_0 state is stable.

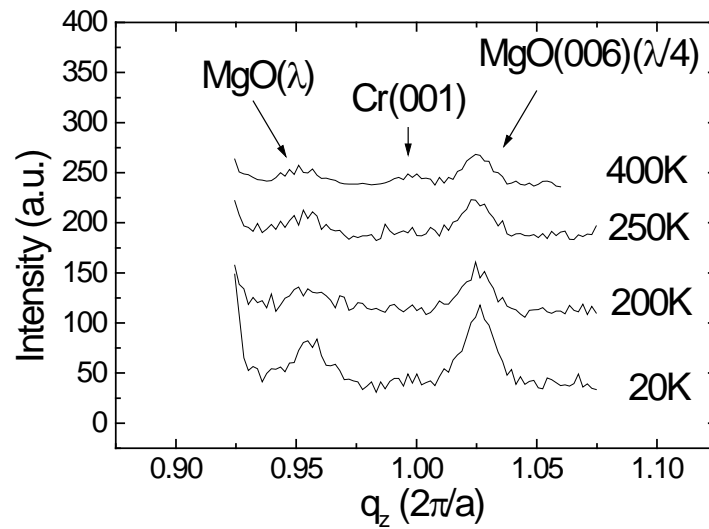


Fig. 4.2.8 The ω - 2θ scan along the out-of-plane $Cr(001)$ direction is shown. The only observed magnetic reflection is a weak contribution of the AF_0 state at 400K.

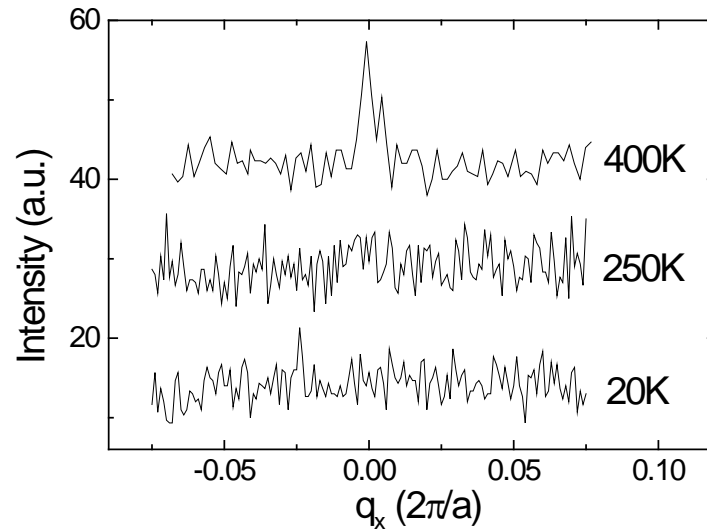


Fig. 4.2.9 The q_x -scans along around the $Cr(001)$ position. There is only a small AF_0 component at 400K present and no satellites.

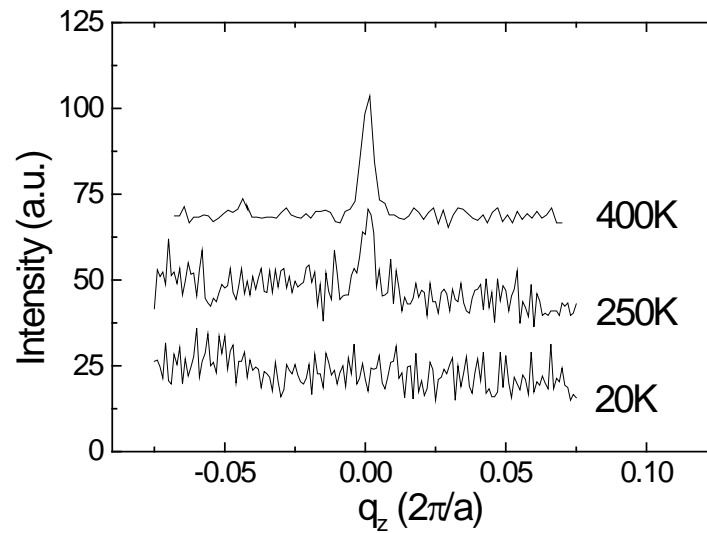


Fig. 4.2.10 The q_z -measurements around $Cr(100)$ showing the out-of-plane polarized AF_0 state at $q_z = 0$.

The out-of-plane ω - 2θ scan, along Cr(001), is shown in fig. 4.2.8. Apart from the substrate reflections, nearly no magnetic contribution is seen. Only at 400K a minor AF_0 intensity shows up. The lack of intensity at $q_z = 1$ for temperatures above 200K determines directly the polarization of the AF_0 state in fig. 4.2.7 as out-of-plane. Secondly, no satellites are observed in the q -scans along Cr(001) proving the absence of any out-of-plane T-SDW. These two facts already indicate a significant difference between the in- and out-of-plane magnetic states of the Cr layer and thus an anisotropic behaviour.

More information on the SDW states is obtained from the scans along the off-specular reflections. The corresponding q_x -scans around the Cr(001) are shown in fig. 4.2.9. These scans intersect in the Cr(001) reciprocal lattice point with the type of measurements in fig. 4.2.8. Only at 400K a relatively small in-plane polarized AF_0 contribution is observed. If in fig. 4.2.9 satellites were present, they would be originating from an in-plane L-SDW or a in-plane T-SDW having its spins also in-plane. Hence, the observed T-SDW in fig. 4.2.7 at 20-200K should have an out-of-plane polarization, similar to that of the AF_0 state. This way of reasoning can be questioned as it is more correct to see the $(\pm\delta, 1, 0)$ side reflections for concluding an out-of-plane polarization of the T-SDW in fig. 4.2.7. However, these satellites were not accessible at that time and further measurements will confirm the hypothesis.

The fourth set of measurements are the q_z -scans around Cr(100) in fig. 4.2.10. No satellite reflections are present, excluding an out-of-plane L-SDW or T-SDW. These q_z scans intersect with the specular q_x -scans at Cr(100). Therefore the out-of-

plane polarized AF_0 state shows up in fig. 4.2.10 at $q_z = 0$. Finally, it should be mentioned that for the off-specular measurements at 20K and 250K, fig. 4.2.9 and fig. 4.2.10, the intensity is slightly reduced and a higher background is present. The reason for this is that those measurements were carried out in a magnet system instead of the orange cryostat or cryofurnace. The corresponding measurements in the orange cryostat are also carried out but only for $-0.05 < q < 0.05$ which is in the worst case just after the center of the satellite. Both measurements do not show any evidence for satellites.

An overview for these out-of-plane polarized AF_1 and AF_0 states is shown in fig. 4.2.11. The points are obtained by a normalized integration over the peaks. The transition occurs at 200-250K while outside this range the intensities are relatively constant.

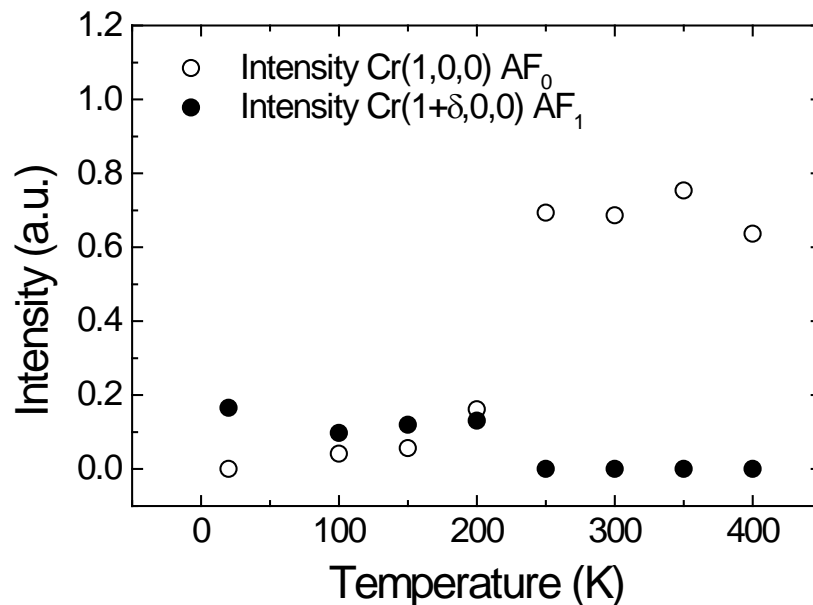


Fig. 4.2.11 *The intensity of the out-of-plane polarized AF_0 and AF_1 structure for sample A is plotted as function of temperature.*

Apart from the magnetic information, the neutron diffraction measurements in transmission geometry can be used to determine the in-plane lattice parameter. This can be directly derived from the location of the AF_0 peak in the q_x -scan around Cr(100). Furthermore, for a cubic Cr unit cell, the position of this reflection should coincide with the out-of-plane nuclear Cr(002) reflection using $\lambda/2$ neutrons. In contrast a difference of 0.3 ± 0.07 deg is found. Based on these results we find an in-plane lattice parameter $a_{//} = 2.895 \pm 0.005$ Å which is within the error in agreement with the independent RBS observations. However, it is important to emphasize that these lattice parameters are obtained by measuring the whole structure. From the RBS measurements it is clear that in the first grown layers, fig. 4.2.4 at 1.7-1.8 MeV, a relaxation occurs and therefore a higher distortion could be present in this region.

- **Magnetic field dependence**

Similar to the spin flop in the Fe/Cr multilayers the itinerant antiferromagnetism in Cr can also be oriented perpendicular to an applied field, as is depicted in fig. 2.21. In bulk single crystalline Cr this process is saturated within 1.5T [Wern68].

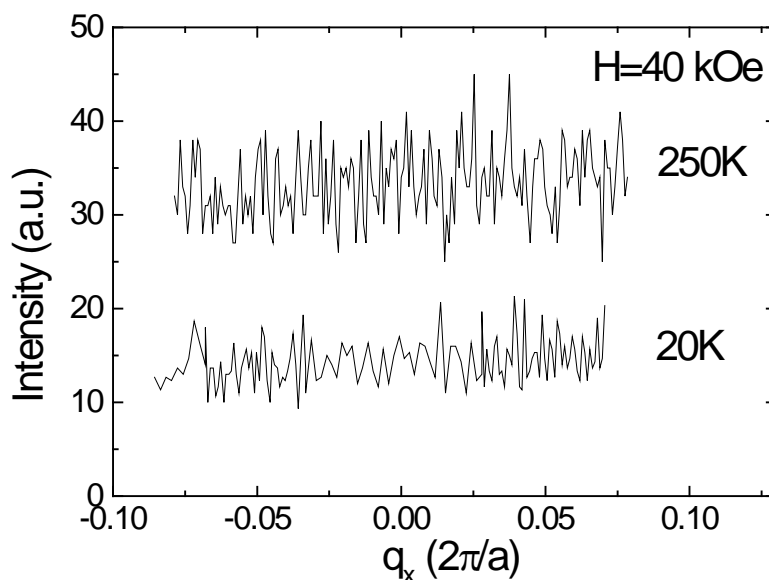


Fig. 4.2.12 The q_x -scan around Cr(001) in a field of 4T perpendicular to the plane thus parallel to the spins. No commensurate AF_0 state (250K, $q_x = 0$) or T-SDW (20K, $q_x = \pm\delta$) with their spins in the plane are observed.

In our case a substrate induced anisotropy effect causes the spins to align perpendicular to the plane of the film. The necessary field to get the spins in the plane is a measure for the strength of this anisotropy. This implies that the AF_0 intensity at Cr(100) would disappear proportional to the formation of a new peak at Cr(001). For the corresponding T-SDW an in-plane polarization would give rise to satellite intensities in the q_x -scan around Cr(001).

Figure 4.2.12 shows the q_x -scan containing the Cr(001) point at a field of 4T at 250K and 20K. At 250K, there is no indication for an in-plane polarized AF_0 state at $q_x = 0$. Neither does any satellite intensity at $(\pm\delta, 0, 1)$ show up at 20K, concluding that the T-SDW remains in-plane

polarized for a field of 4T parallel to the spins applied. Within a field of 4T we could not find any field dependence. For this reason one can conclude that the that the observed spin anisotropy is significant stronger than in a field cooled Cr whisker.

- **Discussion**

Comparing the magnetic state of pure bulk single crystalline Cr and the one observed in the as grown Cr thin film on MgO highlights two main differences. Firstly, the different temperature dependence of the magnetic phase diagram with the observation of the AF_0 state and secondly the preferential Q- and spin direction.

As discussed in paragraph 2.3, the AF_0 state in pure Cr is only observed in defect rich Cr like swaged rods or crushed powder. The high minimum yield of 16% in the RBS measurements indicate the presence of defects. Therefore we conclude that the disruption of the lattice periodicity is the reason for the observation of the AF_0 state in this sample.

Secondly, the observed temperature dependence of the magnetic phase diagram is in agreement with the observations of Bacon [Bacon69] and Window [Win70]. Next to the AF_0 state a broadening of the transition temperatures (T_N and T_{SF}) was found with a suppression of the AF_2 state. In our measurements the AF_2 state could not be observed within the resolution of the experiment.

Williams and Street [Will79,Will81] proposed a model for calculating the magnetic phase diagram in strained chromium. However, according to our results a discrepancy for the description of the AF_0 state in their model remains. The AF_0 state is much more temperature dependent in the Cr film. In the framework of their presented results this could

be explained by a higher defect concentration. In that case, the AF_0 state should be more clearly present at low temperatures, which we can not confirm as it vanishes relative abruptly at 200K. In this respect, epitaxial films allow a separation of the intensities of the AF_0 and the AF_2 state which is not possible in polycrystalline material. Therefore, additional information can be obtained from such structures.

Thirdly, the observed Q- and spin anisotropy is in accord with the averaged deformation of the bcc Cr unit cell. The latter is induced by the adaptation of Cr on MgO. In the in-plane direction the lattice is expanded while for the out-of-plane lattice parameter a contraction is found. The influence of such a deformation is studied theoretically by Barak and the here observed magnetic anisotropy corresponds with his predictions namely spins out-of-plane and Q vector in the plane. Earlier, Bastow et al. [Bast66] carried out compressive cooling experiments in which they found the same behaviour for the Q dependence on stress.

Therefore it is believed that the origin for the observed Q- and spin anisotropy in the T-SDW is the deformed Cr unit cell. Most likely is this also the underlying reason for the spin anisotropy of the AF_0 state.

Finally, another point should be emphasized. The RBS measurements show that the layer is nearly relaxed towards the top. It could be that there is no strain present in the top layers. In addition to the fact that for all temperatures and fields no in-plane spins are observed, this could indicate the presence of a magnetic coupling between a strained and an unstrained part.

These results should be discussed in the framework of the observations of the group of Zabel [Sonn98].

With respect to this work several points can be mentioned.

Firstly, in both studies the Cr spins are mostly oriented out-of-plane for all temperatures. Furthermore, around $T > 200\text{K}$ an out-of-plane polarized AF_0 state dominates the magnetic phase diagram and persists far beyond the Néel temperature of bulk single crystalline Cr. Below 200K a difference shows up.

In the case of Cr on MgO solely an in-plane T-SDW is observed (spins out-of-plane). On the other hand for Cr on Nb/sapphire the I-SDW propagates for the greater part out-of-plane except for one sample where partly an in-plane T-SDW is observed [Sonn98].

From the structural point of view their samples indicate a somewhat better quality. Their RHEED is more streaky so the surface is flatter [Böd99]. In the out-of-plane XRD scans no large difference is discerned. The half width of the XRD ω -scan around Cr(002) is about the same. However, the [111] RBS measurements show large in-plane disorder in the samples on MgO. For their samples on Cr/Nb a larger in-plane disorder as in the out-of-plane direction is found but no direct comparable investigation methods are available.

The in-plane expansion is found to be larger in the samples on MgO. The latter could be the reason that the strain in the samples on Cr could have a more overwhelming effect causing the observed spin- and Q orientation to coincide with the expected behaviour from strain. Care has to be taken in this explanation because the difference is small and still other effects can be involved, like a different electronic interaction with the Nb/MgO substrate or structural effects on a small scale

which are not good accessible by XRD like grain boundaries. High angle XRD gives always the average and is therefore not that sensitive to layers near the substrate. Also the difference in annealing treatment between the samples grown on MgO and the Nb/Sapphire can have its influence.

In summary, the dominant magnetic structure in the temperature range of 20-200K is an in-plane propagating T-SDW having an out-of-plane polarization. In the interval of 200-250K an out-of-plane polarized AF_0 is formed at the expense of the T-SDW. This commensurate state remains stable until 400K. Only for the highest measured temperature of 400K a small in-plane polarized AF_0 contribution shows up at Cr(001). No evidence of a L-SDW was found. The out-of-plane spin direction could not be altered by applying a field of 4 Tesla confirming a significantly stronger anisotropy than in bulk single crystalline Cr.

The presence of the AF_0 state and the preferential q - and spin directions are explained in terms of structural features. The AF_0 originates from the disruption of the lattice due to defects while the anisotropical features are suggested to be related to strain. This strain is most likely caused by the adaption of the Cr unit cell on the MgO unit cell.

4.2.5 The magnetic structure of a MgO(001)/Cr(5000Å)/Fe(75Å)/Ag(75Å) film

- **Temperature dependence**

The magnetic structure in sample B is determined in the similar geometry as used for sample A. The scattering vector \mathbf{q} covers the xz plane and all four possible satellites are scanned at 20K ,100K

, 200K and RT. Figure 4.2.13 shows the q_x -scan along Cr(100). The MgO(220) reflection is completely suppressed by the use of an additional filter. At room temperature, a major contribution from an out-of-plane polarized AF_0 state is found at the Cr(100) position ($q_x = 1$). In addition to this reflection two very weak reflections can be seen at $q_x = 1 \pm 0.025$ revealing a small in-plane T-SDW contribution. Lowering the temperature to 200K causes the T-SDW intensity to grow at the expense of the AF_0 state. At 100K the AF_0 state has completely vanished and only a T-SDW intensity remains. Surprisingly, at 20K the T-SDW has vanished in favour of a re-appearing AF_0 contribution. The ω - 2θ scans around Cr(001) can be seen in fig. 4.2.14. No magnetic reflections are detected at all temperatures. The peak at $q_z = 0.95$ is a diffraction from the substrate, as is shown in fig. 4.2.5. These measurements prove that no major contribution from an out-of-plane T-SDW, or an in-plane polarized AF_0 state is present for temperatures below RT. Thirdly, the q_z -scans around Cr(100) are shown in fig. 4.2.15. This type of scan intersects with the q_x -scans of fig. 4.2.13 at the Cr(100) position. Therefore the out-of-plane polarized AF_0 state ($q_z = 0$) is observed at 20K and RT (200K). The fact that no $(1,0,\pm\delta)$ satellites appear in fig. 4.2.15 indicates that no out-of-plane L-SDW exists in this temperature range. The possible satellites cannot originate from an out-of-plane T-SDW as this state should be detected in the q_z -scan at Cr(001). The fourth type of scans are the q_x -scans around Cr(001), see fig. 4.2.16. Only at 20K two satellites $(\pm\delta,0,1)$ appear. Since for this temperature no satellites are present in the q_x -scans crossing Cr(100), the observed peaks in fig. 4.2.16 prove the existence of an in-plane L-SDW. For higher temperatures no satellites are

observed determining the polarization of the T-SDW in fig. 4.2.13 as out-of-plane.

In summary, the temperature dependence of the magnetic phase diagram of sample B is very similar to that observed for sample A. At temperatures above 200K an out-of-plane polarized AF_0 state is present. Below 200K an in-plane T-SDW is formed having an out-of-plane polarization. A deviation occurs below 100K. The sample covered with the Fe/Ag bilayer partially undergoes a spin orientation towards an in-plane L-SDW. Apart from the L-SDW a small out-of plane polarized AF_0 state reappears.

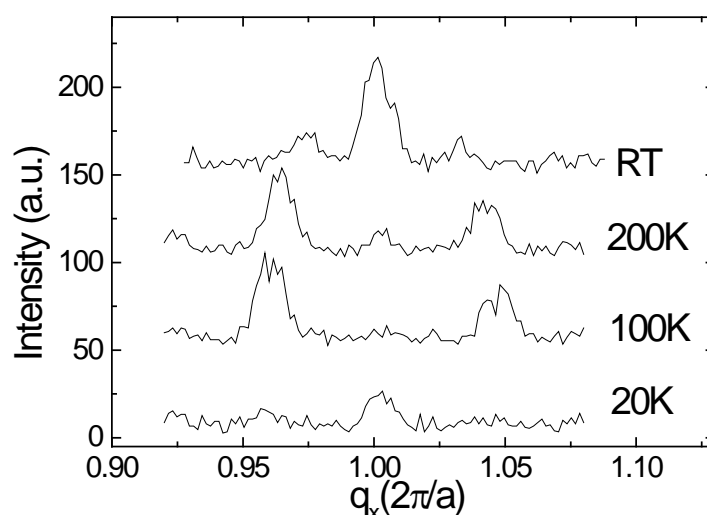


Fig. 4.2.13 The in-plane q_x scan around $Cr(100)$ shows the presence of an in-plane T-SDW and a AF_0 state in sample B.

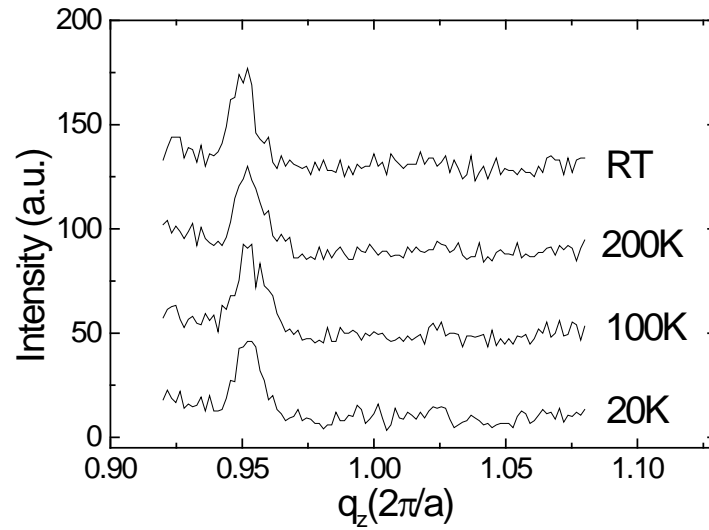


Fig. 4.2.14 The q_z -scan at Cr(001) for sample B is plotted for different temperatures. No magnetic reflections can be perceived.

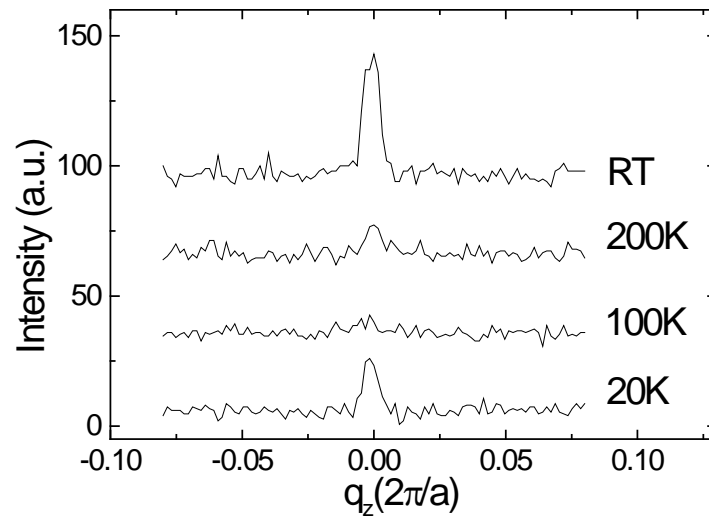


Fig. 4.2.15 The q_z -scan at the Cr(100) position is shown.

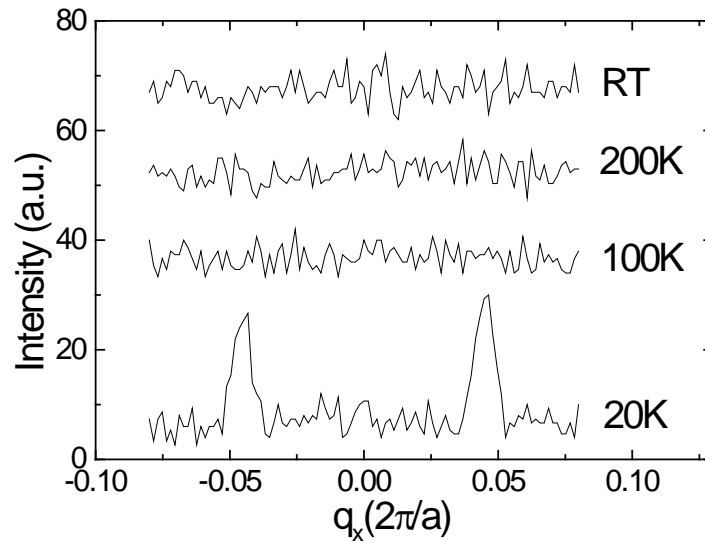


Fig. 4.2.16 The q_x -scans at Cr(001) are shown as function of temperature for sample B.

- **Magnetic field dependence**

Similar to sample A it is tried to align the antiferromagnetic spins by applying a magnetic field. A first attempt is made at 250K with a 4T horizontal magnet. According to the zero field measurements in the previous chapter, the sample should be in the transition between the AF_0 and the T-SDW state as can be seen in fig. 4.2.13.

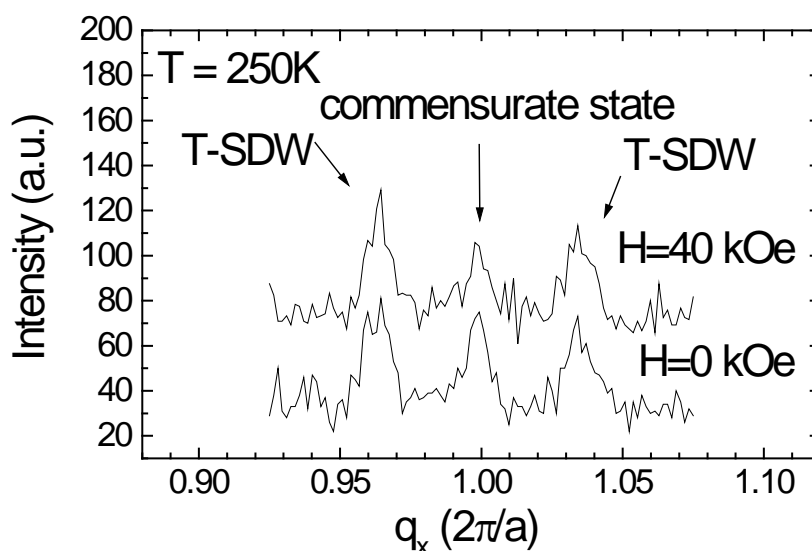


Fig. 4.2.17 It shown that the out-of-plane polarization of the AF_0 state ($q_x=0$) is not affect by a field of 40kOe.

This transitional state is confirmed by the q_x measurements in fig. 4.2.17. Both contributions are present in the scan at zero field. For reorienting the spins, a magnetic field of 40kOe is applied parallel to the spin direction, i.e. perpendicular to plane. As can be seen in fig. 4.2.17, the AF_0 intensity is not significantly affected by the field. Neither can the polarization of the T-SDW be altered by the field. A change in the polarization of the T-SDW cannot be observed in the scans of fig. 4.2.17 since the $(1\pm\delta,0,0)$ satellites are not depending on the polarization. If the spins reorient under influence of the field, then $(\pm\delta,0,1)$ satellite reflections should show up. Figure 4.2.18 shows the scan crossing these points and no intensity is spotted.

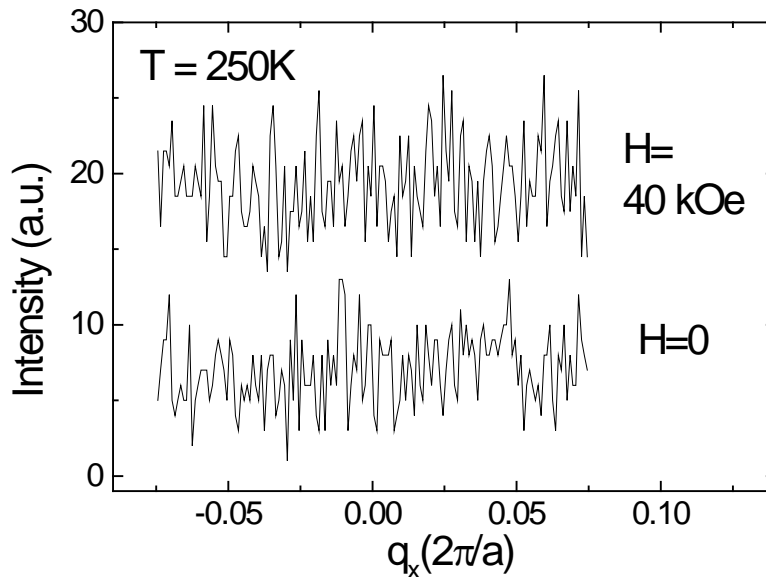


Fig. 4.2.18 The q_x -scan at Cr (001) with and without an external field of 40kOe. No polarizing effect is seen.

Neither is the polarization of the T-SDW affected by the field. Fig. 4.2.18 shows the q_x -scan through Cr(001). Applying the maximum field of 40kOe pulls the spins of the T-SDW in the plane which should result in two $(\pm\delta, 0, 1)$ satellite reflections in these scans. More accuracy is obtained by measuring for a longer time on the maximum of the AF_0 state. Figure 4.2.19 shows field scans at the Cr(100), Cr(001) and $(\delta, 0, 1)$ position. Within the resolution of the experiment no polarization effect can be revealed at a field of 40kOe.

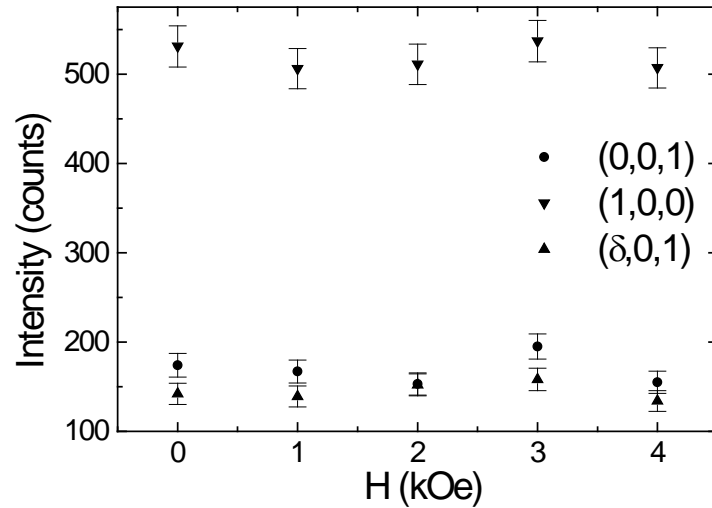


Fig. 4.2.19 Single long counting time intensities taken at the reflections of the polarizable states are shown. No magnetic field dependence is seen.

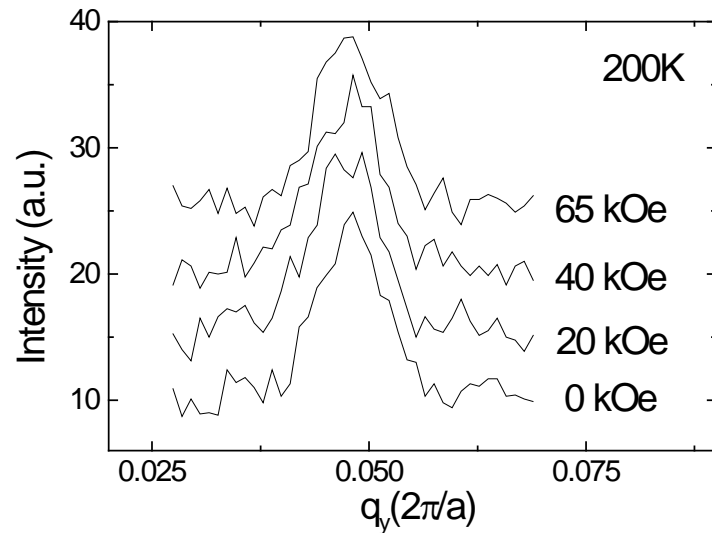


Fig. 4.2.20 The $(1, \delta, 0)$ reflection at 200K as function of field. No magnetic field dependency is seen.

A second attempt is made in a 6.5T vertical magnet system which allows, due to geometrical reasons, only a study of the T-SDW. In this configuration the scattering vector \mathbf{q} spans the xy-plane allowing to map the $(1,0,0)$, $(0,1,0)$, $(1\pm\delta,0,0)$, $(1,\pm\delta,0)$, $(0,1\pm\delta,0)$, $(\pm\delta,1,0)$ reflections. Therefore the in-plane T-SDW is now observed along the $[100]$ and the $[010]$ direction (not shown here). The out-of-plane polarized T-SDW should now appear at the equivalent $(1, \pm\delta,0)$ and $(\pm\delta,1,0)$ positions.

Figure 4.2.20 shows the $(1,\delta,0)$ reflection as function of field at 200K confirm the reductio ad absurdum reasoning. Unfortunately, no field dependence can be observed up to 6.5T. The same field scan is taken at 100K having and neither could a field dependence be found, see fig. 4.2.21.

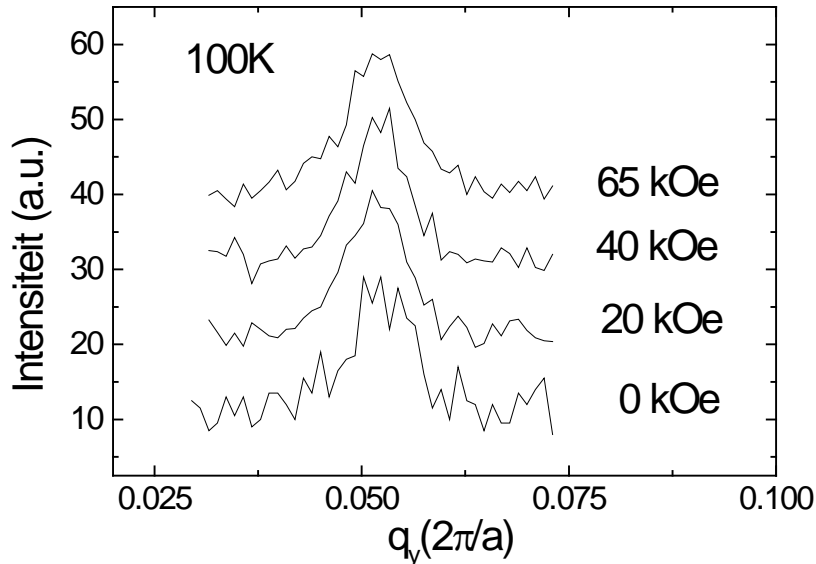


Fig. 4.2.21 The $(1,\delta,0)$ satellite reflection as function of field at 100K. The intensity is not field dependent.

In summary, one can conclude that the observed spin anisotropy in sample b can not be overcome by applying a magnetic field up to 65 kOe.

- **Discussion**

The magnetic phase diagram of sample B is very similar to the one observed for sample A. At high temperatures an out-of-plane polarized AF_0 state is found. The transition towards this AF_0 state starts at 200K and is more smeared out since at 250K still a contribution of the T-SDW state is found. The only difference shows up at the lowest temperature. At 20K the in-plane directed T-SDW has vanished. Instead, a clear in-plane L-SDW shows up together with a reappearance of the out-of-plane polarized AF_0 state. Concerning the magnetic field dependence it is shown that like the uncapped system no polarization of the spins can be discerned up to 65 kOe.

A similar deformation of the Cr unit cell is also observed in the Cr layer capped with an Fe layer and it is therefore assumed to be responsible for the observed out-of-plane direction of the spins and the in-plane Q behaviour. The presence of the AF_0 state at low temperatures is not understood. Worth to mention is that for FeCr alloys a re-entrance of the AF_0 state below the AF_1 state occurs [Faw94].

4.2.6 The magnetic structure of a $MgO(001)/Cr(50\text{\AA})/[Au(30\text{\AA})/Cr(30\text{\AA})]_{10}Cr(5000\text{\AA})$ film

- **Temperature dependence**

The temperature dependence of sample C is studied analogously to the previous samples having the

scattering vector \mathbf{q} in the xz plane. Figure 4.2.22 shows the in-plane q_w -scans at Cr(100). The only magnetic reflections are observed at RT.

At $q_x = 1 \pm 0.03$ an in-plane T-SDW is observed next to an out-of-plane polarized AF_0 state at $q_x = 0$. Both contributions disappear at lower temperatures. Secondly, figure 4.2.23 shows the q_z -scan at Cr(001). As is shown in section 4.2.3 the temperature independent peak at $q_z = 0.95$ originates from the MgO substrate. Only at 200K two satellite reflections show up at $q_z = 1 \pm 0.05$ proving the existence of an out-of-plane T-SDW. Below this temperature and at RT no magnetic contribution is seen.

Thirdly, the q_z -scan at Cr(100) is shown in fig. 4.2.24. At RT the small AF_0 contribution is present at $q_z = 0$. At 200K, two satellite reflections appear at $q_z = \pm 0.05$. In the out-of-plane q_z -scan along Cr(001), see fig. 4.2.23, an out-of-plane T-SDW is present for this temperature. Therefore the observed intensities in fig. 4.2.24 are most probably caused by this T-SDW as the ratio $\frac{1}{2}$ is confirmed. However a possible contribution of an out-of-plane L-SDW cannot be excluded. The same reason explains the strong satellites at 100K and 20K as originating from an out-of-plane L-SDW since no $(0,0,1 \pm \delta)$ satellites are found for these temperatures, see fig. 4.2.24. The intensity of the satellites is doubled as is typically observed during the spin flip transition of single crystals. Finally, the fourth set of scans are the q_x -scans along Cr(001) in fig. 4.2.25. Since there are no $(\pm \delta, 0, 1)$ satellites present, the in-plane T-SDW at RT in fig. 4.2.22 should be polarized out-of-plane. Furthermore, these scans exclude an in-plane L-SDW at all temperatures.

In summary the magnetic phase diagram can be described as follows. At RT, an in-plane T-SDW is

present having the spins out-of-plane polarized. Next to the T-SDW an commensurate contribution is observed with the same polarization. Reducing the temperature to 200K causes the AF_0 state to disappear and the T-SDW reorients perpendicular to the plane having the spins in-plane. At 100K the T-SDW is vanished and an out-of-plane L-SDW is formed. The L-SDW remains stable down to 20K.

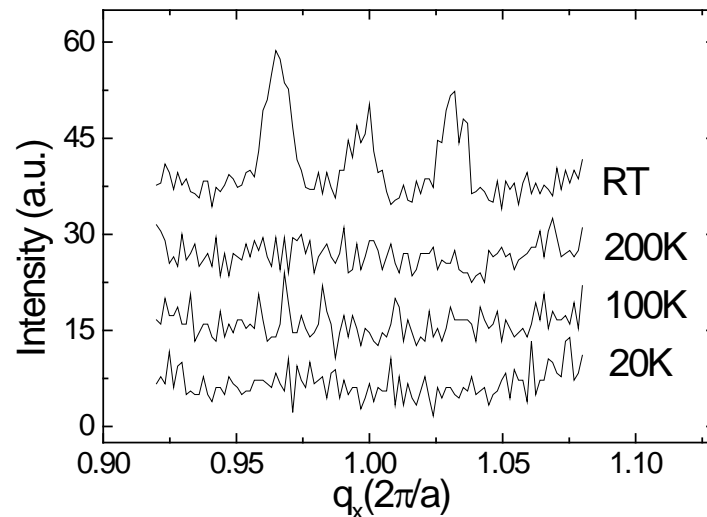


Fig. 4.2.22 The in-plane q_x -scan along $Cr(100)$ is shown. Only at RT an in-plane T-SDW and a out-of-plane polarized AF_0 state is observed.

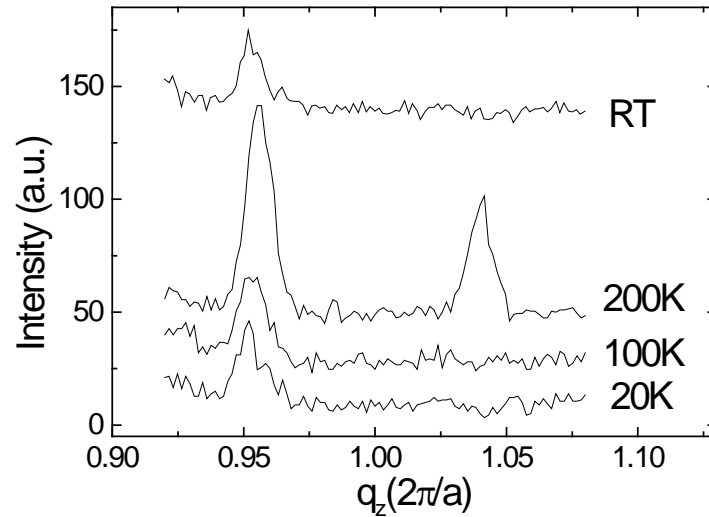


Fig. 4.2.23 The q_z -scan at Cr(001) is shown. The only magnetic reflection appears at 200K and results from a out-of-plane T-SDW.

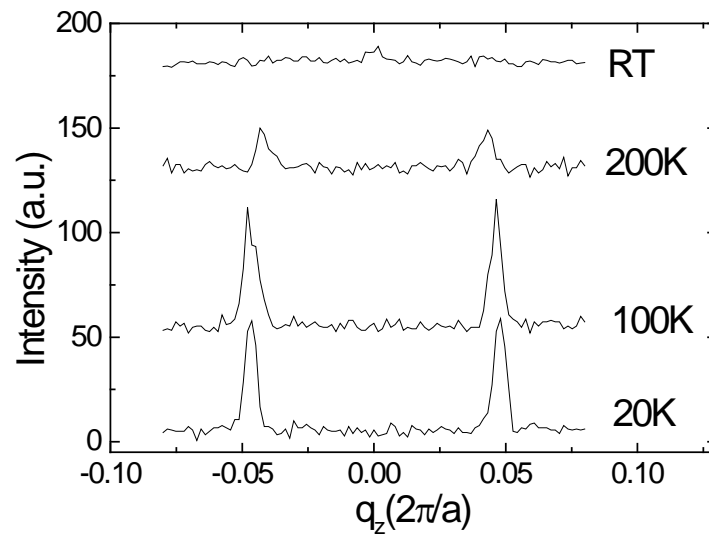


Fig. 4.2.24 The q_z -scan at Cr(100) as function of temperature for sample C. In relationship to the other scans, different magnetic states are probed.

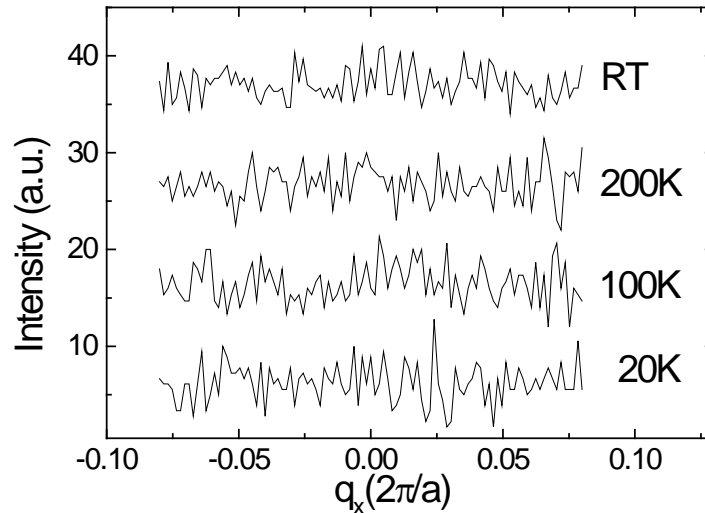


Fig. 4.2.25 The q_x -scans around Cr(001) are shown. No reflections are present excluding an in-plane L-SDW or in-plane polarization of an in-plane T-SDW.

- **Magnetic field dependence**

The study of the magnetic field dependence is limited to 250K because of the limitations of the magnet. Therefore only the out-of-plane T-SDW can be studied. The field is applied along Cr[010] so that the $(1,0,\pm\delta)$ peaks should vanish. Figure 4.2.26 shows the magnetic field scan taken on the maximum of the $(1,0,\delta)$ satellite for 250K, 200K, 150K. The intensities are corrected for the background and normalized by dividing by the intensity at zero field. An integer offset (1,2) is added to separate the curves. For all three temperatures a small decrease down to 80% of the zero field value is observed.

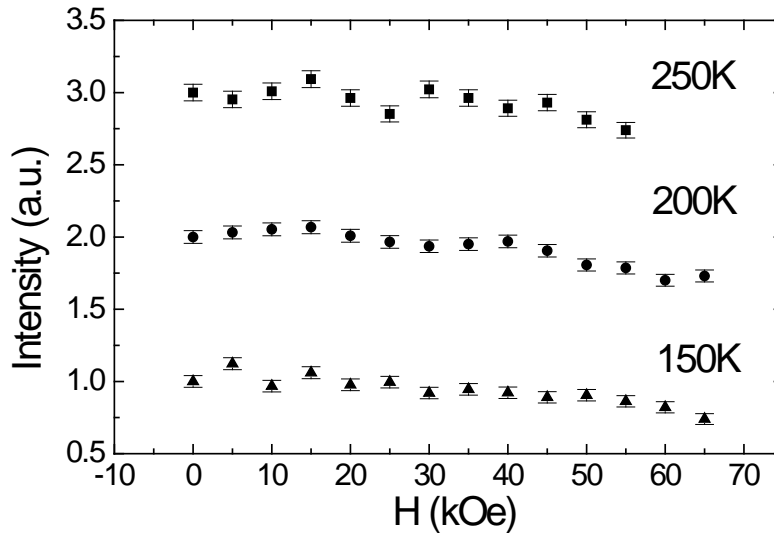


Fig. 4.2.26 The $(1,0, \delta)$ peak as function of field for 150K, 200K, 250K. A small field dependency is present.

- **Discussion**

Compared to the previous samples the magnetic phase diagram of sample C is quite different. The out-of-plane polarized AF_0 and T-SDW occurs now only near RT. At 200K an in-plane polarized T-SDW propagating out-of-plane is observed. This T-SDW reorients towards an out-of-plane L-SDW for lower temperatures. Thus the preferential out-of-plane spin direction for higher temperatures is not strongly present. The in-plane anisotropy is studied by magnetic field measurements. A small polarization effect can be perceived at 65 kOe. Thus the in-plane anisotropy is still higher than for the case of bulk Cr. It is clear that the use of a Cr/Au buffer layer influences the phase diagram significantly. The spin and Q anisotropy is not present and in addition the AF_0 has nearly vanished and the Néel temperature is situated near

RT. All these arguments indicate a less strained growth. Therefore, these observations are in agreement with the fact that the out-of-plane lattice parameter equals nearly the bulk value and the strain vanishes. This is in accord with the small in-plane lattice mismatch between Cr and Au and the fact that the Cr layer is situated further away from the substrate where much of the strain is relieved. On the other hand, one should assume that the effect of the out-of-plane mismatch is less significant. In summary, the influence of an Au/Cr buffer affects the magnetic phase diagram of the Cr strongly. Because of thick Au/Cr buffer and the perfect matching of the Cr and the Au lattices less strain is present in the film. The preferential spin and Q- anisotropy is lost and the contribution of the AF₀ state is reduced.

4.2.7 The magnetic structure of an annealed MgO(001)/Cr(5000Å) film

- **Temperature dependence**

The temperature dependence of the magnetic phase diagram is measured in a cryofurnace with the **q** vector covering the xz plane. Figure 4.2.27 shows the in-plane q_x-scans along Cr(100) for different temperatures. No reflections are present for all measured temperatures.

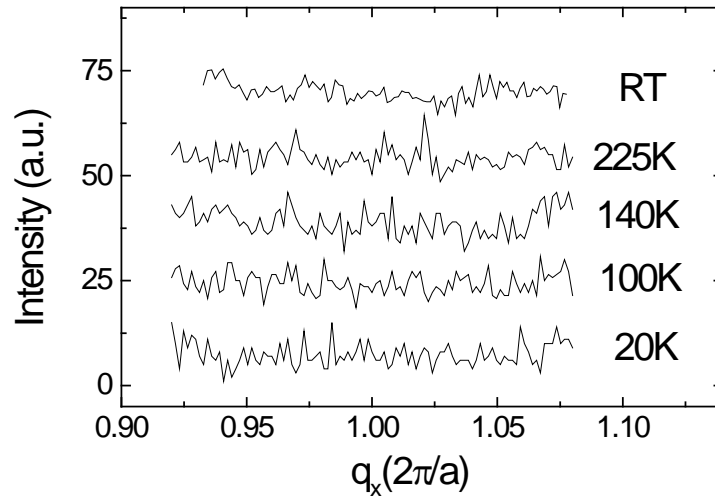


Fig. 4.2.27 The ω - 2θ scan along $Cr(100)$. The structure does not show an in-plane T-SDW or an out-of-plane polarized AF_0 state.

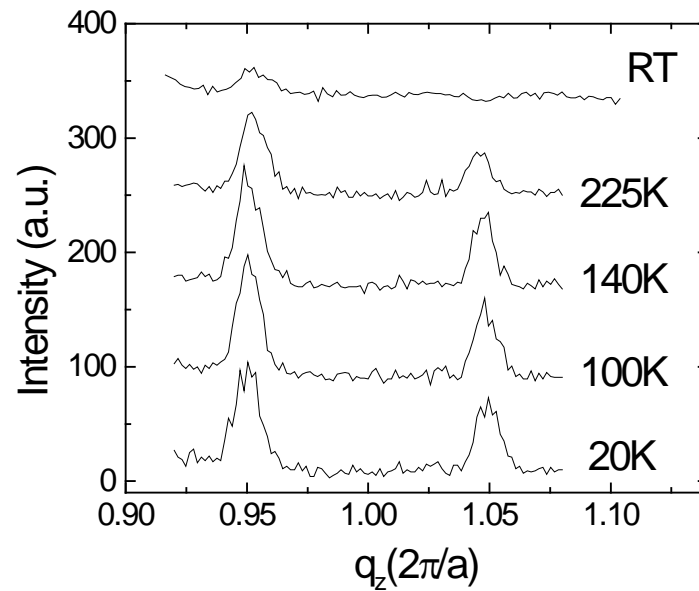


Fig. 4.2.28 The q_z -scan along $Cr(001)$ is shown. An out-of-plane directed T-SDW is formed below RT.

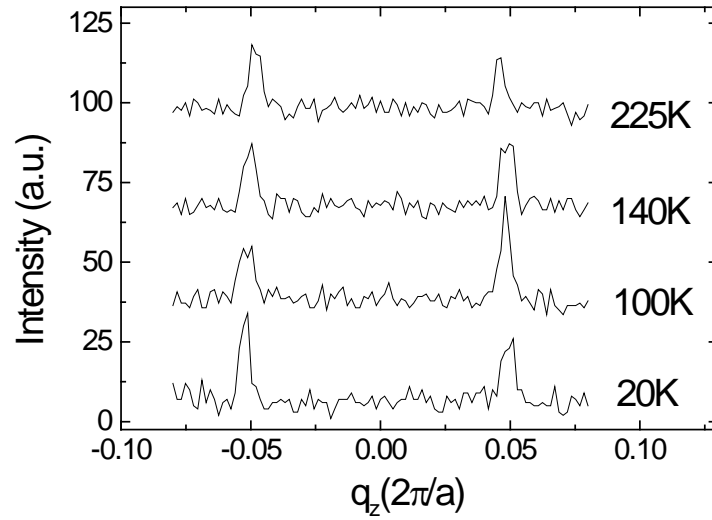


Fig. 4.2.29 The q_z -scans around $Cr(100)$ are shown.

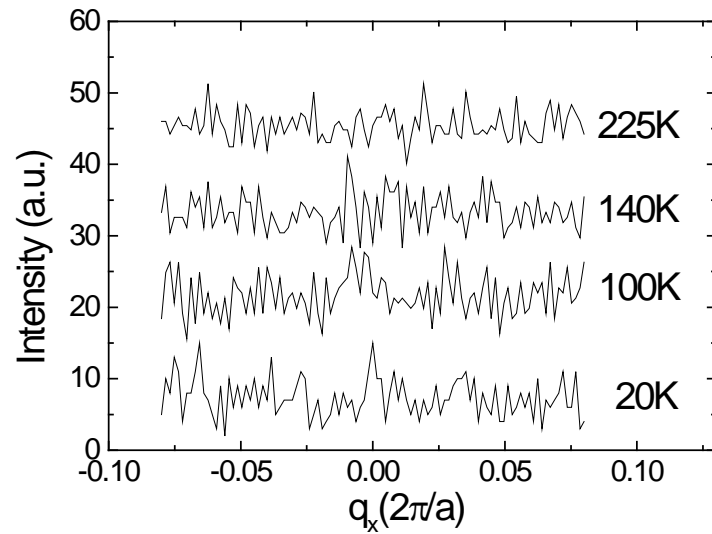


Fig. 4.2.30 Shows the q_x -scans along $Cr(001)$. The structure does not exhibit an in-plane SDW.

These measurements prove that an in-plane T-SDW does not exist and neither does an out-of-plane

polarized AF_0 state. The corresponding ω - 2θ scans along Cr(001) are shown in fig. 4.2.28. At RT there are no magnetic reflections. Below RT, two satellites $(0,0,1\pm\delta)$ show up proving the existence of a T-SDW having an out-of-plane Q vector. This state is stable between 20-200K. Additionally, in relationship to fig. 4.2.27 these results prove that there is no AF_0 state present in the whole measured temperature range.

Since in figure 4.2.28 a T-SDW is present, satellite $(1,0,\pm\delta)$ reflections can be expected if there is no extreme in-plane anisotropy. Figure 4.2.29 shows the corresponding q_z -scans around Cr(100). Indeed, two reflections show up at $(1,0,\pm\delta)$. The maximum intensity of these reflections is about half the value of the peaks in fig. 4.2.28. This $\frac{1}{2}$ ratio can be explained as mentioned in paragraph 2.3. Half of the present T-SDW is polarized along the $[100]$ ($(1,0,\pm\delta)$ reflections) while the other half along $[010]$ ($(0,1,\pm\delta)$ reflections), suggesting an in-plane isotropical behaviour. Nevertheless, one should keep in mind that an out-of-plane L-SDW contributes to these $(1,0,\pm\delta)$ satellites and can therefore not be excluded within the resolution of the measurement. The presence of a L-SDW is most probable at low temperatures. Finally, the q_x -scans along Cr(001) are shown in fig. 4.2.30. Since no reflections are present and an isotropical behaviour can be assumed, one can conclude that this sample does not exhibit an in-plane SDW.

In summary, the annealed sample exhibits only below RT a magnetic structure. The major present state is an out-of-plane T-SDW though minor L-SDW component cannot be excluded.

- **Magnetic field dependence**

As in the previous samples it is attempted to align the spins of the T-SDW perpendicular to the field. Therefore, a field parallel to the Cr[010] direction is applied. If the spins align, then the reflections at $(1,0,\pm\delta)$ should vanish. Figure 4.2.31 shows the $(1,0,\delta)$ peak as function of field measured at 200K. Comparing the zero field state and at the highest available field of 65 kOe one can perceive a certain decrease, which sets in around 30-45kOe.

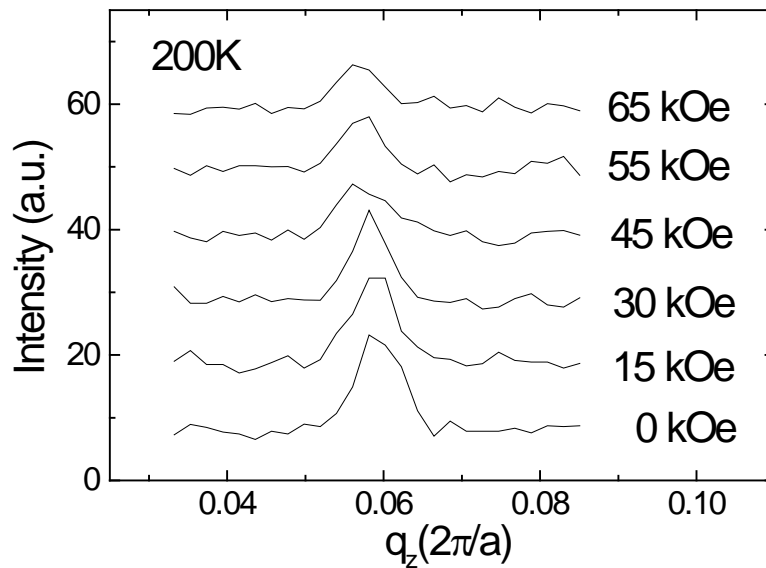


Fig. 4.2.31 The $(1,0,\delta)$ satellite shows a small decrease for a field applied along the [010] direction.

For obtaining better statistics, the angles are set on the maximum value of the peak followed by a field scan. In this way counting time can be gained as the number of points is reduced to one. Figure 4.2.31 shows the result for the $(1,0,\delta)$ satellite corrected for background. The obtained values are

normalized to the zero field state. A continuous decrease down to 50% at 65 kOe is observed. For a complete T-SDW state saturation can be expected at 80-140kOe.

Finally, the same curve is measured at 20K, see fig. 4.2.32. There is a similar decrease in polarization as seen at 200K. In addition the behaviour is more linear.

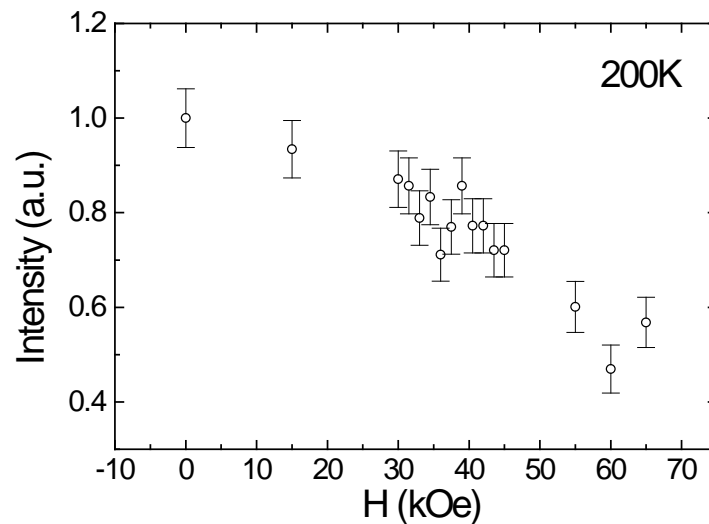


Fig. 4.2.31 The intensity of the $(1,0, \delta)$ peak taken at its maximum is measured as function of field. A decrease down to 50% of the intensity is observed.

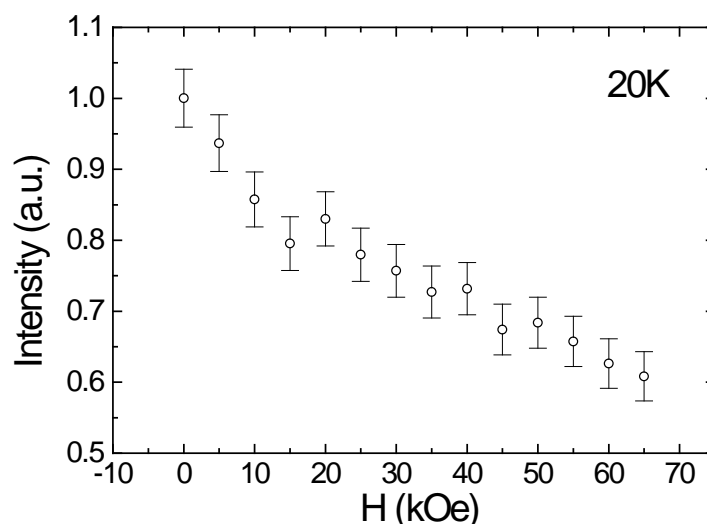


Fig. 4.2.32 The intensity of the $(1,0, \delta)$ peak taken at i 's maximum is measured as function of field at 20K. A decrease down to 60% of the intensity is observed.

- **Discussion**

At first instance a comparison with the unannealed state should be made. After annealing treatment, the AF_0 state has disappeared and the Néel temperature is situated near RT. Additionally, for all temperatures an abundant out-of-plane T-SDW having the spins in-plane is found. Furthermore, the preferential spin orientation is changed towards in-plane for the annealed sample. Magnetic field measurements show that the spins can be more easily rotated in the plane as from out-of-plane towards in-plane. Finally, the in-plane anisotropy is still much larger than in the case of bulk Cr since only 60% polarization is obtained at 65 kOe.

The vanishing of the AF_0 state upon annealing has been earlier observed and can be attributed to the improvement of the structural quality as the defect

concentration is reduced. This is in agreement with fact that the magnetic structure disappears at RT, close to the Néel temperature of bulk single crystalline Cr.

For explaining the origin of the out-of-plane orientation of the T-SDW the following suggestion is made. The vanishing of the AF_0 state and the improvement of the structure as observed from XRD proves that a significant structural relaxation occurred at higher temperatures. During cooling down the structure freezes, the atoms lose their mobility and a strain can occur between the substrate and the Cr if they have a different thermal expansion. At 1000 °C the deformation of MgO is 0.944% [Toull3] and only 0.685 % [Toull2] for Cr. An overview of these values taken from [Toull2, Toull3] is shown in table 4.2.2.

It is acceptable that this effect plays a role since the structural and the magnetic observations are in agreement with the expected deformation taken from the material constants. The out-of-plane lattice parameter is larger than the bulk suggesting a compression. In addition the observed in-plane orientation of the magnetic spins and the out-of-plane propagation of the T-SDW are in accord with such a deformation. And thirdly this deformation is expected from the material properties as can be seen in table. 4.2.2.

To be complete we mention that the elastic deformation coefficients for Cr ($C_{11} = 3.398 \cdot 10^{11}$ N/m², $C_{12} = 0.586 \cdot 10^{11}$ N/m²) and MgO ($C_{11} = 2.9708 \cdot 10^{11}$ N/m², $C_{12} = 0.9536 \cdot 10^{11}$ N/m²) are comparable.

Temperature(K)	$\Delta L/L_0$ MgO	$\Delta L/L_0$ Cr
25	-0.135	-0.098
50	-0.134	-0.098
100	-0.130	-0.091

200	-0.080	-0.051
293	0	0
400	0.128	0.075
500	0.255	0.159
600	0.380	0.254
700	0.518	0.354
800	0.656	0.460
900	0.800	0.570
1000	0.944	0.685
1200	1.244	0.931

Table 4.2.2 *The thermal expansion of Cr and MgO.*

4.2.8 Discussion

In order to shed light on the magnetism in thick Cr films the effect of epitaxial induced strains is studied. Depending on the type of substrate and the preparation conditions different strains are induced in the Cr layer. Although the apparent phase diagrams are complex and strongly different from the bulk single crystalline behaviour, a systematic behaviour that is in agreement with the observations of the group of Zabel [Sonn98, Böd99] is found. The orientation of the antiferromagnetic spins is strongly correlated to the deformation of the Cr unit cell. This behaviour is in agreement with the theoretical predictions from [Barak82]. The argument can hold for the observations by the group of Zabel since in their results also an out-of-plane orientation of the spins is observed together with an in-plane expansion of the lattice parameter of Cr. In our case the explanation remains without inconsistencies regarding the propagation of the I-SDW. Considering the type of I-SDW, transversal or longitudinal, no clear pattern can be discerned.

4.3 The magnetic structure of a Ni array

4.3.1 Introduction

This chapter deals with the magnetism in Ni arrays. Magnetic arrays exhibit interesting properties as is shown in paragraph 2.4. To study this in more systematic way a parallel investigation of a flat Ni film is carried out. The influence of the array structure on the magnetic properties is deduced by comparing the results for the thin film with the Ni array results.

Chapter 4.3.2 will deal with the preparation and the characterization of the structures. The magnetic structure is probed by MFM and MOKE, chapter 4.3.3, and the resistive properties, chapter 4.3.4. Finally the results are discussed in chapter 4.3.5.

4.3.2 Preparation and structural characterization

The growth of a Ni array is based on the technique sketched in fig. 4.3.1. First a double resist layer is spun on top of a Si/SiO₂ (5000Å) substrate. In this bilayer the array pattern is written using an electron beam, see fig. 4.3.1 a,b showing a section. The illuminated areas are developed so that the complementary structure, i.e. a resist mushrooms lattice, remains. Since it is the intention to monitor the resistive and the magnetic properties, two such patterns are introduced in the UHV chamber : a smaller piece (0.3*2 mm²) having contact leads for resistivity measurements and a

larger one (4*4 mm²) for magnetization measurements. Together with these resist patterns two empty SiO₂ substrates are mounted allowing a comparative investigation with a similar Ni thin film.

In the next step a Ni(350Å)/Ag(20Å) layer is evaporated at RT, 1*10⁻¹⁰ mbar and 0.3Å/s by MBE. After the deposition the structures are taken out and finally the resist is dissolved in a bath of boiling acetone, removing the resist mushrooms and leaving the Ni array behind.

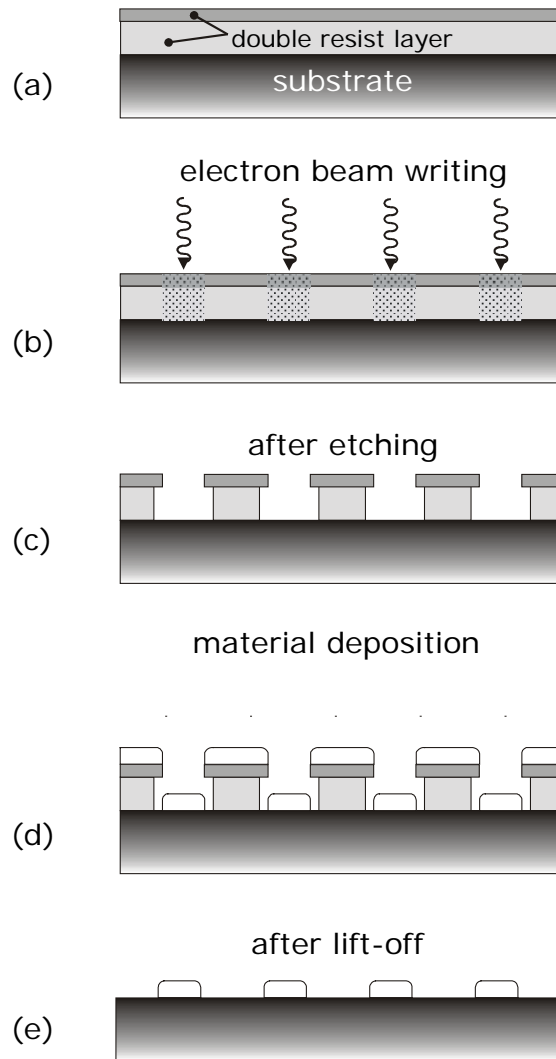


Fig. 4.3.1 The procedure to make microstructures is sketched. The microstructure is written in a double resist layer (a) and (b) using an electron beam. After development (c) a film is deposited (d). Finally, the resist with the superfluous material is removed during the lift-off procedure (e).

The structural characterization is performed by means of AFM and XRD. Figure 4.3.2 shows an AFM picture of the Ni array. The period of the structure is $1.4\ \mu\text{m}$ measured along the magnetic lines. The average width of the Ni lines is about $0.6\ \mu\text{m}$ and they are separated by a gap of $0.8\ \mu\text{m}$. Furthermore for a correct interpretation of the figure it is indispensable to mention that the height of the lines is $36\ \text{nm}$ which is a factor 20 smaller than the width. The structures should be regarded as much less high than wide.

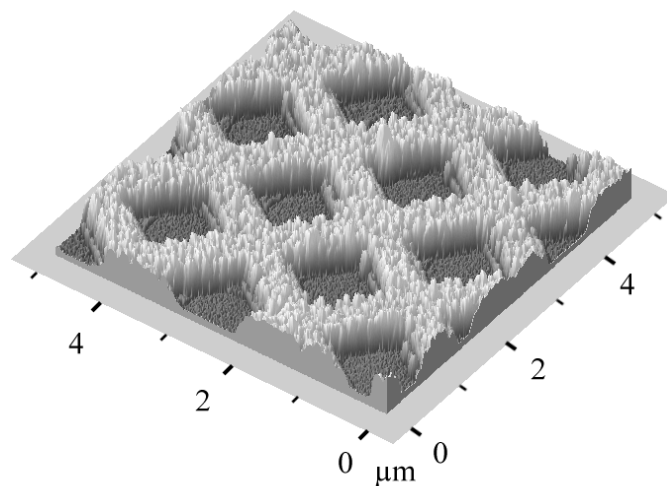


Fig. 4.3.2 Structural characterization of the Ni array. The picture shows a $5 \times 5\ \mu\text{m}^2$ area scanned by AFM. The height of the structure is 360\AA .

The thickness of the layer as determined from the low angle XRD diffraction measurements on the flat sample is 360\AA which is in good agreement with the nominal thickness. Information on the crystalline structure of Ni on amorphous SiO_2 is obtained from the high angle XRD measurements shown in fig. 4.3.3. From the substrate only the $\text{Si}(004)$

reflection at $q = 4.6 \text{ \AA}^{-1}$ can be observed. A Ni(111) reflection shows up at $q = 3.1 \text{ \AA}^{-1}$ and there is a small enhancement of the intensity at the Ni(002) position. Therefore the film is mainly (111) oriented. However the ω -scan around the Ni(111) reflection, present in the inset, shows only a decrease towards 50 cps within 6 deg while the background is about 5 cps. So there is a large spread on the (111) orientation and an epitaxy or texture can be excluded. Hence, no magnetic in-plane effects from the crystalline anisotropy should be expected.

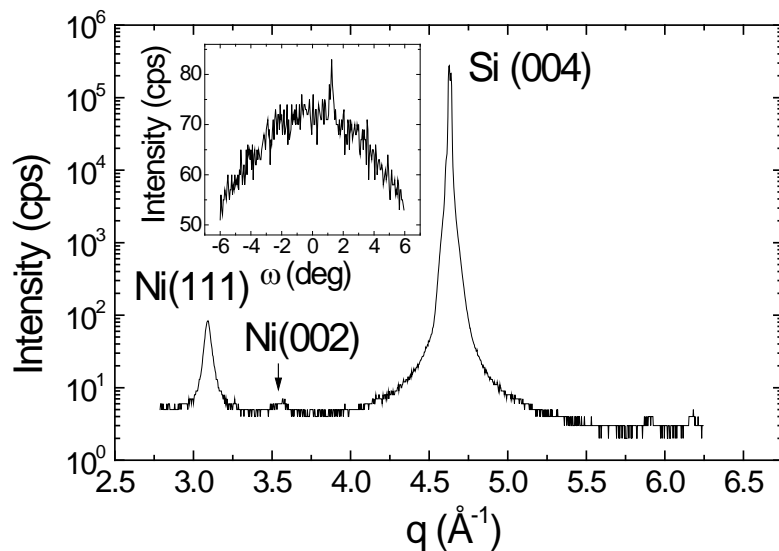


Fig. 4.3.3 The high angle XRD diffraction pattern from a flat Ni film on SiO_2 . Only the Ni(111) reflection is present. The ω -scan in the inset is taken around this Ni (111) reflection.

4.3.3 Magnetic characterization

For the magnetic characterization MFM and MOKE magnetization measurements are carried out. Figure 4.3.4 shows a $5 \times 5 \mu\text{m}^2$ MFM image from the Ni array. The array structuring is resulting from the

magnetic contrast and it shows that the array in figure 4.3.2 is magnetic. No domain structure is observed because the tip (Co larger coercivity) magnetizes the Ni (lower coercivity) array. The tip magnetizes the Ni and any domain structure will therefore vanish. Nevertheless, the MFM measurements show that the structure of fig. 4.3.4 is uniformly magnetic.

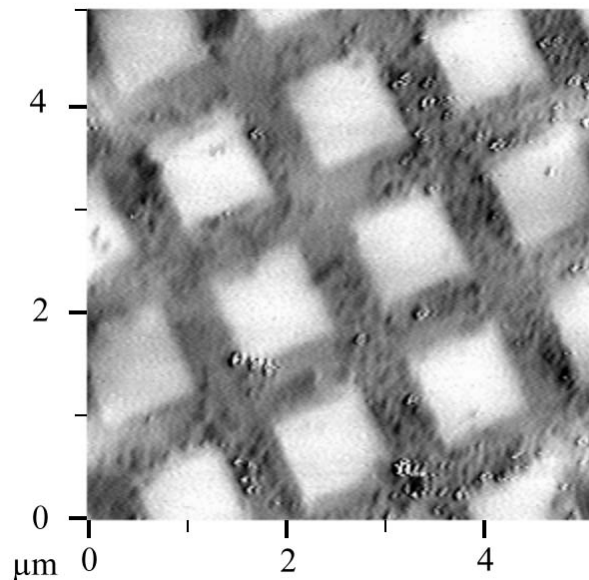


Fig. 4.3.4 A $5 \times 5 \mu\text{m}^2$ MFM image from the Ni array is shown. The magnetic signal corresponds with the Ni array proving it's magnetic nature.

Additional magnetic information related to the shape is obtained from MOKE measurements. In these measurements the field is directed in the plane of the sample. The in-plane direction of the field can easily be changed by rotating the sample. These experiments allow therefore to detect in-plane anisotropy features. Figure 4.3.5 shows the magnetization curve for the flat sample. The remanent magnetisation is quasi 100% and only a

small curvature is observed before the magnetisation changes sign. Secondly, saturation is achieved at 25 Oe . These characteristic magnetisation loops are typical for an easy axis behaviour proving that the magnetization is lying in the plane. Furthermore, no significant in-plane anisotropy is found, i.e. the loop remains the same for the field along other in plane directions.

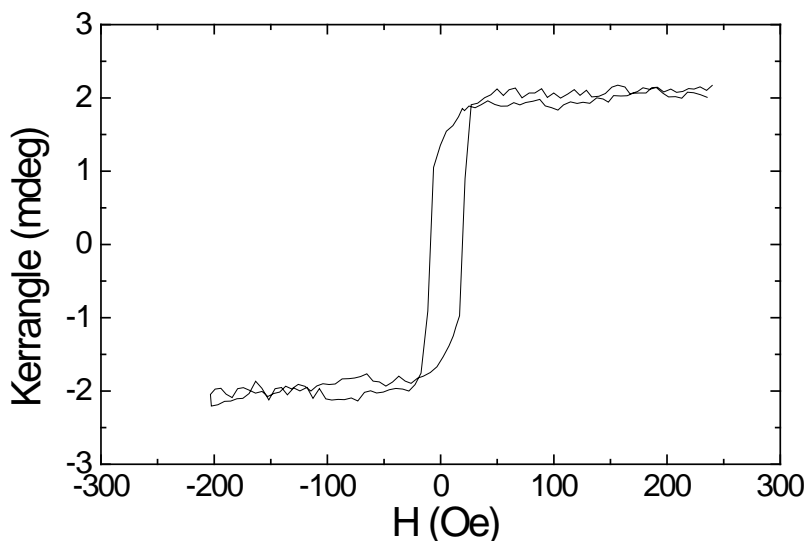


Fig. 4.3.5 The MOKE magnetization measurement is shown for the flat Ni sample. Saturation is obtained at 25 Oe and no in-plane anisotropy is observed.

The results for the Ni array are shown in fig. 4.3.6 and fig. 4.3.7. Figure 4.3.6 shows a MOKE hysteresis curve for such a measurement geometry that part of the Ni lines of the array consists are parallel to the field and the other part is perpendicular oriented to the field.

Starting from saturation, the magnetization shows a reversal decrease of 30% for fields below 500 Oe down to 100 Oe where the irreversible part of the loop starts. Within this hysteretical part of the

loop a further decrease till about 20 Oe is observed. At this point the MOKE signal increases and a peak arises. It is important to emphasize that this peak is not related to the component of the magnetization along the field.

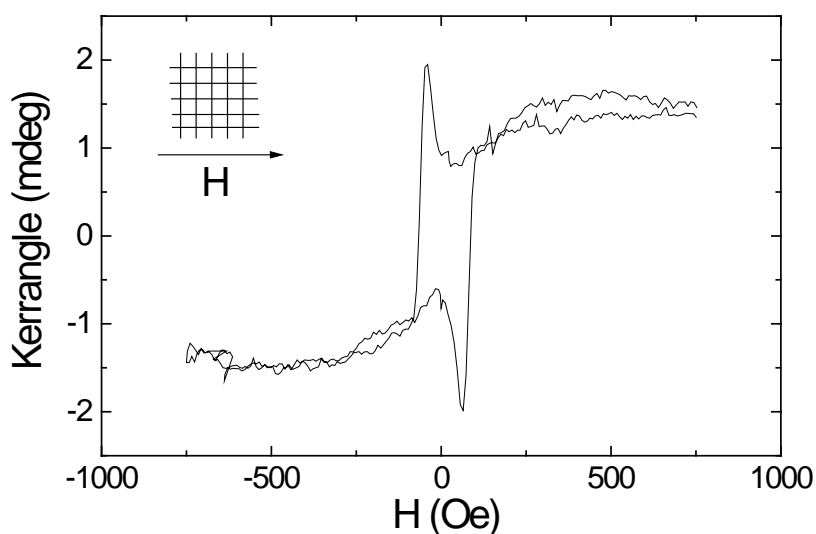


Fig. 4.3.6 The MOKE magnetization loop for a field parallel to the Ni array structure. The measurement geometry with respect to the array is shown in the upper left corner.

This behaviour is due to the presence of a non-zero component of the magnetization perpendicular to the field. It is typical for systems in a magnetic state around zero field and having an easy axis that is not parallel to the field. In this field region the magnetisation is directed along the easy axis. Increasing the field causes a uniform magnetization along the easy axis while for higher fields the magnetization starts to rotate. The MOKE is an indirect way to monitor the magnetisation along the field and is also sensitive to other in-plane components. Therefore these

artefacts show up in the MOKE measurements in contrast to direct methods like SQUID or Vibrating Sample Magnetometry or Alternating Gradient Magnetometry.

At the end, the magnetisation drops through coercivity at 76 ± 5 Oe and again saturation is obtained in a reversal way around 500 Oe.

Secondly, the MOKE curve for the angle between the Ni lines and the field being 45 deg is shown in fig. 4.3.7. The reversal curvature is absent for this geometry. In addition saturation is achieved at a lower field of 250 Oe and also the coercive field is a bit larger, 86 ± 5 Oe. If compared with fig. 4.3.6 it proves that the parallel/perpendicular geometry of fig. 4.3.6 is a harder direction for the magnetisation than the 45 degrees geometry in fig. 4.3.7. For a magnetisation measurement along an easy axis a rectangular shape of the loop is expected with a clear hysteresis since the reversal is mainly based on domain wall movement, see fig. 2.4. On the other hand, rotation of the magnetisation plays a role at higher fields in hard axis measurements. This process is reversible and in certain cases it can also shift the coercive field to zero. Therefore these measurements show that the parallel/perpendicular geometry is harder than the 45 deg geometry.

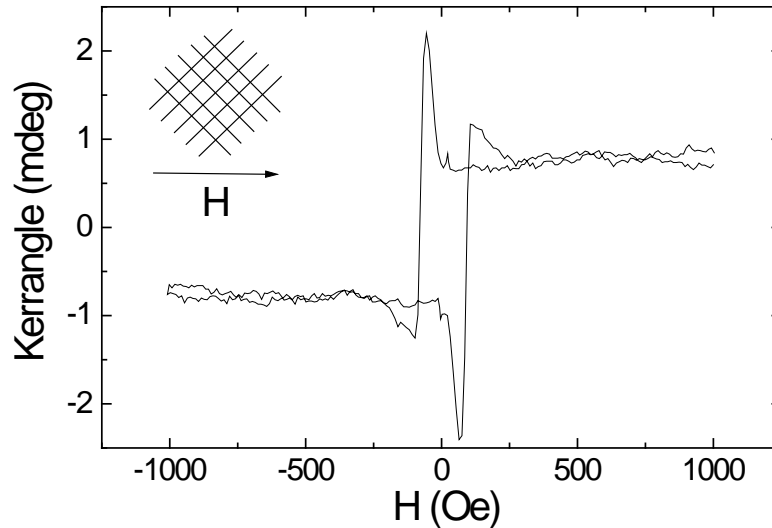


Fig. 4.3.7 The MOKE magnetisation curve in the field-array geometry as shown in the upper left corner. No reversal curvature is present.

The existence of such an effect is already mentioned in the theoretical calculations of Torres et al. [Tor99]. They studied 40 nm thick permalloy arrays. The width of the permalloy lines is $w = 640\text{nm}$ and they are separated by a distance d equal to a multiple of the width w . They showed that for larger separations, $d=2w$ or $d=3w$, a diagonal arrangement shows up at remanence. Thus it is plausible that the observed anisotropy originates from the demagnetisation effects around the holes.

Compared to the thin film, the hysteresis loops on the Ni array show a different behaviour. The introduction of the holes into the film causes an increase of the saturation and the coercive fields. Furthermore, during reversal a non-zero component of the magnetization directed perpendicular to the field is observed.

In conclusion it can be stated that the array structuring influences the magnetic behaviour of the Ni. Firstly, the saturation and the coercitive field is increased. Secondly a significant in plane anisotropy is induced. The array is harder to magnetize for a parallel/perpendicular alignment of the field and array than for the intermediate 45 deg geometry.

4.3.4 Resistivity properties

In paragraph 4.1.7 and 2.1.2 it is shown that features of the magnetic state can be probed using the AMR and the PSHE. These properties will be further exploited for both structures, the flat and array Ni samples. An $0.3 \times 2 \text{ mm}^2$ array with contact leads is used for the measurements. The pattern is oriented in such a way that the Ni lines are resp. parallel and perpendicular to the current path. Therefore it is reasonable to assume that the current is for the greater part carried by the Ni lines pointing along the current path. For the film, the pattern shown in fig. 3.14 is chemically etched using a solution of HCl (30%). Measurements are carried out at 5K, 50K, 150K, 215K and 280K. At each temperature the angle between the magnetic field and the current is varied over more than 90 deg in steps of about 10 deg. For each position a measurement is taken for an up and down sweep of the field, only the up sweep starting from negative field towards positive sign is shown unless otherwise stated. Apart from these measurements a set of calibration points like shown in fig. 4.1.20 is taken. The results for the AMR effect will be discussed in the first section and the PSHE in the second section. Each section will handle first the case of the reference film and secondly the array structure.

- **The Anisotropic Magnetoresistance**

The AMR curves for the thin Ni film will be discussed first. Figure 4.3.8 shows the result at 5K. The left axis shows the resistivity and the right axis is related to the saturation value of the resistivity. The saturation value depends on the angle between the field and the current as shown in formula (2.14).

The main feature in fig. 4.3.8 on which will focus is the resistivity around zero field. In saturation the magnetization is aligned along the field and the resistivity is $\rho_{//} = 9.34 \mu\Omega\text{cm}$ for the current parallel to the field and on the other hand $\rho_{\perp} = 9.21 \mu\Omega\text{cm}$ if they are perpendicular to each other. If the field is lowered, the magnetization changes because of rotation of the magnetization and the formation of variously oriented domains, thus affecting the resistivity. An extremal value is reached at the coercive field. At the coercive field the magnetization is zero and the value of the resistivity is a measure for the distribution of the magnetization with respect to the current direction. It can therefore be used as a tool for studying anisotropy.

Figure 4.3.8 shows that all curves tend towards a resistance value of about $9.28 \mu\Omega\text{cm}$ at zero field. Due to the resolution of the magnet (minimum step size of 10 Oe) it was not possible to measure more carefully this behaviour around zero field and it is unlikely that there is a single resistance value which is unique for all curves.

However, this bending towards an average resistivity value can be understood in the above mentioned framework. At the coercive field the magnetization is zero and the value of the resistivity is a measure for the distribution of the magnetization in the domains. The value of

9.28 $\mu\Omega\text{cm}$ is near the average and suggests an isotropic distribution of the magnetization in the demagnetised state with respect to the current direction, see also formula (2.16). The same set of measurements at 280K is shown in fig. 4.3.9. The resistivity at the coercive field is now slightly higher than the average of $\rho_{//} = 18.28 \mu\Omega\text{cm}$ and $\rho_{\perp} = 18.00 \mu\Omega\text{cm}$, meaning that more components are directed along the current path. Nevertheless, the effect is small and the error is relatively large. An overview for the resistivity at the coercive field for all measured temperatures is given in fig. 4.3.10. The value is normalized with respect to the $\rho_{//}$ and ρ_{\perp} , i.e. $\rho_{//} = 1$ and $\rho_{\perp} = 0$. The error bars are relatively large because they indicate the maximum and minimum measured value of the resistivity at the coercive field at a certain temperature. In the average the figure suggests an isotropic and temperature independent distribution of the magnetic components at the coercive field.

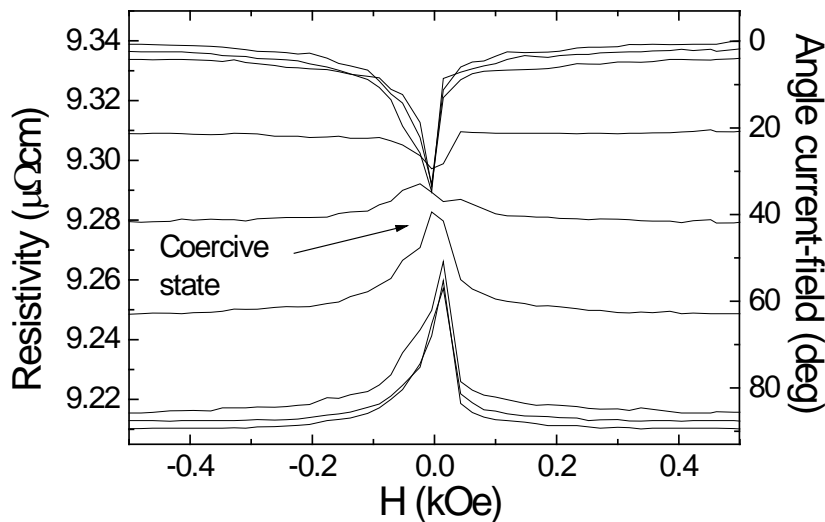


Fig. 4.3.8 The resistance as function of field for different angles between the current and the applied field at 5K for the Ni film.

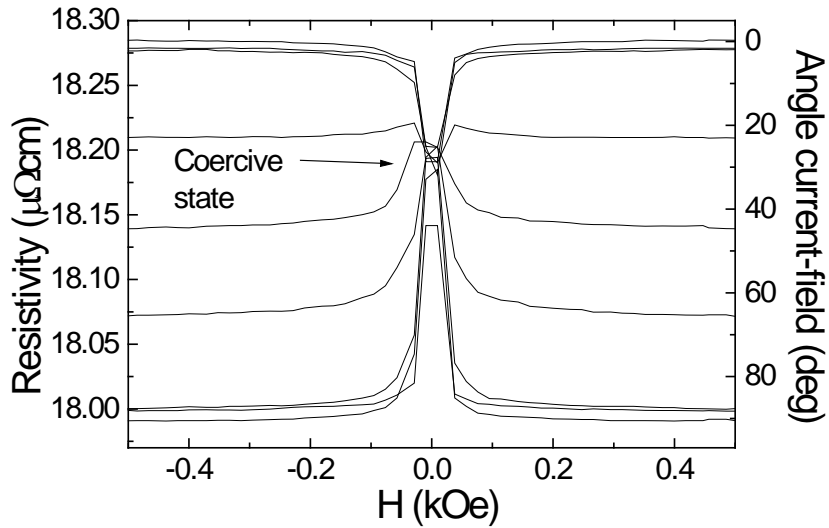


Fig. 4.3.9 The AMR measurements at 280K as function of field while varying the angle between the current and the field for the Ni film.

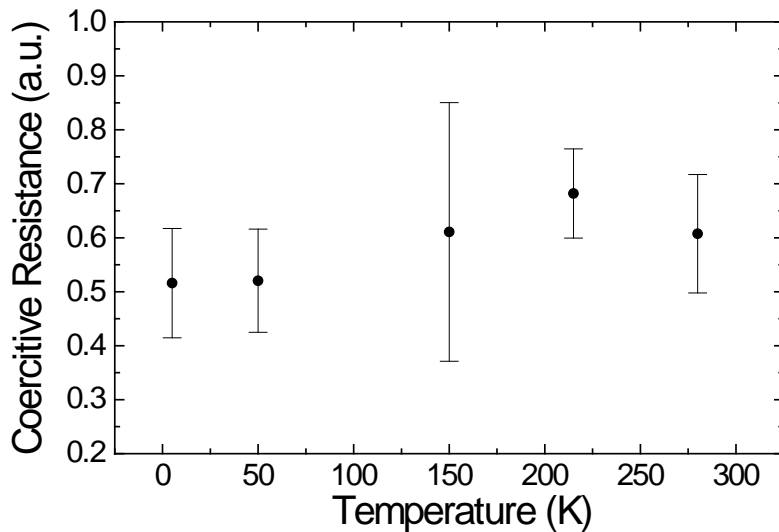


Fig. 4.3.10 The normalized resistivity at the coercitive field is shown as function of

temperature for the Ni thin film. The value varies around 0.5 which is the average of $\rho_{//}$ (1) and $\rho_{\perp}(0)$.

In the second step the same measurements are carried out on the Ni array. Figure 4.3.11 shows the AMR curves at 5K taken for various values of the angle between the field and the current path. The resistivity is a factor 2.7 higher than for the film. The reason is that due to the array structure the effective cross section for the current is reduced. Saturation is now obtained at a higher field value allowing a detailed study around coercivity. The figure shows that there a strong tendency towards a single resistivity value at coercivity for all curves, i.e. $\rho = 25.14 \mu\Omega\text{cm}$. This value is significantly below the average $\rho_{//}$ and ρ_{\perp} . It indicates that at the coercivity the majority of the magnetization is directed perpendicular to the current path. Additionally, these measurements suggests that there exists an angle, $\cong 65$ deg, under which the resistivity is independent on the magnetic state .

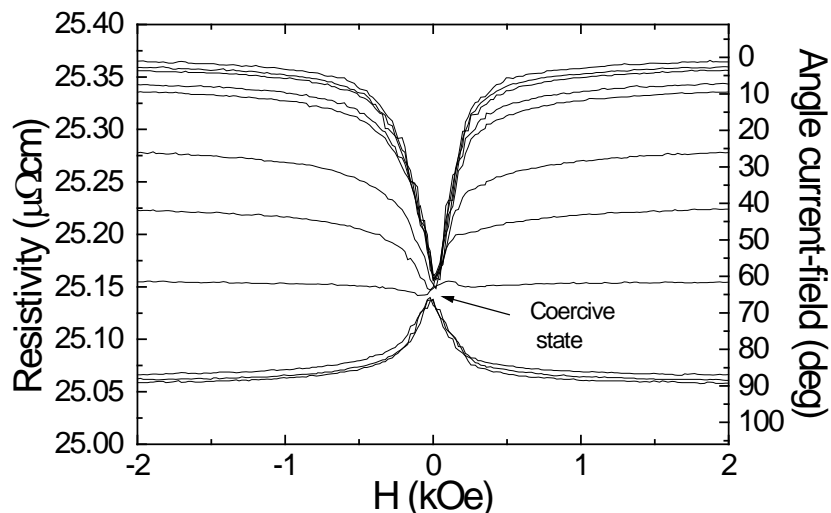


Fig. 4.3.11 *The AMR measurements at 5K for the Ni array are shown. There is a clear evidence for an uniform coercitive value of the resistivity, not depending on the magnetic history.*

The result for 280K is shown in fig. 4.3.12. The resistivity at coercivity is $50.88 \mu\Omega\text{cm}$ which is near the value of $\rho_{//} = 51 \mu\Omega\text{cm}$ ($\rho_{\perp} = 50.3 \mu\Omega\text{cm}$). Furthermore, the resistivity drops in a linear way for higher fields. The latter can be understood as resulting from suppression of the spin disorder resistivity by the field. This effect is only present at high temperatures and is related to fluctuations of the spins on an atomic scale. At zero temperature no fluctuations are present and the spins form a periodic potential so that the contribution to the resistivity is zero. At finite temperatures fluctuations are present and a spin disorder contribution to the resistivity shows up. These spin fluctuations can be suppressed by applying a field. The effect is not present in the thin film which suggested that the introduction of the array structures destabilizes the spin orientation on an atomic scale. Most likely this is a finite size effect because edge features can be neglected since the ratio between the height and width of the lines edges is large. If this effect is taken into account the difference in saturation field for the 0 deg and 90 deg measurement geometry is less clear.

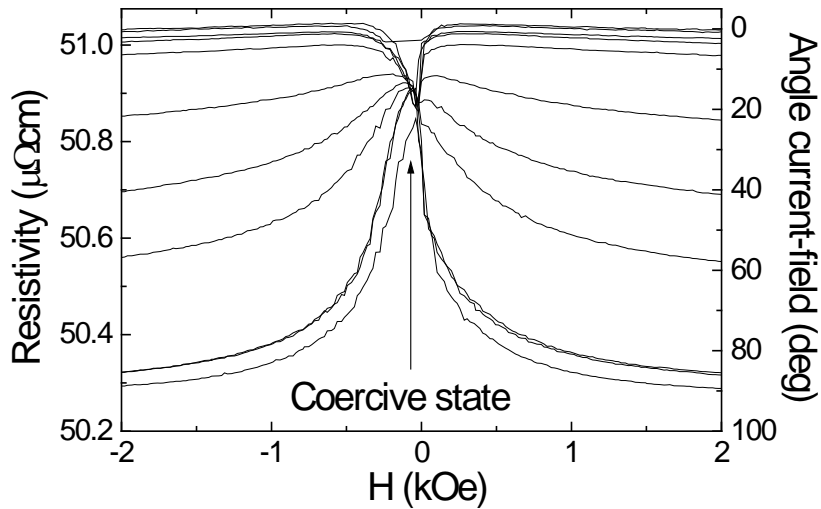


Fig. 4.3.12 The AMR curves at 280K for the Ni array.

Resuming both figures it can be stated that a significant temperature dependence of the resistivity at the coercive field is found. An overview for all temperatures is given in fig. 4.3.13. It shows that the fraction of the anisotropic resistivity at coercivity shifts from 0.3 towards 0.8 in the temperature interval off 5-280K. This temperature dependence is not observed in the thin Ni film.

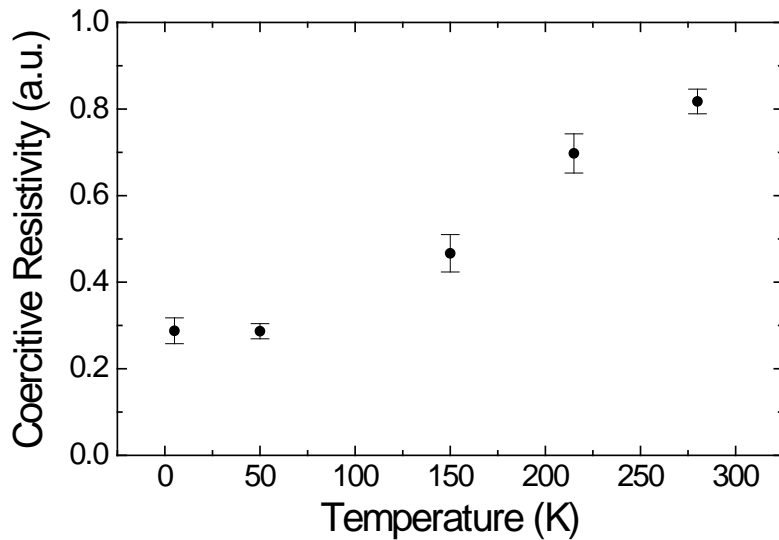


Fig. 4.3.13 *The resistivity at coercivity is shown for the Ni array as function of temperature. The value is normalized to $\rho_{//}$ and ρ_{\perp} for the corresponding temperature. A clear temperature dependence is observed.*

In conclusion there is a single value of the resistivity found at the coercitive field for the array structure. This value is not sensitive to the demagnetisation process since it is within good accuracy reached in all measurement geometries. It can therefore be assumed that this behaviour is related to a type of domain distribution. The array structure can affect the domain distribution via the shape anisotropy. Furthermore, an unquestionable temperature dependence is observed which is not present in the thin Ni film.

- **The Pseudo Hall effect**

The PSHE is simultaneously probed during the AMR measurements. At first instance the thin film behaviour will be enlightened. Secondly, the Ni array is discussed.

Figure 4.3.14 shows an overview of the results at 5K for the Ni film and the angle between the field and the current being -10° , 0° , 10° , 30° , 45° and resp. 90° deg. If the magnetisation is parallel or perpendicular to the current, the PSHE is zero. Therefore no deviation is found for 0° and 90° deg measurement.

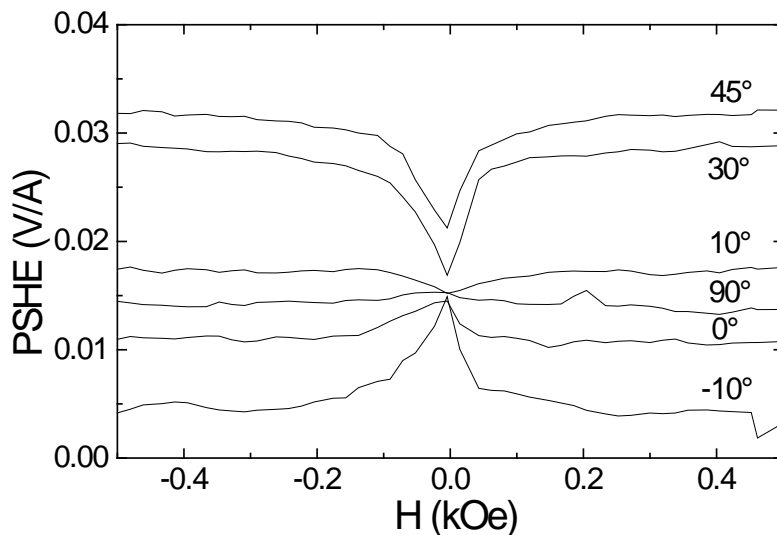


Fig. 4.3.14 The PSHE measurements for the Ni film at 5K. At the coercive field the PSHE vanishes.

On the other hand in agreement with equation (2.17) a maximum is obtained for 45° in the saturation region. If the field is decreased the PSHE vanishes for all curves. This can be interpreted in the following way. The PSHE effect only shows up if there is a component of the magnetisation directed along a direction having an angle of 45°

deg with respect to the current. Additionally, the PSHE has an opposite sign for opposite angles, see fig. 2.8. Therefore a zero PSHE suggests an isotropic distribution of the magnetisation with respect to the ± 45 deg axes.

The results for the Ni film at 280K are shown in fig. 4.3.15 and can be explained in the same way as for 5K. At coercivity no PSHE is measured and the saturation behaviour is understood via formula (2.17). The only difference is that at 280K the saturation field is smaller.

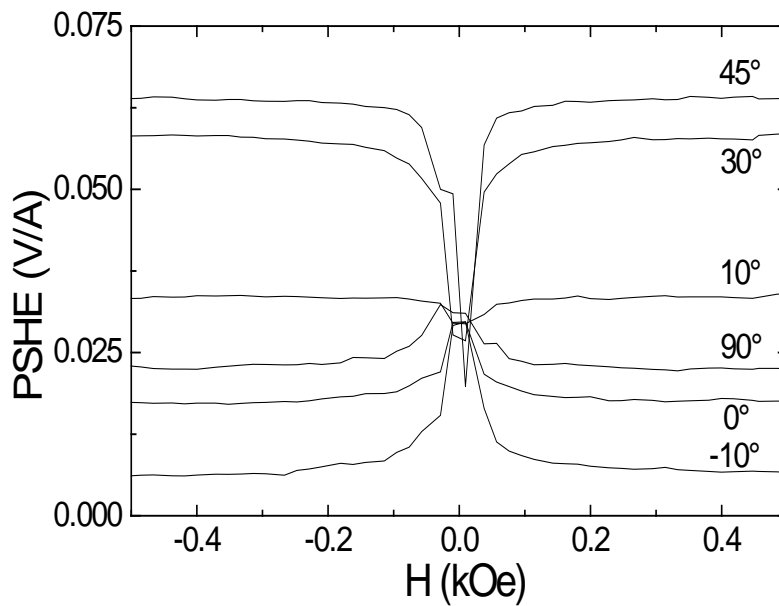


Fig. 4.3.15 The PSHE at 280K for the Ni thin film. The PSHE disappears when coercivity is reached.

In conclusion for the Ni thin film no special behaviour around the coercive field is found. Starting from the saturation value, the PSHE reaches zero at coercivity within the resolution of the experiments.

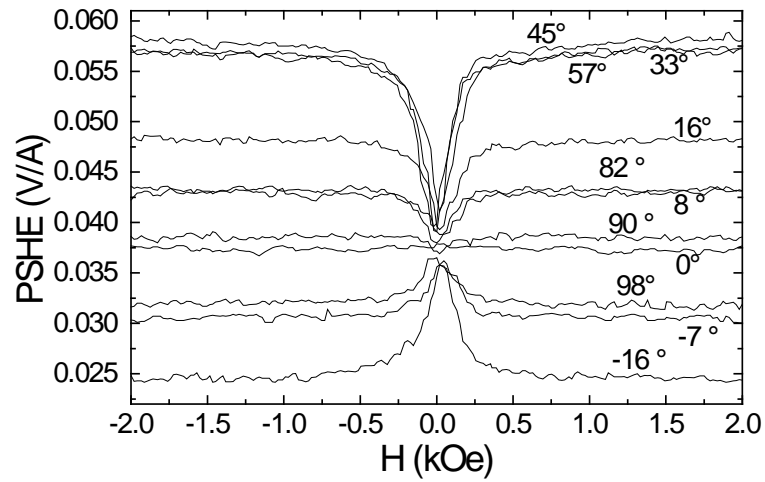


Fig. 4.3.16 The PSHE for the Ni array at 5K. On the average the behaviour is similar to that of the Ni film. Saturation occurs at a higher field.

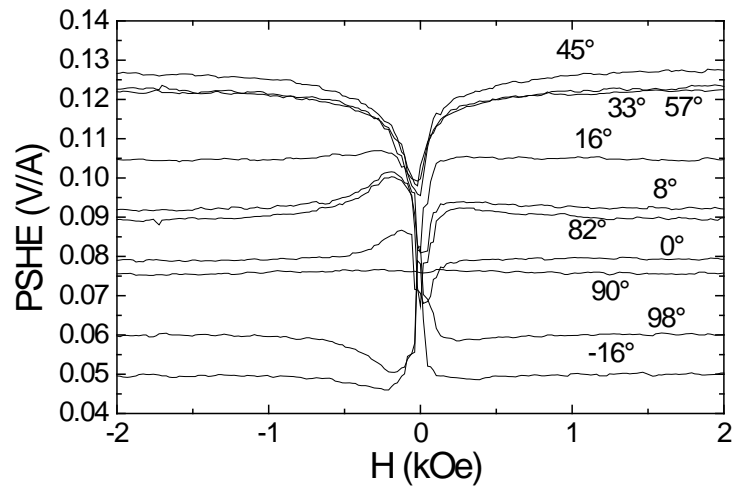


Fig. 4.3.17 The PSHE at 280K for the Ni array. An anisotropy shows up near the coercitive field.

The results for the array at 5K are shown in figure 4.3.16. Like in the AMR measurements, the field region for the switching of the magnetisation is now smeared out, allowing a more detailed analysis. Similar to the thin film these measurements show that near coercivity the PSHE vanishes so that the magnetisation is isotropically distributed around the ± 45 deg axes.

The results for the PSHE at 280K are shown in fig. 4.3.17. The behaviour is slightly different. For the angle between the current equal to 0, 8, 16, 82 deg an increase in PSHE is observed before zero field is reached. This enhancement reveals the presence of a preferential alignment along the intermediate 45 deg axis and is in agreement with the anisotropy observed in the MOKE measurements. If the angle is out of the 0-90 quadrant the opposite effect is found in accord with the sign of the PSHE.

4.3.5 Discussion

The magnetic properties of a sub micron Ni array have been studied. The structure is prepared using e-beam lithography and MBE evaporation. A flat Ni film is simultaneously deposited to serve as a reference. Structural characterization is carried out using XRD and AFM. The magnetic properties are investigated by MFM, MOKE, the AMR and the PSHE effect. The MOKE measurements show that the saturation field for the magnetisation is increased in the Ni array. Furthermore, an in-plane anisotropy related to the shape of the sample is found. The geometry with the magnetic field parallel/perpendicular to the Ni lines acts as a hard axis compared to the intermediate geometry along a 45 deg axis. The presence of this easy behaviour along the intermediate axis is confirmed by the PSHE observations. Finally, the AMR

measurements show a strong temperature behaviour of the distribution of the magnetisation at the coercive state. At high temperatures the magnetisation is for the greater part aligned along the current path. At low temperatures, the majority of the magnetisation is oriented perpendicular to the current path. This coercive state is independent from the history of the sample and suggests a regular distribution of the magnetic domains.

Chapter 5

Conclusions

In this work magnetic properties of layered structures and arrays have been studied. All structures are produced by MBE and if necessary a lateral patterning is obtained using optical - or electron beam lithography. Using three model systems, we have aimed to clarify the role of different anisotropy contributions to the observed magnetic properties.

The first system investigated are the antiferromagnetically coupled Fe/Cr multilayers. After the preparation, the epitaxial $\text{MgO}(001)/[\text{Fe}(26\text{\AA})/\text{Cr}(13\text{\AA})]_{20}$ composition is confirmed using X-ray diffraction. The presence of antiferromagnetically coupled domains is determined from MOKE magnetization measurements and the related GMR effect is observed in magnetoresistivity measurements. At first instance, the magnetization process is studied using unpolarized neutron reflectometry. For the field along the easy axis the magnetic structure remains coherent during magnetization and the observed large size of the domains ($>4 \mu\text{m}$) is confirmed by the MFM measurements. Polarized neutron reflectometry revealed that the magnetization in the Fe layers is lying along one of the two in-plane easy Fe[100] axes. Furthermore, only one of the two possible sequences of antiferromagnetic alternation is observed. The polarized neutron

reflectivity measurements prove that mainly one domain type is present. If a field is applied parallel to the magnetization direction, the spins flop towards perpendicular to the field. Such a spin flop transition has been observed in uniaxial systems and is a reversible process. Due to the fourfold crystal anisotropy in our case and the single domain nature of the sample an irreversible version of this phenomenon could be observed. Since the initial and the final state are well known, it is attempted during further experiments to obtain more information on the nature of the transition. Two models of how the transition can occur have been proposed. The first is a mechanism based on single domain Fe layers, the interlayer domain wall model. The second model is a mechanism based on domain walls within the Fe layers nl. the intralayer domain wall mechanism. MOKE -, SQUID, resistivity and Kerr microscopy are carried out to elucidate the nature but no decisive argument to prefer or to reject one of the two models. Finally, in collaboration with the group of Bottyan [Bottyan] Mössbauer reflectometry and simulations are carried out to enlighten this spin flop transition. The simulations based on the experimental results predict the spin flop field with a good accuracy.

Secondly, thick (5000Å) epitaxial Cr films have been studied. Single crystalline *bulk* Cr is an antiferromagnet below 311K. In contrast, the phase diagrams for Cr *films* are quite distinct and several anisotropic features have been observed. The underlying reason for this behaviour is not yet properly understood and therefore different substrates and preparation conditions are used to gain more insight in the problem. The chromium film grown directly on MgO(001) exhibits an AF₀ structure due to defects and switches to an in-

plane T-SDW below 200K. The antiferromagnetic spins are oriented out of the plane. This anisotropical behaviour is related to the deformation of the Cr unit cell as was predicted theoretically [Barak82]. Capping the Cr layer with an Fe layer does not alter the phase diagram strongly. The T-SDW remains in the plane while the AF_0 reappears at the lowest measured temperature of 20K. At this temperature the in-plane T-SDW has vanished while an in-plane L-SDW has emerged.

Since both observations are in reasonable agreement with the theory of the deformed Cr unit cell, a third Cr film was grown on a thick Au/Cr multilayer buffer. The thick buffer permits a relaxation of the strains induced by the substrate and, secondly, the lattice of Au matches laterally quasi perfect with Cr so that strain effects are reduced, as can be seen from the out of plane Cr lattice parameter determined from XRD measurements. The magnetic phase diagram is in accord with this observation since the outspoken spin anisotropy is lost and the AF_0 phase is diminished.

Finally, the uncapped Cr film on MgO was annealed. The annealing treatment causes a orientation of the spins in the film plane, in contrast to the unannealed state. In addition the Cr out-of-plane lattice parameter is shifted towards a value larger than the bulk value. This compression of the Cr unit cell is assumed to be related to the difference in thermal expansion between Cr and MgO. Such an effect is plausible since a significant relaxation occurred because the AF_0 state, which is related to defects, disappeared after annealing.

Summarizing this section, it can be concluded that a correlation was found between the anisotropy in

the magnetic state of the epitaxial Cr film and the substrate-induced deformation of the Cr matrix.

In the last chapter a Ni array was investigated to reveal the role of the shape anisotropy. The array consists of a 350Å thick Ni film capped with a 20Å Ag layer having a square array of $0.8 \times 0.8 \mu\text{m}^2$ square holes in it that are 0.6 μm separated. For reference, an unpatterned Ni film was studied simultaneously. Structural characterization is carried out by XRD and AFM. The magnetic properties are at first instance investigated with MFM and MOKE. The MOKE measurements show that in the patterned film an easy magnetization axis shows up under an angle of 45 degrees with respect to the square hole lattice. This type of anisotropy is confirmed by the PSHE measurements. Secondly, the AMR measurements show a change in the domain structure in the array as function of temperature. Near RT most of the magnetization is lying along the current path while for low temperatures the magnetization is mainly oriented perpendicular to the current path.

In general it can be stated that the correlation between the structure and the magnetic properties in multiple systems is investigated using anisotropy related mechanisms. Due to the fourfold crystal anisotropy in the antiferromagnetically coupled Fe/Cr layers, a new type of spin flop transition is observed. For the Cr films, the anisotropical behaviour of the antiferromagnetic spins is related to the epitaxial induced strains. Finally, a hole array in a Ni film induces a magnetic shape anisotropy in these films.

References

- [Akul29] N.S. Akulov, Z. Physik 57, 249 (1929); **ibid.** 69, 78 (1931)
- [Aliev97] F.G. Aliev, E. Kunnen, K. Temst, K. Mae, G. Verbanck, J. Barnas, V.V. Moshchalkov, Y. Bruynsereade, Phys. Rev. Lett **78**, 134 (1997)
- [Ank97] J.F. Ankner, H. Kaiser, A. Schreyer, Th. Zeidler, H. Zabel, M. Schäfer, and P. Grünberg, J. Appl. Phys. **81**, 3765 (1997)
- [Arrot66] A. Arrot in Magnetism edited by G. Rado and Suhl vol. IIb, Chapter 4 Antiferromagnetism in metals, 295, (Academic Press, New York 1966)
- [AV98] We would like to thank André Vantomme and his group from Instituut voor Kern- en Stralingsfysica, KULeuven, Belgium, for the collaboration in studying the Cr films using RBS.
- [Bacon61] G.E. Bacon, Acta Cryst. **14**, 823 (1961)
- [Bacon69] G.E. Bacon and N. Cowlam, J. Phys. C, **2**, 238 (1969)

[Bacon75] G.E. Bacon, Neutron Diffraction (Clarendon Press, Oxford 1975)

[Bai88] M.N. Baibich, J.M. Broto, A. Fert, F. Nguyen Van Dau, F. Petroff, P. Etienne, G. Creuzet, A. Friederich, and J. Chazelas, Phys. Rev. Lett. **61**, 2472 (1988)

[Barak82] Z. Barak and Q.B. Walker, J. Phys. F **12**, 483 (1982)

[Bast66] T.J. Bastow and R. Street, Phys. Rev. **141**, 510 (1966)

[Boeck99] J. de Boeck and G. Borghs, Physics World, April 1999, 27

[Boeve99] H. Boeve, J. Das, C. Bruynseraede, J. De Boeck and G. Borghs, J. Appl. Phys. **85**, 4779 (1999)

[Bottyan] We would like to thank the following people for their collaboration in studying the spin flop transition :

Bottyan Laszlo, Nagy Denes Lajos and Major Marton, KFKI Research Institute for Particle and Nuclear Physics, Budapest, Hungary; Johan Dekoster, Johan Meererschaut and M. Rots, Instituut voor Kern- en Stralingsfysica, KULeuven, Belgium.

[Bott98] L. Bottyan, J. Dekoster, L. Déak, A. Q.R. Baron, S. Degroote, R. Moons, D. L. Nagy, and G. Langouche, Hyperfine Interactions **113**, 295 (1998)

[Böd97] P. Bödeker, P. Sonntag, A. Schreyer, and H. Zabel, J. Appl. Phys. **81**, 5247 (1997)

[Böd98] P. Bödeker, A. Hucht, A. Schreyer, J. Borchers, F. Güthoff, and, H. Zabel, Phys. Rev. Lett. **81**, 914 (1998)

- [Böd98b] P. Bödeker, A. Schreyer, P. Sonntag, C. Sutter, G. Grübel, R. Günther, and H. Zabel, *Physica B* **248**, 115 (1998).
- [Böd99] P. Bödeker, A. Schreyer, and H. Zabel, *Phys. Rev. B* **59**, 9408 (1999)
- [Brin94] B. Briner and M. Landolt, *Phys. Rev. Lett.* **94**, 340 (1994)
- [Broe91] F.J.A. den Broeder, W. Hoving and P.J.H. Bloemen, *J. Magn. Magn. Mater.* **93**, 562 (1991)
- [Bürg98] D.E. Bürgler, D.M. Schaller, C.M. Schmidt, F. Meisinger, J. Kroha, J. McCord, A. Hubert, and H.-J. Güntherodt, *Phys. Rev. Lett.* **80**, 4983 (1998)
- [Cam82] I.A. Campbell and A. Fert, in *Ferromagnetic Materials vol. 3* edited by E.P. Wohlfarth, Chapter 9, *Transport Properties of Ferromagnets*, 747, North-Holland Publishing Company (1982)
- [Chamb91] D.D. Chambliss, R.J. Wilson and S. Chiang, *Phys. Rev. Lett.* **66**, 1721 (1991)
- [Chu97] S.G. Chung, *J. Phys. : Condensed Matter* **9**, L219 (1997)
- [Chumakov99] A.I. Chumakov, L. Niesen, D.L. Nagy, E.E. Alp, *Hyp. Int.* **123-124**, 427 (1999)
- [Con92] J. Evetts, *Concise Encyclopedia of Magnetic and Superconducting materials*, Pergamon Press (1992)
- [Cow97] R.P. Cowburn, A.O. Adeyeye and J.A.C. Bland, *Appl. Phys. Lett.* **70**, 2309 (1997)

- [Cui99] B. Cui, W. Wu, L. Kong, X. Sun, and S.Y. Chou, *J Appl. Phys.* **85**, 5534 (1999)
- [Cul72] B.D. Cullity, *Introduction to Magnetic Materials*, Addison-Wesley Publishing Company, Menlo Park, California (1972)
- [Dan99] A.L. Dantas and A.S. Carriço, *Phys. Rev. B* **59**, 1223 (1999)
- [Dao] N. Dao, S.R. Homer, and S.L. Whittenburg, *J. Appl. Phys.* **86**, 3262 (1999)
- [Déak96] L. Déak, L. Bottyan and D.L. Nagy, and H. Spiering, *Phys. Rev. B* **53**, 6158 (1996)
- [Dem98] S. Demuynck, J. Meersschaut, J. Dekoster, B. Swinnen, R. Moons, A. Vantomme, S. Cottenier, and M. Rots, *Phys. Rev. Lett.* **81**, 2562 (1988)
- [Det99] J.M. De Teresa, A. Barhélémy, A. Fert, J.P. Contour, R. Lyonnet, F. Montaigne, P. Seneor, and A. Vaurès, *Phys. Rev. Lett.* **82**, 4288 (1999)
- [Dong97] Dongqi Li, J. Pearson, S.D. Bader, E. Vescovo, D.-J. Huang, P.D. Johnson, and B. Heinrich, *Phys. Rev. Lett.* **78**, 1154 (1997)
- [Dool85] L.R. Doolittle, *Nucl. Inst. Meth.* **B9**, 344 (1985)
- [Ebels97] U. Ebels, A.O. Adeyeye, M. Gester, C. Daboo, R.P. Cowburn, and J.A.C. Bland, *J. Appl. Phys.* **81**, 4724 (1997)
- [Erw86] R.W. Erwin, J. Bochers, M.B. Salamon, S. Sinha, J.J. Rhyne, J.E. Cunningham, and C.D. Flynn, *Phys. Rev. Lett.* **56**, 259 (1986)

[Evoy20] S. Evoy, D.W. Carr, L. Sekaric, Y. Suzuki, J.M. Parpia, and H.G. Craighead, J. Appl. Phys. **87**, 404 (2000)

[Faw88] E. Fawcett, Rev. of Mod. Phys. **60**, 209 (1988)

[Faw94] E. Fawcett, H.L. Alberts, V. Yu. Galkin, D.R. Noakes, and J.V. Yakhmi, Rev. Mod. Phys. **66**, 25 (1994)

[Fedd66] P.A. Fedders, and P.C. Martin, Phys. Rev. **143**, 245 (1966)

[Fer99] P.H. Dedericks and P. Grünberg, Magnetische Schichtsysteme, Vorlesungsmanuskripte. 30 Ferienkurs des Instituts für Festkörperforschung 1999, Forschungszentrum Jülich GmbH Institut für Festkörperforschung (1999)

[Fel93] G.P. Felcher, Physica B **192**, 137 (1993)

[Felcher94] G.P. Felcher, Physica B **198**, 150 (1994)

[Fey77] R. P. Feynman, R. B. Leighton, M. Sands, The Feynman Lectures on Physics vol. II, Addison-Wesley Publishing Company, Menlo Park, California (1977)

[Fuch97] P. Fuchs, U. Ramsperger, A. Vaterlaus, and M. Landolt, Phys. Rev. B **55**, 12546 (1997)

[Full95] E.E. Fullerton, K.T. Riggs, C.H. Sowers, S.D. Bader, and A. Berger, Phys. Rev. Lett. **75**, 330 (1995)

[Full96] E.E. Fullerton, S.D. Bader, and J.L. Robertson, Phys. Rev. Lett. **77**, 1382 (1996)

[Full96b] E.E. Fullerton, S. Adenwella, G.P. Felcher, K.T. Riggs, C.H. Sowers, S.D. Bader, and J.L. Robertson, Physica B **221**, 370 (1996)

[Grün86] P. Grünberg, R. Schreiber, Y. Pang, M.B. Brodsky, and H. Sowers, Phys. Rev. Lett. **57**, 2442 (1986)

[Grün99a] Shi-shen Yan, R. Schreiber, F. Voges, C. Osthöver, and P. Grünberg, Phys. Rev. B **59**, R11 641 (1999)

[Grün99b] P. Grünberg, in Magnetische Schichtsysteme, Vorlesungsmanuscripte 30 Ferienkurs des Instituts für Festkörperforschung 1999 edited by P.H. Dedericks and P. Grünberg, Chapter B9 Zwischenschichtaustauschkopplung : Phänomenologische Beschreibung, Materialabhängigkeit, Forschungszentrum Jülich GmbH Institut für Festkörperforschung (1999)

[Hagin99] C. Haginoya, S. Heike, M. Ishibashi, K. Nakamura, K. Koike, T. Yoshimura, J. Yamamoto, and Y. Hirayama, J. Appl. Phys. **85**, 8327 (1999)

[Halp39] O. Halpern and, M.H. Johnson, Phys. Rev. **55**, 898 (1939)

[Hanson99] M. Hanson, C. Johansson, B. Nilsson, P. Isberg and R. Wäppling, J. Appl. Phys. **85**, 2793 (1999)

- [Har80] W.A. Harrison, *Electronic Structure and the properties of Solids*, W.H. Freeman and company, San Fransisco (1980)
- [Hei94a] B. Heinrich and J.A.C. Bland, *Ultrathin Magnetic Structures I*, Springer-Verlag Berlin (1994)
- [Hei94b] B. Heinrich and J.A.C. Bland, *Ultrathin Magnetic Structures II*, Springer-Verlag Berlin (1994)
- [Heij99] P.A.A. van der Heijden, C.H.W. Swüste, W.J.M. de Jonge, J.M. Gaines, J.T.W.M. van Eemeren, and K.M. Schep, *Phys. Rev. Lett.* **82**, 1020 (1999)
- [Himp98] F.J. Himpfel, J.E. Ortega, G.J. Mankey, R.F. Willis, *Advances in Physics* **47**, 511 (1998)
- [Hol94] P. Holody, L.B. Steren, R. Morel, A. Fert, R. Loloee and P.A. Schroeder, *Phys. Rev. B* **50**, 12999 (1994)
- [Hsu97] S.Y. Hsu, A. Barthélémy, P. Holody, R. Loloee, P.A. Schroeder, and A. Fert, *Phys. Rev. Lett.* **78**, 2652 (1997)
- [Jac75] J.D. Jackson, *Classical Electrodynamics*, John Wiley & Sons, New York (1975)
- [Jia97a] Y. Q. Jia, L. Kong, R. C. Shi and S. Chou, *J. Appl. Phys.* **81**, 5475 (1997)
- [Jia97b] Y.Q. Jia and S. Chou, *J. Appl. Phys.* **81**, 5461 (1997)
- [Koeh66] W.C. Koehler, R. M. Moon, A.L. Trego and A.R. Mackintosh, *Phys. Rev.* **151**, 405 (1966]

- [Koel99] D.D. Koelling, Phys. Rev. B **59**, 6351 (1999)
- [Kohl97] J. Kohlhepp, M. Valkier, A. van der Graaf, F.J.A. den Broeder, Phys. Rev. B **55**, R696 (1997)
- [Kun99] Kunitomo Hirai, Phys. Rev. B **59**, R6612 (1999)
- [Lide98] D.R. Lide, Handbook of Chemistry and Physics 79th edition, 1998-1999, (CRC Press London, 1998)
- [Lomer62] W.M. Lomer, Proc. Phys. Soc. **80**, 489 (1962)
- [Loucks65] T.L. Loucks, Phys. Rev. **139**, A1181 (1965)
- [Malkinski99] L.M. Malkinski, J.-Q Wang, C.T. Seip, J. Wiemann and J.B. Wiley, J. Appl. Phys. **85**, 4471 (1999)
- [Maj86] C.F. Majkrzak, J.W. Cable, J. Kwo, M. Hong, D.B. McWhan, Y. Yafet, J. W. Waszczak, and C. Vettier, Phys. Rev. Lett. **56**, 2700 (1986)
- [Major] <http://frodo.rmki.kfki.hu/~major/eddy/graph2/flip.gif>.
- [Martin98] J.I. Martin, J. Nogués, I.K. Schuller, M.J. Van Bael, K. Temst, C. Van Haesendonck, V.V.Moshchalkov and Y. Bruynseraede, Appl. Phys. Lett. **72**, 255 (1998)
- [Mathieu97] C. Mathieu, C. Hartmann, M. Bauer, O. Buettner, S. Riedling, B. Roos, S.O. Demokritov, H. Hillebrands, B. Bartenlian, C. Chappert, D. Decanini, F. Rousseaux, E. Cambril, A. Müller, B.

Hoffmann, and U. Hartmann, Appl. Phys. Lett. **70**, 2912 (1997)

[Matt90] J. Mattson, B. Brumitt, M.B. Brodsky, and J. B. Ketterson, J. Appl. Phys. **67**, 4889 (1990)

[Meer95] J. Meersschaut, J. Dekoster, R. Schad, P. Beliën and M. Rots, Phys. Rev. Lett. **75**, 1638 (1995)

[Meer98] J. Meersschaut, J. Dekoster, S. Demuynck, S. Cottenier, B. Swinnen and M. Rots, Phys. Rev B **57**, R5575 (1998)

[Mich99] C. Micheletti, R.B. Griffiths, and J.M. Yeomans, Phys. Rev. B **59**, 6239 (1999)

[Mit65] T. Mitsui and C.T. Tomizuka, Phys. Rev. **137**, A564

[Möller96] F.A. Möller, O.P. Magnussen, and R.J. Behm, Phys. Rev. Lett. **77**, 5249 (1996)

[Mosh97] V.V. Moshchalkov, E. Kunnen, K. Temst, A. Hoser in BENSFC experimental reports 1997 edited, by Y. Kirschbaum and R. Michaelsen, 114, Berlin Neutron Scattering Center (1998)

[Mott36] N.F. Mott, Proc. Roy. Soc. **A 153**, 699 (1936)

[Oliv99] We thank Olivier de Haas from the Institut für Festkörper- und Werkstofforschung Dresden, Germany for the Kerr microscopy experiments.

[Over62] A.W. Overhauser, Phys. Rev. **128**, 1437 (1962)

- [Pad99] S. Padovani, F. Scheurer, and J.P. Bucher, Europhys. Lett. **45**, 327 (1999)
- [Par91] S.S.P. Parkin, N. More, and K.P. Roche, Phys. Rev. Lett. **64**, 2304 (1990)
- [Par91b] S.S.P. Parkin, Z.G. Li, and D.J. Smith, Appl. Phys. Lett. **58**, 2710 (1991)
- [Parkin99] S.S.P. Parkin, K.P. Roche, M.G. Samant, P.M. Rice, R. B. Beyers, R. E. Scheuerlein, E.J. O'Sullivan, S.L. Brown, J. Bucchigano, D.W. Abraham, Yu Lu, M. Rooks, P.L. Trouilloud, R.A. Wanner and W.J. Gallagher, J. Appl. Phys. **85**, 5828 (1999)
- [Parr54] L.G. Paratt, Phys. Rev. **95**, 359 (1954)
- [Pap98] N. Papanicolaou, J. Phys. : Condensed Matter **10**, L131 (1998)
- [Prinz95] G. Prinz and K. Hathaway, Physics Today, April 1995, 24
- [Qiang97] Y. Qiang, S.Y. Chou, and J.-G. Zhu, J. Appl. Phys. **81**, 5461 (1997)
- [Rice70] T.M. Rice, Phys. Rev. B **2**, 3619 (1970)
- [Ruhr91] M. Rührig, R. Schäfer, A. Hubert, R. Mosler, J.A. Wolf, S. Demokritov, and P. Grünberg, Phys. Stat. Sol. (a) **125**, 635 (1991)
- [Russek99] S.E. Russek, J.O. Oti, S. Kaka and E.Y. Chen, J. Appl. Phys. **85**, 4773 (1999)
- [Sab66] T.M. Sabine and G.W. Cox, J. Phys. Chem. Solids **27**, 1955 (1966)

- [Sacha99] Alexander Volodin, Laboratorium voor Vaste-Stoffysica en Magnetisme, KULeuven, Belgium, Private communication (1999)
- [Savas99] T.A. Savas, M. Farhoud, H. I. Smith, M. Hwang, and C.A. Ross, J. Appl. Phys. **85**, 6160 (1999)
- [Scha94] R. Schad, C.D. Potter, G. Verbanck, V.V. Moshchalkov, and Y. Bruynsereade, Appl. Phys. Lett. **64**, 3500 (1994)
- [Schä98] A. Hubert and R. Schäfer, Magnetic Domains, Springer-Verlag Berlin (1998)
- [Schein99] M.R. Scheinfein, K.E. Schmidt, K.R. Heim, and G.G. Hembree, Phys. Rev. Lett. **76**, 1514 (1996)
- [Schr97] A. Schreyer, C.F. Majkrzak, Th. Zeidler, T. Schmitte, P. Bödeker, K. Theis-Bröhl, A. Abromeit, J.A. Dura, and T. Watanabe, Phys. Rev. Lett. **79**, 4914 (1997)
- [Shigeto99] K. Shigeto and T. Shinjo, Appl. Phys. Lett. **75**, 2815 (1999)
- [Shull53] C.G. Shull and M.K. Wilkinson, Rev. of Mod. Phys. **25**, 100 (1953)
- [Sim95] J.L. Simonds, Physics Today, April 1995, 26
- [Slon95] J.C. Slonczewski, J. Magn. Magn. Mater **150**, 13 (1995)
- [Smit51] J. Smit, Physica, **16**, 612 (1951)

- [Sonn98] P. Sonntag, P. Bödeker, A. Schreyer, H. Zabel, K. Hamacher, and H. Kaiser, *J. Magn. Magn.* **183**, 5 (1998)
- [Ste54] K.H. Stewart, *Ferromagnetic Domains*, University Press Cambridge (1954)
- [Swag97] H.J.M. Swagten, M.M.H. Willekens and W.J.M. de Jonge in *Frontiers in Magnetism of Reduced Dimension Systems*, edited by V. Bar'yaktar, P. E. Wigen and N. A. Lesnik, Chapter 11 The Giant Magnetoresistance effect, 471, Kluwer Academic Publishers (1997)
- [Tani99] T.Taniyama, I. Nakatani, T. Namikawa, and Y. Yamazaki, *Phys. Rev. Lett.* **82**, 2780 (1999)
- [Temst] Kristiaan Temst, *Laboratorium voor Vaste-Stoffysica en Magnetisme*, KULeuven, Belgium, private communication (1999)
- [Tehrani99] S. Tehrani, E. Chen, M. Durlam, M. Deherrera, J. M. Slaughter, J. Shi and G. Kerszykowski, *J. Appl. Phys.* **85**, 5822 (1999)
- [Toel95] T.S. Toellner, W. Sturhahn, R. Röhlberger, E.E. Alp, C.H. Sowers, and E.E. Fullerton, *Phys. Rev. Lett.* **74**, 3475 (1995)
- [Torr99] L. Torres, L. López-Díaz, O. Alejos, and J. Iñiguez, *J. Appl. Phys.* **85**, 6208 (1999)
- [Toul12] Y.S. Touloukian, *Thermophysical properties of matter vol 12 :Thermal expansion metallic Elements and alloys* (IF/Plenum New York 1977)
- [Toul13]] Y.S. Touloukian, *Thermophysical properties of matter vol 13 :Thermal expansion non metallic solids* (IF/Plenum New York 1977)

- [Tral94] L. Trallori, P. Politi, and A. Rettori, *J. Appl. Phys.* **76**, 6555 (1994)
- [Ume68] H. Umebayashi, G. Shirane, B.C. Frazer, and W.B Daniels, *J. Phys. Soc. Jap.* **24**, **368** (1968)
- [Van95] E.A.M. van Alphen and W.H.M. de Jonge, *Phys. Rev. B*, **51**, 8182 (1995)
- [Viegas98] A.D.C. Viegas, J. Geshev, J.E. Schimdt, E.F. Ferrari, *J. Appl. Phys.* **83**, 7007 (1998)
- [Vri97] J.J. de Vries, J. Kohlhepp, F.J.A. den Broeder, R. Coehoorn, R. Jungblut, A. Reinders, and W.J.M. de Jonge, *Phys. Rev. Lett.* **78**, 3023 (1997)
- [Wang94]. R.W. Wang, D.L. Mills, E.E. Fullerton, J.E. Mattson and S.D. Bader, *Phys. Rev. Lett.* **72**, 920 (1994)
- [Wang99] D. Wang, M. Tondra, J. M. Daughton, C. Nordman, and A.V. Pohm, *J. Appl. Phys.* **85**, 5255 (1999)
- [Wegrowe99] J.-E. Wegrowe, D. Kelly, A. Franck, S.E. Gilbert, and J.-Ph. Ansermet, *Phys. Rev. Lett.* **82**, 3681 (1999)
- [Wern68] S.A. Werner and A. Arrot, *J. Appl. Phys.* **39**, 671 (1968)
- [Will66] D.E.G. Williams, *The Magnetic Properties of Matter* (Longmans Green and Co., LTD 1966)
- [Will79] I.S. Williams, E.S. Raja copal, R. Street, *J. Phys. F*, **9**, 431 (1979)

- [Will81] I.S. Williams and R. Street, *Phil. Mag. B*, Vol. **43**, 893 (1981)
- [Win70] B. Window, *J. Phys. C, Suppl.* **2**, S210 (1970)
- [Wirth99] S. Wirth, S. von Molnár, M. Field, and D.D. Awschalom, *J. Appl. Phys.* **85**, 5249 (1999)
- [Won99] Won-Cheol Jeong, Byung-II Lee and Seung-Ki Joo, *J. Appl. Phys.* **85**, 4782 (1999)
- [Xu99] Y.B. Xu, C. A. F. Vaz, A. Hirohata, C.C. Yao, W.Y. Lee, J.A.C. Bland, F. Rousseaux, E. Cambril and H. Launois, *J. Appl. Phys.* **85**, 6178 (1999)
- [Yu99] J. Yu, U. Rüdiger, A.D. Kent, L. Thomas, and S.S.P. Parkin, *Phys. Rev. B* **60**, 7352 (1999)
- [Zab94] H. Zabel, *Physica B* **198**, 156 (1994)
- [Zab98] H. Zabel and A. Schreyer *Neutron News* **9**, 18 (1998)
- [Zab99] H. Zabel, *J. Phys. : Condens. Matter* **11**, 9303 (1999)
- [Zeid96] Th. Zeidler, F. Schreiber, and H. Zabel, *J. Appl. Phys.* **79**, 4793 (1996)
- [Zep89] W.B. Zeper, F.J.A. Greidanus, P.F. Carcia, and C.R. Fincher, *J. Appl. Phys.* **65**, p4971 (1989)
- [Zvze97] A.K. Zvezdin and V.A. Kotov, *Studies in Condensed Matter Physics, Modern Magneto-optics and Magneto-optical Materials* (IOP Publishing 1997)

Symbols

Vector quantities in the text are written in bold.

$a, a_{\perp}, a_{//}$	lattice parameter, out-of-plane, in-plane
AF_0	antiferromagnetic commensurate state
AF_1	transversal spin density wave state
AF_2	longitudinal spin density wave state
b	nuclear neutron scattering length
\mathbf{B}	magnetic induction
C_{11}, C_{12}	elastic constant

δ	position SDW with regard to the reciprocal lattice
Δ	Laplacian operator
E_d	demagnetisation energy
\mathbf{E}	electric field
E_{IEC}	Interlayer exchange coupling energy
$E_{X,Y}$	x-component of the electric field \mathbf{E}
ε	unity vector along scattering vector direction
f	scattering length
F_{hkl}	Structure factor for the hkl reflection
\mathbf{F}_{magn}	magnetic structure factor
G	Gibbs free energy density
$G_{crystal}$	Gibbs free energy density related to crystal anisotropy
G_{shape}	Gibbs free energy density related to shape anisotropy
G_{total}	Total Gibbs free energy density
\hbar	Planck's constant
\mathbf{H}, H	External magnetic field
H_{sf}	Spin flop field
\mathbf{H}_d	demagnetisation field
I	intensity/current
\mathbf{J}	current density
J_1	bilinear coupling constant
J_2	biquadratic coupling constant
k	wave vector
K_x	anisotropy constant
\mathbf{K}	unity vector along the spin direction
λ	wavelength
λ_v	magnetic volume charge density
m	mass
\mathbf{m}	unity vector magnetization
$\mathbf{M},$	magnetisation
M_s	saturation magnetisation
μ_0	permeability
μ_n	magnetic moment of the neutron
μ_N	nuclear magneton

N	demagnetisation tensor
\mathbf{n}	outward directed unity vector along surface normal
ϕ_d	demagnetisation potential
Ψ	wave function
p	magnetic scattering length
\mathbf{q}	scattering vector
\mathbf{Q}	spin density wave vector
\mathbf{r}	position vector
ρ	resistivity/density
$\rho_{//}$	resistivity for current and magnetisation being parallel
ρ_{\perp}	resistivity for current and magnetisation being perpendicular
σ_s	magnetic surface charge density
σ	Pauli matrices
θ	angle (general)
T_N	Néel temperature
T_{SF}	spin flip temperature
V	Volume/Voltage/Scattering potential

Abbreviations

AES	Auger Electron Spectroscopy
AMR	Anisotropic Magnetoresistance
CEMS	Conversion Electron Mössbauer Spectroscopy
GMR	Giant Magnetoresistance
IAM	Intralayer domain wall model
IEC	Interlayer Exchange Coupling
IEM	Interlayer domain wall model
IMBL	Ion and Molecular Beam Laboratory
LEED	Low Energy Electron Diffraction
MBE	Molecular Beam Epitaxy
MOKE	Magneto-Optical Kerreffect

RBS	Rutherford Backscattering
RHEED	Reflection High Energy Diffraction
PNR	Polarized Neutron Diffraction
PSHE	Pseudo Hall Effect
QMS	Quadrupole Mass Spectrometer
SDW	Spin Density Wave
SMR	Synchrotron Mössbauer Reflectometry
SSF	Surface Spin Flop
C-SDW	Commensurate Spin Density Wave
I-SDW	Incommensurate Spin Density Wave
L-SDW	Longitudinal Spin Density Wave
RT	Room Temperature
STM	Scanning Tunneling Microscopy
T-SDW	Transversal Spin Density Wave
UHV	Ultra High Vacuum
XRD	X-ray Diffraction

Samenvatting

1 Inleiding

Het onderwerp van deze thesis situeert zich in het domein van de magnetische dunne lagen en kleine structuren. Met de huidige preparatietechnieken kunnen diktes tot op atomair niveau gecontroleerd worden terwijl lateraal het submicron gebied toegankelijk is. Deze artificieel manipuleren van de natuur leidt tot nieuwe effecten gerelateerd aan de quantumnatuur van het elektron en de grootte van de structuren. Een van de recente voorbeelden is het 'Giant Magnetoresistance effect' (GMR) [Bai88]. Een afwisselende opeenstapeling van dunne Fe en Cr lagen toonde een grote weerstandsverandering bij het aanleggen van het magneetveld. De ontdekking van dit fenomeen leidde tot een intensief onderzoek vanuit een zowel fundamentele als ook industriële interesses. Als gevolg hiervan zijn er vandaag de dag sensors, leeskoppen en geheugens (MRAM's) op de markt gebaseerd op het GMR effect [Fer99, hfst. D6 en D11, Sim95].

Dit Fe/Cr systeem en de bijhorende eigenschappen vormen ook het basisingrediënt van deze thesis. Voortspruitend uit dit onderzoek op het Fe/Cr systeem is men ook de uitdaging aangegaan van het bestuderen van enkelvoudige epitaxiale Cr lagen welke een complex magnetisch fasediagramma vertonen. Tenslotte zal in een laatste deel de gedurende het onderzoek verkende technieken aangewend worden voor de studie van een Ni film met gaten erin. De bekomen resultaten zullen als volgt ingekleed en uiteengezet worden:

In hoofdstuk 2 zal de nodige algemene achtergrondkennis aangereikt worden door het

introduceren van de drie topics nl. Fe/Cr multilagen, epitaxiale Cr lagen en de gestructureerde Ni film.

Vervolgens, het experimenteel kader waarin dit onderzoek is doorgevoerd wordt vermeld in hoofdstuk 3. Afhankelijk van de nodige informatie heeft men de gepaste techniek gekozen om aldus een beter inzicht te verwerven.

Hoofdstuk 4 zal de experimentele resultaten presenteren. In een eerste deel wordt ingegaan op de magnetische eigenschappen van de Fe/Cr multilagen. De epitaxiale Cr lagen worden besproken in het tweede deel en het hoofdstuk wordt afgesloten met de studie op de Ni films.

Een overzicht van de belangrijkste conclusies is gegeven in hoofdstuk 5.

2 Kennismaking met de structuren en fenomenen

2.1 Fe/Cr multilagen

De eerste structuur die uitvoerig bestudeerd wordt in hoofdstuk 4 is een Fe/Cr multilaag. Deze structuur is epitaxiaal hetgeen wil zeggen dat de kristalroosters van MgO, Fe en Cr op mekaar georiënteerd zijn. Bovendien is de dikte van het Cr zo gekozen dat de Fe lagen antiferromagnetisch gekoppeld zijn. Een aldus schematisch verkregen overzicht is weergegeven in fig. 1. Indien er geen magnetisch veld aanwezig is liggen de magnetisaties in de Fe lagen in het vlak en langsheen de kristalassen. Met inbegrip van de antiferromagnetische koppeling leidt dit tot de vier mogelijke domeinstructuren die geschetst zijn in fig. 1.

richten. Wanneer het veld terug verlaagd wordt tot beneden het spinflopveld zullen die spins zich terug volgens de uniaxiale as richten. Het spinflopveld wordt bepaald door de competitie tussen eenerzijds de verhoging van de anisotropie-energie en anderzijds de verlaging van de Zeemanenergie door het gecreëerde netto magnetisch moment te richten volgens het magneetveld. Het bestudeerde Fe/Cr systeem daarentegen bezit een viervoudige anisotropy. Deze is gevormd door de twee onderlinge loodrecht georiënteerde makkelijke kristalassen [100] en [010] en de tussenliggende type [110] harde assen. In de initiële toestand zijn de magnetisaties in de antiferromagnetisch gekoppelde Fe lagen gericht volgens één van deze assen. Bij het aanleggen van een magneetveld volgens deze as zullen de spins overspringen naar de andere kristal as die loodrecht op het veld georiënteerd is. In tegenstellingen tot voor het uniaxiale systeem is deze transitie irreversiebel. Naast het vaststellen van de initiële en eind toestand van dit fenomeen heeft men gepoogd waar te nemen op welke wijze deze transitie gebeurt.

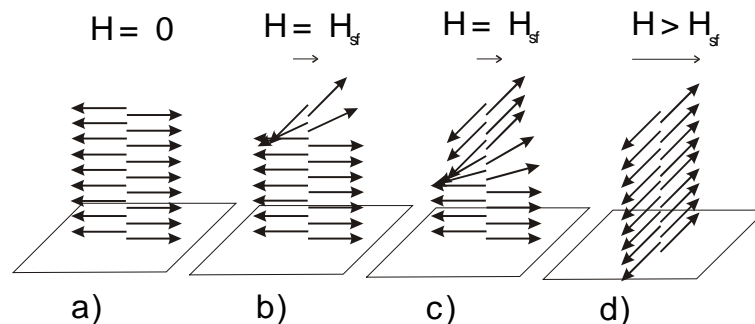


Fig. 3 De spinflop transitie volgens het IEM model. (a) toestand bij veld nul, (b) nucleatie van de domeinwand, (c) propagatie van de domainwand, (d) eindtoestand.

Twee mogelijke modellen zijn naar voorgeschoven. In het eerste model wordt een volledige Fe laag behandeld als een enkele spin. Door het aanleggen van het magneetveld ontstaat er een domeinwand tussen de verschillende Fe lagen zoals getekend in figuur 3. Deze domeinwand ontstaat aan een buitenlaag en verplaatst zich doorheen de multilaag teneinde de spinflop transitie te vervolledigen. Dit model wordt afgekort met IEM (Interlayer domain wall model).

Het tweede model is gebaseerd op domeinwanden binnen een Fe laag en wordt weergegeven in fig. 4. Door het verschuiven van domeinwanden groeien de domeinen waarin de magnetisatie loodrecht op het aangelegd magneetveld georiënteerd staat (ter vereenvoudiging wordt de kleine rotatie van de spins achterwege gelaten).

De verdere discussie van de twee modellen aan de hand van experimentele resultaten wordt besproken in hoofdstuk 4.

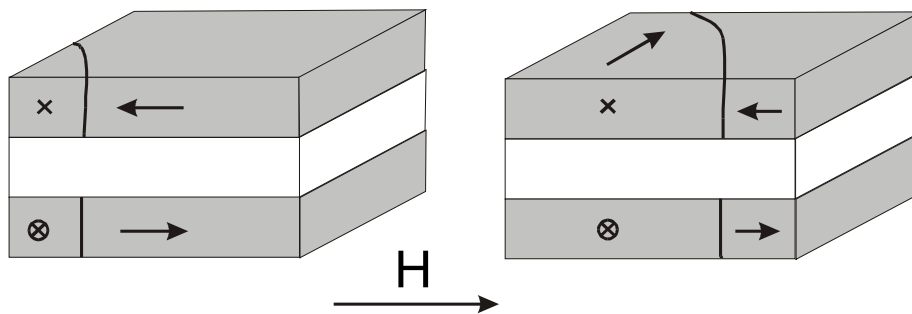


Fig. 4 De spinfloptransitie uitgelegd volgens domeinwandverschuivingen in de Fe lagen.

2.2 Epitaxiale Cr lagen

Voortvloeiend uit het onderzoek op de Fe/Cr multilagen is een interesse ontstaan voor het begrijpen van het magnetisme in dikke (5000Å)

epitaxiale Cr lagen. Reeds vroeger werd aangetoond dat deze structuren een complex en interessant magnetisch fazediagramma vertonen [Sonn98, Böd99]. Om deze fazediagramma's in te leiden zal kort het magnetisme van kristallijn Cr beschreven worden. Chroom als éénkristal is een itinerante antiferromagneet met een Neëltemperatuur van 311K. Beneden deze temperatuur vormt er zich een antiferromagnetische toestand waarvan de spins gemoduleerd zijn. Indien deze modulatie loodrecht op de spins staat (temperaturen boven 123 K) spreekt men van een transversale spindichtheidsgolf AF_1 (T-SDW). Voor temperaturen beneden de spinfliptemperatuur is de modulatie volgens de spinrichting resulterend in een longitudinale spindichtheidsgolf AF_2 (L-SDW). Beide modulaties zijn incommensurabel met het kristalrooster. Een voorstelling van deze structuren wordt gegeven door figuur 5.

AF_0

AF_1

AF_2

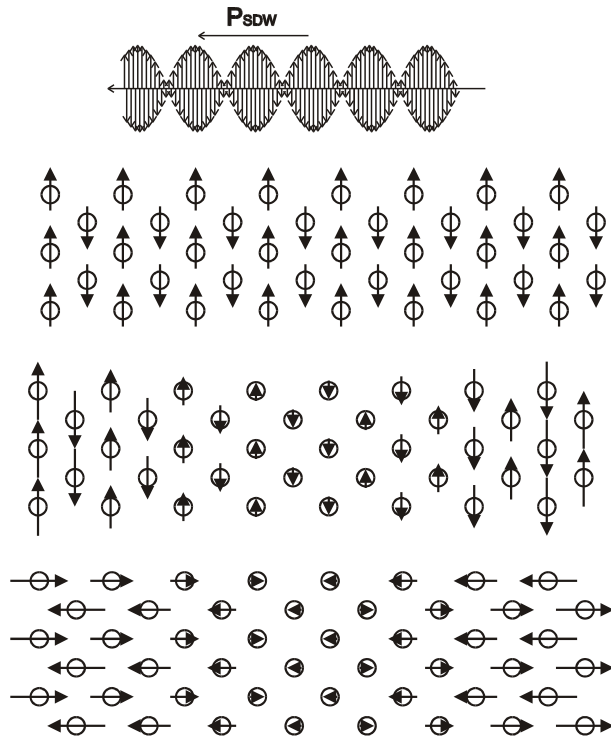


Fig. 5 De magnetische toestanden AF_0 , AF_1 en AF_2 van Cr.

In verstoorde systemen (defecten, onzuiverheden) wordt ook nog een derde fase waargenomen nl. de eenvoudige commensurable toestand AF_0 . De AF_0 toestand komt overeen met het eenvoudige beeld van een antiferromagneet zoals getoond in figuur 5. De manier waarop deze toestanden voorkomen in de hier bestudeerde lagen wordt besproken in hoofdstuk 3.

2.3 Een Nikkel gatenrooster

Het laatste deel handelt over een submicron Ni structuur. Kleine magnetische puntstructuren genieten van een grote interesse vanuit zowel het

fundamentele aspect alsook mogelijke toepassingen. Vooral roosters van magnetische punten, zie fig. 6, staan in de belangstelling. In dit werk zal het 'negatief' van zo'n structuur bestudeerd worden. Cowburn [Cow97] en Torres [Torr99] toonde reeds vroeger aan dat in deze systemen interessante magnetische effecten geobserveerd konden worden.

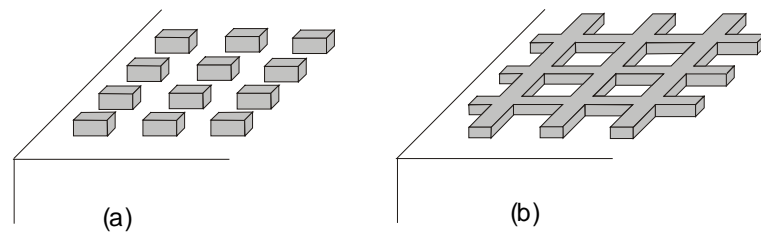


Fig. 6 *Het magnetisch puntrooster (a), en het negatief hiervan, het gatenrooster (b).*

3 Experimentele technieken

Het hedendaags wetenschappelijk onderzoek laat toe, in samenwerkingsverband, om over meerdere technieken te beschikken ter studie van fysische fenomenen. De hier bestudeerde structuren zijn vervaardigd m.b.v. MBE. Structurele informatie is vergaard uit RHEED-, XRD-, RBS- en AFM-experimenten. De magnetische en elektrische karakterisatie is gebaseerd op MOKE-, SQUID-, MFM-, neutronenreflectiviteits-, neutronendiffractie-, synchrotron Mössbauer reflectiviteits-, en (magneto) weerstandsmetingen.

4 Experimentele resultaten

4.1 Fe/Cr multilagen

In hoofdstuk 2.1 werd de structurele als ook de magnetische voorstelling van een Fe/Cr multilaag getoond in fig. 1. Het monster waarop gefocust zal worden is een $\text{MgO}(001)/[\text{Fe}(26\text{\AA})/\text{Cr}(13\text{\AA})]_{20}$ multilaag. De epitaxie, de antiferromagnetische koppeling en het GMR effect zijn bevestigd uit XRD, MOKE en magnetoweerstandsmetingen. Gepolariseerde neutronenreflectiviteitsmetingen tonen aan dat in de bestudeerde multilaag voornamelijk één van de vier voorheen genoemde domein structuren aanwezig is. Indien er een magnetisch veld wordt aangelegd langsheen deze magnetisatie-richting dan verspringt de magnetisatie van de antiferromagnetisch gekoppelde gebieden naar de andere kristalrichting, m.a.w. ze staat nu loodrecht op het aangelegde magneetveld. Figuur 7 laat het gepolariseerde neutronenreflectiviteitsexperiment zien meting waarin deze spinfliptransitie waargenomen is. In deze metingen verkrijgt men informatie over de magnetisatie-richting door de spin van het neutron te controleren en te meten. Antiferromagnetische domeinen met de magnetisatie parallel aan het aangelegde magneetveld worden weergegeven door de down-down/up-up intensiteit. Domeinen waarvan de magnetisatie loodrecht op de veldrichting staat geven aanleiding tot spinflipverstrooiing (up-down/down-up) intensiteit. De ferromagnetische gebieden worden niet waargenomen (andere periodiciteit). Bij een veld van ongeveer 250 Oe wordt een volledige omwisseling van de spinflip- en niet-spinflipintensiteiten waargenomen. Na de waarneming is een speurtocht op touw gezet naar de natuur van deze transitie, het onderscheiden van een IEM of IAM mechanisme. In eerste instantie werd een beroep gedaan directe technieken zoals MFM en Kerrmicroscopie, welke echter wegens experimentele tekortkomingen geen informatie opleverden.

Vervolgens werd aangetoond dat deze transitie ook waarneembaar is in magnetisatiemetingen. MOKE-metingen leverde informatie over het gedrag van de toplagen wegens de beperkte indringdiepte van het licht. SQUID metingen daarentegen zijn gevoelig aan het volledige monster en kunnen bovendien als functie van temperatuur worden uitgevoerd. Het vergelijken van de breedte van de transitie, waargenomen door beide technieken kan uitsluitsel geven over de aard. Ten tweede werd de transitie opgemeten en bestudeerd als functie van de temperatuur. De derde fase bestond uit gebruikmakend van het PSHE te speuren naar een IEM mechanisme. In de laatste experimentele fase is men gestart met SMR metingen. Tot nu toe konden deze experimenten geen doorslaggevend argument aanreiken voor een onderscheid tussen het IEM en IAM. Tenslotte werd in samenwerking met de groep van Bottyan [Bottyan] de experimentele data ingevoerd in een theoretisch IEM model.

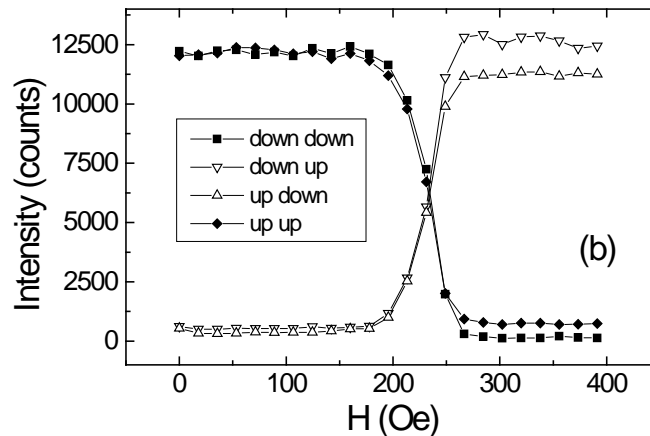


Fig. 7 *De spinflop transitie waargenomen volgens de gepolarizeerde neutronreflectiviteits experimenten.*

Samenvattend, heeft men antiferromagnetisch gekoppelde Fe/Cr superroosters gegroeid en gekarakteriseerd. In dit hoofdstuk is men dieper ingegaan op de magnetische structuur en het magnetisatieproces van deze antiferromagnetisch gekoppelde structuren. De aanwezige domainstructuur is niet isotroop verdeeld en er werd een nieuw type van spinfloptransitie waargenomen. In het verdere verloop heeft men via verschillende wegen de aard van deze transitie proberen te ontsluiëren. Twee modellen zijn naar voren geschoven voorgesteld welke aan de hand van verschillende technieken getoest zijn. Een duidelijk antwoord op de wijze waarop de transitie verloopt blijft tot nu toe achterwege.

4.2 Epitaxiale Cr lagen

Naar aanleiding van het de waarnemingen door Zabel [Sonn98, Böd99] werd de studie van het magnetisch fasediagramma van epitaxiale Cr lagen gegroeid op MgO(001) aangevat. In eerste instantie werd het eenvoudigste systeem, een MgO(001)/Cr(5000Å) gefabriceerd. Dit monster wordt verder aangeduidt met de benaming 'monster A'. Neutronendiffractiemetingen als functie van de temperatuur toonde de aanwezigheid aan van een in-het-vlak propagerende en uit-het-vlak gepolariseerde T-SDW aan beneden 200K. Voor hogere temperaturen (tot 400K) werd een AF₀ toestand waargenomen die uit-het-vlak gepolariseerd is. Het is duidelijk dat dit fasediagramma sterk verschilt van het éénkristallijn gedrag. Bovendien wordt er een sterke anisotropie waargenomen. De spins zijn uit-het-vlak georiënteerd en de I-SDW ligt in-het-vlak. De AF₀ toestand is verklaard door de aanwezigheid van roosterdefecten zoals ook reeds in het verleden werd waargenomen [Bacon69] . De

anisotropie in de spin- en golfvector richting is waarschijnlijk te wijten aan de aanpassing van de Cr eenheidscel op MgO. Magnesiumoxide heeft een 3% grotere roosterparameter. Dit zou kunnen resulteren in een expansie van de eenheidscel in het vlak en een contractie in de normale richting. Deze deformatie is experimenteel door XRD, RBS en neutronendiffractie waargenomen. Barak [Barak82] toonde theoretisch aan dat voor een zulke deformatie de spins preferentieel volgens de contractie richting staan en de golfvector volgens de expansie richting. Daar het hier om een éénmalig samengaan gaat van het theorie en experiment en dat het bovendien reeds herhaaldelijk werd aangetoond dat ook andere resultaten bekomen kunnen worden [Sonn98], heeft men een diepere studie aangevat. Vooreerst werd eenzelfde dikke Cr-laag gegroeid en bedekt met een Fe-toplaag. In andere experimenten werd een reoriëntatie van de I-SDW voortplantingsrichting waargenomen indien men de Cr-laag met een Fe-laag bedekt [Böd99]. Daarom heeft men ook MgO(001)/Cr(5000Å) bedekt met een Fe-laag, monster B. Ten derde heeft men een dikke Cr-laag gegroeid op een [Cr(30Å)/Au(30Å)]₁₀ multilaag. Deze bufferstructuur laat een verdere epitaxiale groei toe van een Cr laag. Bovendien kunnen nu spanningen geïnduceerd door het substraat relaxeren. Aansluitend hierop is Au gekozen vanwege de kleine roostermisfit met Cr, 0.1%. Men verwacht als dusdanig een verandering van de waargenomen anisotropie in monster A. Ten vierde heeft men monster A uitgestookt gedurende 1 uur op 100°C in UHV condities. Dit uitstoken kan eventueel de spanningen relaxeren. Het uitgestookte monster krijgt benaming D. Een overzicht van de roosterafstand in de richting loodrecht op het oppervlak is gegeven door tabel 1.

Monster	a_{\perp}
Bulk	$2.88459 \pm 0.00005\text{\AA}$
A	$2.882 \pm 0.001\text{\AA}$
B	$2.8831 \pm 0.0005\text{\AA}$
C	$2.8843 \pm 0.0005\text{\AA}$
D	$2.8853 \pm 0.0005\text{\AA}$

Tabel 1 *De roosterparameter in de uit het vlak richting van Cr.*

Waargenomen werd dat voor monster B het fazediagramma gelijkaardig is aan dat van monster A. De spins staan uit-het-vlak en er is een transitie van de AF_0 toestand ($T > 250\text{K}$) naar een uit-het-vlak gepolarizeerde, en in-het-vlak propagerende T-SDW ($T < 200\text{K}$). Enkel bij 20K werd een verschil waargenomen door de aanwezigheid van een in-het-vlak L-SDW. In monster C daarentegen is geen duidelijke voorkeur meer betreffende de richting van de spins. Bij kamertemperatuur staan de spins uit-het-vlak. Er wordt een AF_0 - en een T-SDW toestand waargenomen. Bij 200K is de AF_0 contributie verdwenen. De T-SDW staat nu uit-het-vlak gericht en met de spins in-het-vlak. Verder koelen tot 100K stabiliseert een uit-het-vlak gerichte L-SDW. In het vierde monster wordt enkel een uit-het-vlak gerichte T-SDW waargenomen waarbij de spins in-het-vlak liggen. De AF_0 toestand is verdwenen. Deze in het vlak anisotropie is in overeenstemming met het gedrag van de roosterparameter, zie tabel 1. Voor monster D is er een expansie van a_{\perp} waargenomen. De oorzaak van deze elongatie is waarschijnlijk te wijten aan

thermische spanningen tussen het MgO en Cr. Het verdwijnen van de AF₀ toestand is een teken een relaxatie bij hogere temperaturen. Bij het afkoelen 'stolt' de structuur en kunnen er thermische spanningen ontstaan. Daar de thermische expansie van MgO groter is dan die voor Cr zal deze laatste gecompriemd worden.

Tenslotte heeft men waar mogelijk de invloed van een magnetisch veld nagegaan. Het bleek dat de anisotropie in dunne lagen groter is dan in de Cr éénkristallen.

Ter beëindiging, in dit hoofdstuk heeft men gepoogd meer inzicht te krijgen in het complex fazediagramma van epitaxiale Cr lagen. Door de keuze van een gepast substraat heeft men aangetoond dat er een correlatie bestaat tussen de deformatie van de Cr eenheidscel en de richting van de antiferromagnetische spins. Vervolgens is de voortplantingsrichting van de I-SDW ook gecorreleerd aan deze deformatie.

4.3 Nikkel

In het laatste deel werd een experimentele studie uitgevoerd van Ni gatenrooster. De structuur bestaat uit een Si/SiO₂(5000Å)/ Ni(350Å)/Ag(20Å) film met een vierkant rooster van 0.6*0.8µm² gaten. De structuur is bekomen m.b.v. MBE te combineren met optische lithografie en lift-off technieken. Naast de gatenstructuur werd ook een volle Ni film gegroeid ter referentie. De structurele karakterisatie is doorgevoerd door AFM en XRD terwijl voor de magnetische karakterisatie MFM en MOKE aangewend is. MOKE metingen op zowel de film als het gatenrooster toonde aan dat de gatenstructuur een anisotropie veroorzaakt. Het magnetiseren volgens de Ni lijnen vertoont een harder gedrag dan de magnetisatie volgens de

diagonalen van de gaten. Dit fenomeen werd ook waargenomen in het PSHE.

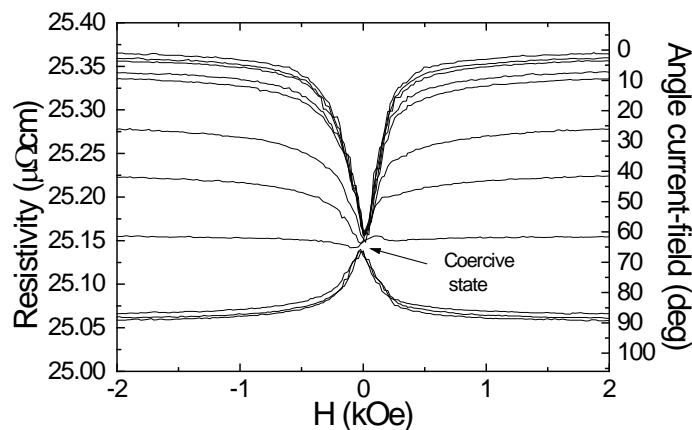


Fig. 8 De weerstand bij 5K als functie van stijgend veld voor verschillende hoeken tussen de stroom- en veldrichting is getoond.

Ten tweede werd er informatie als functie van de temperatuur bekomen uit het AMR effect. Figuur 8 toonde het verloop van de weerstand bij 5K als functie van veld voor verschillende hoeken tussen de stroom- en veldrichting.

Onafhankelijk van het magnetisatieproces duikt er een welbepaalde weerstandswaarde op bij het coërcitief veld. Vanwege het AMR effect is deze waarde gerelateerd aan de domeinstructuur. Deze waarde is niet in overeenstemming met een isotrope verdeling van de domeinen zoals waargenomen voor de volle Ni film. Bovendien kent deze waarde een temperatuursafhankelijkheid welke getoond wordt in figuur 9.

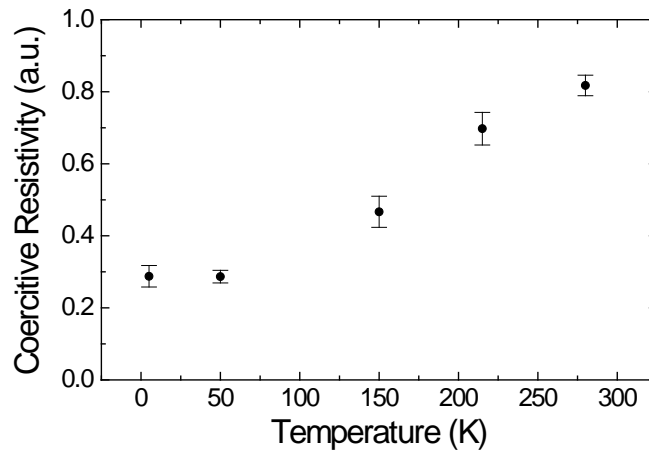


Fig. 9 *De weerstand bij coercitiviteit genormaliseerd op het totale AMR effect is getoond als functie van temperatuur.*

Al concluderende kan men vermelden dat een submicron Ni structuur vervaardigd, gekarakteriseerd en bestudeerd werd. Ter referentie werd een parallele studie van een volle Ni film uitgevoerd. De aanwezigheid van gaten wijzigt significant de magnetische eigenschappen van het film. Vooreerst wordt een viervoudige anisotropie waargenomen. Ten tweede werd er gebaseerd op het AMR effect een wijziging van de domeinstructuur bij het coërcitief veld als functie van de temperatuur opgemeten.

5 Conclusies

In dit werk heeft men Fe/Cr multilagen, epitaxiale Cr lagen en Ni gatenroosters onderzocht op correlaties tussen structurele- en magnetische eigenschappen. Er werd een duidelijke invloed van structurele anisotropieën op de magnetische

eigenschappen gevonden. In de Fe/Cr lagen werd een nieuw type spinfloptransitie waargenomen t.g.v. de kristalanisotropie. In de epitaxiale Cr-lagen werd spin- en propagatie-anisotropie van de I-SDW vastgesteld die gecorreleerd is aan de deformatie van de Cr-eenheidscel. Tenslotte werd aangetoond dat gaten in een Ni film een viervoudige anisotropie induceren gepaardgaande met een temperatuursafhankelijkheid van de magnetische domeinen.

Publications

Modification of structure, electric and magnetic properties of epitaxially grown Ag(001)/Fe(001) superlattices

G. Gladyszewski, J. Barnás, K. Temst, G. Verbanck, R. Schad, P. Beliën, E. Kunnen, F. Bodart, Y. Bruynseraede, *Journal of Magn. and Magn. Mat.* **156**, 381-382 (1996)

Epitaxially grown Ag(001)/Fe(001) superlattices

G. Gladyszewski, K. Temst, R. Schad, P. Beliën, E. Kunnen, G. Verbanck, Y. Bruynseraede, *Thin Solid Films* **275**, 180-183 (1996)

Periodic enhancement of the Electron-Electron Interactions and the Magnetoresistance in Magnetic Co/(Cr/Ag)/Co Multilayers

F.G. Aliev, E.Kunnen, K.Temst, K. Mae, G. Verbanck, J. Barnas, V.V. Moshchalkov, and Y. Bruynseraede, *Phys. Rev. Lett.* **78**, 134-137 (1997)

Coupling and Magnetoresistance in Co/Cr/Ag/Co structures

E. Kunnen, F.G. Aliev, K. Temst, G. Verbanck, K. Mae, M.J. Van Bael, J. Barnas, V.V. Moshchalkov and Y. Bruynseraede in V.G. Bar'yakhtar et al. (eds.), *Frontiers in Magnetism of Reduced*

Dimension Systems, 501-506 (1998) ISBN 0-7923-5026-X

Characterization of granular Ag films grown by low-energy cluster beam deposition

W. Bouwen, E. Kunnen, K. Temst, P. Thoen, M.J. Van Bael, F. Vanhoutte, H. Weidele, P. Lievens and R. E. Silverans, *Thin Solid Films* **354**, 87-92 (1999)

The magnetic structure of epitaxial Cr films on MgO

E. Kunnen, K. Temst, V.V. Moshchalkov, Y. Bruynseraede, S. Mangin, A. Vantomme, A. Hoser, *Physica B* **279-278**, 738 (2000)

Magnetic order and the spin flop transition in Fe/Cr superlattices

K. Temst, E. Kunnen, V.V. Moshchalkov, H. Maletta, H. Fritzsche and Y. Bruynseraede, *Physica B* **279-278**, 684 (2000)

Structure of Ag/Fe superlattices probed at different length scales

G. Gladyszewski, K. Temst, K. Mae, R. Schad, E. Kunnen, G. Verbanck, Y. Bruynseraede
Accepted for publication in *Thin Solid Films*.

Curriculum Vitae

Eddy Kunnen is geboren op 12 november 1971 te Bree, België. In 1990 volbracht hij zijn middelbare studies aan het Heilig Kruis College te Maaseik. De richting natuurkunde werd in 1991 aangevat in het Limburgs Universitair centrum waar hij in 1993 het kandidaatsdiploma behaalde. Hij studeerde in 1995 af als licentiaat in de Natuurkunde (cum laude) aan de Katholieke Universiteit Leuven. Het eindwerk werd uitgevoerd in het Laboratorium voor Vaste-Stoffysica en Magnetisme en is getiteld 'De invloed van bestraling en uitgloeijing op de eigenschappen van Fe/Ag superroosters'. Aansluitend hierop werd in hetzelfde laboratorium in 1996 het doctoraatsonderzoek op dunne en kleine magnetische structuren aangevat. Gefinancierd door het 'Vlaams Instituut voor de bevordering van het Wetenschappelijk-Technologisch Onderzoek in de industrie' (IWT) werd in 2000 onder het promotorschap van Prof. Dr. Y. Bruynseraede en Dr. K. Temst dit proefschrift tot het behalen van de graad 'Doctor in de wetenschappen' voorgelegd. Sinds maart 2000 is Eddy Kunnen als onderzoeker verbonden aan het Inter Universitair Micro-Electronica Centrum (IMEC).

